GIANT RADIO SOURCES AND EPISODIC ACTIVITY IN RADIO GALAXIES

A Thesis

Submitted For the Degree of

DOCTOR OF PHILOSOPHY

to the Tata Institute of Fundamental Research

by

Chiranjib Konar

NCRA
TIFR, PUNE
Pune – 411 007

FEBRUARY 2008

To Sykes, my parents, my grandma and Arpita

DECLARATION

I hereby declare that the work presented in the thesis entitled "**GIANT RADIO SOURCES AND EPISODIC ACTIVITY IN RADIO GALAXIES**" is entirely original and has been carried out by me at the National Centre for Radio Astrophysics, Tata Institute of Fundamental Research, Pune, India under the supervision of Prof. D. J. Saikia. I also declare that it has not been submitted elsewhere for the award of any degree or diploma.

Whenever any result/material of other investigators has been quoted in this thesis, they have been duely acknowledged.

Chiranjib Konar

CERTIFICATE

I hereby certify that the matter presented in the thesis entitled "**GIANT RADIO SOURCES AND EPISODIC ACTIVITY IN RADIO GALAXIES**" is entirely original and has been carried out by Mr. Chiranjib Konar at the National Centre for Radio Astrophysics, Tata Institute of Fundamental Research, Pune, India under my supervision, and that it has not been submitted elsewhere for the award of any degree or diploma.

Prof. D. J. Saikia
(Research Supervisor
NCRA-TIFR)

Acknowledgements

In 1999, immediately after finishing my M.Sc. from the University of Calcutta I joined TIFR, Mumbai as a junior research fellow (JRF). I did my graduate school course work there and then moved to NCRA, Pune for working on radio astronomy. It was fun for me to learn the techniques of radio astronomy. The first thing I learnt is how interferometry enables us to make radio images of sources in the sky. It was really confusing in the beginning. However, as time passed by, things were becoming clearer and clearer and the real fun began. I still remember those days when I was just learning `AIPS` (Astronomical Image Processing Software). I used to approach many people in NCRA for clarifications about AIPS. Those who spent significant amount of time in teaching me `AIPS` in the beginning are Subhasish Roy and C.S. Stalin and D.J. Saikia (my thesis supervisor). Both Subhasish and Stalin were Ph.D. students at that time. Subhasish was a student of NCRA and Stalin was a student of UPSO (Uttar Pradesh State Observatory) which has been renamed as ARIES (Aryabhatta Research Institute of Observational Sciences). He often used to visit NCRA for his radio observational work and I had a wonderful time with him. I had a wonderful time with the rest of the NCRA students, and I thank them for their help and company. I often reminisce the kind of exchange of arguments I used to have with Subhasish.

I thank members of the graduate studies committee (GSC) of TIFR, Mumbai. I thank the then chairperson of GSC Prof. Sunil Mukhi and the medical officer Dr. Agarkar who gave me useful pieces of advice during the time when I had a health problem.

I successfully finished my course work and joined NCRA in July 2001. I still remember the day I finally arrived at NCRA, that was Jul 10, 2001. I took a few courses in my first year in NCRA and I started working with Prof. D. J. Saikia since October, 2002. I thank Prof. Saikia for his grand supervision. I had reasonable freedom to do things the way I wanted. I have always had a great help from Prof. D. J. Saikia without which my Ph. D. would not have been possible. I would like to thank all the non-academic staff members as well for their kind help and cooperation extended to me and to all other members of NCRA-TIFR. I thank our librarian Ms. Sunita Barve for helping me and all other students for anything related to library issues. I thank also other library staff members (Sanjay, Suresh and Dalvi) who helped all students including me in different ways.

I express my sincere gratitude to my Polish collaborators Prof. Jerzy Machalski (JM) and Prof. M. Jamrozy (MJ) for their contributions in our major project on spectral ageing analysis of giant radio sources and double-double radio galaxies, which constitute a major fraction of my thesis. Without their cooperation this

major project would not have been finished. I remember spending wonderful time in Poland with MJ and JM in May-June, 2005. I learnt a lot from both of them. About my foreign visit, I should also mention my visit to ASTRON, Netherlands where Subhasish gave me good company as I was staying in his rented house in Dwingeloo. I also thank my other collaborators, namely C.H. Ishwara-Chandra, Neeraj Gupta, Vasant Kulkarni, Karl-Heinz Mack, Aneta Siemiginowska, Ashok Singal, Ł. Stawarz and Paul Wiita for their advice and inputs. I also thank Vasant and Gopal-Krishna, my review committee members, for their advice and comments on parts of my thesis.

I also feel obliged to express my sincere gratitude to a few persons who are not directly involved in the work I am presenting in this thesis, but discussions with them have always been fruitful. Low frequency mapping is always a tricky game and whenever one is stuck with that, the name which comes first in mind is Prof. A. Pramesh Rao. I thank Prof. A. Pramesh Rao who has always been friendly and helpful regarding discussions on astronomy and low-frequency mapping. I would like to thank Prof. Govind Swarup for several interesting discussions while taking 11 o'clock tea in the NCRA canteen. Discussions used to be on astronomy, general physics and his experience in life, which I always liked. Recently, I have been greatly benefited by Dr. Martin J. Hardcastle for the discussions on the various formalisms of estimation of equipartition magnetic field in the lobes of radio galaxies. In addition, I have spent a wonderful time with Subhasish Roy, Sabyasachi Pal, Jayanta Roy, Bhaswati Bhattacharyya and Nirupam Roy. With all of them I often had some or the other academic discussions (besides non-academic ones) which may not be related to my thesis but helped to keep my enthusiasm up. I acknowledge the computer related help from Vasant, Venkatsubramani, Shekhar as well as from Subhasish Roy, Jayanta Roy, Nirupam Roy, Sandeep Sirothia and Sabyasachi Pal.

Most of the observations presented in this thesis has been made with the GMRT. I thank all the staff members of GMRT including the telescope operators for their help and support which has made this possible.

I express my sincere gratitude to my parents and grandma not only for my Ph.D. degree but also for the entire education I have had till today. I owe my entire education to them in some sense. Their inspiration led me to the stage where I am today. Besides my parents, I like to thank my home-tutor (during my school days) Mr. Dibyendu Mukherjee whose inspiration is also worth mentioning. I thank all the teachers in my primary school, secondary school, under graduate college and university. I would like to thank Arpita, my better half, for the support and encouragement she provided.

Synopsis

Thesis Title: Giant Radio Sources and Episodic Activity in Radio Galaxies

Degree Registered: Ph.D.

Name of the student: Chiranjib Konar

Name of the supervisor: Prof. D. J. Saikia

Giant radio sources (GRSs) are the largest single objects in the Universe and represent the late stages of evolution of double-lobed radio sources. These are interesting objects to study a number of astrophysical questions ranging from understanding the evolution of radio sources to probing the external environment on these scales. GRSs have been identified both with radio galaxies and quasars and are defined to be those with a projected linear size $\gtrsim$1 Mpc ($H_0 = 71$ km s^{-1} Mpc^{-1}, $\Omega_m = 0.27$, $\Omega_{vac} = 0.73$). The limit of 1 Mpc is chosen merely for convenience, as there is a continuity in the sizes of radio sources.

A small but significant number of GRSs show a new pair of radio lobes closer to the nucleus in addition to the more distant and older pair of radio lobes. Such structures which have also been seen in a few sources of smaller dimensions have been christened as double-double radio galaxies (DDRGs). These sources represent the most striking examples of episodic nuclear activity.

In this thesis we present a number of new results based on our study of both GRSs and DDRGs. Our multifrequency radio observations of a sample of these sources using the Giant Metrewave Radio Telescope (GMRT) and the Very Large Array (VLA) have helped determine their structures and spectra over a large frequency range. These observations have been used to make reliable estimates of the spectral ages, injection spectral indices and to assess

the importance of inverse-Compton scattering of the cosmic microwave background (CMB) photons on the diffuse radio emission of the lobes of GRSs. We have reported the discoveries of a new DDRG, J0041+3224, with the GMRT, and also of old diffuse radio emission enveloping a young double-lobed source in the radio galaxy 4C29.30. We have presented a detailed spectral ageing analysis of 4C29.30 and the well-known DDRG, J1453+3308 and have shown that the inner lobes are indeed significantly younger than the more extended emission. We have used the symmetry parameters of both the inner and outer doubles of DDRGs to probe the environments in which these features lie.

Giant radio sources

It is widely believed that double radio sources evolve from the most compact giga-Hertz peaked spectrum (GPS) sources to the compact steep spectrum (CSS) sources, and then to the normal-sized radio sources (NSRSs) before evolving to form the GRSs. The GPS sources are typically $\lesssim$ few tens of pc, the CSS sources are defined to be $\lesssim$10 kpc while the NSRSs range upto hundreds of kpc. The radio power-linear size or P-D diagram for the 3CR and giant sources shows a deficit of sources with radio luminosity greater than about 2×10^{27} W Hz^{-1} at 1.4 GHz and sizes over a Mpc. Such a trend where the luminosity decreases as the source ages is broadly consistent with models of evolution of radio sources. However, the P-D diagram suggests a sharp decline in the distribution of sizes of GRSs at about 2 Mpc. There is also a deficit of GRSs at redshifts $\gtrsim 1$.

To understand the evolution of GRSs one needs to consider the effects of synchrotron and inverse-Compton losses as well as the external environment. The equipartition magnetic field strength in the radio lobes, B_{eq}, estimated using the classical formula (see, e.g., Miley 1980), is smaller than the equivalent magnetic field of the microwave background radiation, B_{iC}, for giant sources; while the reverse is true for the smaller powerful sources such as those chosen from the 3CR sample. If the values of B_{eq} are representative of the true magnetic field, the inverse-Compton losses dominate for the GRSs, while synchrotron radiation losses are more important for the smaller powerful sources. Although the difference is less marked if one uses the magnetic field estimates using the Beck & Krause (2005) formalism, this is still likely

to limit the number of GRSs at large redshifts. At least in the nearby Universe, GRSs are usually found in regions of low galaxy density. It has been suggested in the literature that a low density intergalactic medium (IGM) and/or a more powerful central engine may help the formation of these giant structures. However, recent studies have not found any significant evidence for the GRSs to have more prominent radio cores compared with smaller radio sources of similar luminosity. The large sizes are perhaps a combination of large ages and a low density external environment through which the jets propagate.

In this thesis we first present the results of our observations of a sample of 17 GRSs with the VLA and the GMRT. These observations have either helped clarify the radio structures or provided new information at a different frequency for these sources. The broad line radio galaxy, J0313+4120, has an asymmetric, curved radio jet and a variable radio core, consistent with a moderate angle of jet inclination to the line of sight. We suggest that the lobes of emission in J0139+3957 and J0200+4048 may be due to an earlier cycle of nuclear activity. We have identified a few candidates with either GPS or steep spectrum radio cores (SSCs), which may be a sign of renewed activity. If confirmed, this would indicate a trend for SSCs to occur preferentially in GRSs. In this sample of GRSs we also suggest that the prominence of diffuse emission decreases with redshift, possibly due to inverse-Compton losses. We have also imaged the highest redshift giant quasar, J1432+1548 at a redshift of 1.005 with the GMRT at 333 and 617 MHz. Although we detect a radio jet and have been able to demonstrate that the outer components are related, we do not detect a prominent bridge of radio emission.

For a sample of 10 GRSs we have presented multifrequency observations from $\sim$240 to 8000 MHz using both the GMRT and the VLA to determine reliably physical parameters, such as their spectra, spectral ages, magnetic field strengths and possibly injection spectral indices. We have estimated the magnetic field via different formalisms and find that the field strength estimated using the Beck & Krause (2005) formalism is larger than the classical equipartition value by a factor of about 3. Inverse-Compton losses with the CMB photons dominate over synchrotron radiative losses in the lobes of GRSs if the magnetic field is close to the classical equipartition values. This trend is not as prominent if the fields are close to those estimated using

the Beck & Krause (2005) formalism. The maximum spectral ages for the observed emission in our sources range from ∼6 to 36 Myr with a median value of ∼20 Myr using classical magnetic field estimates. The corresponding values using the magnetic fields from the Beck & Krause formalism range from ∼5 to 38 Myr with a median value of ∼22 Myr. These ages could be increased typically by a factor of ∼1.2 if the spectral age is extrapolated to the position of the core.

In all but one case (SE lobe of J1313+6937) the spectral age increases with distance from the hotspot regions, confirming that acceleration of particles mainly occurs at the hotspots. Most of the GRSs do not exhibit zero spectral age in the hotspots, as also found in earlier studies of smaller radio sources. This is likely to be largely due to contamination by more extended emission due to relatively modest resolutions of the images. The injection spectral indices estimated using low frequency measurements as well, range from ∼0.55 to 0.88 with a median value of ∼0.6. We explore possible correlations between the injection spectral index ($\alpha_{\rm inj}$) and the largest linear size, 1.4 GHz luminosity and redshift. For this sample we have explored the symmetry parameters of these radio sources and suggest that the external environment is asymmetric on these large scales.

Episodic activity in radio galaxies

One of the important issues concerning galaxies with an active galactic nucleus (AGN) is the duration of their AGN phase and whether such periods of activity are episodic. In the currently widely accepted paradigm, AGN activity is believed to be intimately related to the 'feeding' of a supermassive black hole whose mass ranges from $\sim10^6$ to 10^{10} $M_\odot$. Such an active phase may be recurrent with an average total timescale of the active phases being $\sim10^8$ to 10^9 yr. One of the more striking examples of episodic jet activity is when a new pair of edge-brightened radio lobes is seen closer to the nucleus before the 'old' and more distant radio lobes have faded. Such sources, as has been stated earlier, are called DDRGs. In such sources the newly-formed jets propagate outwards through the cocoon formed by the earlier cycle of activity, rather than the general intergalactic or intracluster medium, after traversing through the interstellar medium of the host galaxy. Approximately a dozen or so of such DDRGs are known in the literature.

In this thesis we report the discovery of a new DDRG, namely J0041+3224, with the help of the GMRT, and subsequent multifrequency observations with both the GMRT and the VLA. This object is somewhat unusual in the sense that the inner double is quite prominent, unlike other known DDRGs with an extended inner double. Although the frequency coverage is somewhat limited we find that the spectra of the lobes of the inner double are flatter than those of the outer double, as expected due to radiative losses.

In addition to the DDRGs, diffuse relic radio emission due to an earlier cycle of activity may also be visible around a young radio source with a classical double-lobed structure. We report the discovery of one such object, namely 4C29.30, where the diffuse emission has an extent of $\sim$640 kpc while the young inner double-lobed structure has an overall size of only about 36 kpc. We have made a detailed multifrequency study of this source from $\sim$240 to 8500 MHz using the GMRT, the Effelsberg telescope and the VLA. From similar resolution data we estimate the spectral index of the outer diffuse emission to be about 1.3 while that of the inner double is about 0.8. We estimate the spectral age of the outer diffuse emission to be $\gtrsim$200 Myr while that of the inner double is $\lesssim$33 Myr. Evidence for variability of the core flux density is also found.

We have also done multifrequency observations with the GMRT and the VLA and a detailed spectral ageing analysis of the well-known DDRG J1453+3308. The spectrum of the outer double has a spectral index of $\sim$0.6 till about a few hundred MHz and steepens towards higher frequencies, yielding a spectral age of $\sim$50 Myr. The inner double exhibits a straight spectrum of spectral index of $\sim$0.6, yielding an age $\lesssim$2 Myr. The low frequency spectral index should give us an estimate of the injection spectral index, suggesting that this value has not changed between the two cycles of activity.

To explore their environments, the symmetry parameters of the inner and outer doubles of a sample of about a dozen well-defined DDRGs have been examined. We find that the inner doubles tend to be statistically more asymmetric in both the armlength and the flux density ratios compared to the outer doubles. Defining the symmetry parameters to be greater than unity, the median values of the armlength ratio are $\sim$1.3 and 1.1 for the inner and outer doubles respectively. The corresponding values for the flux density ratios are $\sim$2.5 and 1.4 respectively. The outer doubles appear more

misaligned relative to the parent optical object, possibly due to a combination of the extended lobe emission responding to density gradients in the external medium and any possible motion of the parent galaxy.

The thesis has been arranged in 9 chapters as follows. The introduction is presented in Chapter 1 while Chapter 2 describes the observations of a sample of 17 GRSs made with the GMRT and the VLA, and the results obtained from these observations. Our observations of the giant quasar, J1432+1548 are presented in Chapter 3. GMRT observations of a selected sample of 10 GRSs, estimates of their magnetic field using different formalisms and the use of their symmetry parameters to probe the external environments are presented in Chapter 4. The GMRT observations of these sources have been combined with VLA observations to estimate the spectral ages of these sources. These results, as well as an examination of a possible correlation of the injection spectral indices with luminosity, redshift and size are presented in Chapter 5. Chapter 6 reports the discovery of a new DDRG, J0041+3224, and an examination of the symmetry parameters of the inner and outer doubles. Multifrequency GMRT and VLA observations as well as a spectral ageing analysis of the known DDRG J1453+3308 are presented in Chapter 7. In Chapter 8, we present our multifrequency observations with the GMRT and VLA as well as a spectral ageing analysis of the radio galaxy 4C29.30 where we have found relic diffuse radio emission in which a younger, smaller double-lobed source is embedded. The main conclusions and possible future work are presented in Chapter 9.

PUBLICATIONS

Refereed Publications

1. J1432+158: the most distant giant quasar;
   Singal Ashok K., **Konar C.**, Saikia D. J., 2004, **MNRAS**, 347, L79.

2. Radio observations of a few giant sources;
   Konar C., Saikia D. J., Ishwara-Chandra C. H., Kulkarni V. K., 2004, **MNRAS**, 355, 845.

3. J0041+3224: a new double-double radio galaxy;
   Saikia D. J., **Konar C.**, Kulkarni V. K., 2006, **MNRAS**, 366, 1391.

4. Spectral ageing analysis of the double-double radio galaxy J1453+3308;
   Konar C., Saikia D. J., Jamrozy M., Machalski J., 2006, **MNRAS**, 372, 693.

5. HI gas in rejuvenated radio galaxies: GMRT observations of the DDRG J1247+6723;
   Saikia D. J., Gupta Neeraj, **Konar C.**, 2007, **MNRAS**, MNRAS, 375, L31.

6. Intermittent jet activity in radio galaxy 4C29.30?;
   Jamrozy M., **Konar C.**, Saikia D. J., Stawarz Ł., Mack K.-H., Siemiginowska A., 2007, **MNRAS**, 378, 581.

7. A multifrequency study of giant radio sources - I. Low-frequency Giant Metrewave Radio Telescope observations of selected sources;
   Konar C., Jamrozy M., Saikia D. J., Machalski J., 2008, **MNRAS**, 383, 525.

8. A multifrequency study of giant radio sources-II. Spectral ageing analysis of the lobes of selected sources;
   Jamrozy M., **Konar C.**, Machalski J., Saikia D. J., 2008, **MNRAS**, in press (arXiv0712.0162J).

Conference Proceedings/Poster Papers

1. A study of giant radio galaxies;
   Konar Chiranjib, Saikia D. J., Ishwara-Chandra C. H., Kulkarni V. K., 2003, **BASI**, 31, 437.

2. Re-acceleration in the lobes of giant radio galaxies;
   Konar C., Machalski J., Saikia D. J., Jamrozy M., 2005, **AIPC**, 801, 375.

3. Giant radio sources;
   Konar C., Saikia D. J., Machalski J., Jamrozy M., Singal A. K., Mathur S., 2005, A paper presented in **URSI General Assembly 2005 in Delhi, India**.

4. Episodic activity in radio galaxies;
   Saikia D. J., **Konar C.**, Jamrozy M., Machalski J., Gupta Neeraj, Stawarz Ł., Mack K.-H., Siemiginowska A., 2006, A paper presented in the international conference, **The central engine of Active Galactic Nuclei, held in X'ian, China during October 2006**.

5. Recurrent activity in radio galaxies;
   Jamrozy M, **Konar C.**, Machalski J., Mack K.-H., Saikia D.J., Siemiginowska A., Stawarz Ł., 2007, A paper presented in an international conference, **Extragalactic Jets: theory and observation from radio to gamma ray, held in Girdwood, Alaska during May 2007**.

List of Figures

List of Tables

Contents

CHAPTER 1

Introduction

Galaxies are systems of stars and interstellar medium (ISM) embedded in dark-matter halos. They may contain several times 10^6 to a few times 10^{12} stars. It was Edwin Hubble, an American astronomer, who first categorised galaxies in a comprehensive way. The main categories are elliptical, spiral, lenticular and irregular galaxies (see Carroll & Ostlie 1996). Our Galaxy, the Milky Way, is a spiral galaxy which contains about 10^{11} to 10^{12} stars, while the Andromeda galaxy, the nearest neighbour, is also a spiral and is at a distance of about 2.5 million light years from us.

1.1 AGNs

Many galaxies harbour an active galactic nucleus (AGN) which is characterised by a stellar or semi-stellar nucleus which exhibits evidence of variability at different wavelengths. Most AGNs also have prominent emission lines. A small fraction of the AGNs are powerful radio emitters and have jets of relativistic plasma squirting out from the AGN and traversing distances upto about a Mpc. In extreme cases, such as in quasars, the nuclear light is extremely bright and can outshine the emission from the host galaxy. It is widely believed that the AGN phenomenon occurs due to accretion of matter onto a supermassive black hole of mass $\sim 10^6$ to 10^{10} $M_\odot$ residing at the centre of the galaxy.

Continuum spectra of AGNs: AGNs emit in almost all bands of the electromagnetic spectrum, starting from x-ray, hard x-ray to far infrared and radio wavelengths. As mentioned earlier, only a small fraction of AGNs, typically $\lesssim$10%, are powerful radio sources and are referred to as radio loud objects. The radio weak objects are referred to as radio quiet AGNs. Most AGNs are luminous in x-ray wavelengths. AGNs have a ratio of x-ray luminosity to optical luminosity that is much greater than that of a normal galaxy-centre. In addition to emission from the AGNs, x-ray emission has been seen from jets, lobes and hotspots in dozens of radio loud objects.

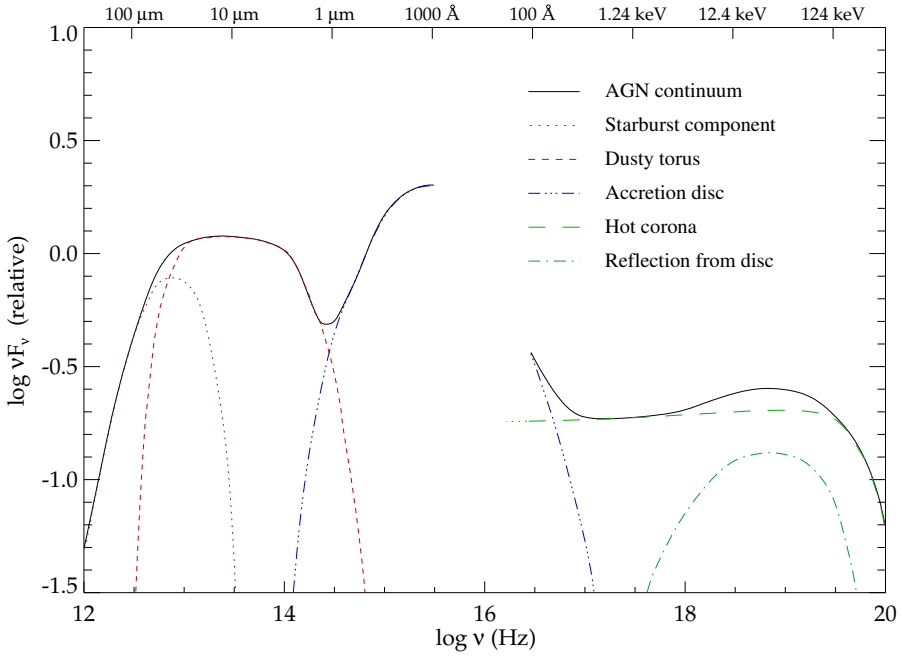

Figure 1.1: A typical composite continuum spectrum of AGNs. (Credit: James C. Manners, 2002, Ph.D. thesis, available as an electronic form in http://www.roe.ac.uk/ jcm/thesis/thesis.html)

The main features in a typical AGN continuum spectrum (Fig. 1.1) are the 'big blue bump' (from ∼4000 to at least ∼1000 Angstroms), 'near-infrared inflection' (which appears as a dip between 1 μm and 1.5 μm), the 'infrared

bump' (longward from 1 μm inflection), 'submillimetre break' (which is the strongest feature seen in the continua of normal quasars and basically is a sharp drop in emission), 'x-ray continuum' (which can be described as a power law from energies of 1 keV to about 10-20 keV and a cut-off beyond 100 keV) and 'soft x-ray excess' below 1 keV (Krolik 1999 and Manners 2002). Many AGNs also emit strongly at higher energies in the MeV and TeV ranges, while the radio loud objects show stronger radio emission at the lower frequencies.

Optical-UV continuum and emission lines of AGNs: A large number of broad and narrow emission lines are seen in addition to the broad continuum features such as the 'big blue bump' (see Fig 1.2). These lines are unusually strong compared to normal galaxies. This feature of an AGN spectrum makes the AGNs different from the spectra of stars and galaxies. In the stars, the lines are generally weak and mostly observed in absorption rather than in emission. The lines which we see most often in AGN along with the Optical-UV continuum are Lyα, Balmer lines, CIV1549 doublet and [OIII]5007 Angstroms.

At x-ray wavelengths we often see Fe Kα x-ray line at 6.4 keV. In some AGNs we see broad lines (widths of several thousands of km s^{-1}) along with narrow lines (widths of several hundreds of km s^{-1}), and in some AGNs we see only the narrow lines. These emission lines are often used to discover these objects (see Krolik 1999 and Manners 2002).

Variability of AGNs: Many AGNs are variable on time scales of years and months, weeks and even days. The variability does not appear to be periodic. Most of the AGNs are variable in the optical band with a typical amplitude

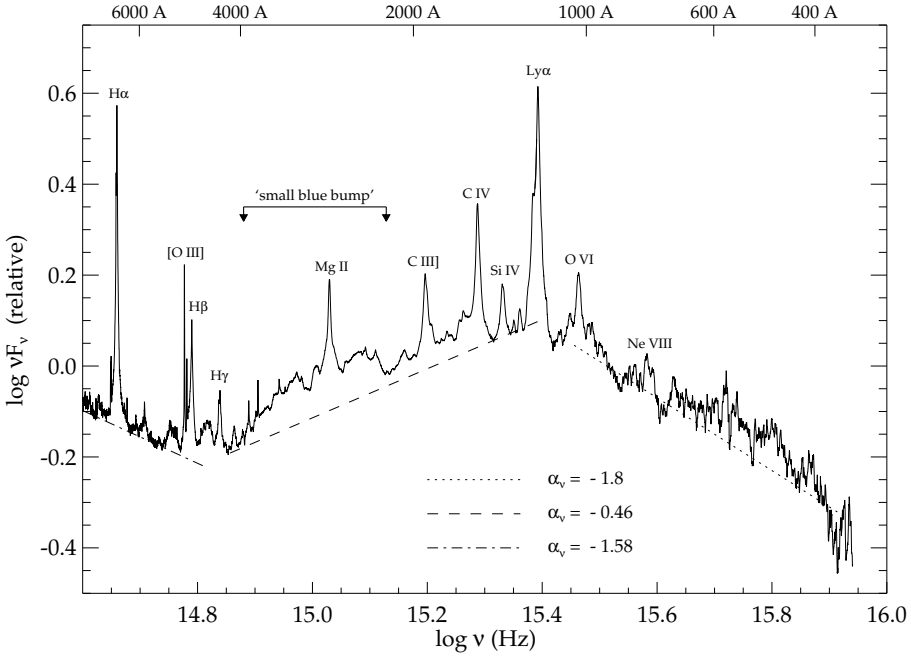

Figure 1.2: Optical - UV composite quasar spectrum. (Credit: James C. Manners, Ph.D. thesis, available as an electronic form in http://www.roe.ac.uk/ jcm/thesis/thesis.html)

of about 10% or so in a few years. But some of the AGNs vary by up to 2 to even 4 magnitudes or more. It is often assumed that most, if not all, AGNs are variable at some level. Some of the members of AGNs, e.g, Blazars, BL Lacs, OVVs (Optically Violently Variables), are amongst the most extremely active variable sources known in the Universe.

Radio emission: The AGN luminosity in radio band typically ranges from $\sim 10^{30}$ to $\sim 10^{38}$ W. Even for the strongest radio emitting AGNs, total radio emission is $\lesssim 1\%$ of the bolometric luminosity. Radio emitting structures range from parsec-scale central cores to well collimated jets and lobes extending over several hundreds of kpc. The AGNs have been classified as radio loud and radio quiet ones in terms of the relative strength of radio emission compared to that of other bands. To quantify the boundary between radio

loud and radio quiet AGNs, the widely accepted ratio, $R = \frac{L_\nu(6cm)}{L_\nu(B)}$ is considered; where $L_\nu(6cm)$ is the monochromatic radio luminosity at 6 cm and $L_\nu(B)$ is the monochromatic optical luminosity at B band (4400 Angstroms). The value separating the radio loud and radio quiet objects is $R = 10$ (Visnovsky et al. 1992; Stocke et al. 1992; Kellerman et al. 1994).

Members of the AGN-class: There are many different kinds of AGNs and they bear names depending on either how they were discovered or according to the properties they exhibit. Some of the well-known members are 'radio loud quasars', 'radio quiet quasars', 'broad line radio galaxies', 'narrow line radio galaxies', 'optically violently variable (OVV) quasars', 'BL Lac objects', 'Seyfert I galaxies', 'Seyfert II galaxies' and 'LINERs' (Low-Ionisation Nuclear Emission Regions). Some AGNs such as Seyferts are found in spiral galaxies while radio galaxies are associated with the elliptical galaxies. The host galaxies of quasars could be either spirals or ellipticals (Krolik 1999; Carroll & Ostlie 1996).

Canonical picture of an AGNs: In the canonical picture of an AGN, there is a supermassive ($\sim 10^6 M_\odot$ to $\sim 10^9 M_\odot$) black hole at the centre of an AGN. The black hole has an accretion disk which is surrounded by an obscuring molecular torus. There is a narrow line region (NLR) and a broad line region (BLR) around the black hole. The BLR and NLR are pictorially shown in Fig. 1.3. However, for radio loud AGNs there are two oppositely moving jets emanating from the central black hole, in addition to the above components.

Approximate scale of different components of an AGN: For a black hole of mass $\sim 10^8 M_\odot$, the Schowarzschild radius is $\sim 3 \times 10^{13}$ cm, the accretion disk extends from $\sim 1 - 30 \times 10^{14}$ cm from the central black hole, and the BLR extends from $\sim 2 - 20 \times 10^{16}$ cm from the black hole. The inner radius of the torus is $\sim 10^{17}$ cm and the NLR is located within $\sim 10^{18} - 10^{20}$ cm from the black hole. The radio jets can extend from few tens of pc to several hundreds of kpc on opposite sides of the black hole and perpendicular to the accretion disc (see Fig 1.3; Urry & Padovani 1995).

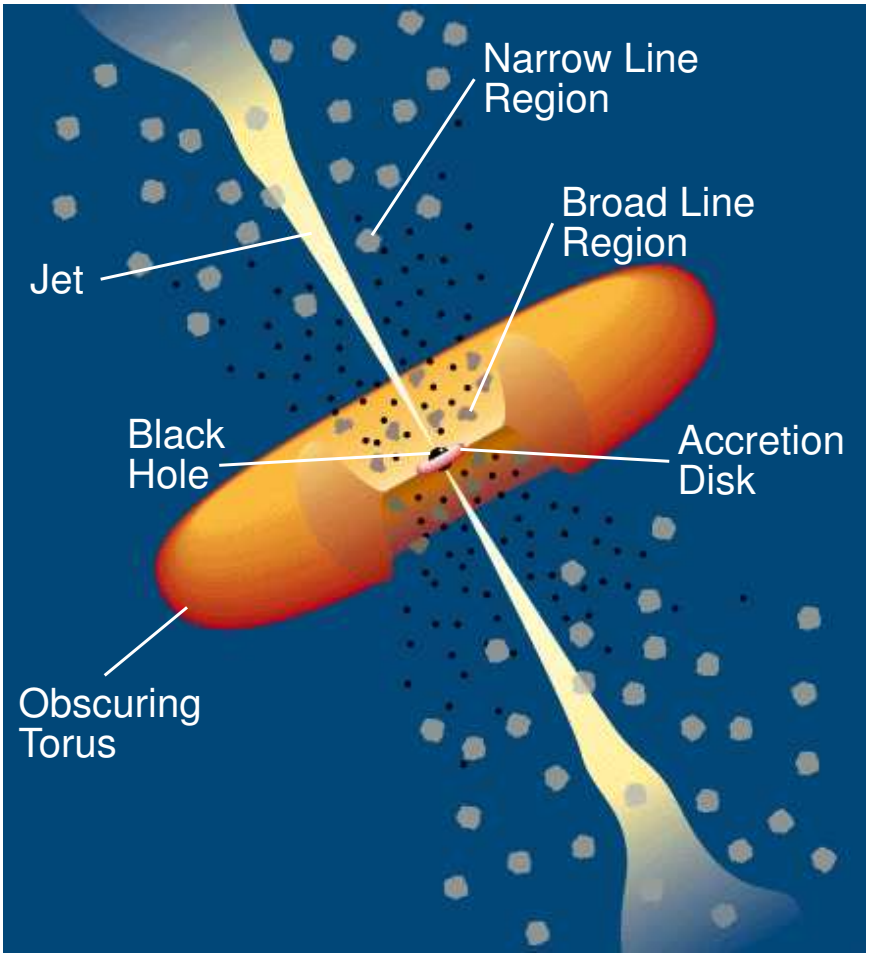

Figure 1.3: The Model for Radio-Loud AGN.
Credit: C.M. Urry and P. Padovani, available in http://heasarc.gsfc.nasa.gov/docs/cgro/images/epo/gallery/agns/index.html.

Orientation dependent unification scheme: Since all AGNs are believed to be driven by the same mechanism, namely accretion into the supermassive black hole, one might expect them to show all the properties of AGNs we have discussed so far. In actual practice this does not seem to be the case. For example, among the Seyfert galaxies, Type Is show broad emission lines, while Type IIs do not, Type Is have stronger continuum emission than Type IIs, and Type Is show higher amplitude in variability than Type IIs. Similarly, radio loud quasars show broad emission lines while radio galaxies usually have narrow lines; radio loud quasars often have prominent one sided jets while radio galaxies of similar radio luminosity usually have either no detected jets or more symmetric weaker jets. Also, the quasars are normally more variable than the radio galaxies.

A natural question that automatically arises in the context of AGNs is "What gives rise to the differences between Type I and Type II AGNs?". There have been many attempts to understand the apparent differences between different kinds of AGNs to be arising due to the effects of orientation and bulk relativistic motion of the jets while the AGNs are intrinsically similar (Lawrence 1987; Barthel 1989; Antonucci 1993; Urry & Padovani 1995). Therefore, in these schemes, which are referred to as unification schemes, there is a reduction in the diversity of AGNs.

In the unification scheme for the high luminosity radio galaxies and quasars which have similar edge brightened radio structures, the radio galaxies are seen along a line of sight which makes a large angle with respect to the axis of the torus or jet. As a result the BLR is obscured by the molecular torus and we do not see the broad emission lines. On the other hand, the quasars are seen at a smaller angles to the line of sight and hence the broad emission lines are visible. A similar scheme for unifying low luminosity radio

galaxies with BL Lac objects which have edge darkened structures has been suggested. For radio quiet objects, such as the Seyfert I and Seyfert II galaxies, a similar scheme for unification appears to be broadly consistent with the observations. An important difference between the unification scheme for radio loud objects and that of other AGNs is the inclusion of relativistic jets of synchrotron emitting plasma in radio loud AGNs. The relativistic beaming and Doppler shifts associated with the jets are sources of further anisotropy in addition to the obscuration by the torus.

1.2 Radio galaxies and quasars

The extended radio emission from radio galaxies and quasars can be broadly classified into two classes: Fanaroff-Riley class I (FRI) and Fanaroff-Riley class II (FRII). FRII sources are characterised by bright hotspots at the outer edges of lobes and are often referred to as edge brightened sources, while the FRI objects have diffuse lobes of emission with no edge brightened structures (see Fig. 1.4 and Fig. 1.5; Fanaroff & Riley 1974). The FRI sources are of lower luminosity and have reasonably symmetric jets on opposite sides which expand to form the diffuse lobes of emission. The FRII sources on the other hand are of higher luminosity and when detected have narrow well-collimated jets which link the core to the outer hotspots. The sizes of radio sources range from less than a few tens of pc for giga-Hertz peaked spectrum (GPS) sources to a few Mpc for the giant radio sources (GRSs). GRSs are defined to be those with a projected linear size $\gtrsim$1 Mpc ($H_0 = 71$ km s^{-1} Mpc^{-1}, $\Omega_m = 0.27$, $\Omega_{vac} = 0.73$; Spergel et al. 2003; these values of the cosmological parameters have been used throughout this thesis). The limit of 1 Mpc is merely for convenience, as there is a continuity in the sizes of radio sources.

It is widely believed that the double-lobed radio sources evolve from the most compact GPS sources to the compact steep spectrum (CSS) sources and then to the normal-sized radio source before evolving to form the GRSs. The radio power-linear size or P-D diagram for the 3CR and giant sources shows a deficit of sources with radio luminosity greater than about 2×10^{27} W Hz^{-1} at 1.4 GHz and sizes over a Mpc. Such a trend where the luminosity decreases as the source ages is broadly consistent with the models of evolution of radio sources (Kaiser, Dennett-Thorpe & Alexander 1997; Kaiser and Alexander 1999; Blundell, Rawlings & Willott 1999; Manolakou and Kirk 2002; Barai and Wiita 2006).

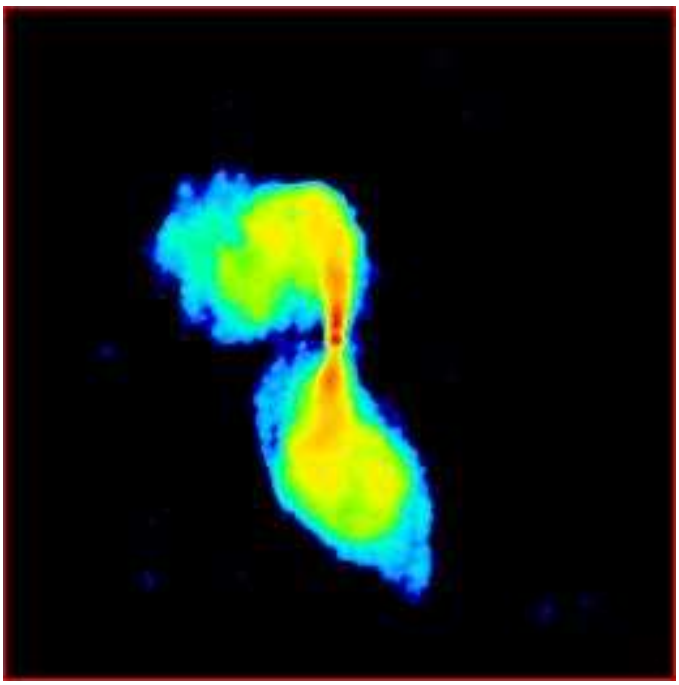

Figure 1.4: Radio image of 3C 272, an FRI radio galaxy. This image has been taken from http://www.jb.man.ac.uk/atlas/icon.html.

It has also been reported by a number of authors that radio sources show evidence of episodic activity (e.g. Junkes et al. 1993; Schoenmakers et al. 2000; Schilizzi et al. 2001; Saripalli et al. 2002, 2003; Marecki et al. 2003; Gizani & Leahy 2003; Saikia et al. 2006). Radio sources sometimes show

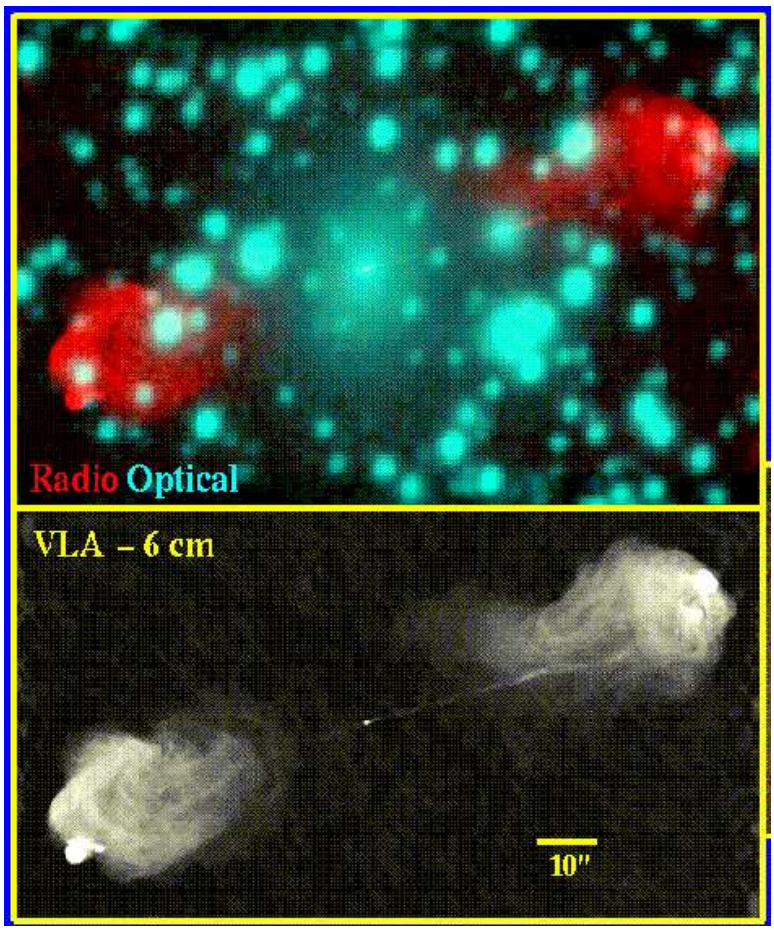

Figure 1.5: Radio image of Cygnus A (3C 405), an FRII radio galaxy. Top panel: Radio image overlayed on a wide-field optical image taken with the 0.9-m telescope at Kitt Peak National Observatory, courtesy of Frazer Owen as described by Owen at al. (1997). Bottom panel: Very Large Array (VLA) image of Cygnus A at 6 cm, which clearly shows the core, jet and hotspots. (This image has been taken from http://www.astr.ua.edu/keel/agn/cygnusa.html).

two pairs of radio lobes associated with the same optical host galaxy; these are believed to have formed due to episodic activity of the central engine and have been christened as double-double radio galaxies (DDRGs, see Fig. 1.6).

GRSs and DDRGs: GRSs and DDRGs are astrophysically interesting objects in terms of understanding the evolution of radio galaxies and the

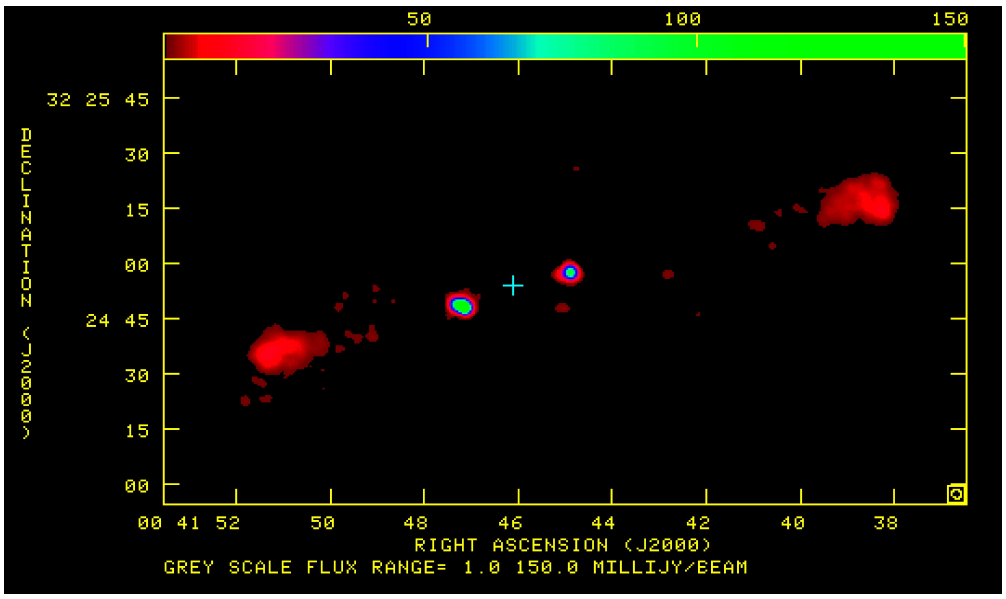

Figure 1.6: GMRT 1287-MHz image of a newly discovered DDRG (Saikia et al. 2006).

episodic jet activity which gives rise to DDRGs. In this thesis we have studied different aspects of GRSs and DDRGs. Our multifrequency observations with the Giant Metrewave Radio Telescope (GMRT) at low frequencies and with the Very Large Array (VLA) at high frequencies have helped us clarify various issues regarding their structures, evolution, ages, radio spectra, effect of inverse-Compton scattering against the cosmic microwave background (CMB) photons by the emitting particles of the radio lobes, environment of GRSs and the injection spectral indices ($\alpha_{\rm inj}$; defined as $S_\nu \propto \nu^{-\alpha}$) of the radio lobes.

GRSs: Recent attempts to identify GRSs from large radio surveys such as WENSS (Westerbork Northern Sky Survey, Rengelink et al. 1997), NVSS (NRAO VLA Sky Survey, Condon et al. 1998), FIRST (Faint Images of the Radio Sky at Twenty-cm, Becker, White & Helfand 1995) and SUMSS (Sydney University Molonglo Sky Survey, Bock et al. 1999; Mauch et al.

2003 and Murphy et al. 2007) have significantly increased their numbers to ∼150 or so. (Machalski, Jamrozy & Zola 2001; Chyży et al. 2005; Saripalli et al. 2005).

GRSs are useful for studying the late stages of the evolution of radio sources, constraining orientation-dependent unification schemes, improving our understanding of the physical properties of radio galaxies and probing the external environments (e.g. Subrahmanyan & Saripalli 1993; Subrahmanyan, Saripalli & Hunstead 1996; Mack et al. 1998; Ishwara-Chandra & Saikia 1999; Kaiser & Alexander 1999; Blundell, Rawlings & Willott 1999 and references therein; Schoenmakers et al. 2000, 2001).

To understand the evolution of GRSs, one needs to consider the effects of synchrotron and inverse-Compton losses as well as the external environment. The equipartition magnetic field strength in the radio lobes, B_{eq}, estimated using the classical formula (see, e.g., Miley 1980), is smaller than the equivalent magnetic field of the microwave background radiation, B_{iC}, for giant sources; while the reverse is true for the smaller powerful sources such as those chosen from the 3CR sample. If the values of B_{eq} are representative of the true magnetic field, the inverse-Compton losses dominate for the GRSs, while synchrotron radiation losses are more important for the smaller powerful sources. Although the difference is less marked if one uses the magnetic field estimates using the Beck & Krause (2005) formalism, this is still likely to limit the number of GRSs at large redshifts. At least in the nearby Universe, GRSs are usually found in regions of low galaxy density. It has been suggested in the literature that a low density intergalactic medium (IGM) and/or a more powerful central engine may help the formation of these giant structures. However, recent studies have not found any significant evidence for the GRSs to have more prominent radio cores compared with smaller

radio sources of similar luminosity (Ishwara-Chandra & Saikia 1999). The large sizes are perhaps a combination of large ages and a low density external environment through which the jets propagate.

DDRGs: One of the important issues concerning galaxies is the duration of their AGN phase and whether such periods of activity are episodic. In the currently widely accepted paradigm, activity is believed to be intimately related to the 'feeding' of a supermassive black hole whose mass ranges from $\sim 10^6$ to 10^{10} $M_\odot$. Such an active phase may be recurrent with an average total timescale of the active phases being $\sim 10^8$ to 10^9 yr (cf. Marconi et al. 2004, and references therein).

Of the galaxies harbouring an AGN, a small fraction appears to be luminous at radio wavelengths. For example, in the SDSS (Sloan Digital Sky Survey) quasars, $\sim$8 per cent of the bright ones (i <18.5) are radio loud in the sense that the ratio of radio to x-ray flux exceeds unity (Ivezić et al. 2002, 2004). Although what physical conditions determine loudness still remains unclear, Nipoti, Blundell & Binney (2005) have suggested recently that this may simply be a function of the epoch at which the source is observed.

For the radio-loud objects, an interesting way of probing their history is via the structural and spectral information of the lobes of extended radio emission. Such studies have been used to probe sources which exhibit precession or changes in the ejection axis, effects of motion of the parent galaxy, backflows from hotspots as well as X-shaped sources and major interruptions of jet activity. For example, the radio galaxy 3C388 exhibits two distinct regions of emission separated by a jump in spectral index, which has been interpreted to be due to two different epochs of jet activity (Burns, Schwendeman & White 1983; Roettiger et al. 1994). A ridge of emission,

reminiscent of a jet but displaced towards the south of the nucleus in the radio galaxy 3C338 could also be due to intermittent jet activity (Burns et al. 1983). Other suggestions of distinct epochs of jet activity based on spectral index studies include Her A, where the bright inner regions have flatter spectra with sharp boundaries delineating them from the more extended lobe emission, especially in the western lobe (Gizani & Leahy 2003), and 3C310 where the inner components B and D have substanially flatter spectra than the surrounding lobes (van Breugel & Fomalont 1984; Leahy, Pooley & Riley 1986). An interesting example of different epochs of jet activity is the well-studied radio galaxy Cen A, where in addition to the diffuse outer lobes there are the more compact inner lobes and a northern middle lobe or NML (Burns, Feigelson & Schreier 1983; Clarke, Burns & Norman 1992; Junkes et al. 1993). Morganti et al. (1999) have detected a large-scale jet connecting the northern lobe of the inner double and the NML, and have suggested that the formation of the NML may be due to a 'bursting bubble' in which plasma accumulated in the inner lobe bursts out through a nozzle. A lobe of emission on only one side of the nuclear region has also been seen in the GPS source B0108+388, and has been suggested to be a relic of a previous cycle of jet activity (Baum et al. 1990). However, the one-sidedness of the emission is puzzling (cf. Stanghellini et al. 2005), and it would be interesting to examine whether a 'bursting bubble' model may also be applicable in such cases.

One of the more striking examples of episodic jet activity is when a new pair of radio lobes is seen closer to the nucleus before the 'old' and more distant pair of radio lobes have faded. Such sources, as has been stated earlier, have been christened as DDRGs by Schoenmakers et al. (2000). They proposed a relatively general definition of a DDRG as a double-double radio

galaxy consisting of a pair of double radio sources with a common centre. They also suggested that the two lobes of the inner double should have an edge-brightened radio morphology to distinguish it from knots in a jet. In such sources the newly-formed jets propagate outwards through the cocoon formed by the earlier cycle of activity rather than the general intergalactic or intracluster medium, after traversing through the interstellar medium of the host galaxy. Approximately a dozen or so of such DDRGs are known in the literature (Saikia, Konar & Kulkarni 2006, and references therein). We have included objects such as 3C236 (Schilizzi et al. 2001) and J1247+6723 (Marecki et al. 2003) in this category since the principal difference is only in the size of the inner double which is $\lesssim$few kpc. It is important to identify more DDRGs not only for understanding episodic jet activity and examining their time scales, but also for studying the propagation of jets in different media. For example, to explain the edge-brightened hotspots in the inner doubles of the DDRGs, Kaiser, Schoenmakers & Röttgering (2000) presented an analytical model predicting how the new jets give rise to an inner source structure within the region of the old, outer cocoon. Assuming values of a number of free model parameters, e.g. the density of the external environment surrounding the old jets, the exponent of the density distribution as a function of the radial distance from the radio core, the initial energy distribution in the shock caused by the jet, they predicted a lower limit for the power of the old jets, and dynamical ages of the outer (older), t_{out}, and inner (younger), t_{inn}, double structures of a few selected DDRGs. In particular, for the source J1453+3308 they found $t_{out} = 215$ Myr and $t_{inn} = 1.6$ Myr. They have also suggested that warm (T$\sim 10^4$K) clouds of gas in the intergalactic medium are dispersed over the cocoon volume by surface instabilities induced by the passage of the cocoon material.

1.3 Spectral ageing of GRSs and DDRGs

Spectral ageing analyses of radio sources could provide useful insights into the physical properties and processes inside the radio lobes. For example, in the FRII radio sources particles are accelerated in the hotspots and diffuse outwards to form extended lobes and bridges of radio emission. Due to radiative losses the spectra are expected to steepen with distance from the hotspots. However, the variation of spectral index from the hotspot can be modified if there is significant reacceleration of particles in the lobes of these sources. In the absence of significant reacceleration the steepening of spectral index with distance from the hotspots can in principle be used to estimate the spectral age of the radiating particles. The theory of spectral ageing analysis is well described by a number of authors (Kardashev 1962, Pacholczyk 1970). However, while interpreting these ages, possible caveats related to the evolution of the local magnetic field in the lobes should be borne in mind (e.g. Wiita & Gopal-Krishna 1990; Rudnick, Katz-Stone & Anderson 1994; Jones, Ryu & Engel 1999; Blundell & Rawlings 2000; Kaiser et al. 2000).

Assumptions of spectral ageing analysis: We have performed our spectral ageing analysis under the assumptions that i) the magnetic field is constant in time and equal to the equipartition field, ii) each strip of plasma is a discrete element of plasma and there is no mixing of plasma between two adjacent strips, iii) the radiative lifetime of emiting plasma is much longer than the synchrotron age we are measuring, iv) any strip of plasma has been injected into the lobe with a power-law energy distribution and the index of the power law is same throught the lifetime of the source and v) the timescale

in which the radiating particles get isotropised in pitch angle is much shorter than the radiative ages of the particles.

We have considered three spectral ageing models, namely Kardashev-Pacholczyk (KP; Kardashev 1962; Pacholczyk 1970), Jaffe-Perola (JP; Jaffe and Perola 1973) and Continuus Injection (CI; Kardashev 1962; Pacholczyk 1970) models which we have considered. In the KP model, the assumption is that the electrons maintain their pitch angles throughout their lifetime; whereas in the JP model the pitch angles are assumed to be scattered and isotropised in a timescale much smaller compared with the spectral age of the source. Whenever there is a discrete element of plasma which has been injected in a time scale small compared to its life time, the KP and JP models may be appropriate. The CI model is applicable to a source where there is a continuous injection of particles. We fit the spectral ageing models to the flux-density values at different radio frequencies using the `SYNAGE` (Murgia 1996) package. The fits have three free parameters, namely the normalisation parameter, the injection spectral index ($\alpha_{\rm inj}$) and the break frequency ($\nu_{\rm br}$).

1.4 An outline of the thesis

We have conducted multifrequency observations of a sample of GRSs and DDRGs with the GMRT and the VLA to study their structure, evolution, radio spectra, spectral ages, injection spectral indices and the effect of inverse-Compton scattering on the diffuse emission of the lobes.

The GMRT is a synthesis imaging radio telescope located near a village called 'Khodad' which is about 80 km north of Pune city in India. The GMRT consists of thirty 45-m antennas. Twelve antennas are randomly placed within a central 1 km by 1 km square (the "Central Square") and the

remainder form the irregularly shaped Y (6 on each arm) over a total extent of about 25 km. Further details about the array can be found at the GMRT website at `http://www.gmrt.ncra.tifr.res.in`. At present, its frequency bands of operation are 150, 234, 325, 610 and 1280 MHz. Multifrequency observations of GRSs for this thesis work have been done at 234, 325, 610 and 1280 MHz bands with the GMRT. It is a unique instrument to conduct observations to look at the GRSs at low frequencies with relatively high resolution. To perform a spectral ageing analysis it is important to constrain the entire radio spectrum by as many frequencies of observations as possible. For constraining $\alpha_{\rm inj}$, low frequency measurements are crucial and the GMRT has played an important role in that.

The outline of the thesis is as follows. The introduction is presented in Chapter 1 while Chapter 2 describes the observations of a sample of 17 large radio sources made with the GMRT and the VLA, and the results obtained from these observations. Our observations of the giant quasar, J1432+1548 are presented in Chapter 3. GMRT observations of a selected sample of large radio sources, estimates of their magnetic field using different formalisms and also their symmetry parameters to probe the external environments are presented in Chapter 4. The GMRT observations of these sources have been combined with VLA observations to estimate the spectral ages of these sources. These results as well as an examination of a possible correlation of the injection spectral indices with luminosity, redshift and size are presented in Chapter 5. Chapter 6 reports the discovery of a new DDRG, J0041+3224 and an examination of the symmetry parameters of the inner and outer doubles. Multifrequency GMRT and VLA observations as well as spectral ageing analysis of the known DDRG J1453+3308 are presented in Chapter 7. In Chapter 8, we present our multifrequency observations with

the GMRT and VLA as well as spectral ageing analysis of the radio galaxy 4C29.30 where we have discovered relic diffuse radio emission in which a younger, smaller double-lobed source is embedded. The conclusions and possible future work are presented in Chapter 9.

References

Antonucci R, 1993, ARA&A, 31, 473

Barai P., Wiita P.J., 2006, MNRAS, 372, 381

Barthel P.D., 1989, ApJ, 336, 606

Baum S.A., O'Dea C.P., de Bruyn A.G., Murphy D.W., 1990, A&A, 232, 19

Beck R., Krause M., 2005, Astron. Nach., 326, 414

Becker R.H., White R.L., Helfand D.H., 1995, ApJ, 450, 559

Blundell K.M., Rawlings S., 2000, AJ, 119, 1111

Blundell K.M., Rawlings S., Willott C.J., 1999, AJ, 117, 677

Bock D.C.-J., Large M.I., Sadler, E.M., 1999, AJ, 117, 1578

Burns J.O., Feigelson E.D., Schreier E.J., 1983, ApJ, 273, 128

Burns J.O., Schwendeman E., White R.A., 1983, ApJ, 271, 575

Carroll & Ostlie, 1996, An Introduction to Modern Astrophysics. Addison-Wesley Publishing Company, Inc., USA

Chyży K. et al., 2005, Baltic Astron., 14, 358 (astro-ph/0310606)

Clarke D.A., Burns J.O., Norman M.L., 1992, ApJ, 395, 444

Condon J.J., Cotton W.D., Greisen E.W., Yin Q.F., Perley R.A., Taylor G.B., Broderick J.J., 1998, AJ, 115, 1693

Fanaroff B.L., Riley J.M., 1974, MNRAS, 167, 31

Gizani N.A.B., Leahy J.P., 2003, MNRAS, 342, 399

Ishwara-Chandra C.H., Saikia D.J., 1999, MNRAS, 309, 100

Ivezić Z., et al. 2002, AJ, 124, 2364

Ivezić Z., et al. 2004, ASPC, 311, 347

Jaffe W.J., Perola G.C., 1973, A&A, 26, 423

Jones T.W., Ryu D., Engel A., 1999, ApJ, 512, 105

Junkes N., Haynes R.F., Harnett J.I., Jauncey D.L., 1993, A&A, 269, 29

Kaiser C.R., Alexander P. 1999, MNRAS, 302, 515

Kaiser C.R., Dennett-Thorpe J., Alexander P., 1997, MNRAS, 292, 723

Kaiser C.R., Schoenmakers A.P., Röttgering H.J.A., 2000, MNRAS, 315, 381

Kardashev N.A., 1962, SvA, 6, 317

Kellermann K.I., Sramek R.A., Schmidt M., Green R.F., Shaer D.B., 1994, AJ, 108, 1163

Krolik J.H., 1999, Active Galactic Nuclei. Princeton University Press, Princeton, New Jersey

Lawrence A., 1987, PASP, 99, 309

Leahy J.P., Pooley G.G., Riley J.M., 1986, MNRAS, 222, 753

Machalski J., Jamrozy M., Zola S., 2001, A&A, 371, 445

Mack K.-H., Klein U., O'Dea C. P., Willis A. G., Saripalli L., 1998, A&A, 329, 431

Manners J.C., 2002, Ph.D. thesis, the University of Edinburgh

Manolakou K., Kirk J.G., 2002, A&A, 391, 127

Marconi A., Risaliti G., Gilli R., Hunt L.K., Maiolino R., Salvati M., 2004, MNRAS, 351, 169

Marecki A., Barthel P.D., Polatidis A., Owsianik I., 2003, PASA, 20, 16

Murphy T., Mauch T., Green A., Hunstead R.W., Piestrzynska B., Kels A.P., Sztajer P., 2007, MNRAS, 382, 382

Mauch T., Murphy T., Buttery H.J., Curran J., Hunstead R.W., Piestrzynski B., Robertson J.G., Sadler E.M., 2003, MNRAS, 342, 1117

Miley G., 1980, ARA&A, 18, 165

Morganti R., Killeen N.E.B., Ekers R.D., Oosterloo T.A., 1999, MNRAS, 307, 750

Murgia M., 1996, Laurea Thesis, University of Bologna

Nipoti C., Blundell K.M., Binney J., 2005, MNRAS, 361, 633

Owen at al., 1997, ApJ, 488, L15

Pacholczyk A.G., 1970, Radio Astrophysics. Freeman & Co., San Francisco

Rengelink R.B., Tang Y., de Bruyn A.G., Miley G.K., Bremer M.N., Roettgering H.J.A., Bremer M.A.R., 1997, A&AS, 124, 259

Roettiger K., Burns J.O., Clarke D.A., Christiansen W.A., 1994, ApJ, 421, 23L

Rudnick L., Katz-Stone D.M., Anderson M.C., 1994, ApJS, 90, 955

Saikia D.J., Konar C., Kulkarni V.K., 2006, MNRAS, 366, 1391

Saripalli L., Hunstead R. W., Subrahmanyan R., Boyce E. 2005, AJ, 130, 896

Schilizzi R.T. et al., 2001, A&A, 368, 398

Saripalli L., Subrahmanyan R., Udaya Shankar N., 2002, ApJ, 565, 256

Saripalli L., Subrahmanyan R., Udaya Shankar N., 2003, ApJ, 590, 181

Schoenmakers A.P., de Bruyn A.G., Röttgering H.J.A., van der Laan H., Kaiser C.R., 2000, MNRAS, 315, 371

Schoenmakers A.P., de Bruyn A.G., Röttgering H.J.A., van der Laan H., 2001, A&A, 374, 861

Spergel D.N. et al., 2003, ApJS, 148, 175

Stanghellini C., O'Dea C.P., Dallacasa D., Cassaro P., Baum S.A., Fanti R., Fanti C., 2005, A&A, 443, 891

Stocke J.T., Morris S.L., Weymann R.J., Foltz C.B., 1992, ApJ, 396, 487

Subrahmanyan R., Saripalli L., 1993, MNRAS, 260, 908

Subrahmanyan R., Saripalli L., Hunstead R.W., 1996, MNRAS, 279, 257

Urry C.M., Padovani P., 1995, PASP, 107, 803

van Breugel W., Fomalont E.B., 1984, ApJ, 282, 55L

Visnovsky K.L., Impey C.D., Foltz C.B., Hewett P.C., Weymann R.J., Morris S.L., 1992, ApJ, 391, 560

Wiita P.J., Gopal-Krishna, 1990, ApJ, 353, 476

CHAPTER 2

Radio observations of a few giant sources

2.1 Abstract

We present multifrequency observations with the GMRT and VLA of a sample of seventeen largely GRSs. These observations have either helped clarify the radio structures or provided new information at a different frequency. The broad line radio galaxy, J0313+413, has an asymmetric, curved radio jet and a variable radio core, consistent with a moderate angle of inclination to the line of sight. We attempt to identify steep spectrum radio cores (SSCs), which may be a sign of recurrent activity, and find four candidates. If confirmed, this would indicate a trend for SSCs to occur preferentially in GRSs. From the structure and integrated spectra of the sources, we suggest that the lobes of emission in J0139+399 and J0200+408 may be due to an earlier cycle of nuclear activity. We find that inverse-Compton losses with the CMB photons dominate over synchrotron radiative losses in the lobes of all the sources, consistent with earlier studies. We also show that the prominence of the bridge emission decreases with increasing redshift, possibly due to inverse-Compton losses. This could affect the appearance and identification of GRSs at large redshifts.

2.2 Introduction

GRSs are the largest single objects in the sky, and their large sizes enable us to look at their structures in detail even with the only moderate resolutions possible at low frequencies (e.g., at 240 MHz with the GMRT). As discussed in Chapter 1, these sources are important for studying the late stages of the evolution of radio sources as well as for other astrophysical issues such as probing their environments and their evolution with redshift.

In this chapter we first report GMRT and VLA observations of a sample of largely giant sources. A few of the sources were earlier classified as GRSs, but now have projected sizes smaller than 1 Mpc, based on a revised value of the Hubble constant. We have nevertheless included these sources in this chapter, since there is a continuity of sizes and the limit of a Mpc is a working definition to identify those in the late stages of evolution. These observations have either helped clarify the radio structures or provided new information on these sources at a different frequency. We examine the radiative losses in these sources using the classical equipartition magnetic field (e.g. Miley 1980), and show that inverse-Compton losses dominate over synchrotron radiative losses in the lobes, consistent with earlier studies (e.g. Ishwara-Chandra & Saikia 1999, hereinafter referred to as IC99; Schoenmakers et al. 2000a). In order to develop strategies for identifying GRSs at high redshifts we investigate the prominence of bridge emission, $f_{\rm bridge}$, as a function of redshift, and find that $f_{\rm bridge}$ decreases with increasing redshift. These diffuse regions of emission are more likely to be affected by inverse-Compton losses, which would affect the appearance and identification of giants at large redshifts. We explore the evidence for the steep-spectrum cores (SSCs) ($\alpha_{\rm core}\lesssim -0.5$, $S_\nu \propto \nu^\alpha$), which might indicate renewed activity,

being more common in GRSs compared with the smaller-sized objects, and identify candidate SSCs in our sample. Assuming that nuclear activity may be recurrent, we attempt to identify lobes from earlier episodes of nuclear activity on the basis of the structure and their overall radio spectra.

Table 2.1: Observing log

Teles-cope	Array Conf.	Obs. Freq. GHz	Sources	Obs. Date
GMRT		0.6	J0657+481	2003 January 10
GMRT		0.6	J0313+413, J1313+695	2003 September 06
GMRT		0.6	J1604+375, J2042+751	2004 January 01
GMRT		0.6	J1702+422	2004 January 17
GMRT		1.3	J0139+399	2003 August 19
VLA	BnC	1.4	J0657+481, J1101+365 J1200+348, J1235+213 J1313+695	2000 March 10
VLA	BnC	1.4	J0135+379, J0313+413 J1604+375, J1637+417 J1702+422, J2312+187	2000 March 13
VLA	D	5	J0135+379, J0139+399 J0200+408, J0754+432 J0819+756, J1101+365 J1919+517, J2042+751 J2312+187	2000 July 24
VLA	D	5	J1200+348, J1313+696 J1604+375, J1637+417 J1702+422	2000 August 18
VLA	D	5	J0657+481	2000 September 11

2.3 Observations and analyses

The observations were made in the standard fashion, with each source observation interspersed with observations of the phase calibrator. The primary flux density calibrator was either 3C48, 3C147 or 3C286, with all flux densities being on the Baars et al. (1977) scale. The observing time on the source

varied from about an hour to a few hours. However, the low-frequency data were sometimes significantly affected by ionospheric disturbances.

The observations with the VLA were made in the snap-shot mode in the L and C bands with approximately 10 to 20 minutes on the source. The flux densities are again on the Baars et al. (1977) scale. All the data were calibrated and analysed in the standard way using the NRAO `AIPS` package. Spectral indices were estimated from our data only for regions or features which were unlikely to be significantly affected by any missing flux density.

The observing log for both the GMRT and the VLA observations is given in Table 2.1 which is arranged as follows. Columns 1 and 2 show the name of the telescope, and the array configuration for the VLA observations; column 3 shows the approximate frequency of the observations in GHz, while the sources observed and the dates of the observations are listed in Columns 4 and 5 respectively. The precise frequencies in MHz are shown in each image and are also listed in Table 2.2.

2.4 Observational results

The images of the sources are presented in Figures 2.1 − 2.17, while the observational parameters and some of the observed properties are presented in Table 2.2, which is arranged as follows. Column 1: Name of the source; column 2: frequency of observations in units of MHz, and the letter G or V representing either GMRT or VLA observations; columns 3-5: the major and minor axes of the restoring beam in arcsec and its PA in degrees; column 6: the rms noise in units of mJy/beam; column 7: the integrated flux density of the source in mJy estimated by specifying an area enclosing the entire source. We examined the change in flux density by specifying different areas

and found the difference to be within a few per cent of the total. The flux densities at different frequencies have been estimated over similar areas.

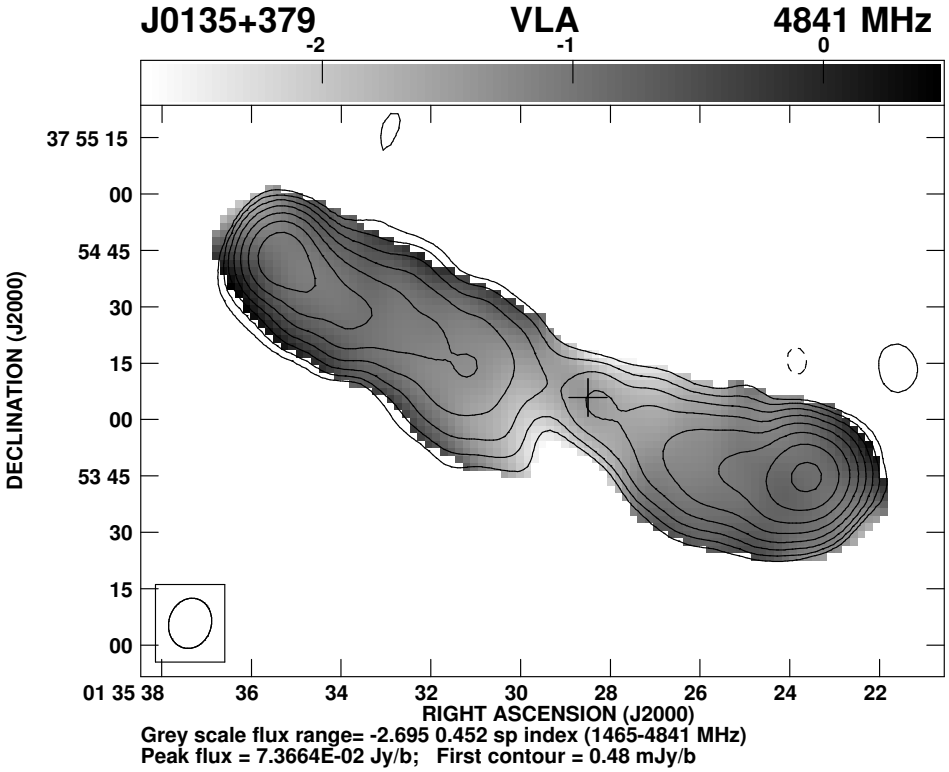

Figure 2.1: Radio image of J0135+379. The contour levels for all the images in this chapter are -1, 1, 2, 4, 8, 16, ... times the first contour level. The peak brightness in the image in units of Jy/beam and the level of the first contour in units of mJy/beam are given below all the images. The restoring beam is indicated by an ellipse. The + sign indicates the positions of the optical identification available in the literature. In four of the images the spectral index distribution in gray is superimposed on the total-intensity contours.

Columns 8, 11 and 14: component designation, where W, E, N, S and C denote the western, eastern, northern, southern and core components respectively; columns 9 and 10, 12 and 13, and 15 and 16: the peak and total flux densities of each of the components in units of mJy/beam and mJy. The core flux densities were sometimes evaluated by imaging the source using the longer spacings so that the core appears reasonably isolated. The

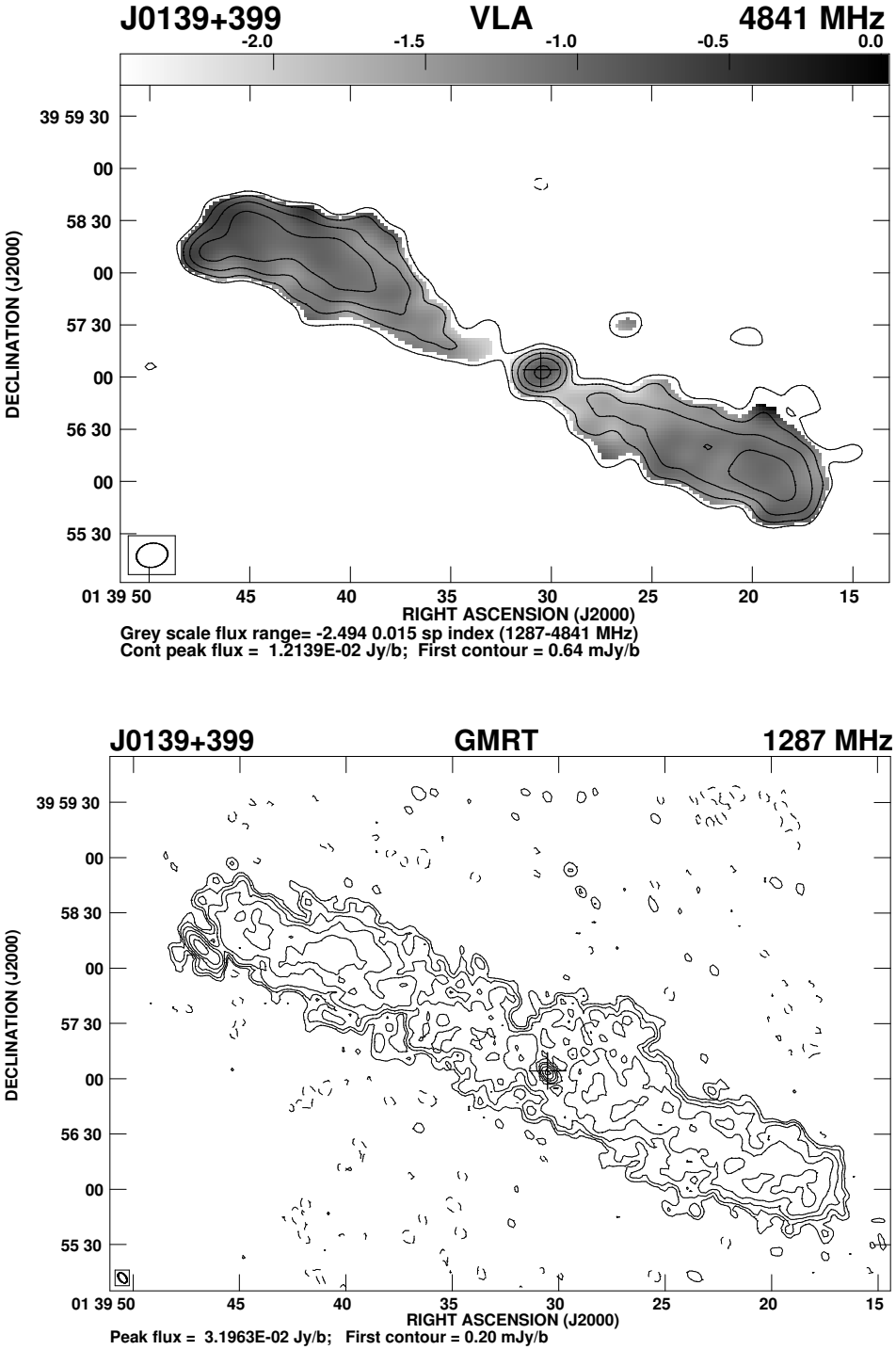

Figure 2.2: Radio images of J0139+399

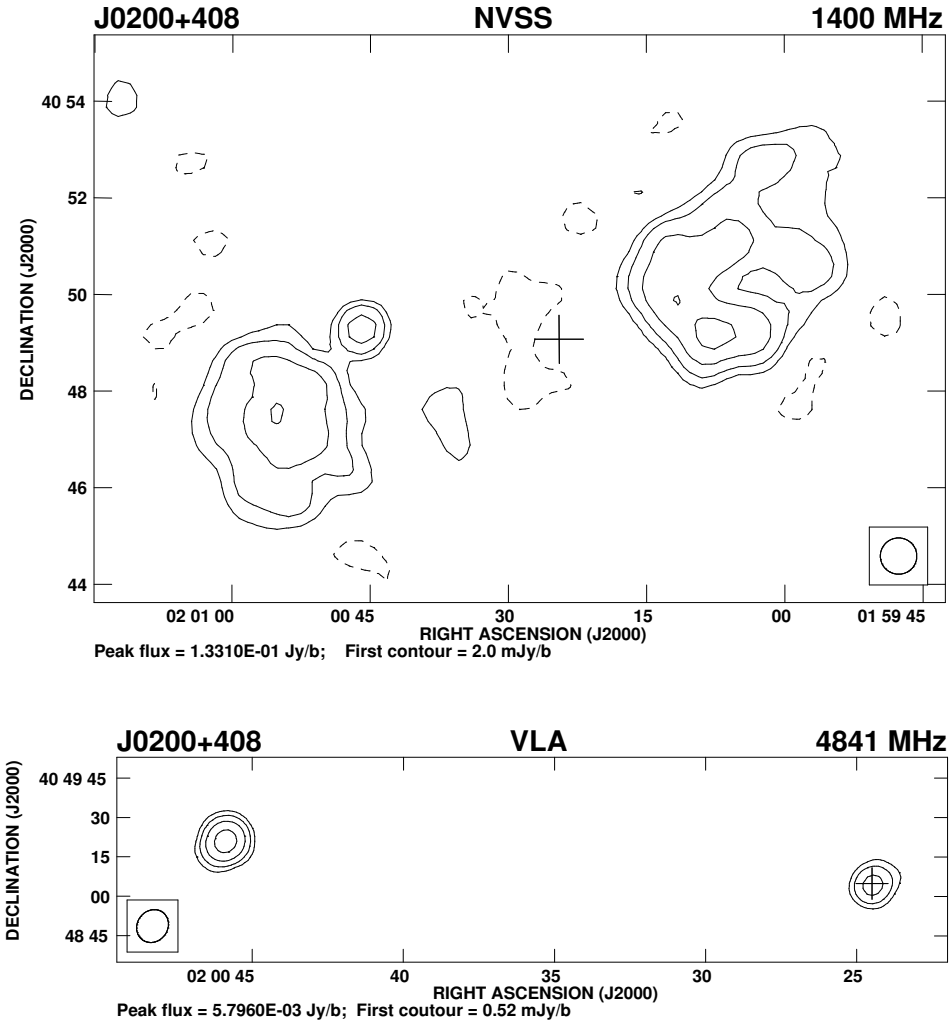

Figure 2.3: Radio images of J0200+408.

superscript g indicates that the flux densities have been estimated from a two-dimensional Gaussian fit to the core component. A ? denotes a possible detection of a core component which requires further confirmation.

(a) Notes on the sources

J0135+379, 3C46: VLA B- and C-array images at L-band (Gregorini et al. 1988; Vigotti et al. 1989) show the extended lobes of emission. Higher-resolution A-array observations by Neff et al. (1995) list the core flux density

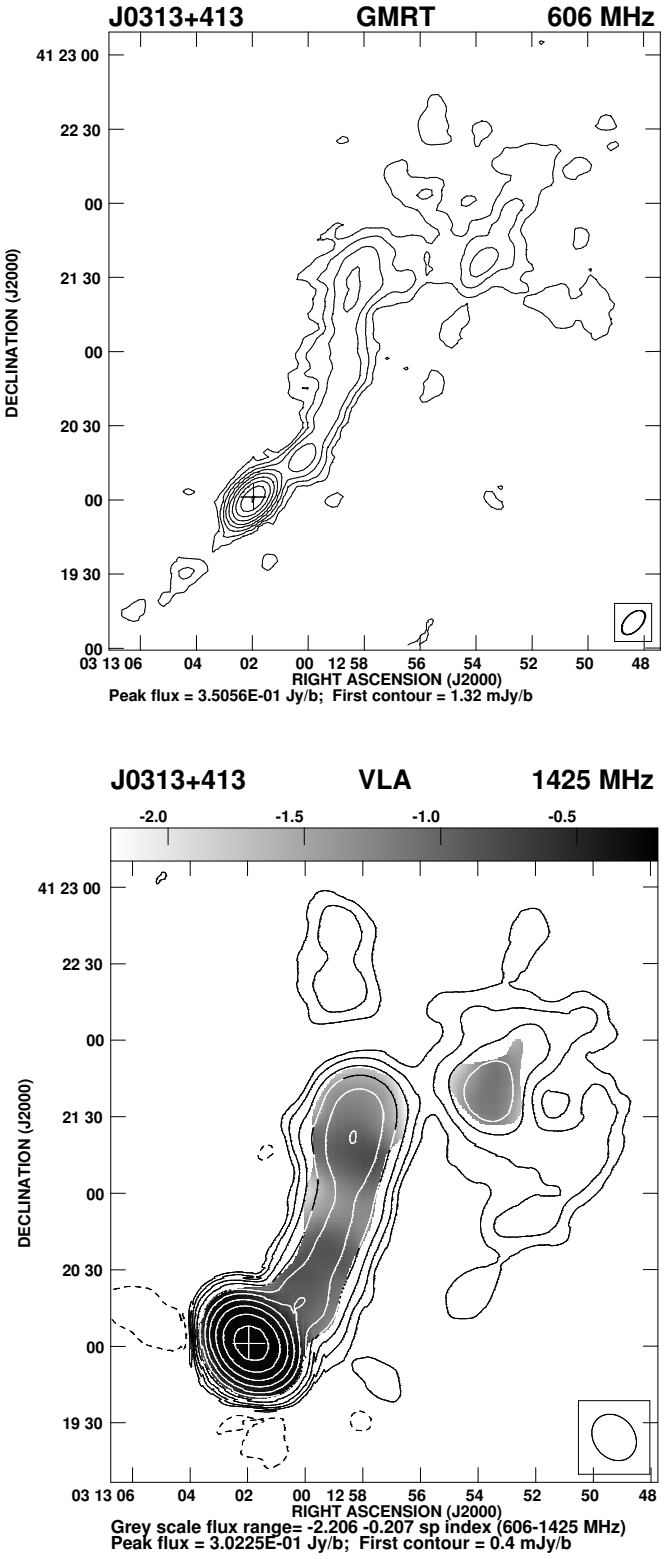

Figure 2.4: Radio images of J0313+413

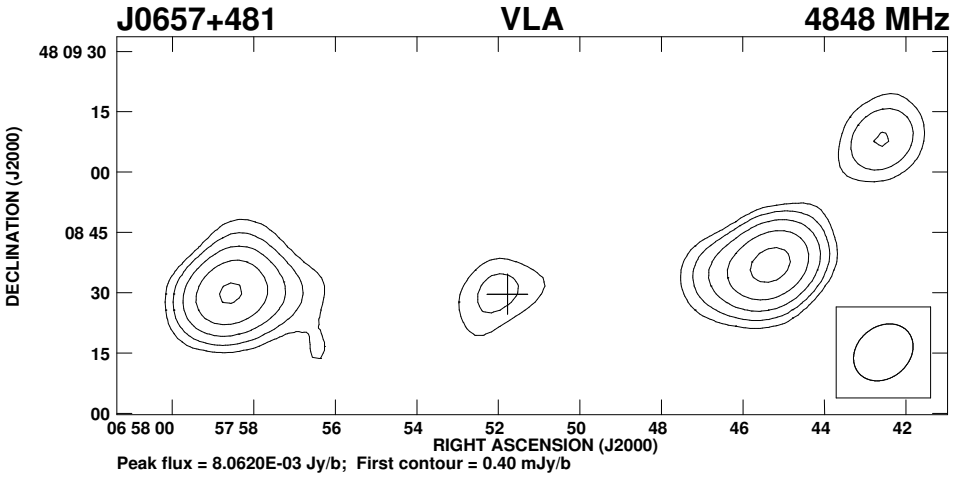

Figure 2.5: Radio image of J0657+481

as 11 and 3.6 mJy at 1478 and 4848 MHz, suggesting it might be a steep-spectrum core. The λ6cm value is similar to the value of 2.3 mJy estimated by Giovannini et al. (1988), but no significant core emission is seen in the tapered image of Neff et al. which has an rms noise of 0.4 mJy/beam. The λ20cm value is not consistent with the estimate of 3 mJy by Gregorini et al. (1988). We made an image using the longer spacings, and find the core flux density to be $\sim$1.2 mJy at 4841 MHz and $\lesssim$1.1 mJy at 1465 MHz, yielding a spectral index $\gtrsim$0.1. In Fig. 2.1, we present the λ6cm image and the spectral index image between L and C bands superimposed on it. The spectral index, α varies from -0.9 to -1.6 in the western lobe, and from -1.0 to -1.8 in the eastern one. The implied ages using the formalism of Myers & Spangler (1985) are $\sim 2.3\times10^7$ and $\sim 3.0\times10^7$ yr respectively.

J0139+399, 4C39.04: The large-scale structure showing the relaxed lobes has been reported earlier by a number of authors (e.g. Hine 1979; Vigotti et al. 1989). The flux densities listed in Table 2.2 suggest that the spectral index of the entire source between 1.3 and 4.8 GHz is -1.34 while that of

the core is -0.8. The existence of an SSC was noted earlier (e.g. Hine 1979; Klein et al. 1995). Similar-resolution observations of about 5 arcsec between 1.4 and 5 GHz (Fomalont & Bridle 1978; Gregorini et al. 1988; Bondi et al. 1993; Klein et al. 1995) also yield a core spectral index of ~ -0.8. This is consistent with the 10.6 GHz value of 4 ± 1 mJy (Mack et al. 1994). Saripalli et al. (1997) find the core to be a compact source with a flux density of 20 ± 5 mJy from VLBI observations at 1.67 GHz with a resolution of 25 mas. Our GMRT image highlights the diffuse lobes and bridge of emission, and well resolves the possibly unrelated source to the north-east (RA 01^h 39^m $46.^s9$, Dec 39° $58'$ $11.''3$), which appears to be an FRI type of source with a flux density of 42 mJy at 1287 MHz. The spectral index, α varies from -1.1 to -1.8 in the western lobe, and from -0.7 to -1.5 in the eastern one, suggesting that the ages are $\sim3\times10^7$ and $\sim4.5\times10^7$ yr respectively. Our values of core flux density are similar to those measured by Gregorini et al. (1988) and Bondi et al. (1993) at the L and C bands respectively, suggesting that the core has not varied over a time scale of $\gtrsim$10 yr.

J0200+408, 4C40.08: It has been classified as a double source with no detected radio core (Vigotti et al. 1989; Gregorini et al. 1988; Schoenmakers et al. 2000a). The NVSS image (Fig. 2.3) shows the diffuse large-scale structure along a PA of 110° with no prominent hotspot at the outer edges. Our VLA observations at 4.8 GHz reveal a radio core which is coincident with the optical identification and has a flux density of 2.6 mJy. We also detect the compact component to the east which has a spectral index of ~ -0.6 using the NVSS flux density at 1.4 and our value at 5 GHz. An examination of the Digital Sky Survey (DSS) image shows a faint galaxy coincident with the radio position of this compact component, suggesting that this is an unrelated source.

Table 2.2: The observational parameters and observed properties of the sources

Source	Freq.	Beam size			rms	S_I	Cp	S_p	S_t	Cp	S_p	S_t	Cp	S_p	S_t
	MHz	$''$	$''$	$^\circ$	mJy /b	mJy		mJy /b	mJy		mJy /b	mJy		mJy /b	mJy
J0135+379	V1465	14.0	11.5	34	0.18	1217	W	218	640	C	$\lesssim$1.1		E	199	579
	V4841	13.5	11.2	165	0.12	356	W	74	184	C^g	1.2	1.1	E	59	172
J0139+399	G1287	6.2	3.8	37	0.05	1201	W	4.5	600	C^g	34	35	E	10	579
	V4841	18.0	13.8	101	0.16	203	W	7.6	85	C^g	11	12	E	9.4	110
J0200+408	V4841	13.0	11.5	146	0.13		W			C^g	2.8	2.6	E	5.9	5.8
J0313+413	G606	11.8	6.6	137	0.33		Jet	20	179	C^g	348	375	N	8.8	129
	V1425	19.5	15.9	39	0.10		Jet	13	63	C^g	302	308	N	5.5	21
J0657+481	G617	28.1	10.3	90	0.81	259	W	74	152				E	53	94
	V1425	13.6	8.0	75	0.10	73	W	23	40	C	$\lesssim$0.6		E	19	29
	V4848	15.9	12.8	131	0.10	22	W	8.1	10	C^g	0.7	0.9	E	7.0	9.3
J0754+432	V4816	16.8	12.8	82	0.10	38	N	1.9	11	C^g	16	16	S	1.0	7.4
J0819+756	V4841	20.5	11.1	60	0.10	181	W	19	106	C^g	46	46	E	4.6	30
J1101+365	V1425	15.2	5.0	104	0.10	111	N	17	48	C?	$\sim$0.6	$\sim$0.8	S	23	60
	V4841	24.1	14.7	107	0.10	38	N	11	17	C?	$\sim$0.6	$\sim$0.6	S	12	20
J1200+348	V1465	15.7	5.0	109	0.10	198	N	65	132	C	$\lesssim$0.2		S	20	64
	V4873	15.3	13.8	70	0.11	77	N	33	50	C	$\lesssim$0.3		S	16	26
J1235+213	V1385	16.9	12.1	103	0.27	2975	W	543	1549				E	586	1431
J1313+696	G605	8.1	4.6	151	0.20	2499	N	39	1441	C	$\lesssim$2.0		S	27	1046
	V1425	14.9	6.5	121	0.10	1383	N	54	797	C^g	4.6	7.0	S	40	585
	V4873	20.4	12.2	60	0.13	431	N	30	255	C^g	4.1	4.3	S	18	172
J1604+375	G613	7.8	4.8	171	0.10	264	N	14	111	C^g	5.4	6.4	S	53	142
	V1425	32.3	10.4	58	0.21	106	N	17	43	C^g	1.9	2.9	S	31	56
	V4873	37.9	11.8	116	0.14	25	N	4.9	7.5	C^g	1.4	1.5	S	9.3	14

Table 2.2: The observational parameters and observed properties of the sources

Source	Freq.	Beam size			rms	S_I	Cp	S_p	S_t	Cp	S_p	S_t	Cp	S_p	S_t
	MHz	$''$	$''$	$^\circ$	mJy /b	mJy		mJy /b	mJy		mJy /b	mJy		mJy /b	mJy
J1637+417	V1425	23.0	8.6	54	0.10	52	N	5.1	14	C^g	3.9	3.9	S	19	34
	V4873	41.3	11.8	119	0.12	19	N	2.0	4.7	C^g	2.3	2.1	S	9.6	11
J1702+422	G602	15.6	14.0	26	0.26	393	N	56	235	C	$\lesssim$1.7		S	39	159
	V1425	21.7	6.7	53	0.11	172	N	26	102	C	$\lesssim$0.6		S	17	72
	V4848	45.1	12.0	120	0.11	51	N	12	31	C^g	1.7	1.7	S	6.5	18
J1919+517	V4866	24.7	18.7	74	0.23	70	N	23	53	C^g	5.3	5.7	S	4.2	14
J2042+751	G599	29.5	14.2	143	1.80	4078	N	82	1208	C^g	152	174	S	1001	2623
	V4816	20.0	10.9	110	0.16	471	N	5.1	66	C^g	250	249	S	76	172
J2312+187	V1425	14.2	12.7	179	0.26	1885	N	311	802	C^g	3.2	4.1	S	356	1069
	V4866	14.2	13.7	120	0.12	538	N	102	230	C^g	2.9	3.6	S	123	307

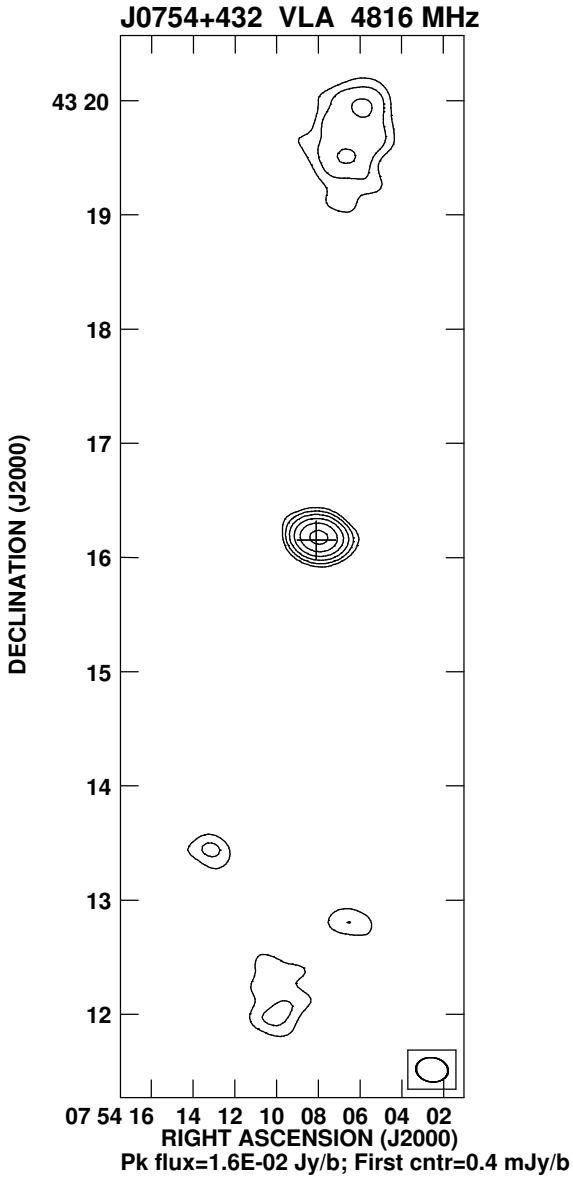

Figure 2.6: Radio image of J0754+432

J0313+413: The large-scale structure of this broad line radio galaxy (Marchã et al. 1996) was presented by de Bruyn (1989) with rather coarse resolution. Subsequent published observations with the VLA and VLBI have revealed a prominent core and a weak jet-like extension (Patnaik et al. 1992; Henstock et al. 1995; Taylor et al. 1996; Schoenmakers et al. 2000a; Fey & Charlot

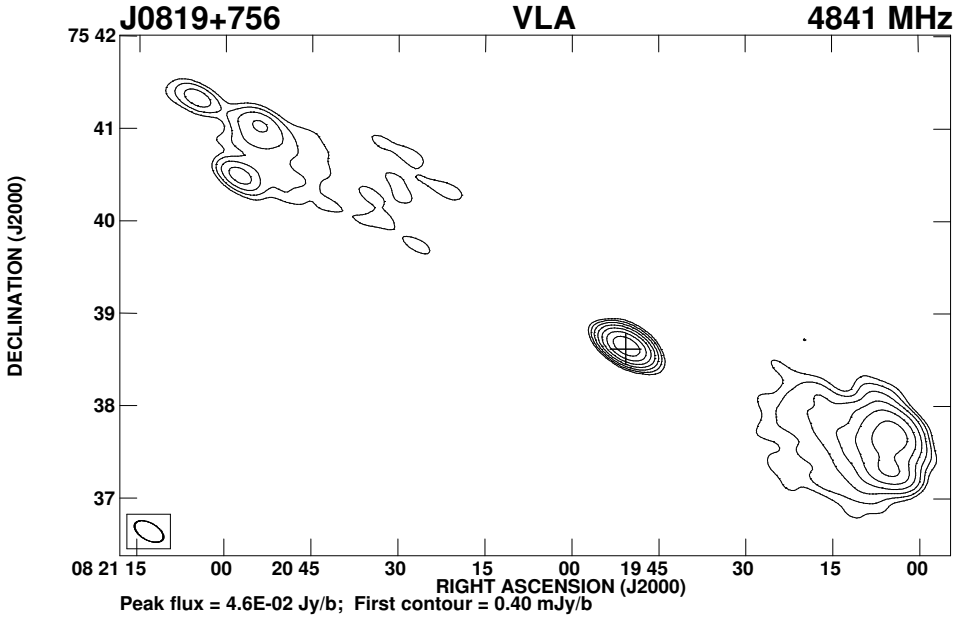

Figure 2.7: Radio image of J0819+756

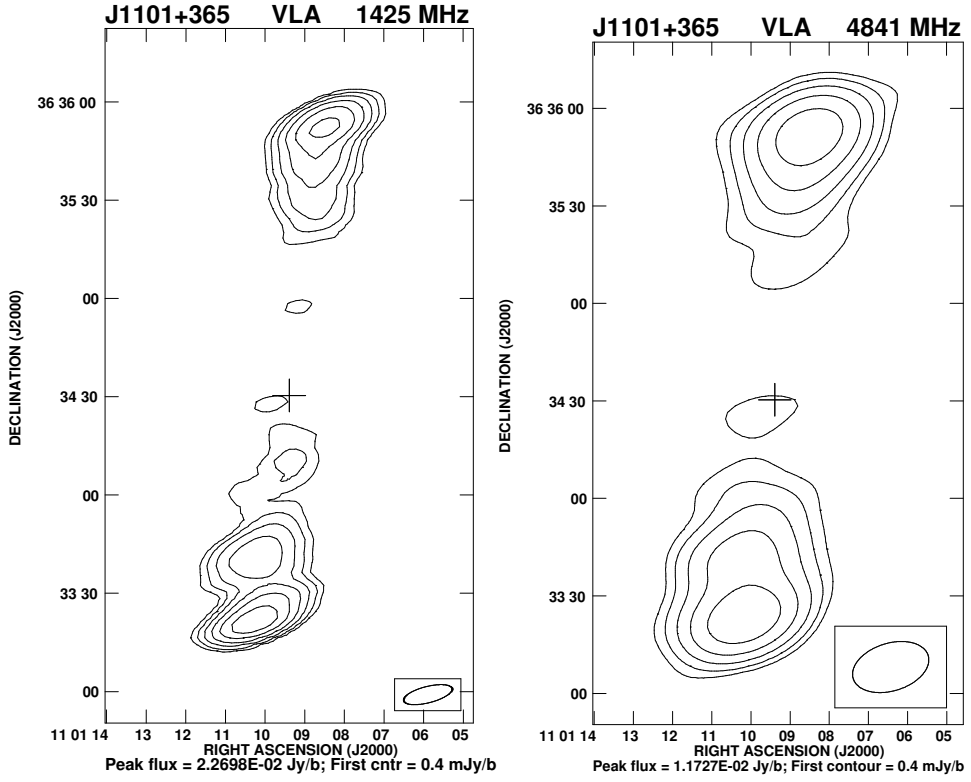

Figure 2.8: Radio images of J1101+365

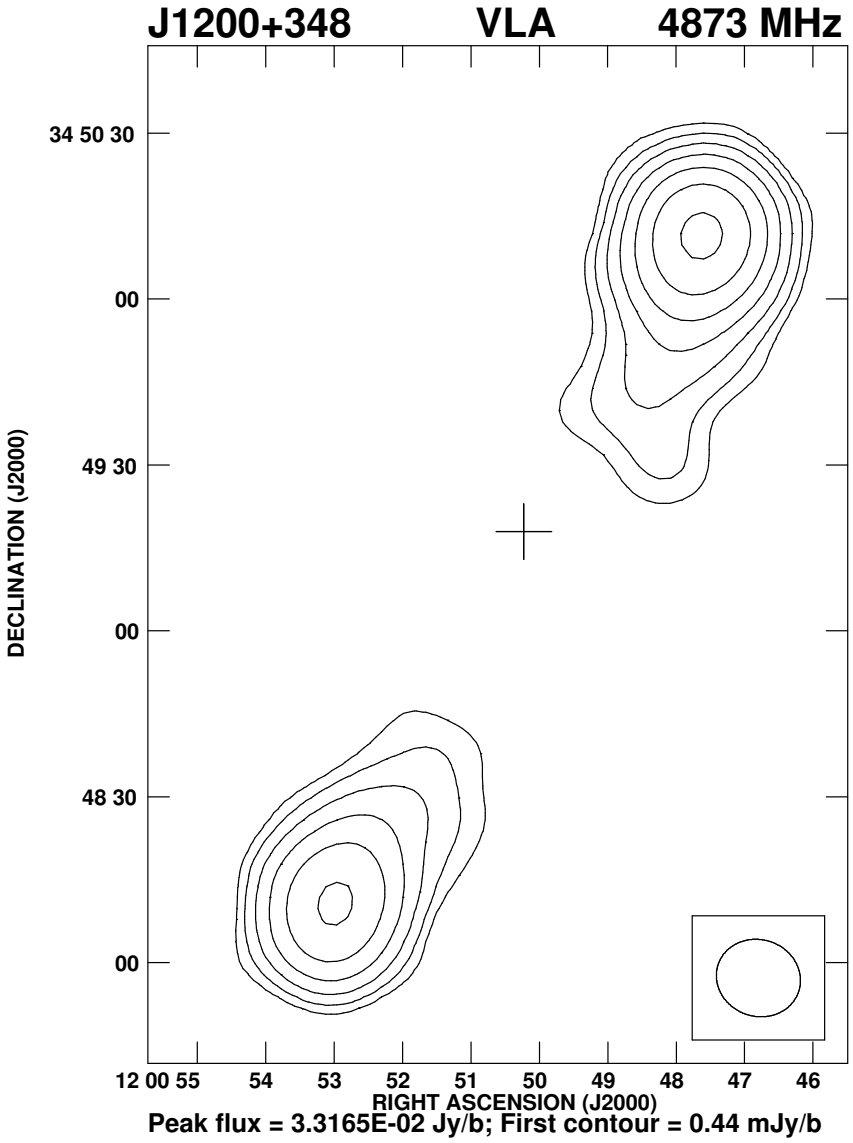

Figure 2.9: Radio image of J1200+348

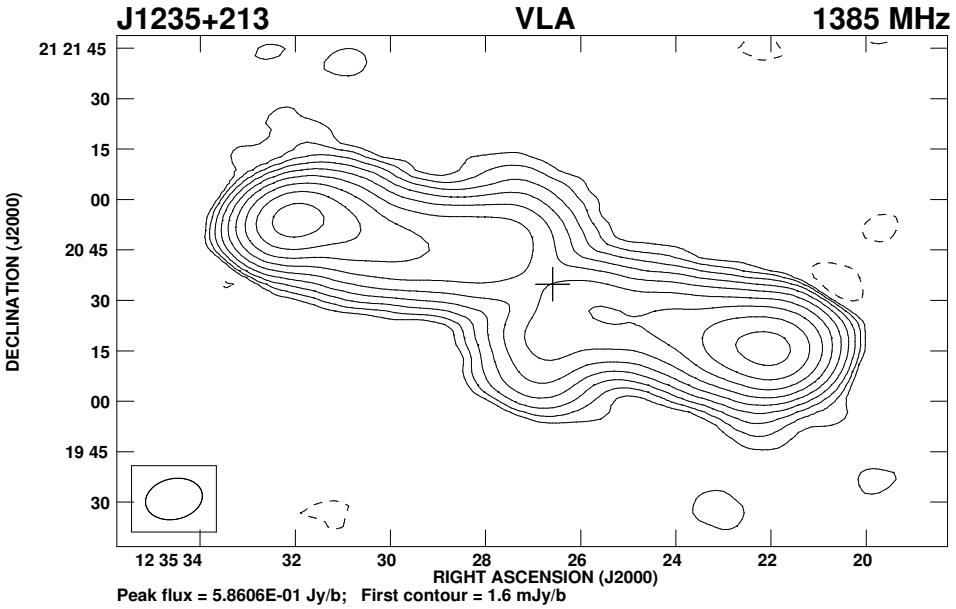

Figure 2.10: Radio image of J1235+213

2000). Our GMRT image at 606 MHz reveals a curved radio jet extending over a distance of 250 kpc, and then bending abruptly to enter the northern hotspot. Convolving the GMRT image to that of our VLA image at 1425 MHz shows the core to have a flat radio spectrum of -0.21 while in the jet the average value of α is ~ -1.1, with the values close to the peaks of emission being ~ -0.9.

J0657+481, 7C: The GMRT image at 617 MHz shows the bridge of emission (Konar et al. 2003) while the VLA 4.8-GHz image shows the radio core co-incident with the galaxy. The core has an inverted spectrum with a spectral index $\gtrsim$0.3 between 1.4 and 4.8 GHz. The component to the north-west is possibly unrelated. This GRS was identified by Cotter et al. (1996) from the 7C survey.

J0754+432: The WENSS, NVSS and FIRST images have been presented by S99. Our 4.8-GHz VLA image shows the core to have a flat spectrum

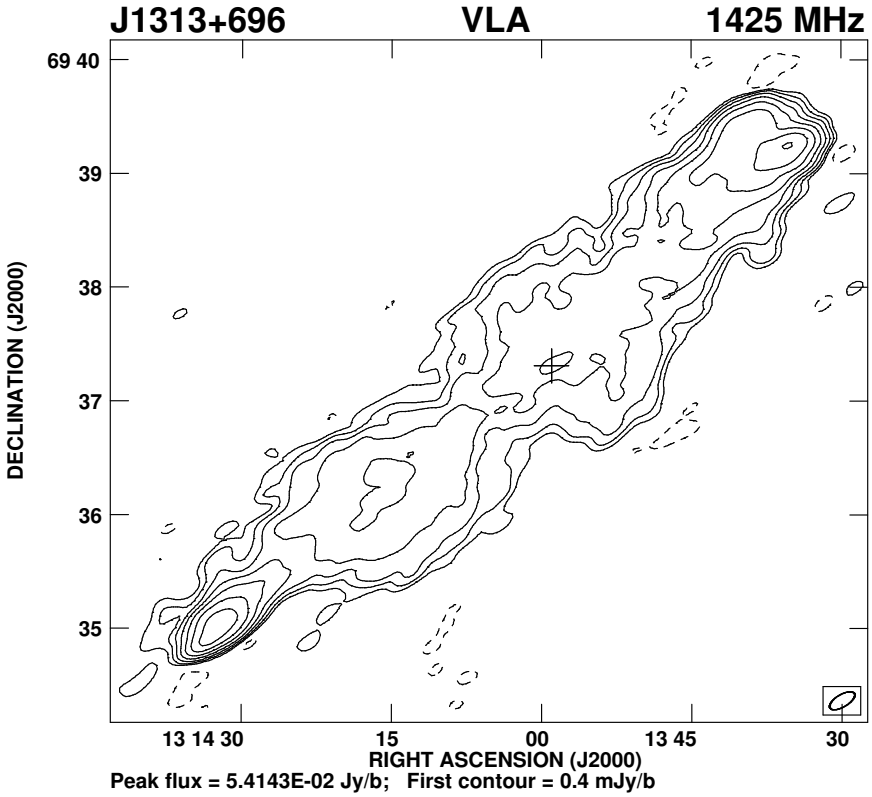

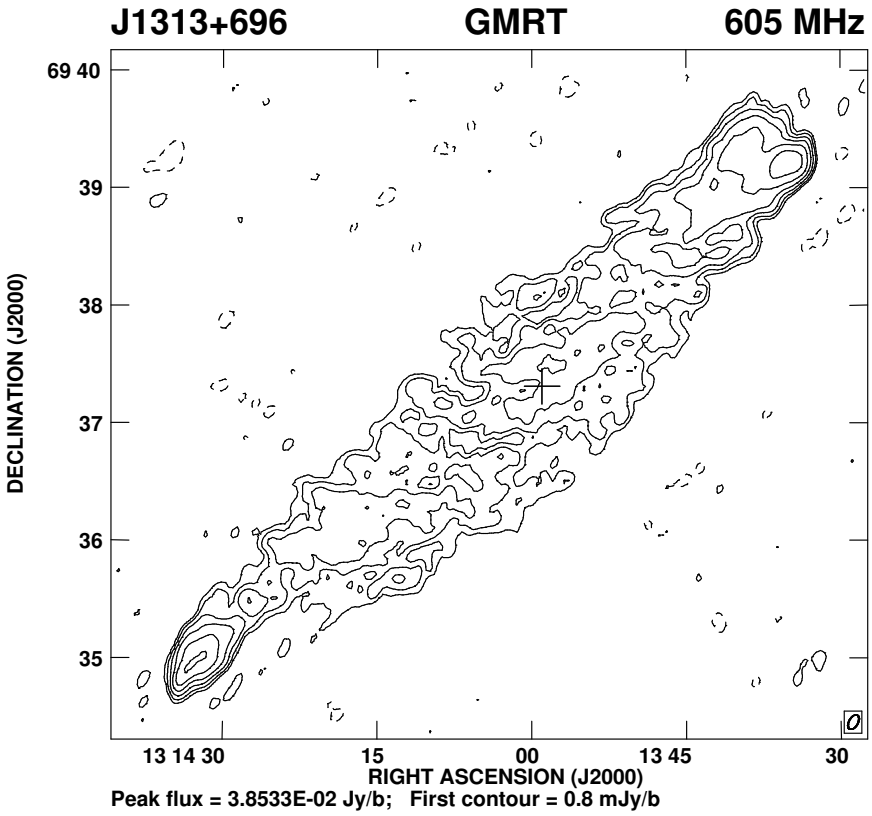

Figure 2.11: Radio images of J1313+696

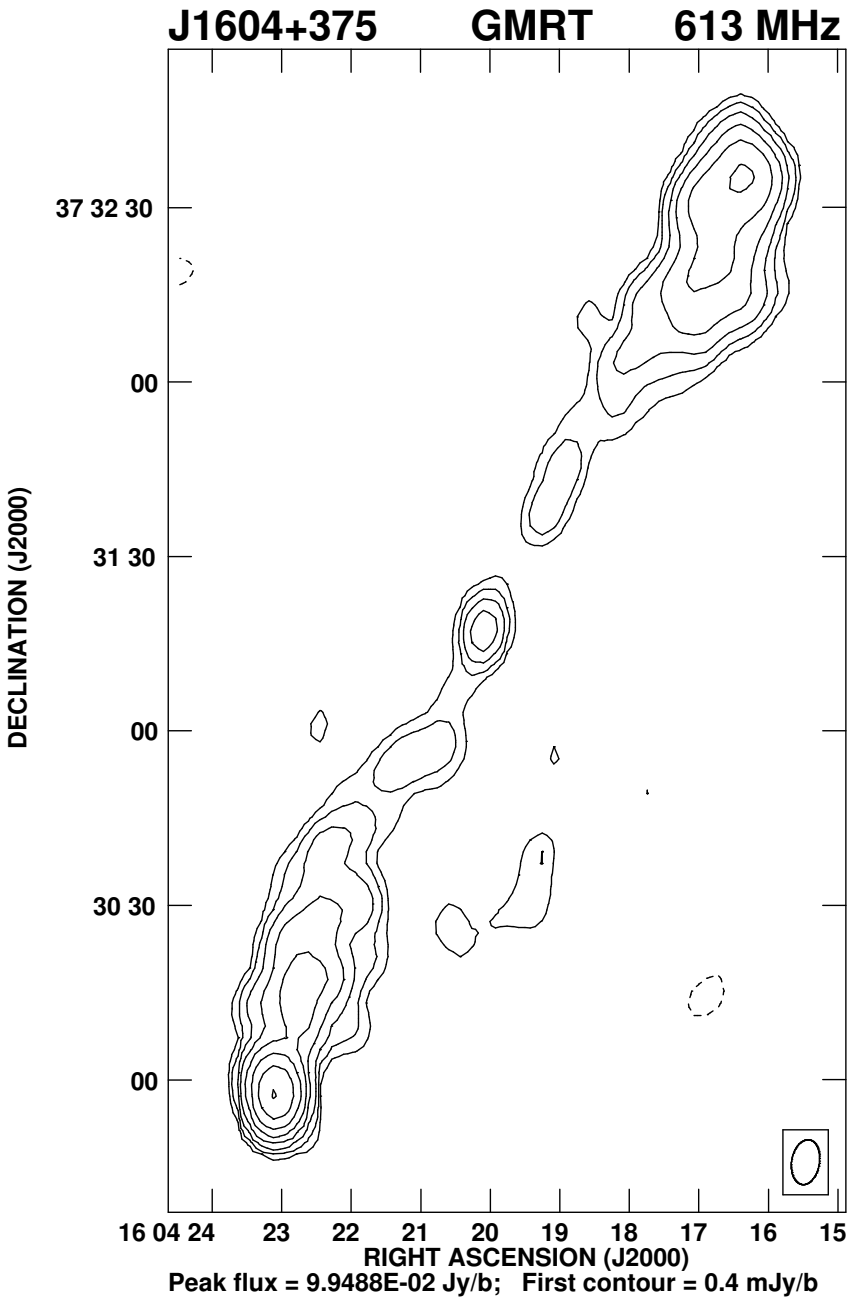

Figure 2.12: Radio image of J1604+375

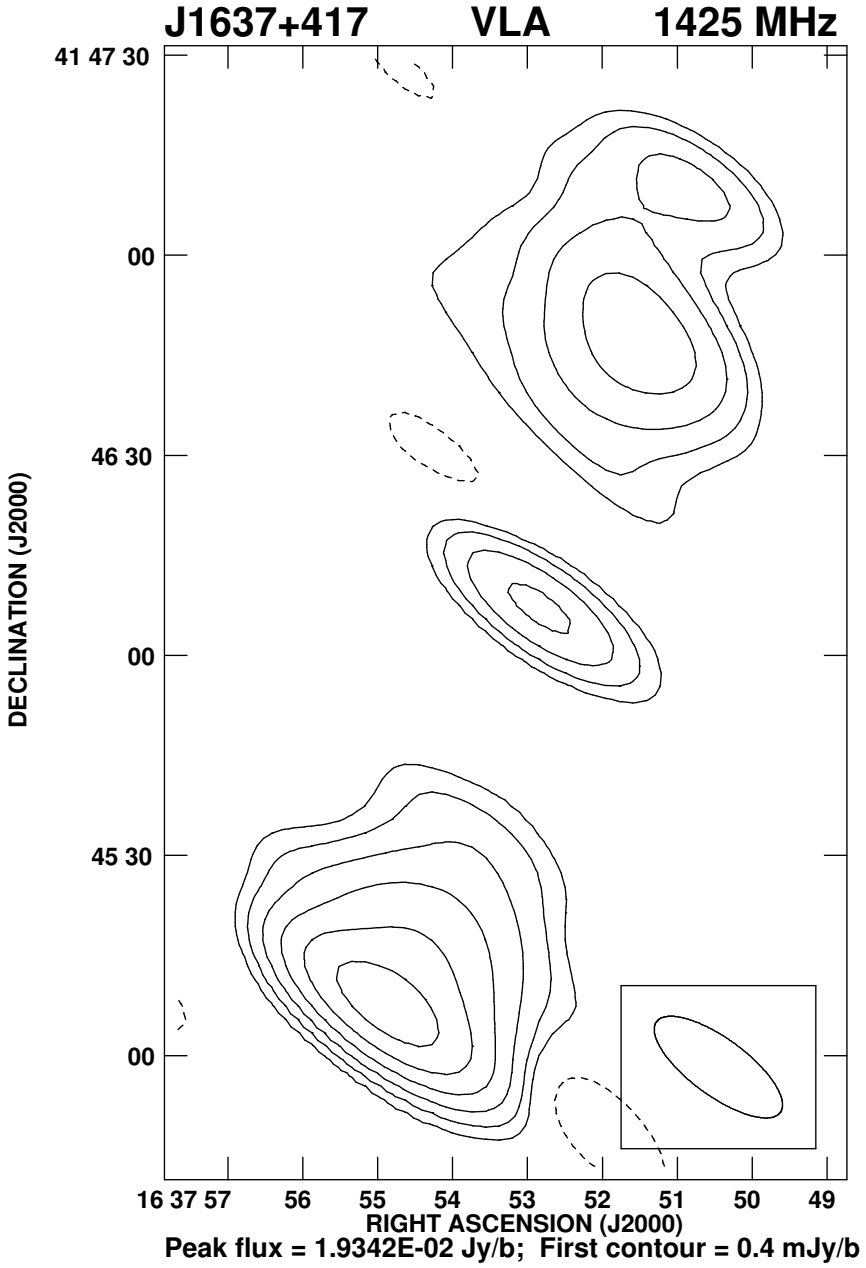

Figure 2.13: Radio image of J1637+417

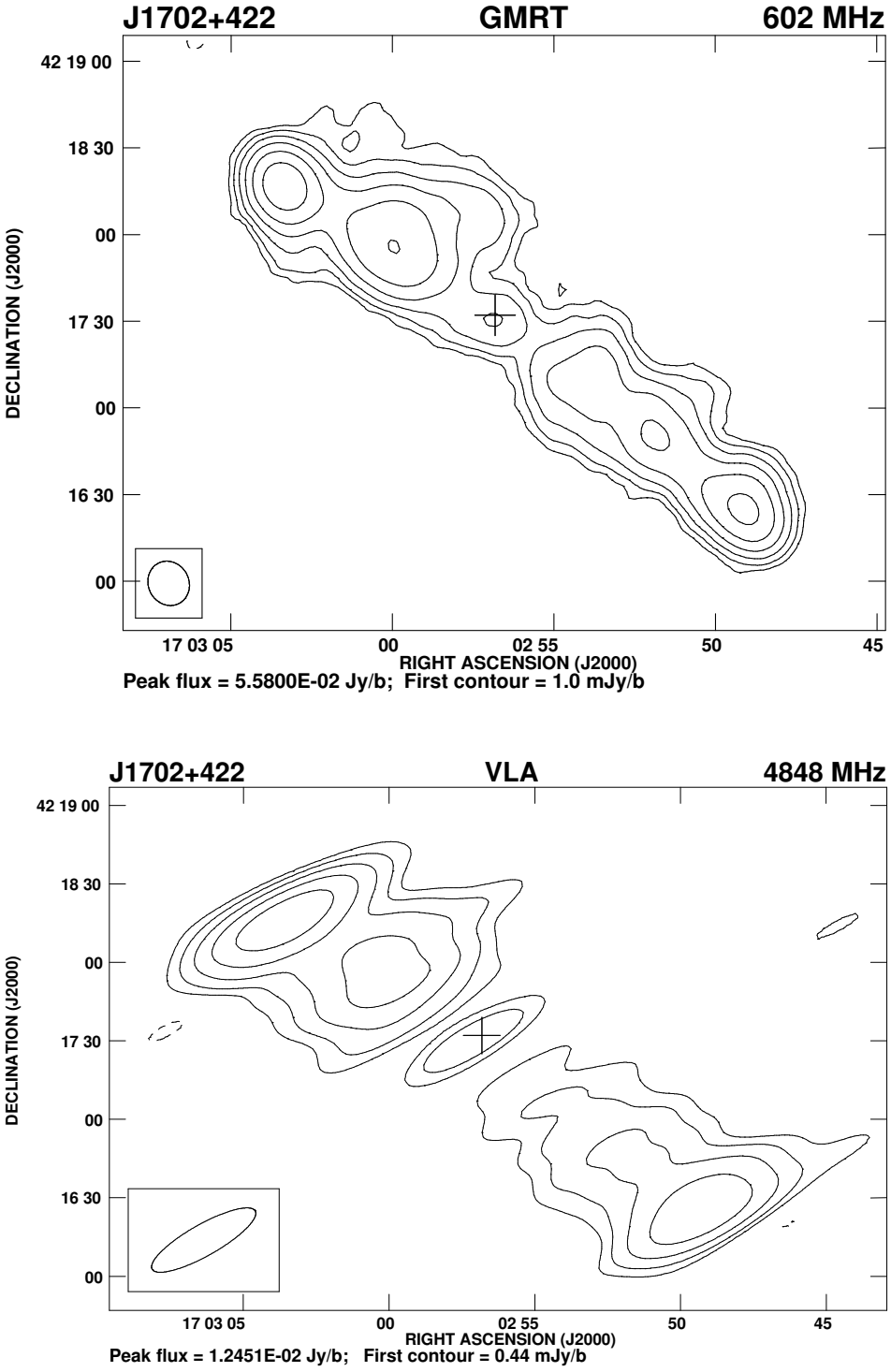

Figure 2.14: Radio images of J1702+422

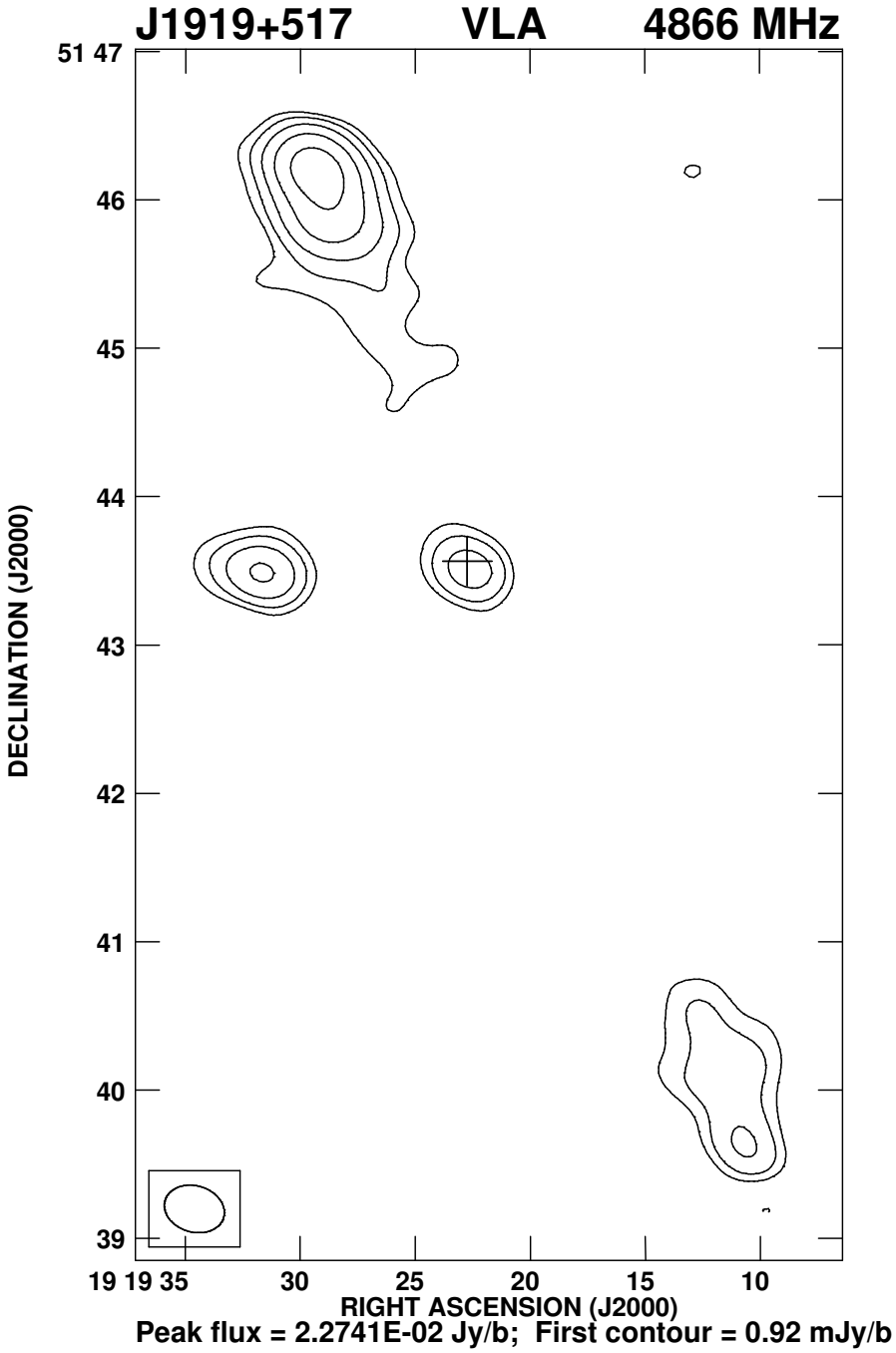

Figure 2.15: Radio image of J1919+517

($\alpha \sim 0.07$), and the southern lobe to consist of three features which are also visible in the FIRST image. The spectral indices of the western, southern and eastern features using the flux densities from the FIRST and our images are -0.51, -1.0 and -0.58 respectively. The weaker features are more compact and significantly flatter, suggesting that these are possibly unrelated to the GRS.

J0819+756: The WENSS and NVSS images have been presented by S99, while a VLA L-band image with a resolution of 8 arcsec has been published by Lara et al. (2001). Our core flux density at 4.8 GHz is 46 mJy, which is much lower than the value of 57 mJy found by Lara et al. at 4.9 GHz, suggesting variability of the core flux density. This would be consistent with its prominent core and a small angle of inclination to the line of sight. This giant source has multiple hotspots; the furthest component towards the north-east being an unrelated source (cf. Lara et al. 2001).

J1101+365, 7C: This GRS has been identified from the 7C survey by Cotter et al. (1996). We detect a possible core which has a flat radio spectrum between 1.4 and 4.8 GHz.

J1200+348: A VLA C-array image at 1465 MHz of this GRS from the GB/GB2 sample has been published by Machalski & Condon (1985).

J1235+213, 3C274.1: The core flux density has an average value of $\sim$12 mJy at 963 MHz (Bedford et al. 1981; Kerr et al. 1981) and 3 mJy at 4874 MHz (Strom et al. 1990), yielding a core spectral index of -0.85.

J1313+696, 4C69.15: The 1.4-GHz image shows the prominent bridge of emission, with a weak radio core. The limit on the core flux density at 605 MHz suggests that the core spectrum turns over at $\lesssim$1 GHz. The core spectral index between 1.4 and 4.8 GHz is -0.4.

J1604+375, 7C: The GMRT 613-MHz image shows possible evidence of a

curved twin-jet structure, with the overall structure resembling an S-shaped source. Such structures could arise due to precession of the jet axis.

J1637+417, 7C: The core spectral index from our VLA observations is ~ -0.50, suggesting that it could be an SSC.

J1702+422, 7C: The GMRT 602-MHz image shows a prominent bridge of emission with no core component. Our estimate of the core flux density of $\lesssim$0.6 mJy at 1.4 GHz is consistent with a weak feature of 0.66 mJy seen in the FIRST image. Our 4.8-GHz image shows a core with a flux density of 1.7 mJy showing that it has an inverted radio spectrum ($\alpha\gtrsim 0.8$).

J1919+517: The WENSS and a Westerbork L-band image have been presented by S99, and it has been observed with low resolution at 10.7 GHz with the Effelsberg telescope (Mack et al. 1997 and references therein). Our VLA 4.8-GHz image clearly shows the radio core with a flux density of 5.7 mJy, which combined with the 1.4 GHz value listed by S99 yields a spectral index of ~ -1.0. The component east of the core is possibly unrelated and has a flux density of 9.2 mJy at 4866 MHz.

J2042+751, 4C74.26: This GRS, identified with a quasar, has a prominent core and a one-sided radio jet (Riley et al. 1989; Riley & Warner 1990; Pearson et al. 1992). The total flux density of the core at 5 GHz decreased from 0.42 to 0.31 Jy between 1986 and 1988 (Riley et al. 1989). Our estimate of 250 mJy at 4816 MHz in 2000 is consistent with a strongly variable radio core.

J2312+187, 3C457: The spectral indices of both the northern and southern lobes between 1.4 and 4.9 GHz varies from ~ -0.9 to -2.0, suggesting a spectral age of $\sim 3.5\times10^7$ yr. The region with a flatter spectral index at the edge of the southern lobe is close to the position of the unrelated source identified by Leahy & Perley (1991). The core spectral index is -0.1 between

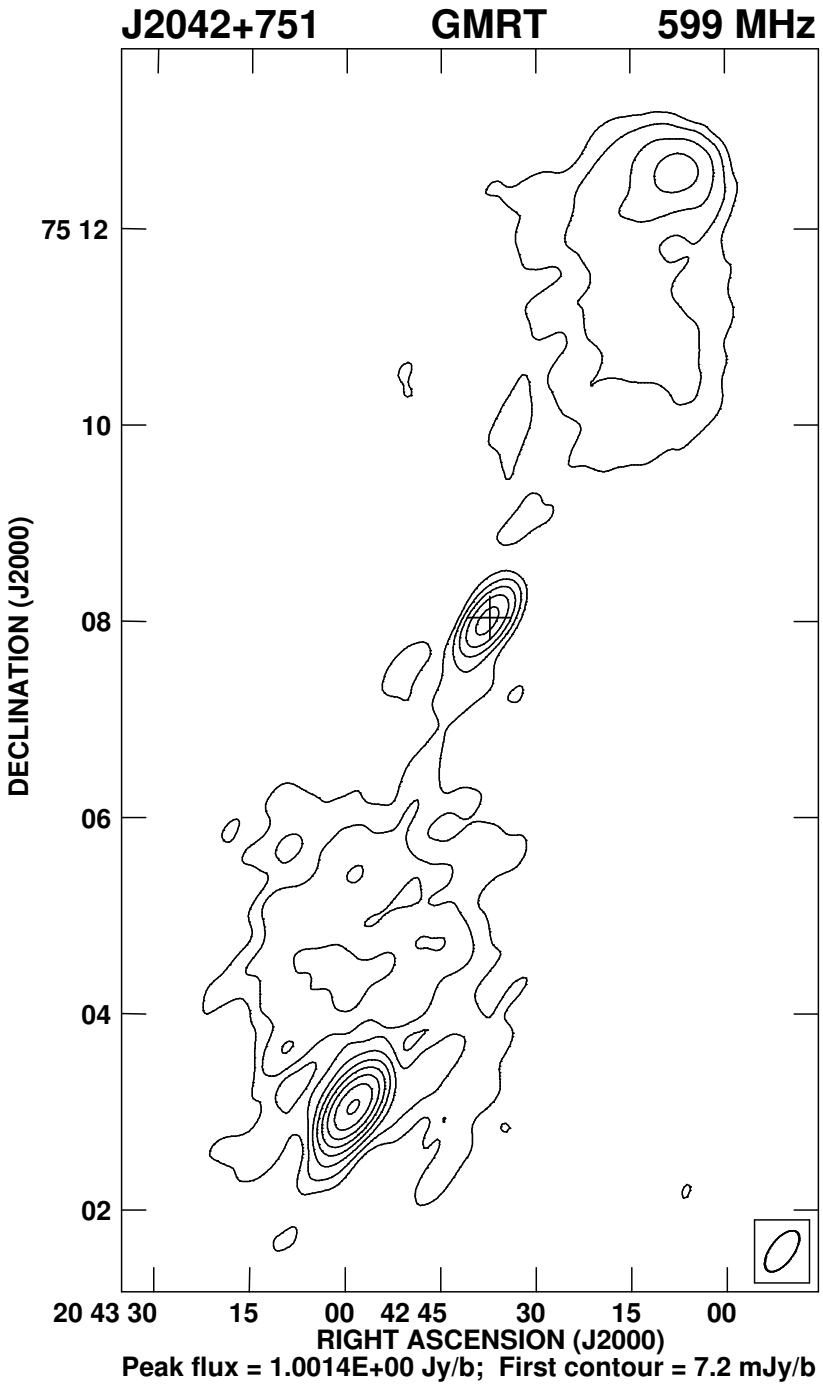

Figure 2.16: Radio image of J2042+751

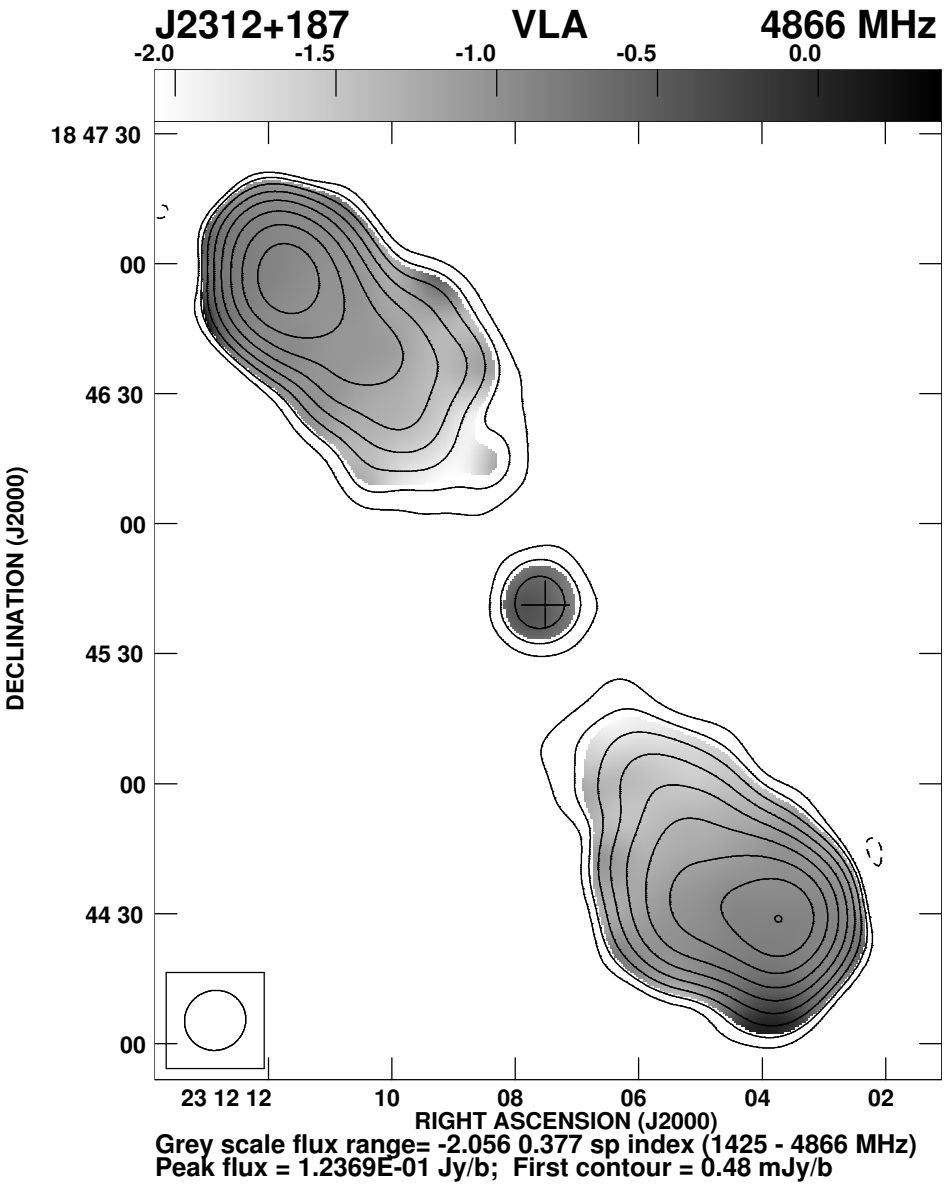

Figure 2.17: Radio image of J2312+187

1.4 and 4.9 GHz.

2.5 Discussion and results

(a) Radiative losses

For the sources listed in Table 2.2 we estimate the minimum energy density, u_{min} and the equipartition magnetic field, B_{eq} for all the extended components (Miley 1980; Longair 1994). These are listed in Table 2.3 which is arranged as follows. Columns 1 and 2: source name and an alternative name. Column 3: optical identification where G denotes a galaxy and Q a quasar; column 4: redshift; columns 5 and 6: the largest angular size in arcsec and the corresponding projected linear size in kpc; column 7: the luminosity at 1.4 GHz in logarithmic units of W Hz^{-1}; column 8: the fraction of emission from the core, f_c, at an emitted frequency of 8 GHz. For sources without detailed spectral information, spectral indices of 0 and -0.9 have been assumed for the cores and lobes respectively. Columns 9 and 12: component designation; columns 10, 11 and 13, 14: the corresponding minimum energy density, u_{min}, in units of 10^{-14} J m^{-3} and the equipartition magnetic field, B_{eq}, in nT ($1T = 10^4$ G) for the extended components. For sources such as J0200+408, where most of the lobe emission has been resolved out in our images, we have used the NVSS images for estimating these parameters. The minimum energy density and equipartition magnetic field have been estimated for the extended emission assuming a cylindrical or spheroidal geometry, a filling factor of unity and that energy is distributed equally between relativistic electrons and protons. The size of the lobes has been estimated from the lowest contours in the available images. The luminosity has been estimated between 10 MHz

Table 2.3: Physical properties of the sources

Source	Alt. name	Opt. Id.	Redshift	LAS	l	$P_{1.4}$	f_c	Cmp.	u_{min}	B_{eq}	Cmp.	u_{min}	B_{eq}
									10^{-14}			10^{-14}	
				$''$	kpc	W Hz^{-1}			J m^{-3}	nT		J m^{-3}	nT
J0135+379	3C46	G	0.4373	150	846	27.01	$\sim$0.004	W	26.36	0.53	E	20.67	0.47
J0139+399	4C39.04	G	0.2107	370	1259	26.15	0.07	W	19.30	0.46	E	11.83	0.36
J0200+408	4C40.08	G	0.0827	920	1414	24.61	0.05	W	1.09	0.11	E	1.40	0.12
J0313+413	B3	G	0.136	570	1357	25.34	0.86	Jet	44.44	0.69			
J0657+481	7C	G	0.776	133	989	26.34	0.04	W	14.57	0.40	E	14.55	0.40
J0754+432		G	0.3474	485	2368	25.67	0.35	N	0.99	0.10	S	0.55	0.08
J0819+756		G	0.2324	454	1666	25.97	0.31	W	3.39	0.19	E	2.69	0.17
J1101+365	7C	G	0.750	154	1131	26.49	$\sim$0.01	N	4.25	0.21	S	4.35	0.22
J1200+348		G	0.55	145	927	26.43	$\lesssim$0.006	N	8.01	0.29	S	5.75	0.25
J1235+213	3C274.1	G	0.422	151	834	27.28	0.004	W	24.45	0.51	E	26.48	0.53
J1313+696	DA340	G	0.106	388	745	25.60	0.01	N	6.54	0.27	S	5.24	0.24
J1604+375	7C	G	0.814	178	1346	26.54	0.04	N	45.55	0.70	S	21.42	0.48
J1637+417	7C	G	0.867	134	1035	26.36	0.09	N	3.65	0.20	S	5.47	0.24
J1702+422	7C	G	0.476	196	1160	26.16	0.03	N	5.04	0.23	S	6.88	0.27
J1919+517		G	0.284	429	1825	25.95	0.06	N	4.40	0.22	S	3.54	0.20
J2042+751	4C74.26	Q	0.104	610	1151	25.68	0.42	N	2.73	0.17	S	3.83	0.20
J2312+187	3C457	G	0.427	190	1056	27.09	0.006	N	18.34	0.44	S	19.30	0.46

and 100 GHz using the known spectral indices of the extended emission or else assuming a value of -0.9.

The minimum energy densities are in the range of $\sim$1 to 45 $\times$ 10^{-14} J m^{-3} with a median value of about 5.8 $\times$ 10^{-14} J m^{-3}, while the equipartition magnetic field for the lobes range from 0.08 to 0.7 nT with a median value of 0.25 nT. We examine the relative importance of synchrotron and inverse-Compton losses in the lobes of these radio sources. The equipartition magnetic field of the lobes for all the sources are less than the equivalent magnetic field of the microwave background radiation at the redshift of the source, B_{iC}=0.32$(1 + z)^2$ nT. This suggests that the inverse-Compton losses are larger than the synchrotron radiative losses in the evolution of the lobes of these giant sources, consistent with earlier results (e.g. IC99).

The dominance of inverse-Compton losses is likely to severely affect the appearance and identification of GRSs at high redshifts due to the suppression of bridge emission by inverse-Compton losses against the cosmic microwave background radiation, which increases sharply with redshift. This could lead to 'tail-less' hotspots leading to their classification as independent radio sources (e.g. Baldwin 1982). For the sources discussed here, we quantify the prominence of the bridge emission, f_{bridge}, as the ratio of emission from the bridge to that of the total emission, estimated from either single-dish or low-resolution observations available in the literature. The flux density from the bridge has been estimated by subtracting the 'hot-spot' and core flux densities from the total flux density. The 'hot-spot' flux densities have been estimated by smoothing our images to a uniform linear resolution of $\sim$70 kpc and taking the peak flux densities at the outer edges as a measure of the 'hot-spot' flux densities. It was possible to do this for 14 of the objects in our sample. With observations of higher linear resolution, one could

get better estimates of the 'hot-spot' flux densities. A plot of f_{bridge} at an emitted frequency of 1.4 GHz against redshift is shown in Fig. 2.18. The error bars indicate a $\pm 1\sigma$ error in f_{bridge} adopting an error of 10 per cent in the flux densities. The plot clearly shows an inverse correlation, with a Spearman rank correlation coefficient of 0.52, corresponding to a confidence level of >95 per cent, suggesting that suppression of bridge emission could affect the identification of GRSs at high redshifts.

(b) Relic radio emission

In order to understand the nature of episodic activity in the nucleus of the parent galaxy, which sometimes manifests itself as a double-double radio galaxy (Schoenmakers et al. 2000b), we attempt to identify relic radio emission from an earlier cycle of nuclear activity. The lifetime of a relativistic electron at an observed frequency, ν_o, due to both synchrotron and inverse-Compton losses is given by

$$\tau = \frac{5.03 \times 10^4}{[(1+\mathrm{z})\nu_\mathrm{o}]^{1/2} \mathrm{B}_\mathrm{eq}^{3/2} [1 + (\mathrm{B}_\mathrm{iC}/\mathrm{B}_\mathrm{eq})^2]} \ \mathrm{Myr},$$

where ν_o is in MHz and the magnetic fields B_{iC} and B_{eq} are in units of 10^{-10} T (e.g. Mack et al. 1998). For a median redshift of $\sim$0.4 as in our sample of sources and a median magnetic field of 0.25 nT, the lifetime of the relativistic electron at an observed frequency of 1400 MHz is $\sim 4 \times 10^7$ yr. For a velocity of advancement of 0.1c, the outer hotspots would traverse a distance of $\sim$1.2 Mpc during this time period.

Radio sources, with an inactive nucleus for timescales $\gtrsim \tau$, may be characterised by a very relaxed lobe with no hotspot at the outer edges and a steep radio spectrum ($\alpha \lesssim -1.0$). Detection of a radio core in such a source

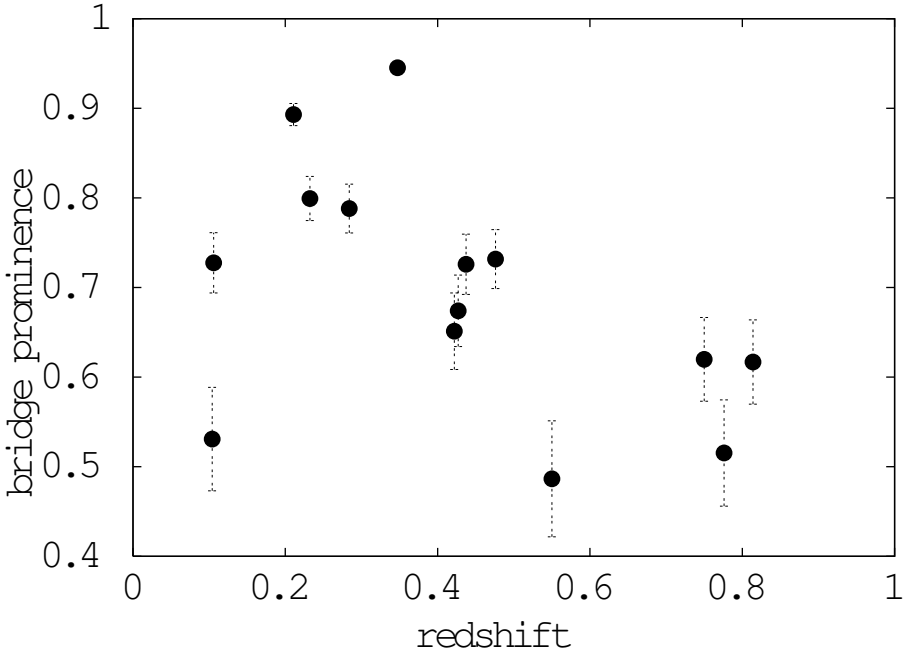

Figure 2.18: The fraction of bridge emission, f_{bridge} at an emitted frequency of 1.4 GHz plotted against the redshift.

could indicate the beginning of a new period of activity. Such sources can be distinguished from the low-luminosity FRI sources. Although FRI sources also have lobes without hotspots, these sources are characterised by radio jets which expand to form the diffuse lobes of emission, reflecting ongoing activity in the nucleus of the parent galaxy. Also, the spectral indices of FRI sources are usually flatter, consistent with the radio luminosity−spectral index correlation (e.g. Laing & Peacock 1980)

Two candidate sources with evidence of relic radio emission are J0139+399 and J0200+408. J0139+399 has a very relaxed morphology with no hotspots, a weak radio core (Fig. 2.2 and Fig. 2.3), no jets and a spectral index of -1.34 from similar resolution GMRT and VLA data at L and C bands respectively. The second candidate, J0200+408, has similar structural features and a very steep spectrum of -1.78 using the flux density at 325 MHz (S99) and the NVSS value at 1400 MHz.

(c) Steep-spectrum cores (SSCs)

The cores of extended double-lobed sources usually tend to have flat and complex radio spectra with $\alpha \gtrsim -0.5$. The occurrence of SSCs with $\alpha \lesssim -0.5$ is indeed rare, and is often due to contamination of the measured low-frequency flux density by more extended emission (e.g. Saikia, Kulkarni & Porcas 1986). However, the occurrence of an SSC suggests that the emission is largely optically thin, which could be due to small-scale jets and/or lobes not resolved by the existing observations. One of the well-known sources with an SSC is the GRS 3C236 where the core spectral index was estimated by Mack et al. (1997) to be -0.61 ± 0.01. VLBI imaging of the SSC shows it to consist of a core, jet and two oppositely-directed lobes of emission (Schilizzi et al. 2001). The small- and large-scale structure of 3C236 suggests that it could be considered to be a double-double radio galaxy, which is a sign of recurrent activity. It is interesting to note that 3C236 shows evidence of star formation and also HI absorption against a lobe of the inner radio source (Conway & Schilizzi 2000; Schilizzi et al. 2001; O'Dea et al. 2001), which could be due to infall of gas fuelling the central engine. Another possible SSC is associated with the giant radio galaxy DA240 and has a spectral index of $\sim -0.56 \pm 0.01$ (Mack et al. 1997). VLBI observations of the core with an angular resolution of 25 mas shows that it possibly has a twin-jet structure (Saripalli et al. 1997).

Of a sample of 30 radio galaxies, with known cores observed with the VLA A-array between 1.4 and 15 GHz, no radio core, except the GRS DA240, showed evidence of a straight, steep radio spectrum. The radio core of DA240 was found to have a flux density of 191 and 110 mJy at 1465 and 4885 MHz, yielding a spectral index of ~ -0.5 (Saikia et al., in preparation). Only three

of these 30 sources are GRSs, the other two being NGC315 and NGC6251, both of which have flat-spectrum cores. Similarly for a sample of 17 sources from the Molonglo Reference Catalogue observed with the VLA A-array between 1.4 and 15 GHz, the cores tend to have flat and complex spectra. Only two sources whose low-frequency flux densities were significantly affected by contamination from more extended emission appeared to have steep spectra (Ishwara-Chandra & Saikia 2000). Only two of these 17 sources are GRSs, the remaining ones being of smaller sizes.

Considering the rarity of SSCs and the occurrence of two of these with known GRSs, it is meaningful to enquire whether this is entirely due to chance or it might have a deeper significance. For example, if the occurrence of SSCs is related to recurrent activity, the preferential occurrence of SSCs in GRSs might enable us to get further insights into the time scales of recurrent activity. Towards this end, we have tried to identify SSC candidates in the present sample of GRSs and have identified four candidates. As discussed in Section 2.4, J0139+399, J1235+213 and J1919+517 appear to have $\alpha_{\rm core}\lesssim-0.8$, while J1637+417 is a more marginal case with a steep spectrum, $\alpha_{\rm core} \sim -0.5$. For confirmation, the spectra of these candidate SSCs need to be determined over a larger frequency range from higher resolution observations. If confirmed, this would indicate a higher incidence of SSCs among GRSs compared with smaller-sized sources as discussed earlier, which is possibly related to the time scales of recurrent activity.

(d) Core prominence and variability

The fraction of emission from the core at an emitted frequency of 8 GHz, f_c, ranges from $\lesssim$0.004 to $\sim$0.86, with a median value of $\sim$0.04. The values

of f_c are usually comparable to the other sources of similar radio luminosity. The four sources with prominent cores ($f_c \gtrsim 0.2$) are J0313+413, J0754+432, J0819+756 and J2042+751, the first three of which are associated with galaxies and J2042+751 with a quasar. Given the prominence of the cores, it is reasonable to assume that these galaxies lie close to $\sim 45^\circ$ to the line of sight, the dividing line between galaxies and quasars in the unified schemes (e.g. Barthel 1989). The classification of J0313+413 as a broad line radio galaxy (Marchã et al. 1996), the detection of broad hydrogen Balmer lines in J0754+432 and a broad component in the Hα line of J0819+756 (Schoenmakers et al. 2001) are consistent with this interpretation. For an inclination angle of $\sim 45^\circ$ their intrinsic sizes would increase to $\sim$1900, 3350 and 2350 kpc respectively.

The GMRT and VLA images of the radio galaxy J0313+413 show a prominent radio jet which curves towards the north and then bends abruptly towards the west (Fig. 2.4). There is also a suggestion of a weak counter-jet in the GMRT image at 606 MHz. The jet to counter-jet brightness ratio varies from $\sim$7 to 20 along the length of the jet. If the asymmetry is due to relativistic beaming, this implies a jet speed of $\sim 0.4-0.6c$ for an inclination angle of $\sim 45^\circ$. We have also compiled the core flux densities of J0313+413 in Table 2.4. Although the data are not homogeneous, measurements of a higher flux density with higher resolution compared with coarser-resolution observations at a different epoch at both 5 and 8 GHz suggests that the core is variable, which is consistent with the assumed angle to the line of sight. The giant quasar J2042+751 (4C74.26) which has a prominent core, exhibits a one-sided radio jet and variability of the core flux density by approximately 50 per cent over a two-year time scale (Riley & Warner 1990). Our value of the core flux density at 4816 MHz is only 250 mJy compared with previous

Table 2.4: Core flux densities of J0313+413

Teles-cope	resn. $''$	Date	Freq. MHz	S mJy	Ref.
GMRT	8.8	2003 September 06	606	375	1
VLA-A	2.0	1995 July 10	1415	309	6
VLA-BnC	17.6	2000 March 13	1425	308	1
VLBA	0.0048	1997 January 10−12	2320	270	3
VLA-B	2.0	1994 August 06	4710	408	6
VLA-C	4.4	1980 July 13,14	4885	337	2
VLBI	0.0014	1993 Junuary 9−16	4992	461	7
VLA-A	0.2	1990 February 19−23	8400	673	5
VLBA	0.0012	1997 January 10−12	8550	290	3
VLA-CnD	8.0	1997 September-October	8460	458	4
VLA-C	1.4	1980 July 13,14	15035	465	2

1: Konar et al. 2004; 2: Saikia et al. 1984; 3: Fey et al. 2000; 4: Dennett-Thorpe et al. 2000; 5: Patnaik et al. 1992; 6: Taylor et al. 1996; 7: Henstock et al. 1995.

measurements in the range of 310 to 420 mJy (Riley et al. 1989; Pearson et al. 1992), consistent with a strongly variable core. In the quasar 4C74.26, the inferred orientation angle of $\lesssim 49^\circ$ (Pearson et al. 1992) implies an intrinsic size $\gtrsim 1525$ kpc.

2.6 Concluding remarks

Multifrequency GMRT and VLA observations of a sample of seventeen largely GRSs have either helped clarify the radio structures or provided new information at a different frequency. The broad line radio galaxy, J0313+413, has an asymmetric, curved radio jet and a variable radio core, consistent with a moderate angle of inclination to the line of sight, while J1604+375 shows evidence of a precessing twin-jet structure. We identify four candidate steep spectrum radio cores, which may be a sign of recurrent activity. J0139+399, J1235+213 and J1919+517 appear to have $\alpha_{\rm core}\lesssim -0.8$, while J1637+417 is a

more marginal case with $\alpha_{\rm core} \sim -0.5$. The spectra of these candidate SSCs need to be determined over a larger frequency range from higher resolution observations. If confirmed, this would indicate a higher incidence of SSCs among GRSs, compared with sources of smaller dimensions, which is possibly related to the time scales of recurrent activity. From the structure and integrated spectra of the sources, we suggest that the diffuse lobes of emission in J0139+399 and J0200+408 may be due to an earlier cycle of nuclear activity. We find that inverse-Compton losses with the cosmic microwave background radiation dominate over synchrotron radiative losses in the lobes of all the sources, consistent with earlier studies. We also show that the prominence of the bridge emission decreases with redshift, possibly due to inverse-Compton losses. This would affect the appearance and identification of GRSs at large redshifts.

References

Baars J.W.M., Genzel R., Pauliny-Toth I.I.K., Witzel A. 1977, A&A, 61, 99

Baldwin J.E., 1982, in Heeschen D.S., Wade C.M., eds, Proc. IAU Symp. 97, Extragalactic Radio Sources, Reidel, Dordrecht, p21

Bedford N.H., Kerr A.J., Mathur S.H., Morison I., Spencer R.E., Stannard D., 1981, MNRAS, 195, 245

Barthel P.D., 1989, ApJ, 336, 606

Bondi M., Gregorini L., Padrielli L., Parma P., 1993, A&AS, 101, 431

Conway J.E., Schilizzi R.T., 2000, In EVN Symposium 2000, eds J.E. Conway, A.G. Polatidis, R.S. Booth, Y.M. Pihlström, Onsala Space Observatory, p. 123

Cotter G., Rawlings S., Saunders R., 1996, MNRAS, 281, 1081

de Bruyn A.G., 1989, A&A, 226, L13

Dennett-Thorpe J., Marchã M.J., 2000, A&A, 361, 480

Fey A.L., Charlot P., 2000, ApJS, 128, 17

Fomalont E.B., Bridle A.H., 1978, AJ, 83, 725

Giovannini G., Feretti L., Gregorini L., Parma P., 1988, A&A, 199, 73

Gregorini L., Padrielli L., Parma P., Gilmore G., 1988, A&AS, 74, 107

Henstock D.R., Browne I.W.A., Wilkinson P.N., Taylor G.B., Vermeulen R.C., Pearson T.J., Readhead A.C.S., 1995, ApJS, 100, 1

Hine R. G., 1979, MNRAS, 189, 527

Ishwara-Chandra C.H., Saikia D.J., 1999, MNRAS, 309, 100 (IC99)

Ishwara-Chandra C.H., Saikia D.J., 2000, MNRAS, 317, 658

Kerr A.J., Birch P., Conway R.G., Davis R.J., Stannard D., 1981, MNRAS, 197, 921

Klein U., Mack K.-H., Gregorini L., Parma P., 1995, A&A, 303, 427

Konar C., Saikia D.J., Ishwara-Chandra C.H., Kulkarni V.K., 2003, BASI, 31, 437

Konar C., Saikia D.J., Ishwara-Chandra C.H., Kulkarni V.K., 2004, MNRAS, 355, 845

Laing R.A., Peacock J.A., 1980, MNRAS, 190, 903

Lara L., Cotton W.D., Feretti L., Giovannini G., Marcaide J.M., Márquez I., Venturi T., 2001, A&A, 370, 409

Leahy J. P., Perley R. A., 1991, AJ, 102, 537

Longair, M. S., 1994, High Energy Astrophysics, Cambridge University Press, Cambridge.

Machalski J., Condon J. J., 1985, AJ, 90, 5

Mack K.-H., Gregorini L., Parma P., Klein U., 1994, A&AS, 103, 157

Mack K.-H., Klein U., O'Dea C.P., Willis A.G., 1997, A&AS, 123, 423

Mack K.-H., Klein U., O'Dea C. P., Willis A. G., Saripalli L., 1998, A&A, 329, 431

Marchã M.J.M., Browne I.W.A., Impey C.D., Smith P.S., 1996, MNRAS, 281, 425

Miley G. K., 1980, ARA&A, 18, 165

Myers S. T., Spangler S. R., 1985, ApJ, 291, 52

Neff S.G., Roberts L., Hutchings J.B., 1995, ApJS, 99, 349

O'Dea C.P., Koekemoer A.M., Baum, S.A., Sparks W.B., Martel A.R., Allen M.G.,

Patnaik A.R., Browne I.W.A., Wilkinson P,N., Wrobel J.M., 1992, MNRAS, 254, 655

Pearson T. J., Blundell K. M., Riley J. M., Warner P. J., 1992, MNRAS, 259, L13

Riley J. M., Warner P. J., 1990, MNRAS, 246, L1

Riley J. M., Warner P. J., Rawlings S., Saunders R., Pooley G. G., Eales S. A., 1989, MNRAS, 236, L13

Saikia D.J., Shastri P., Kapahi V.K., Sinha R.P., Swarup G., 1984, JA&A, 5, 429

Saikia D.J., Kulkarni V.K., Porcas R.W., 1986, MNRAS, 219, 719

Saripalli L., Patnaik A.R., Porcas R.W., Graham D.A., 1997, A&A, 328, 78

Schilizzi R.T. et al., 2001, A&A, 368, 398

Schoenmakers A.P., Mack K.-H., de Bruyn A.G., Röttgering H.J.A., Klein U., van der Laan H., 2000a, A&AS, 146, 293

Schoenmakers A.P., de Bruyn A.G., Röttgering H.J.A., van der Laan H., Kaiser C.R., 2000b, MNRAS, 315, 371

Schoenmakers A.P., de Bruyn A.G., Röttgering H.J.A., van der Laan H., 2001, A&A, 374, 861

Strom R.G., Riley J.M., Spinrad H., van Breugel W.J.M., Djorgovski S., Liebert J., McCarthy P.J., 1990, A&A, 227, 19

Taylor G.B., Vermeulen R.C., Readhead A.C.S., Pearson T.J., Henstock D.R., Wilkinson P.N., 1996, ApJS, 107, 37

Vigotti M., Grueff G., Perley R., Clark B.G., Bridle A.H., 1989, AJ, 98, 419

CHAPTER 3

J1432+158: the most distant giant quasar

3.1 Abstract

We present low-frequency, GMRT observations at 333 and 617 MHz of the most-distant giant quasar, J1432+158, which is at a redshift of 1.005. The radio source has a total angular extent of 168 arcsec, corresponding to a projected linear size of 1.35 Mpc. This makes it presently the largest single object observed beyond a redshift of one. The objectives of the GMRT observations were to investigate the possibility of detecting a bridge of emission at low frequencies, which may be suppressed due to inverse-Compton losses against the CMB photons. We detect a jet-like structure connecting the core to the western hotspot, while the eastern hotspot is found to be largely tail-less with no significant bridge emission. The estimated life-time for the radiating electrons in the tail of the western lobe appears smaller than the travel time of the radiating particles from the hotspot, suggesting either in-situ acceleration or dissipation of energy by the jet at this location. The pressure of the intergalactic medium at $z \sim 1$ estimated from the minimum energy density calculations appears to be marginally lower than the value extrapolated from nearby GRSs.

3.2 Introduction

It is well known that there is a dearth of GRSs at redshifts $\gtrsim$1. Therefore, any GRS found at a redshift of 1 or greater is of special importance. A possible reason for the dearth of GRSs at high redshifts is due to inverse-Compton scattering of the radiating particles against the CMB photons, which decreases the bridge emission of the diffuse radio lobes of GRSs. This could, in principle, lead to the identification of the hotspots and the core of a distant GRS as unrelated radio sources. At present, two GRSs with redshifts >1 are known, namely 4C39.24 which is associated with a galaxy at a redshift of 1.88 and has been studied in some detail by Law-Green et al. (1995) and the object of our study, namely J1432+158.

In this chapter, we present low-frequency, GMRT observations at 333 and 617 MHz of the most-distant giant quasar, J1432+158, which is at a redshift of 1.005 (see Hintzen, Ulvestad & Owen 1983), so that $1''$ corresponds to $\sim$8 kpc, and discuss the nature of this source. One of the effects which makes it difficult to identify giants at large redshifts is the suppression of bridge emission by inverse-Compton losses against the CMB photons, which increases strongly with redshift (Gopal-Krishna, Wiita & Saripalli 1989). This could lead to 'tail-less' hotspots leading to their classification as independent radio sources (e.g. Baldwin 1982). The problem would be more acute if there are no detected cores and radio jets. The objectives of the GMRT observations were to investigate the possibility of detecting bridges of emission at low frequencies, and/or a radio jet, with the broader goal of developing strategies for identifying high-redshift giant sources.

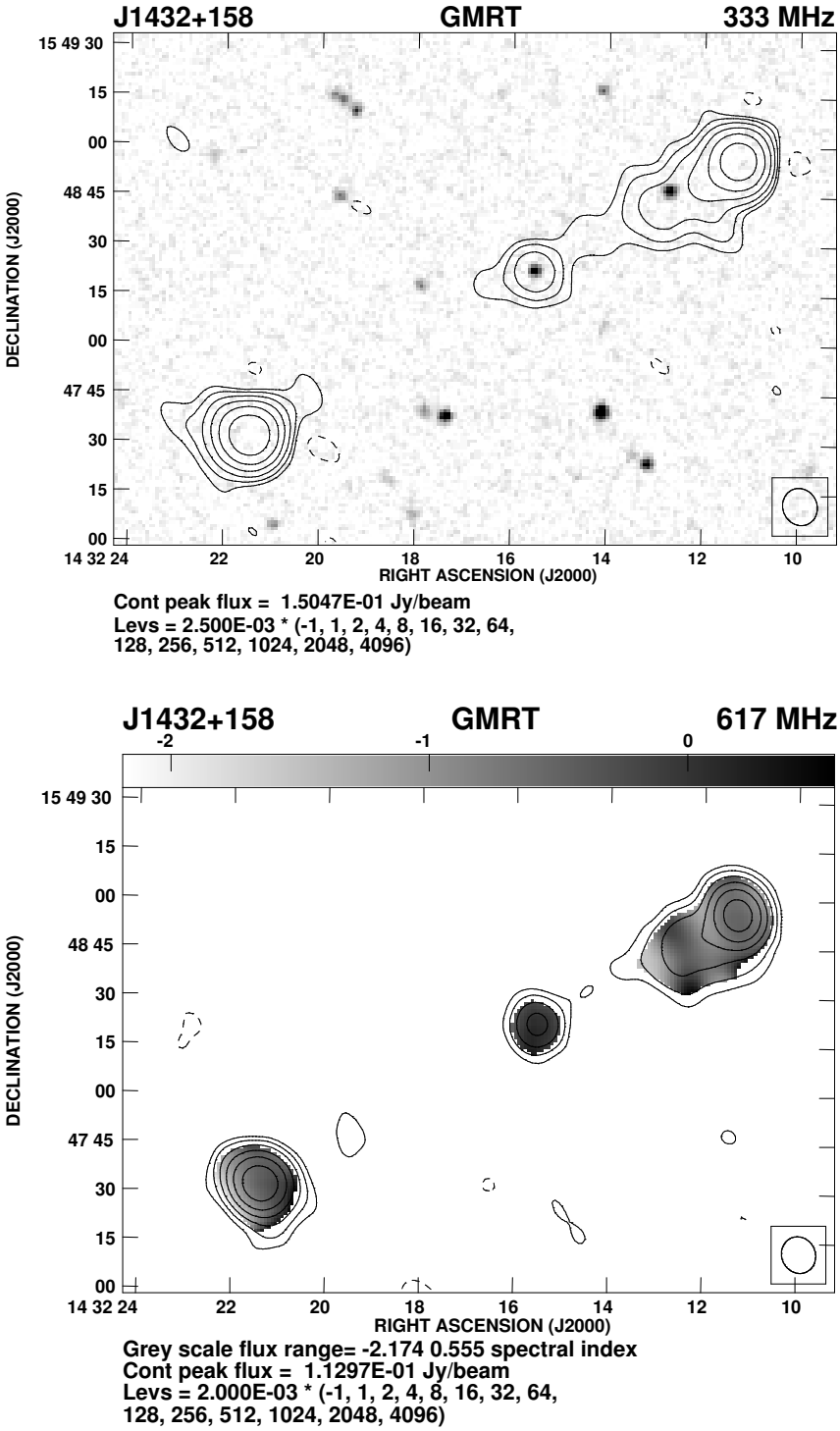

Figure 3.1: Top panel: The 333-MHz image with an angular resolution of 11.″4×10.″3 along a position angle of 24° is shown superimposed on the optical field. Bottom panel: The 617-MHz image is shown convolved to the same resolution as the 333-MHz image with the spectral index between 333 and 617 MHz being shown in grey.

3.3 Observations

The GMRT observations were made at 333 and 617 MHz on 2002 Aug 24 and 2003 Jul 11 respectively. The observations were made in the standard fashion, with each source observation interspersed with observations of the phase calibrator. The source was observed for about 8 hours at 333 MHz, although a significant amount of data had to be edited out due to ionospheric disturbances. The observations at 617 MHz were made in the 'snapshot' mode with only about one hour being spent on the source. The primary flux density calibrator was 3C286 whose flux density was estimated on the VLA scale. The phase calibrator at 333 MHz was 3C298 whose flux density was estimated to be 29.6±0.3 Jy, while at 610 MHz the phase calibrator was J1445+099 with a flux density of 2.39±0.02 Jy. The data analyses were done using the `AIPS` of the National Radio Astronomy Observatory.

3.4 Results

The GMRT images of J1432+158 at 333 and 617 MHz are presented in Fig. 3.1. The 333-MHz image with an angular resolution of $11.''4 \times 10.''3$ along a position angle of 24° is superimposed on the optical field, showing the radio core to be coincident with the optical quasar. The 617-MHz image is shown convolved to the same resolution as the 333-MHz image with the spectral index image, α, (defined as $S_\nu \propto \nu^\alpha$), between 333 and 617 MHz being shown in grey. Both the images show the three main components of the source, the western lobe, the weak nuclear component coincident with the position of the optical quasar, and the eastern lobe. The 333-MHz image shows evidence of a jet-like extension towards the north-western component,

but no bridge of emission is seen between the eastern hot-spot and the radio core. While the western hotspot appears to have a tail of emission extending towards the core, no significant tail is seen in the eastern hotspot at either 333 or 617 MHz. These images are consistent with the NVSS and FIRST images which are shown in Fig. 3.2. The higher-resolution FIRST image shows the core to be extended, with a deconvolved angular size of $1.''6 \times 1.''0$ along a position angle of 117°, consistent with the direction of the jet-like structure seen in the 333-MHz image.

The observed parameters of J1432+158, from both the GMRT images as well as from the NVSS and FIRST images at 1400 MHz are listed in Table 3.1, which is arranged as follows. Column 1: Name of the telescope, column 2: frequency of observations in units of MHz, columns 3-5: the major and minor axes of the restoring beam in arcsec and its PA in degrees; column 6: the rms noise in units of mJy/beam; column 7: the integrated flux density of the source in mJy estimated by specifying an area around the source; columns 8, 11 and 14: component designation; columns 9 and 10, 12 and 13, and 15 and 16: the peak and total flux densities of each of the components in units of mJy/beam and mJy.

3.5 Discussion and remarks

The overall angular size of J1432+158 is 168 arcsec which corresponds to a projected linear size of 1.35 Mpc. This makes it the largest single object observed beyond a redshift of one. Since it is associated with a quasar, it is expected to be inclined at less than $\sim 45°$ to the line of sight, implying that its intrinsic size is at least 1.9 Mpc. Given its large size it may be relevant to enquire whether all the three components are physically related.

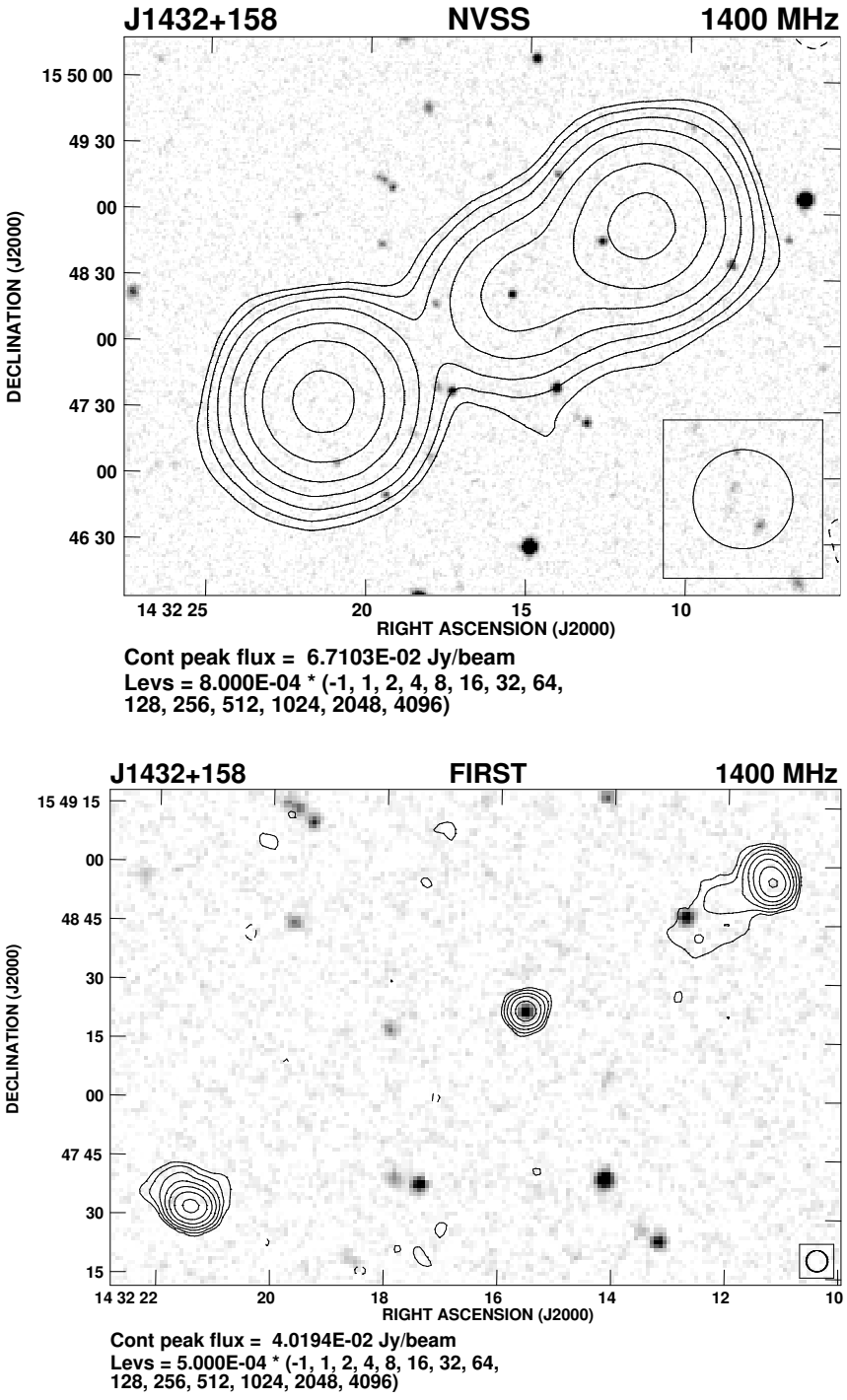

Figure 3.2: The NVSS (top panel) and FIRST (bottom panel) images at 1400 MHz with angular resolutionsof 45 and 5.4 arcsec respectively shown superimposed on the optical field.

Table 3.1: The observational parameters and observed properties of J1432+158

Telescope	Freq.	Beam size			rms	S_I	Cp	S_p	S_t	Cp	S_p	S_t	Cp	S_p	S_t
	MHz	$''$	$''$	$^\circ$	mJy /b	mJy		mJy /b	mJy		mJy /b	mJy		mJy /b	mJy
GMRT	333	11.4	10.3	24	0.58	510	W	135	257	C	20	26	E	150	218
GMRT	617	11.4	10.3	24	0.58	340	W	97	167	C	20	22	E	113	146
VLA-NVSS	1400	45.0	45.0	0	0.28	167	W	67	75	C	19		E	64	71
VLA-FIRST	1400	5.4	5.4	0	0.15	142	W	35	68	C	14	15	E	40	65

Both the outer components have a steep radio spectrum, while the core has a flat spectrum, similar to standard double-lobed radio sources. The structure of the western lobe, and the presence of a jet-like extension from the core towards this lobe, confirms that these two features are indeed related. If the eastern component is unrelated, these two features would form a weak-cored, one-sided source, which is indeed very rare (cf. Saikia et al. 1989). Also, no optical object is found associated with the eastern component in the DSS prints. The collinearity of the structure formed by the three main components, where the complement of the angle formed at the nucleus by the outer hot-spots is only 2°, and the rough symmetry of the flux density and the location of the outer hotspots strongly suggest that all three components are related. The arm-length and flux density ratio of the lobes are ∼1.4 and 1.1 respectively, which is similar to that of other giant radio sources (see Ishwara-Chandra & Saikia 1999, hereinafter referred to as IC99). However, it is the jet-side which appears to be closer to the radio core, demonstrating the existence of asymmetries on Mpc scales either due to clusters of galaxies or filamentary structures likely to form in hierarchical structure-formation scenarios. The overall spectral index of the source, and the flux density of the different components using our measurements and values estimated from the NVSS image are shown in Fig. 3.3. The integrated flux densities at 5 GHz from the NRAO Green Bank survey are also shown (Gregory & Condon 1991; Becker, White & Edwards 1991). The spectral index of the entire source is -0.84 ± 0.03, while the western and eastern components have steep spectral indices of -0.86 ± 0.08 and -0.79 ± 0.06 respectively, and the core has a flat spectral index of -0.04 ± 0.02. The spectral index image between 333 and 617 MHz (Fig. 3.1) shows that the component in the tail of the western lobe does not show evidence of any significant spectral steepening. Its spectral

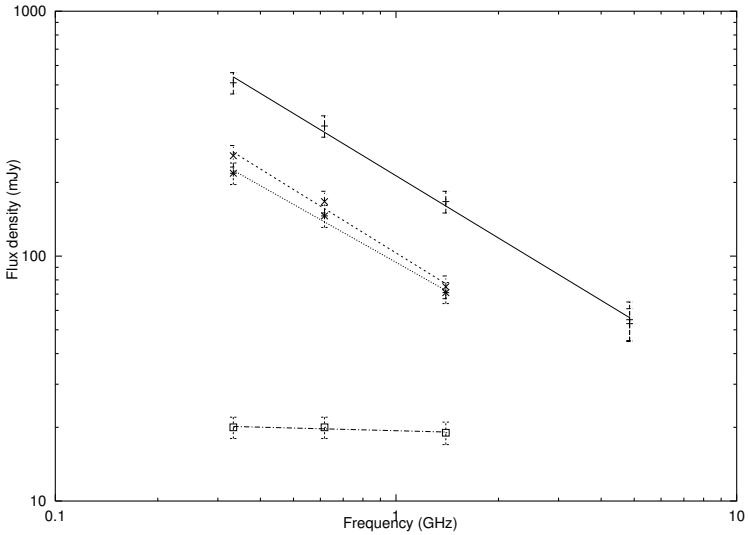

Figure 3.3: The integrated spectrum (+, continuous line) of J1432+158, and the spectra of the western (×, dashed), eastern (∗, dotted) and core (□, dashed-dotted) components. The lines show the linear least-square fits to the points.

index of ~ -0.6 between 333 and 617 MHz is similar to that of the hotspot, the low-frequency spectrum appearing marginally flatter than the higher-frequency value. The flux density of the core measured by Hintzen, Ulvestad & Owen (1983) at 1415 MHz with an angular resolution of 1.″6×1.″0 is 11 mJy compared with the FIRST value of 15 mJy with an angular resolution of 5.″4 arcsec. The difference is possibly largely due to the different resolutions of these observations.

The minimum energy density for a synchrotron radio source component is given by (see e.g., Miley 1980),

$$u_{\rm m} = 4.5 \times 10^{-11} \left[\frac{(1+z)^{3-\alpha}\, S_0\, \nu_0^{-\alpha}\, (\nu_2^{0.5+\alpha} - \nu_1^{0.5+\alpha})}{\theta_x \theta_y\, s\, (0.5+\alpha)} \right]^{4/7} \quad \mathrm{J\,m^{-3}}. \tag{3.1}$$

Here z is the redshift, S_0 (Jy) is the flux density at frequency ν_0 (GHz),

α is the spectral index with ν_1 and ν_2 (GHz) as the lower and upper cut off frequencies presumed for the radio spectrum, with $\nu_1 < \nu < \nu_2$, θ_x and θ_y (arcsec) represent the size of the source component along its major and minor radio axes, and s is the pathlength through the component along the line of sight in kpc. We have assumed an equal energy distribution between the electrons and the heavy particles, taken the volume filling factor to be unity and also assumed that the magnetic field vector lies in the plane of the sky.

The values of the minimum energy density and magnetic field are 3.6×10^{-12} J m^{-3} and 2.0 nT for the western hotspot and 2.6×10^{-12} J m^{-3} and 1.7 nT for the eastern one. Here we have integrated the radio emission from 10 MHz to 100 GHz, and used the deconvolved sizes of the components. The values for the component in the the tail of the western lobe are 3×10^{-13} J m^{-3} and 0.6 nT respectively. Assuming that the spectral break lies beyond 5 GHz, the radiative life-time of the electron is only about 3×10^6 yr, with the inverse-Compton losses being a factor of about 5 higher than the synchrotron losses. The projected distance of this feature from the hotspot is $\sim$220 kpc, which would take $\gtrsim 7 \times 10^6$ yr for particles moving backwards with velocities $\lesssim$0.1c (e.g. Ishwara-Chandra et al. 2001). This suggests that there could be re-acceleration of particles in this component, or it could be part of the jet either forming a knot of emission or another hotspot. This is consistent with the lack of spectral steepening in this region.

The minimum energy of the bridges and lobes of GRSs may be used to estimate the pressure in the IGM, whose emissivity is otherwise not directly detectable, by assuming that the lobes are in pressure equilibrium with it (e.g. Subrahmanyan and Saripalli 1993, hereinafter referred to as SS93; Mack et

al. 1998; IC99; Schoenmakers et al. 2000). The pressure of such a hot, diffuse, non-relativistic IGM should vary with redshift as $P_z \sim P_0(1+z)^5$. SS93 estimated $P_0 \sim 10^{-15}$ Pa, based on Saripalli's (1988) values for minimum energy in the lobes of 8 GRSs, which appeared systematically lower than other similar estimates in the literature. Saripalli (1988) and SS93 suggested that their values were lower as these represented $u_{\rm m}$ in diffuse bridges as compared to the estimates made for the entire lobes in the literature. However, the expression for $u_{\rm m}$ used by Saripalli (1988) is lower by a factor of $\sim$3.5, and when corrected for this, the median value is $\sim 2 \times 10^{-14}$ J m^{-3}, in good agreement with other estimates in the literature. This corresponds to $P_0 \sim 5 \times 10^{-15}$ Pa. There could be a marginal trend for an increase in P with redshift (SS93; IC99; Schoenmakers et al. 2000); however, possible caveats using the presently available samples have been highlighted by IC99 and Schoenmakers et al. (2000). Our estimate for the component in the tail of the western lobe in the quasar J1432+158 yields $P \sim 10^{-13}$ Pa, while the expected value for P_z at z=1.005 is $\sim 1.5 \times 10^{-13}$ Pa. Although this is higher than the measured value by $\sim$1.5, estimates of P_z in the diffuse bridges and lobes of a sample of GRSs at cosmologically interesting redshifts of $\gtrsim$1, are required to examine critically the assumption of pressure balance with the IGM and the variation of pressure with redshift.

References

Baldwin J.E., 1982, in Heeschen D.S., Wade C.M., eds, Proc. IAU Symp. 97, Extragalactic Radio Sources, Reidel, p 21

Becker R.H., White R.L., Edwards A.L., 1991, ApJS, 75, 1

Gopal-Krishna, Wiita P.J., Saripalli L., 1989, MNRAS, 239, 173

Gregory, P.C., Condon, J.J., 1991, ApJS, 75, 1011

Hintzen P., Ulvestad J., Owen F., 1983, AJ, 88, 709

Ishwara-Chandra C.H., Saikia D.J., 1999, MNRAS, 309, 100 (IC99)

Ishwara-Chandra C.H., Saikia D.J., McCarthy P.J., van Breugel W.J.M., 2001, MNRAS, 323, 460

Law-Green J.D.B., Eales S.A., Leahy J.P., Rawlings S., Lacy M., 1995, MNRAS, 277, 995

Mack K.-H., Klein U., O'Dea C.P., Willis A.G., Saripalli L., 1998, A&A, 329, 431

Miley G.K., 1980, ARA&A, 18, 165

Saikia D.J., Junor, W., Muxlow, T.W.B., Tzioumis, A.K., 1989, Nature, 339, 286

Saripalli L., 1988, Ph.D. Thesis, Indian Institute of Science, Bangalore

Schoenmakers A.P., Mack K.-H., de Bruyn A.G., Röttgering H.J.A., Klein U., van der Laan H., 2000, A&AS, 146, 293

Subrahmanyan R., Saripalli, L., 1993, MNRAS, 260, 908 (SS93)

CHAPTER 4

A multifrequency study of giant radio sources

I. Low-frequency Giant Metrewave Radio Telescope observations of selected sources

4.1 Abstract

We present low-frequency observations with the GMRT of a sample of GRSs, and high-frequency observations of two of these sources with the VLA. From multifrequency observations of the lobes we estimate the magnetic field strengths using three different approaches, and show that these differ at most by a factor of ∼3. For these large radio sources the inverse-Compton losses usually dominate over synchrotron losses when estimates of the classical minimum energy magnetic field are used, consistent with earlier studies. However, this is often not true if the magnetic fields are close to the values estimated using the formalism of Beck & Krause. We also examine the spectral indices of the cores and any evidence of recurrent activity in these sources. We probe the environment using the symmetry parameters of these sources and suggest that their environments are often asymmetric on scales of ∼1 Mpc, consistent with earlier studies.

4.2 Introduction

Multifrequency observations of GRSs are extremely useful for studying a number of astrophysical questions related to these sources. We have selected a representative, but somewhat heterogeneous, sample of 10 edge-brightened, large radio sources spread over about two decades in luminosity and lying between redshifts of ∼0.1 and 0.8 for observations with the GMRT and the VLA over a large frequency range. The objectives of these observations are to estimate their spectral ages, injection spectral indices ($\alpha_{\rm inj}$), and also examine the range of magnetic field estimates using different formalisms and their effect on the estimates of the spectral ages. It is worth noting here that a reliable determination of the spectra of the lobes over a large frequency range from our observations would help get reliable estimates of the physical parameters of the lobes such as their magnetic fields. We also explore any evidence of recurrent activity and attempt to probe the environments of these sources on Mpc scales using their symmetry parameters.

With the current cosmological parameters, eight of the 10 sources in our sample have projected linear sizes $\gtrsim$1 Mpc. Seven of the ten sources are from the sample of giant radio sources studied by Machalski, Jamrozy & Zola (2001) and Machalski et al. (2006, hereinafter referred to as MJZK), while the remaining three are from our earlier study (Konar et al. 2004). In this chapter we report GMRT observations of nine of these sources at a number of frequencies ranging from ∼240 to 1300 MHz, and also VLA observations for two of the sources, namely J1604+3731 and J1702+4217, at 4860 MHz, and for J1702+4217 at 8440 MHz as well. The GMRT 605-MHz and VLA 1425-MHz images of one of the sources, J1313+6937, have been published earlier (Konar et al. 2004), while the VLA 4873-MHz image is presented in this

chapter. The values of the flux densities at all the above three frequencies and derived parameters have been presented here for completeness. New GMRT images of J1343+3758 at 316 and 604 MHz are presented here, although the source has been studied earlier by Jamrozy et al. (2005). The observations presented here for this sample provide information on their low-frequency emission and help establish the spectra of the lobes over a large frequency range. These spectra have been used to estimate the magnetic fields of the lobes using three different formalisms to understand the possible range of these values, make a comparative study of the relative importance of inverse-Compton and synchrotron losses, and explore some of the consequences. We also discuss the core strengths and symmetry parameters of these sources to probe their environments and compare with earlier studies.

In Chapter 5 we use the results of our observations to estimate the spectral ages and injection spectral indices of these sources and examine possible correlations of $\alpha_{\rm inj}$ with luminosity, redshift and size.

4.3 Observations and analyses

Both the GMRT and the VLA observations were made in the standard fashion, with each target source observations interspersed with observations of the phase calibrator. The primary flux density calibrator was any one of 3C48, 3C147 and 3C286 with all flux densities being on the scale of Baars et al. (1977). The total observing time on the source was about a few hours for the GMRT observations while for the VLA observations the time on source ranged from 10 to 20 minutes. The low-frequency GMRT data were sometimes significantly affected by radio frequency interference, and these data were flagged. All the data were analysed in the standard fashion using the

Table 4.1: Observing log

Telescope	Array Conf.	Obs. Freq. MHz	Sources	Obs. Date
(1)	(2)	(3)	(4)	(5)
GMRT		241	J1155+4029	2005 March 16
GMRT		239	J1604+3438	2005 December 28
GMRT		334	J0912+3510	2003 September 20
GMRT		316	J0927+3510	2003 September 20
GMRT		334	J1155+4029	2005 December 25
GMRT		316	J1343+3758	2003 September 20
GMRT		334	J1604+3731	2006 March 09
GMRT		334	J1604+3438	2006 April 04
GMRT		334	J2312+1845	2005 September 08
GMRT		604	J0720+2837	2003 September 05
GMRT		606	J0912+3510	2003 September 05
GMRT		606	J0927+3510	2003 September 06
GMRT		604	J1343+3758	2003 September 06
GMRT		605	J1155+4029	2005 March 16
GMRT		614	J1604+3438	2005 December 28
GMRT		613	J1604+3731	2004 January 01
GMRT		602	J1702+4217	2004 January 17
GMRT		1289	J1604+3731	2006 January 01
GMRT		1288	J1702+4217	2005 December 04
VLA	BnC	1425	J2312+1845	2000 March 13
GMRT		1258	J1155+4029	2005 November 30
GMRT		1265	J1604+3438	2006 July 12
VLA[a]	D	4860	J1604+3731	1993 December 23
VLA[a]	D	4860	J1702+4217	1993 December 23
VLA	D	4873	J1313+6937	2000 August 18
VLA[a]	D	8440	J1702+4217	1993 December 23
VLA[a]	D	9040	J1604+3731	1993 December 23

[a] archival data from the VLA

NRAO AIPS package. All the data were self calibrated to produce the best possible images

The observing log for both the GMRT and the VLA observations is given in Table 4.1 which is arranged as follows. Columns 1 and 2 show the name of the telescope, and the array configuration for the VLA observations; column 3 shows the frequency of the observations in MHz, while columns 4 and 5 list the sources observed and the dates of the observations respectively.

4.4 Observational results

The GMRT images of the sources at the different frequencies are presented in Fig. 4.1–4.10, while the observational parameters and some of the observed properties are presented in Table 4.2, which is arranged as follows. Column 1: Name of the source; column 2: frequency of observations in units of MHz, with the letter G or V representing either GMRT or VLA observations; columns 3-5: the major and minor axes of the restoring beam in arcsec and its position angle (PA) in degrees; column 6: the rms noise in units of mJy beam^{-1}; column 7: the integrated flux density of the source in mJy estimated by specifying an area enclosing the entire source. We examined the change in flux density by specifying different areas and found the difference to be within a few per cent of the total. The flux densities at different frequencies have been estimated over similar areas. Columns 8, 11 and 14: component designation, where W, E, N, S and C denote the western, eastern, northern, southern and core components respectively; columns 9 and 10, 12 and 13, and 15 and 16: the peak and total flux densities of each of the components in units of mJy beam^{-1} and mJy respectively. The core flux densities were sometimes evaluated by imaging the source using the longer spacings so that

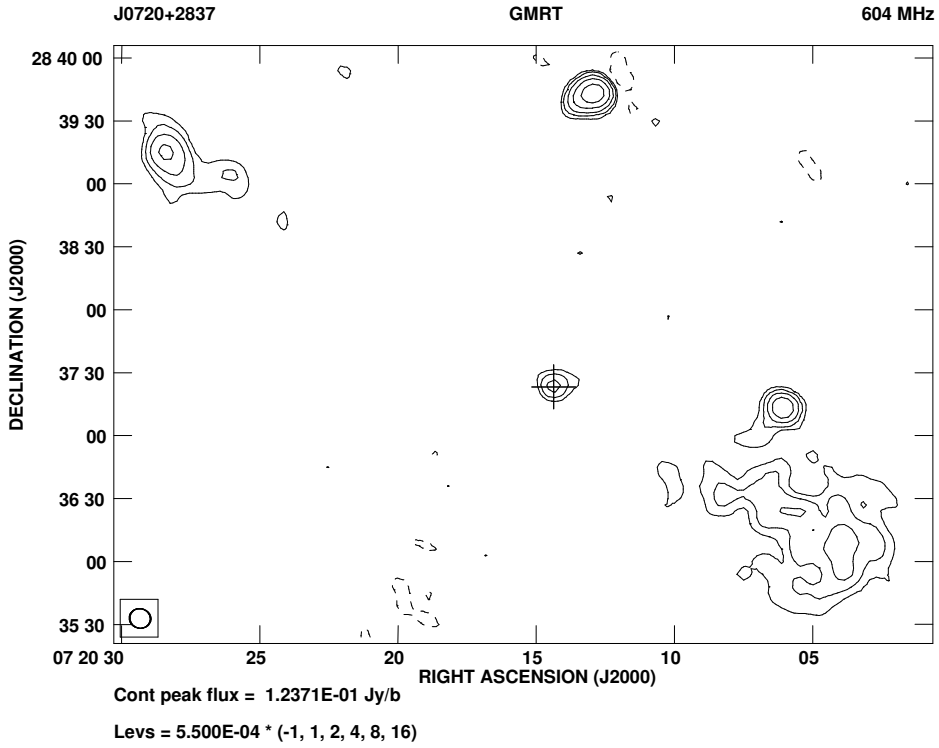

Figure 4.1: The contour levels and the peak brightness for all the images are given below each one of them. In all the images the restoring beam is indicated by an ellipse and the + sign indicates the position of the optical host galaxy. At the top of each image are given the IAU name of the source, the telescope with which it was observed and the frequency of observations in MHz respectively.

the core appears reasonably isolated. The superscript g indicates that the flux densities have been estimated from a two-dimensional Gaussian fit to the core component. In this Table we also list the flux densities at 4860 MHz for seven of the sources whose images have been published by MJZK, and also the lobe flux densities for J2312+1845 at 1425 and 4866 MHz from the images published by Konar et al. (2004).

(a) Notes on the sources

Notes on the overall structure and spectra of the cores are presented in this chapter while those based on spectral ages of the lobes are presented in the

next chapter (Chapter 5).

J0720+2837: The eastern lobe has a more prominent hot-spot compared with the western lobe, the ratio of the peak flux density being ∼1.7, while the western lobe has more extended emission with the ratio of the total flux density being ∼2.5 in our 604-MHz image. By convolving the 604-MHz image (Fig. 4.1) to a similar resolution as that of the VLA 4860-MHz image (MJZK) yields a spectral index, α, ($S_\nu \propto \nu^{-\alpha}$), for the core of 0.63 and 0.59 using the peak and total flux densities respectively estimated from two-dimensional Gaussian fits. The flux densities of the two unrelated sources in the field, the northern one at RA: $07^{\rm h}\ 20^{\rm m}\ 13.^{\rm s}02$, Dec: $28^\circ\ 39'\ 42.''58$, and the western one at RA: $07^{\rm h}\ 20^{\rm m}\ 06.^{\rm s}09$, Dec $28^\circ\ 37'\ 12.''9$ have also been estimated from the similar-resolution images. All positions are in J2000 co-ordinates. These are 20.1 and 3.3 mJy at 604 and 4860 MHz respectively for the northern source, with the corresponding values for the western source being 11.3 and 0.74 mJy. The spectral indices for these sources are 0.87 and 1.31 respectively.

J0912+3510: There is a pair of optical galaxies ∼2.6 arcsec from the position of the radio core (MJZK), which has a peak brightness of ∼0.4 mJy beam^{-1} in the 4860-MHz image. It is not certain if either of these galaxies is associated with the radio source. The core is not unambiguously detected at 606 MHz, the limit being ∼0.6 mJy beam^{-1} from the full-resolution image. Convolving the 606-MHz image (Fig. 4.2) to that of the 4860-MHz one shows that the central component has a peak brightness of 0.85 mJy beam^{-1}, but its position is displaced by ∼14 arcsec to the north of the core seen in the 4860-MHz image.

J0927+3510: This source has been identified as a possible DDRG by MJZK based on their 4860-MHz VLA image. Our 606-MHz GMRT image (Fig.

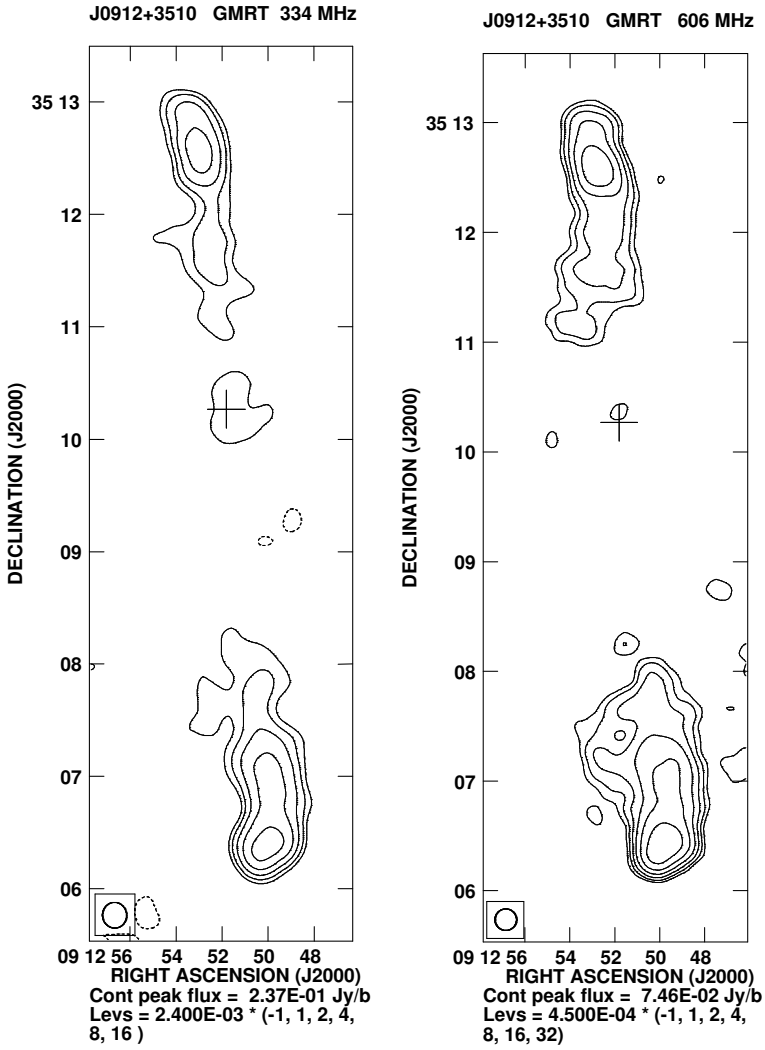

Figure 4.2: Radio images of J0912+3510

4.3) also shows clearly the inner components with the optical host galaxy in between. Using the integrated flux densities at 316, 606 and 4860 MHz from images of the same resolution yields spectral indices of ∼1.35 and 1.17 for the inner western and eastern components respectively (see also Chapter 5). The steep spectral indices suggest that these features are likely to be enhancements in the tail emission rather than a new pair of lobes.

J1155+4029: It is very asymmetric in its arm-length (see Fig. 4.4) as well as flux density ratios. The arm-length ratio is ∼2.1, while the ratios of the

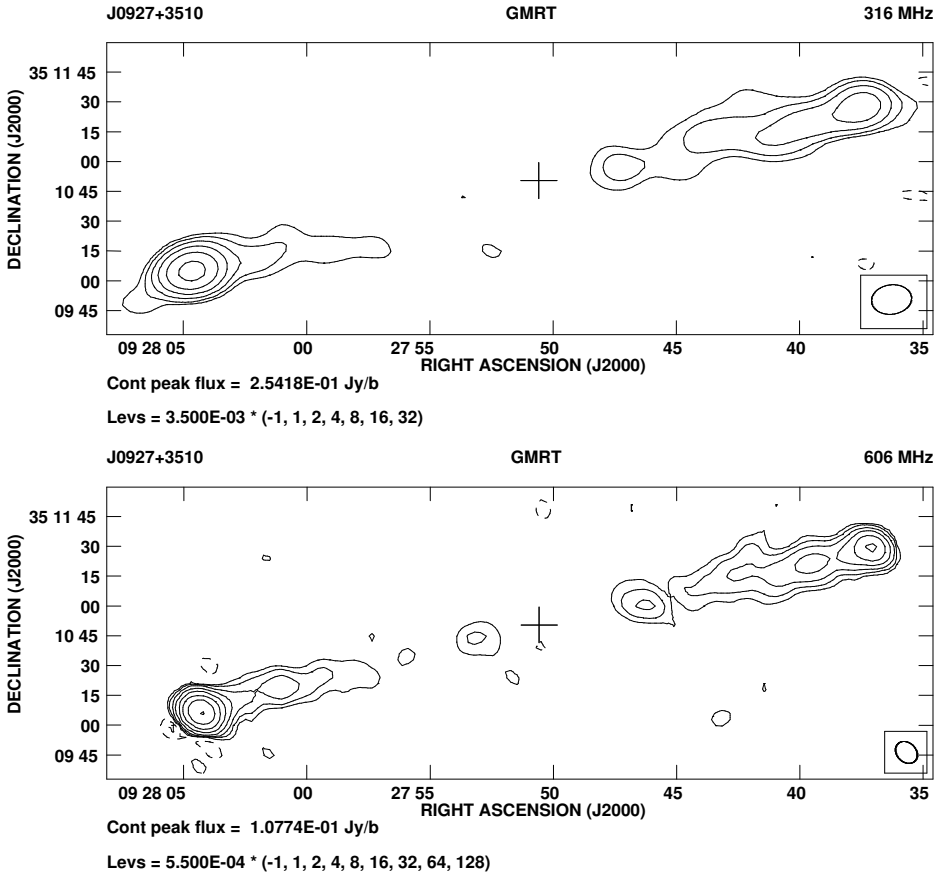

Figure 4.3: Radio images of J0927+3510

peak and total flux densities estimated from the 605-MHz image are ∼14 and 7 respectively with the nearer (eastern) lobe being brighter. The ratios are similar at the other frequencies. In our sample of 9 GRSs, it has the highest value of core fraction of 0.14 at a frequency of 8 GHz in its rest frame. However, the core has a spectrum which is peaked at ∼1 GHz (see Section 4.2), suggesting that it might be a mas-scale double.

J1343+3758: This source (see Fig. 4.6), which has been studied in some detail by Jamrozy et al. (2005), has an arm-length ratio of ∼1.3 with the more relaxed (western) lobe being closer to the nucleus. This source has a core with a flat spectrum with α ∼0.1 between 604 and 4860 MHz.

J1604+3438: This source (see Figs. 4.7 and 4.8) was listed as a possible

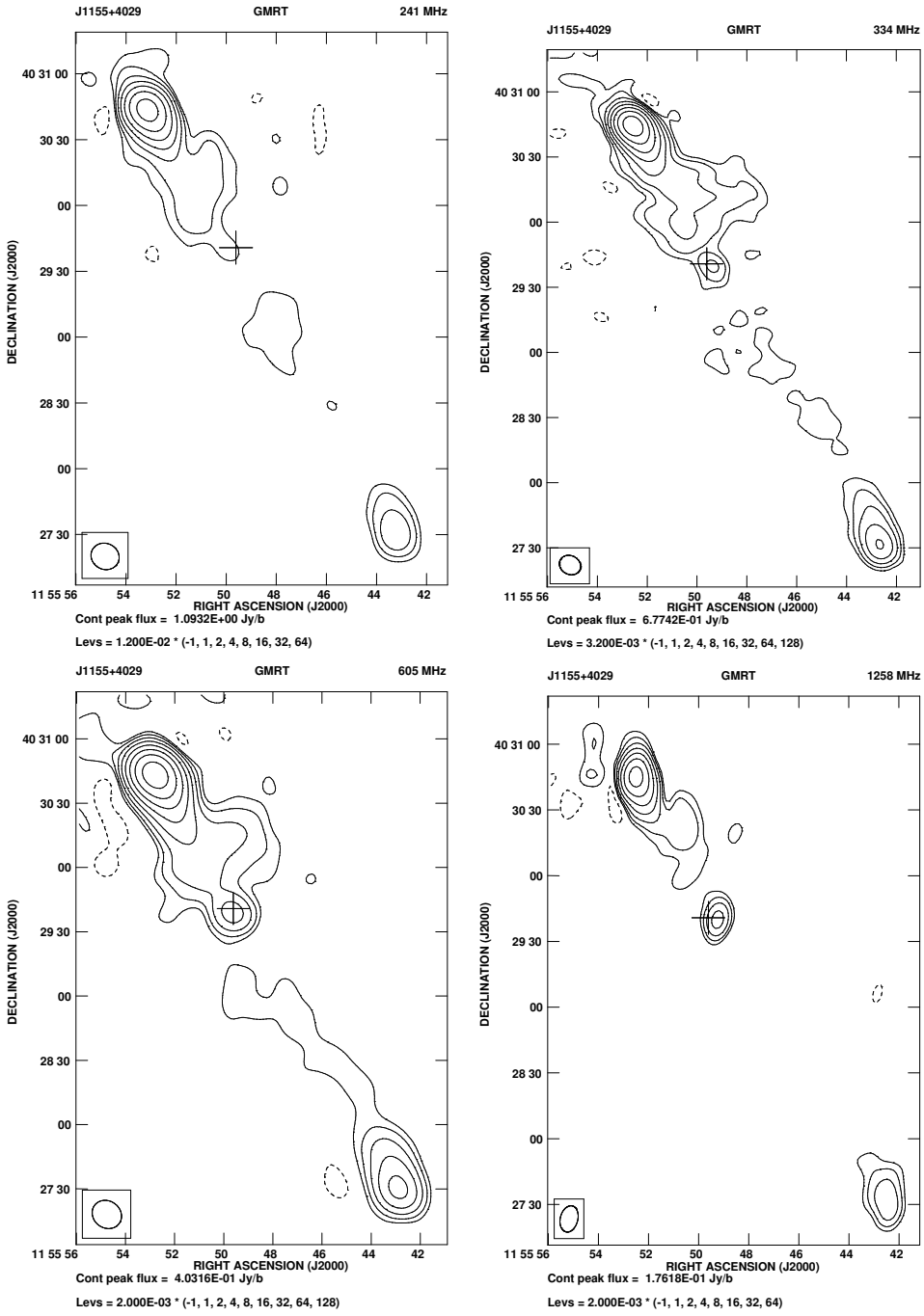

Figure 4.4: Radio images of J1155+4029

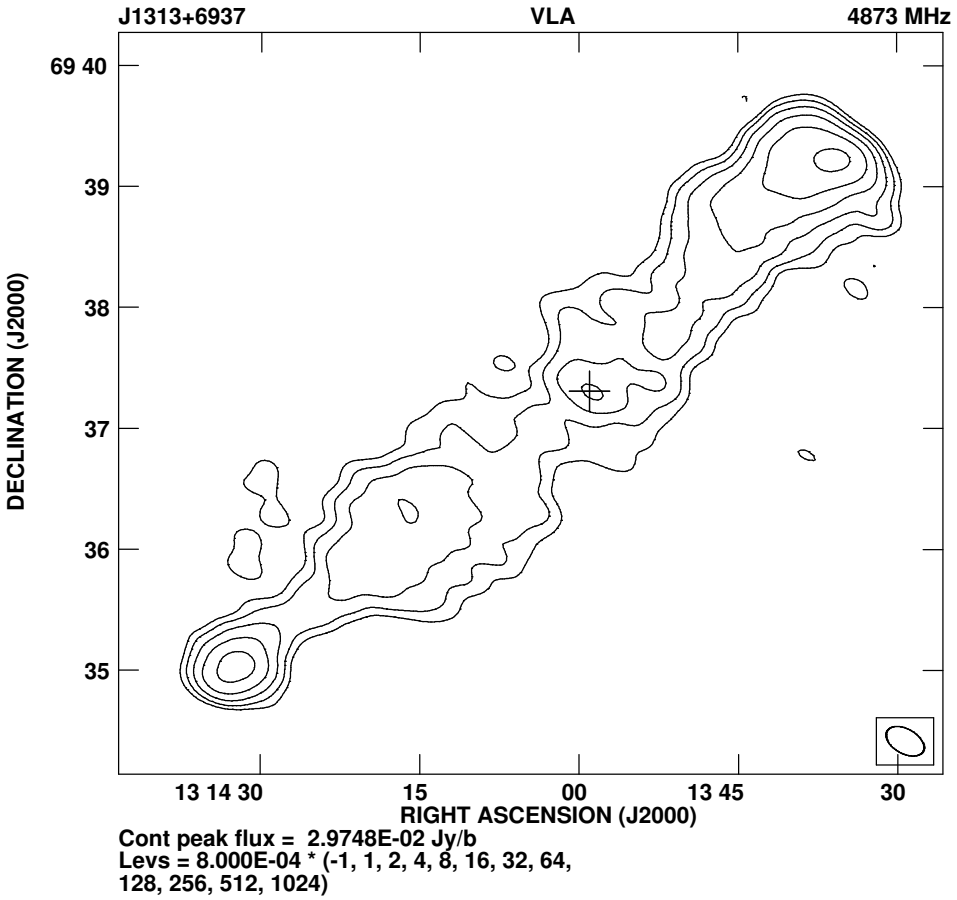

Figure 4.5: Radio image of J1313+6937

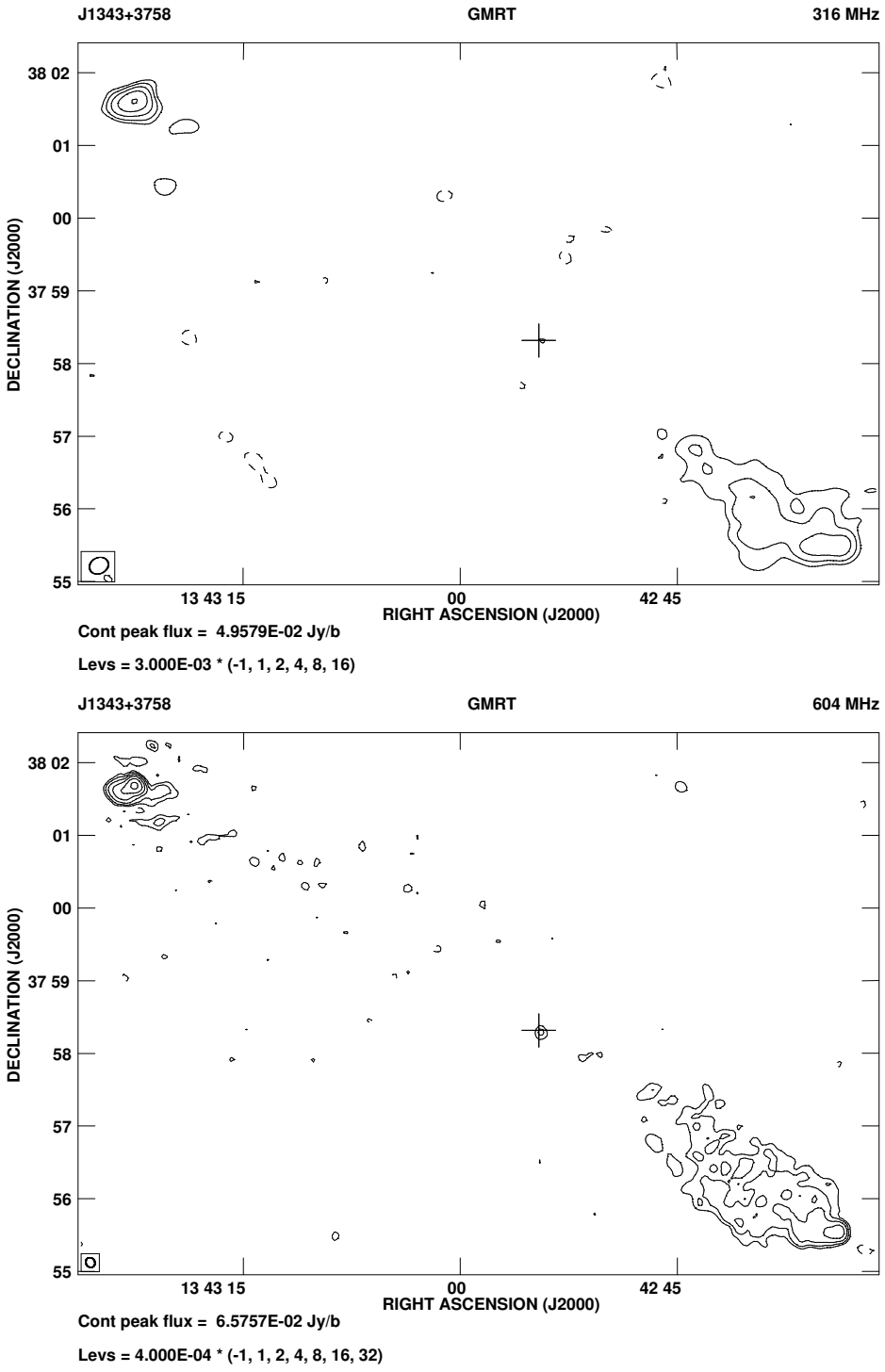

Figure 4.6: Radio images of J1343+3758

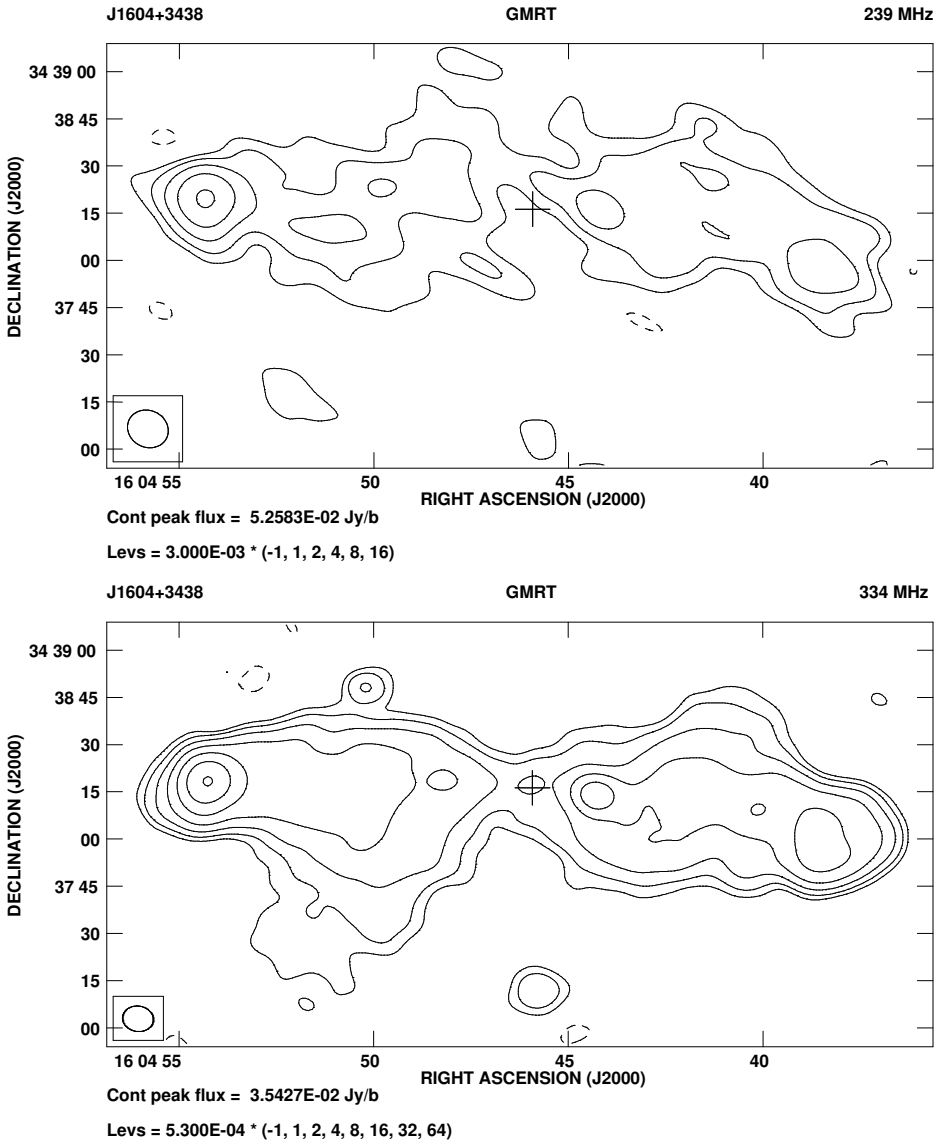

Figure 4.7: Radio images of J1604+3438

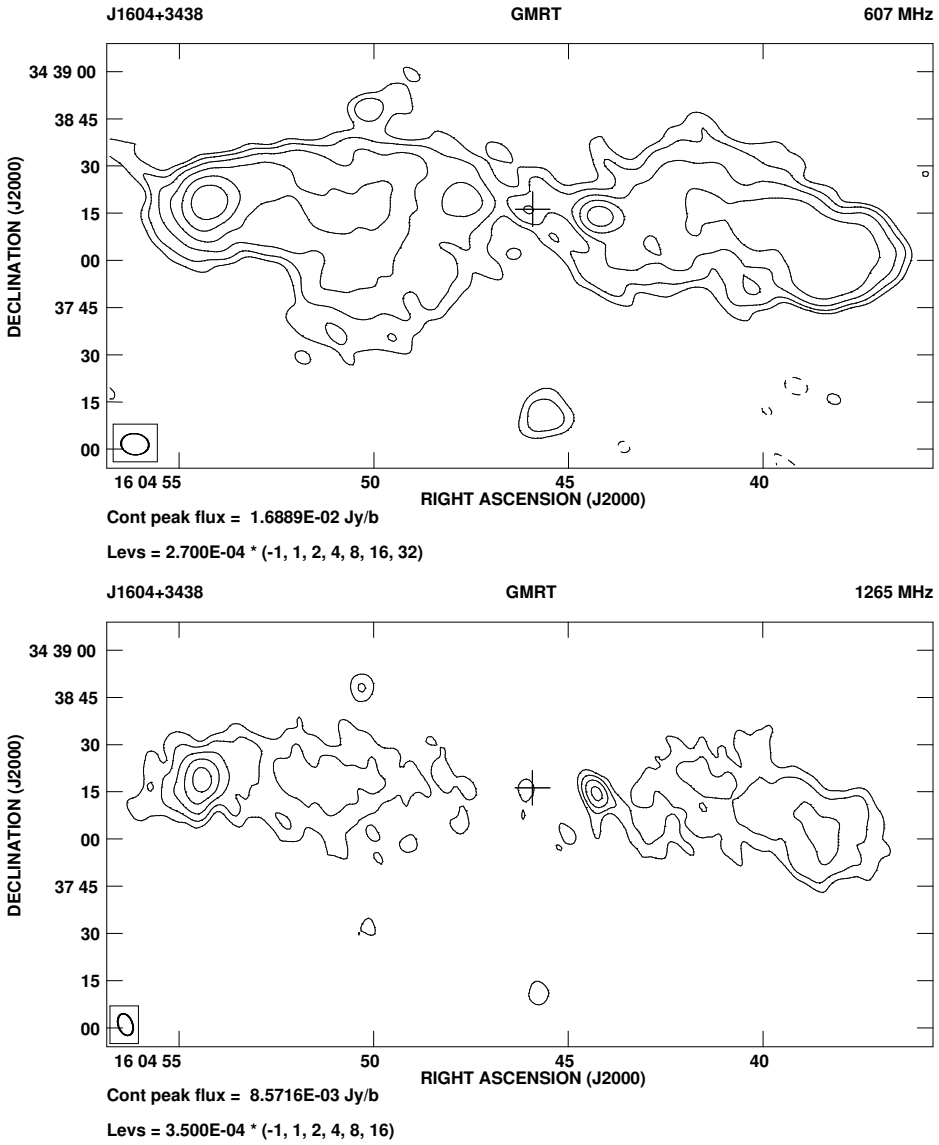

Figure 4.8: Radio images of J1604+3438

Table 4.2: The observational parameters and observed properties of the sources

Source	Freq.	Beam size			rms	S_I	Cp	S_p	S_t	Cp	S_p	S_t	Cp	S_p	S_t
	MHz	$''$	$''$	$^\circ$	mJy beam^{-1}	mJy		mJy beam^{-1}	mJy		mJy beam^{-1}	mJy		mJy beam^{-1}	mJy
(1)	(2)	(3)	(4)	(5)	(6)	(7)	(8)	(9)	(10)	(11)	(12)	(13)	(14)	(15)	(16)
J0720+2837	G604	10.1	9.3	73.3	0.18	96	W	3.2	65	C^g	2.8	3.3	E	5.3	26
	V4860	19.1	11.9	70	0.03	16	W	1.1	6.7	C^g	0.85	1.0	E	2.0	7.9
J0912+3510	G334	13.7	12.9	4	0.78	488	N	28	175				S	52	309
	G606	11.8	11.8	0	0.11	257	N	13	82				S	24	171
	V4860	20	20	0	0.04	56	N	5.6	20	C	$\lesssim$0.4		S	11	36
J0927+3510	G316	20	14.8	98	0.92	376	W	48	160				E	149	214
	G606	12.2	9.6	43	0.11	192	W	20	74				E	74	118
	V4860	22	11.7	73	0.03	27	W	4.5	11	C^g	0.14	0.14	E	13	16
J1155+4029	G241	13.1	11.8	63	3.24	2120	NE	1087	1774	C	14		SW	96	307
	G334	10.1	8.6	61	1.18	1502	NE	684	1241	C^g	15	24	SW	54	219
	G605	14.2	12.5	53	0.73	769	NE	403	630	C^g	22	28	SW	41	105
	G1258	12.2	8.0	166	0.46	367	NE	175	294	C^g	22	23	SW	15	48
	V4860	17.8	12.2	92	0.04	99	NE	55	74	C^g	13	14	SW	6.6	11
J1313+6937	G605	8.1	4.6	151	0.20	2499	NW	39	1441	C	$\lesssim$2.0		SE	27	1046
	V1425	14.9	6.5	121	0.10	1383	NW	54	797	C^g	4.6	7.0	SE	40	585
	V4873	20.4	12.2	60	0.13	431	NW	30	255	C^g	4.1	4.3	SE	18	172
J1343+3758	G316	16	13.2	117	0.83	455	SW	22	318	C	$\lesssim$3.0		NE	48	144
	G604	8.4	7.3	29	0.11	253	SW	5.3	165	C^g	1.0	1.4	NE	15	87
	V4860	15	15	0	0.03	42	SW	3.4	25	C^g	1.1	1.1	NE	6.7	16
J1604+3438	G239	13.2	11.7	63	1.51	518	W	21	242				E	52	277
	G334	9.8	8.1	81	0.15	510	W	14	241	C	$\lesssim$2.4		E	35	270
	G614	7.7	5.1	86	0.07	232	W	6.6	108	C	$\lesssim$1.0		E	14	125
	G1265	7.1	4.5	20	0.07	152	W	3.6	67	C	$\lesssim$0.5		E	8.6	83
	V4860	15.0	10.0	72	0.06	36	W	2.1	16	C^g	1.0	1.1	E	6.5	19

Table 4.2: The observational parameters and observed properties of the sources

Source	Freq.	Beam size			rms	S_I	Cp	S_p	S_t	Cp	S_p	S_t	Cp	S_p	S_t
	MHz	$''$	$''$	$^\circ$	mJy beam^{-1}	mJy		mJy beam^{-1}	mJy		mJy beam^{-1}	mJy		mJy beam^{-1}	mJy
(1)	(2)	(3)	(4)	(5)	(6)	(7)	(8)	(9)	(10)	(11)	(12)	(13)	(14)	(15)	(16)
J2312+1845	G334	14.1	8.7	85	1.90	8131	NE	954	3510	C	$\lesssim$18		SW	1089	4537
	V1425	14.2	12.7	179	0.26	1885	NE	311	802	C^g	3.2	4.1	SW	356	1069
	V4866	14.2	13.7	120	0.12	538	NE	102	230	C^g	2.9	3.6	SW	123	307
J1604+3731	G334	10.4	7.8	68	0.35	522	N	41	222	C^g	10	12	S	106	284
	G613	7.8	4.8	171	0.10	264	N	14	111	C^g	5.4	6.4	S	53	142
	G1289	8.3	7.7	26	0.25	144	N	12	61	C^g	3.8	4	S	32	81
	V4860	13.4	13.1	93	0.01	29	N	4.6	11	C^g	1.3	1.6	S	10	17
J1702+4217	G602	12.3	4.4	124	0.10	381	NE	30	220	C^g	1.5	1.9	SW	14	158
	G1288	2.7	2.3	170	0.06	242	NE	7.6	141	C^g	1.3	1.2	SW	3.8	102
	V4860	13.7	13	65	0.02	48.3	NE	9.7	28	C^g	1.0	1.3	SW	5.9	19
	V8440	8.8	7.2	63	0.01	23	NE	4.1	14	C^g	1.4	1.5	SW	1.8	8

DDRG by MJZK on the basis of their VLA image at 4860 MHz. Although higher-resolution observations are required to determine the existence of any hot-spot in the inner structure, the spectral indices of the features which have been suggested to be the inner double are steep. Convolving the GMRT 1265-MHz image to the same resolution as that of the VLA 4860-MHz one, the spectral indices of the western component of the inner structure is $\sim$1.0 while for the eastern one $\alpha\sim$1.8. The core spectral index from these images is $\sim$0.3. The steep spectral indices could be affected by contamination with emission from the backflow. Higher resolution images to determine the structure and spectral indices are required to confirm the DDRG nature of the source.

J1604+3731, 7C: The GMRT 610-MHz image suggests a curved twin-jet structure on opposite sides of the core (Konar et al. 2004). The core is visible in all the GMRT images and in the VLA 4860-MHz and 9040 MHz images made from the archival data (see Fig. 4.9). The core has a straight steep spectrum with a spectral index of about 0.76$\pm$0.05, which may be due to either small-scale jets and/or lobes not resolved in the existing observations. This needs to be investigated.

J1702+4217, 7C: The core has a flat-spectrum with a spectral index of $\sim$0.2 between 600 and 5000 MHz, and the core flux density rising towards higher frequencies. The images of this source can be seen in Fig. 4.10.

J2312+1845, 3C457: The 334-MHz image (Fig. 4.10) of the source shows its large scale structure with a barely detected core. The core is contaminated with the diffuse emission of the northern lobe. The core spectral index is $\sim$0.1 between 1425 and 4866 MHz (see Konar et al. 2004).

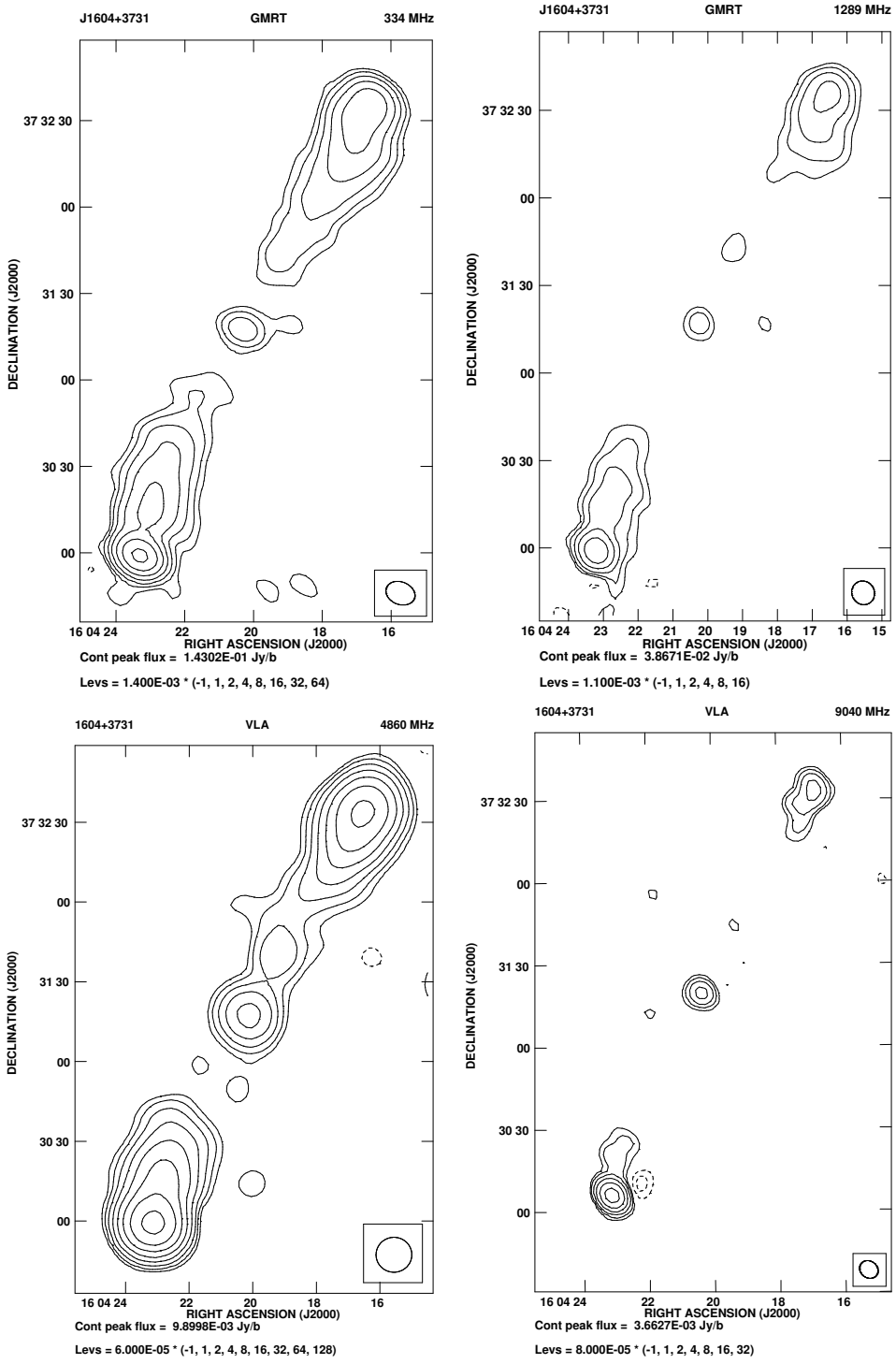

Figure 4.9: Radio images of J1604+3731

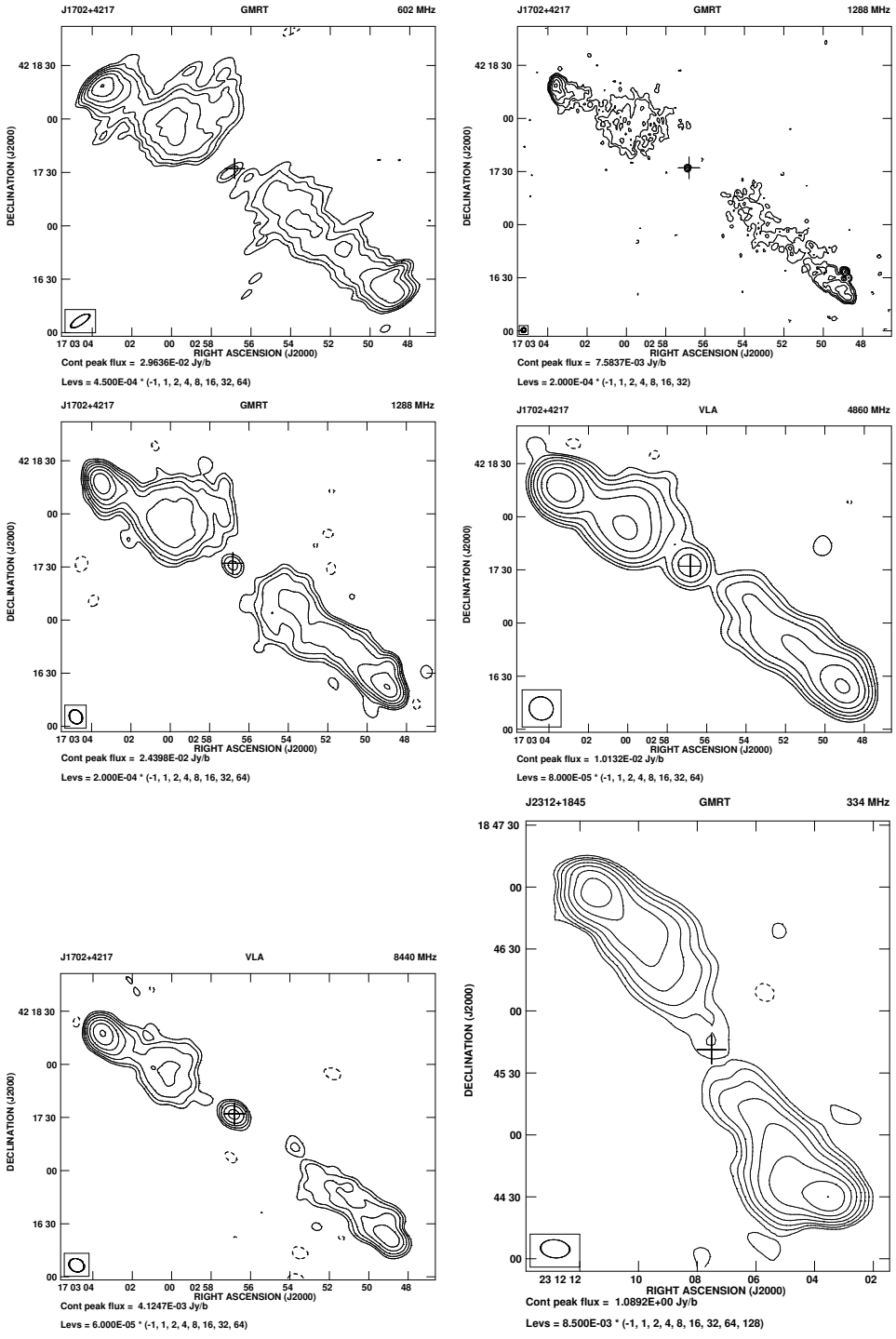

Figure 4.10: Radio images of J1702+4217 and J2312+1845

Table 4.3: Physical properties of the sources

Source	Alt. name	Opt. Id.	Redshift	LAS	l	$P_{1.4}$	f_c	R_θ	R_S	References
				$''$	kpc	W Hz^{-1}				
(1)	(2)	(3)	(4)	(5)	(6)	(7)	(8)	(9)	(10)	(11)
J0720+2837		G	0.2705	370	1520	25.02	0.06	1.37	1.06	1
J0912+3510		G	0.2489	375	1449	25.44	$\lesssim$0.009	1.66	1.82	1
J0927+2510		G	0.55*	345	2206	26.02	0.005	1.02	1.48	1
J1155+4029		G	0.53*	229	1437	26.55	0.14	2.00	0.15	1
J1313+6937	DA 340	G	0.106	388	745	25.60	0.01	1.30	0.68	2
J1343+3758		G	0.2267	684	2463	25.32	0.03	1.32	0.63	1,3
J1604+3438		G	0.2817	200	846	25.50	$\lesssim$0.009	1.09	1.20	1
J1604+3731	7C	G	0.814	178	1346	26.60	0.04	1.02	0.69	1,4
J1702+4217	7C	G	0.476	196	1160	26.19	0.04	1.33	0.69	4
J2312+1845	3C457	G	0.427	190	1056	27.11	0.006	1.05	0.75	2

1: Machalski et al. (2006); 2: Konar et al. (2004); 3: Jamrozy et al. (2005); 4: Konar et al. (2007)
An asterisk in column 4 indicates an estimated redshift.

4.5 Discussion and results

Some of the physical properties of the sources are listed in 4.3 which is arranged as follows. Columns 1 and 2: source name and an alternative name. Column 3: optical identification where G denotes a galaxy; column 4: redshift; columns 5 and 6: the largest angular size in arcsec and the corresponding projected linear size in kpc; column 7: the luminosity at 1.4 GHz in logarithmic units of W Hz^{-1}; column 8: the fraction of emission from the core, f_c, at an emitted frequency of 8 GHz. For estimating f_c, core spectral indices have been estimated wherever possible, otherwise a value of 0 has been assumed. The separation ratio R_θ, defined to be the separation of the farther hotspot or lobe from the core or optical galaxy to the nearer one, and the flux density ratio, R_S at an emitted frequency of 5 GHz in the same sense, are listed in columns 9 and 10 respectively. References for the radio structure which contains a 5-GHz image are listed in column 11. For monochromatic luminosity at 1400 MHz emitted frequency, we have used NVSS images for the total flux density and spectral indices between ∼600 and 5000 MHz for all sources except J1604+3438 and J2312+1845 for which we used the spectral indices between ∼600 and 1400 MHz and between ∼1400 and 5000 MHz respectively.

(a) Radiative losses

For all the lobes listed in Table 4.2 we first determine the minimum energy magnetic field strength using the formalism of Miley (1980) by integrating the spectrum between 10 MHz and 100 GHz. We have repeated the calculations by integrating the spectrum from a frequency corresponding to a minimum Lorentz factor, $\gamma_{\rm min}$∼10 for the relativistic electrons to an upper limit of 100

GHz, which corresponds to a Lorentz factor ranging from a few times 10^4 to 10^5 depending on the estimated magnetic field strength (see Hardcastle et al. 2004; Croston et al. 2005 and Appendix A). These estimates are referred to as classical-1 and classical-2 respectively in this chapter. The expressions we use for the more general case of a curved radio spectrum in the classical formalisms are described in Appendix A. We also estimate the magnetic field strength, $B_{\rm eq}$(rev), using the formalism of Beck & Krause (2005) which is an equipartition magnetic field. Their formula (equation (A18)) has the parameter $\mathbf{K}_0$ which is the ratio of the number density of protons to that of electrons in the energy range where losses are small. It is relevant to note that in this formalism particle energy is dominated by the protons. Estimating $\mathbf{K}_0=(\frac{m_p}{m_e})^{\alpha}$ as given by their equation (7) for $\alpha \approx \alpha_{\rm inj}$ which depends on the low-frequency spectral index in the observed synchrotron spectrum, we can constrain the proton spectrum and hence estimate the revised magnetic field strength, $B_{\rm eq}$(rev).

We have estimated the magnetic field strengths for the extended lobes of all the sources in our sample using the different approaches, except for J0720+2837 where the spectral coverage is comparatively poor. We have assumed either a cylindrical or spheroidal geometry and a filling factor of unity, and have estimated the sizes of the lobes from the lowest contours in the available low-frequency images at either 330 or 605 MHz. In some sources such as the the eastern lobe of J1343+3758 the emission appears quite compact while in others such as in J1702+4217 there are prominent bridges of emission. The magnetic field in nT (1T = 10^4 G) estimated from the different approaches as well as the equivalent magnetic field of the CMB at the redshift of the source, $B_{\rm iC}=0.32(1+z)^2$ nT, are listed in Table 4.4, which is self explanatory. A comparison of the magnetic field estimates from

Table 4.4: Magnetic field estimates of the lobes

Source	Comp.	Magnetic field estimates					Equivalent
		JP: class-1	JP: class-2	KP: class-1	KP: class-2	Beck-Krause	CMB field
		nT	nT	nT	nT	nT	nT
(1)	(2)	(3)	(4)	(5)	(6)	(7)	(8)
J0912+3510	N	0.11±0.01	0.16±0.02	0.11±0.01	0.16±0.02	0.34±0.05	0.50
	S	0.13±0.01	0.21±0.02	0.13±0.01	0.21±0.02	0.39±0.05	
J0927+3510	NW	0.13±0.01	0.27±0.03	0.13±0.01	0.27±0.03	0.38±0.05	0.77
	SE	0.14±0.01	0.25±0.02	0.14±0.01	0.25±0.02	0.35±0.04	
J1155+4029	NE	0.50±0.05	1.15±0.11	0.50±0.05	1.13±0.11	1.52±0.18	0.75
	SW	0.32±0.03	0.70±0.07	0.31±0.03	0.68±0.07	0.99±0.12	
J1313+6937	NW	0.19±0.02	0.29±0.03	0.19±0.02	0.29±0.03	0.60±0.08	0.39
	SE	0.15±0.01	0.23±0.02	0.15±0.01	0.23±0.02	0.48±0.06	
J1343+3758	SW	0.13±0.01	0.23±0.02	0.13±0.01	0.23±0.02	0.40±0.05	0.48
	NE	0.20±0.02	0.33±0.03	0.20±0.02	0.32±0.03	0.60±0.08	
J1604+3438	W	0.17±0.02	0.24±0.02	0.17±0.02	0.24±0.02	0.52±0.07	0.53
	E	0.20±0.02	0.28±0.03	0.20±0.02	0.28±0.03	0.60±0.08	
J1604+3731	N	0.26±0.03	0.52±0.05	0.26±0.03	0.51±0.05	0.58±0.07	1.05
	S	0.37±0.04	0.73±0.07	0.37±0.04	0.72±0.07	0.83±0.10	
J1702+4217	NE	0.20±0.02	0.30±0.03	0.20±0.02	0.30±0.03	0.48±0.06	0.70
	SW	0.20±0.02	0.30±0.03	0.20±0.02	0.30±0.03	0.47±0.06	
J2312+1845	NE	0.40±0.04	0.86±0.08	0.40±0.04	0.85±0.08	1.23±0.15	0.65
	SW	0.43±0.04	0.91±0.09	0.43±0.04	0.90±0.09	1.32±0.16	

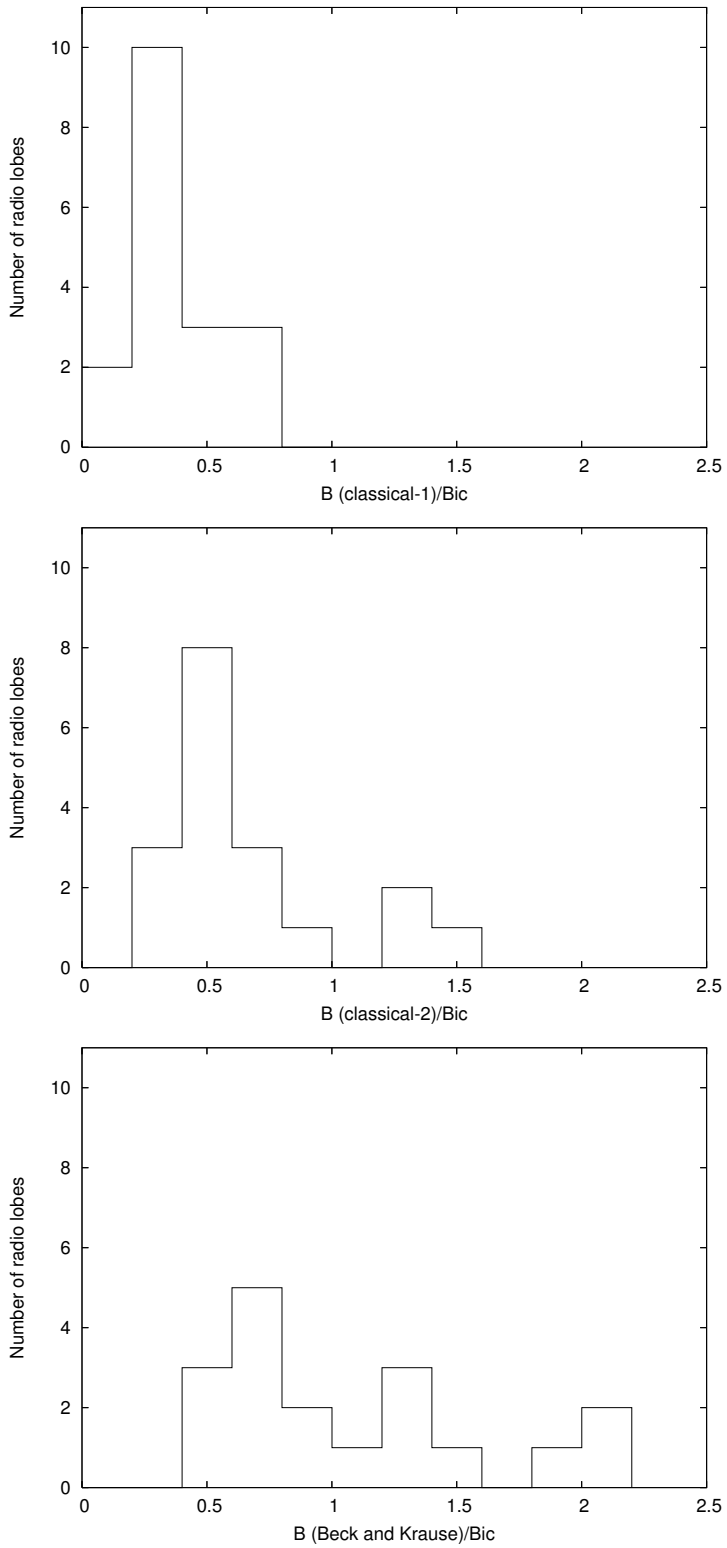

Figure 4.11: The distributions of the ratios of the magnetic field strength estimated using the classical-1, classical-2 and Beck & Krause (2005) formalisms and the equivalent magnetic field, B_{iC}, of the CMB, shown in the upper, middle and lower panels respectively.

the different approaches (Fig. 4.12) shows that the field strengths estimated using the Beck & Krause and classical-2 formalisms are larger than those of classical-1 by factors of $\sim$3 and $\sim$2 respectively. An independent check of our classical-2 estimates was done by Martin Hardcastle using the formalism of Hardcastle et al. (2004) and the values were found to be consistent.

We examine the relative importance of synchrotron and inverse-Compton losses in the lobes of these radio sources. The ratio of the magnetic field strength estimated from the different approaches to that of the equivalent magnetic field of the CMB for the different lobes are shown in Fig. 4.11. It is seen clearly that the magnetic field estimated from the classical-1 approach is always less than B_{iC}, suggesting that inverse-Compton losses are usually larger than the synchrotron radiative losses for giant radio sources as suggested earlier (e.g. Gopal-Krishna, Wiita & Saripalli 1989; Ishwara-Chandra & Saikia 1999; Konar et al. 2004). The median value of the ratio, r_B, of the magnetic field estimate to B_{iC} is $\sim$0.34. However, for the field estimates using the classical-2 and Beck & Krause formalisms the corresponding values of the ratio r_B are $\sim$0.51 and 0.91 respectively. In the latter case, synchrotron losses are more important in approximately half the cases. This could have a significant effect on the identification of GRSs. For example, a combination of increased synchrotron losses combined with the inverse-Compton losses could make it more difficult to detect the bridges of emission in high-redshift GRSs, thereby leading to the possible classification of the hotspots and the core as unrelated radio sources.

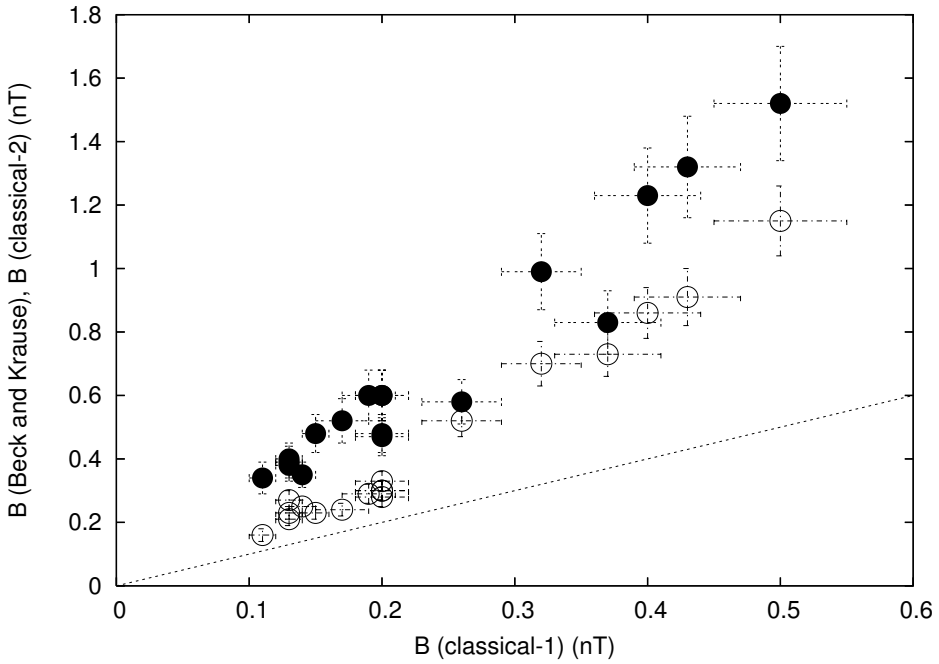

Figure 4.12: The magnetic field strength estimated using the formalisms of Beck & Krause (2005) shown by filled circles and classical-2 (see text and Croston et al. 2005) shown by open circles are plotted against the classical-1 estimates (see text and Miley 1980). The dashed line represents field strengths estimated using the Beck & Krause and classical-2 formalisms being equal to the classical-1 estimates.

Table 4.5: Core flux densities of J1155+4029

Teles-cope	resn. $''$	Date	Freq. MHz	S mJy	Ref.
(1)	(2)	(3)	(4)	(5)	(6)
GMRT	9.9	2005 Mar 16	241	14	1
GMRT	9.3	2005 Dec 25	334	15	1
GMRT	6.1	2005 Mar 16	605	21	1
GMRT	9.9	2005 Nov 30	1258	22	1
VLA-B	5.4	FIRST	1400	22	2
VLA-D	14.7	2004 Jul 31	4860	13	1

1: Konar et al. (2007); 2: FIRST

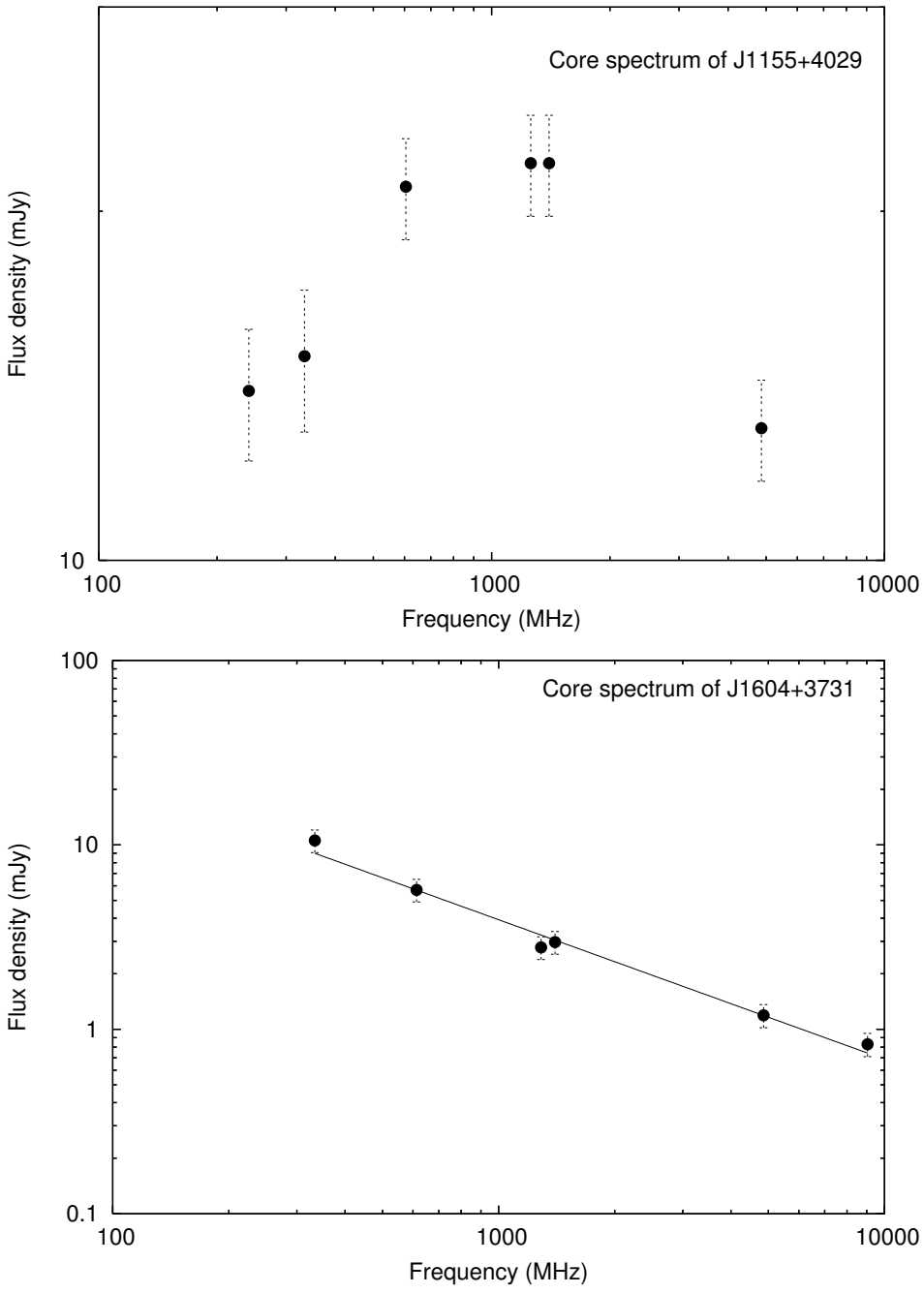

Figure 4.13: Upper panel: core spectrum of J1155+4029; lower panel: a least-square fit of a power-law to the core spectrum of J1604+3731.

Table 4.6: Core flux densities of J1604+3731

Teles-cope	resn. $''$	Date	Freq. MHz	S mJy	Ref.
(1)	(2)	(3)	(4)	(5)	(6)
GMRT	7.2	2006 Mar 09	334	10.56	1
GMRT	5.1	2004 Jan 01	613	5.70	1
GMRT	3.5	2006 Jan 01	1289	2.78	1
VLA-BnD	5.4	FIRST	1400	2.97	2
VLA-D	10.6	1993 Dec 23	4860	1.19	1
VLA-D	6.6	1993 Dec 23	9040	0.82	1

1: Konar et al. (2007); 2: FIRST

(b) Core properties

The fraction of emission from the core at an emitted frequency of 8 GHz, f_c, ranges from $\lesssim$0.005 to $\sim$0.14, with a median value of $\sim$0.04. The values of f_c are usually comparable to the other sources of similar radio luminosity. The three sources with prominent cores ($f_c \gtrsim 0.04$) are J0720+2837, J1155+4029 and J1604+3731. Out of these three sources J0720+2837 and J1604+3731 have a steep spectrum core. The flux densities of the core of J1155+4029 and J1604+3731 where multiple measurements are available are listed in Tables 4.5 and 4.6 respectively along with the approximate resolution and the epoch of observations. For these sources when contamination of core emission by diffuse extended emission at the lower frequencies seem significant, the source has been remapped with a lower uv-cutoff of 5 kλ to minimise contamination by the extended emission. The GRS J0720+2837 has core spectral index of 0.57 between 604 and 4860 MHz, while J1604+3731 has a core spectral index of 0.76 determined from a power law fit (Fig. 4.13) with the observations covering a range of frequencies between 334 and 9040 MHz. The core spectrum of J1155+4029 (Fig. 4.13) is reminiscent of a giga-Hertz peaked spectrum (GPS) source. It would be interesting to determine from mas-scale

resolution observations whether the core is resolved into a pc-scale double. It is worth mentioning that the GPS core of the GRS J1247+6723 is resolved into a small-scale double with a size of ∼14 pc, suggesting recurrent activity (Marecki et al. 2003; Saikia, Konar & Kulkarni 2006). It is also relevant to note that the core does not exhibit any evidence of significant variability as in the case of other GPS sources (e.g. O'Dea 1998 for a review). For example the core flux densities from the FIRST (Faint Images of the Radio Sky at Twenty-centimeters) survey at 1400 MHz and our GMRT 1258-MHz image are similar even though they are temporally far apart.

(c) Environment and morphology of GRSs

The lobes of the GRSs lie well beyond the extent of the parent host galaxies and can be used to probe the environment on these scales which could affect the structure and symmetry parameters of these objects (e.g Subrahmanyan et al. 1996). Although GRSs often occur in regions of low galaxy density, Subrahmanyan et al. noted that two of the sources in their sample, namely B1545−321 and B2356−611, which have continuous bridges from the hotspots to the core show a significant excesses in galaxy counts. Ishwara-Chandra & Saikia (1999) and Schoenmakers et al. (2000) noted that the GRSs tended to be marginally more asymmetric than smaller sources of similar luminosity, excluding the compact steep spectrum sources. For example, considering the higher luminosity objects in a restricted range Ishwara-Chandra & Saikia noted that the median value of the separation ratio is ∼1.39 compared with ∼1.19 for 3CR galaxies of similar luminosity but smaller sizes. The median value for these 9 sources in our sample is again ∼1.33 (see Fig.

4.14), consistent with the earlier estimate although the statistical uncertainties are now larger because of the small sample size. The distribution does not show a significant peak towards smaller values. For a source inclined at $\gtrsim$45° to the line of sight, the expected separation ratio is only ∼1.15 for a hotspot advance speed of ∼0.1c (see Scheuer 1995). A plot of the separation ratio against the fraction of emission from the core (Fig. 4.14), which is often used as a statistical indicator of orientation of the source axis to the line of sight, shows no significant correlation suggesting that large-scale environmental asymmetries play a significant role. It is worth noting that although J1155+4029, which has the most prominent core (f_c=0.14), and has the highest value of the separation ratio, the nearer component is brighter by a factor of ∼6 (Fig. 4.14), demonstrating that density asymmetries are likely to again play a significant role in the observed asymmetries. It is also relevant to note that J1155+4029 has a GPS core; it is important to determine its structure with mas resolution and investigate whether it might be a compact double with a rather weak core.

Although flux density ratios would be affected by relative contributions of the hotspot and backflow emission which have different velocities, in addition to effects of evolution of individual components with age, it can be seen in Fig. 4.14 that in 6 of the 10 sources the nearer component is brighter, as is expected for jets going through a denser medium (Jeyakumar et al. 2005). In spite of the difficulties noted above, weak trends for the components on the jet side in quasars to be stronger have been reported (e.g., Garrington, Conway & Leahy 1991), illustrating that relativistic effects also play a role. However, in these giant radio sources, environmental effects seem to dominate. It would be interesting to explore the fields of these sources both via optical galaxy counts and deep x-ray observations.

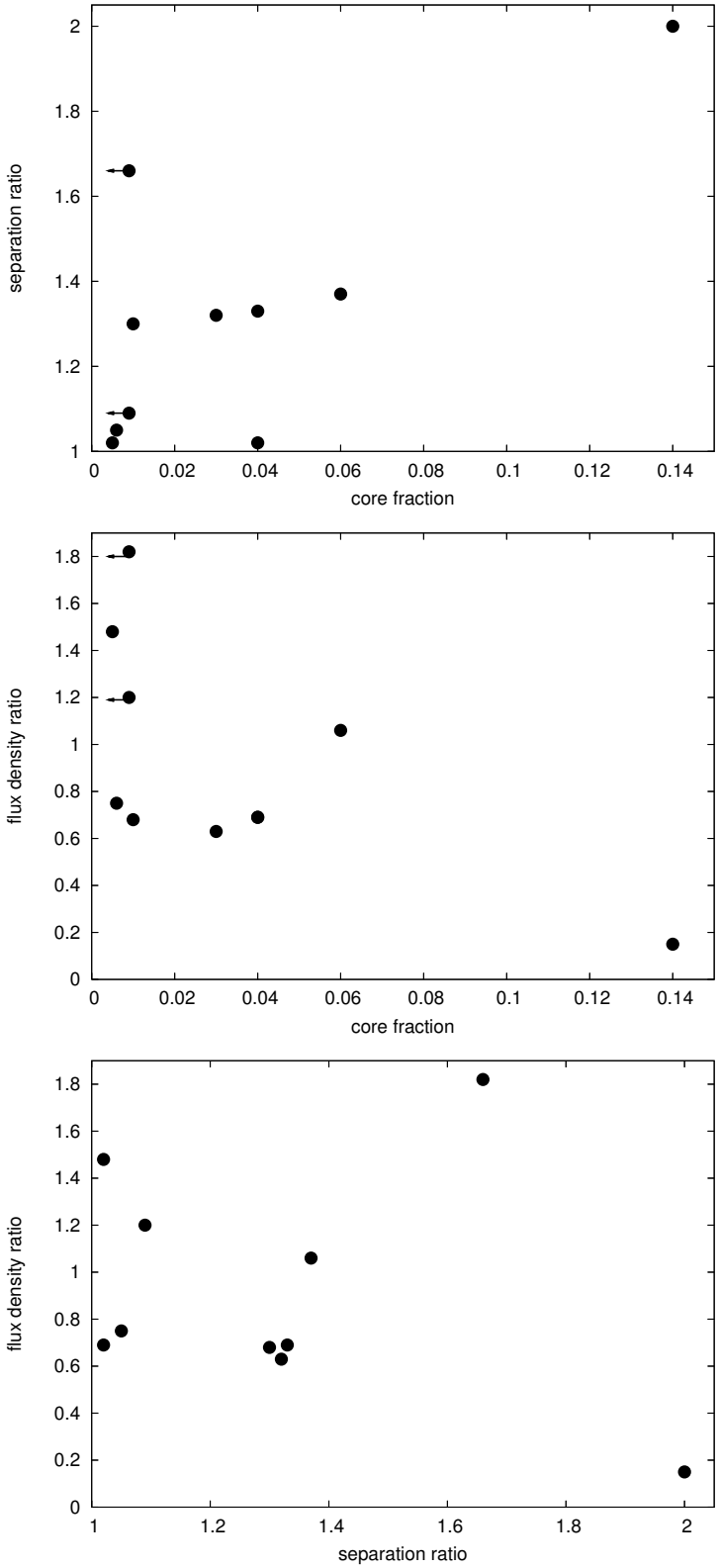

Figure 4.14: The separation ratios and flux density ratios are plotted against the fraction of emission from the core at an emitted frequency of 8 GHz in the upper and middle panels respectively. In the lower panel the flux density ratio is plotted against the separation ratio.

4.6 Concluding remarks

We have presented multifrequency radio images of a selected sample of ten giant radio galaxies, largely at low radio frequencies with the GMRT. We have also presented a few high-frequency images made from VLA data. We have listed the flux densities of components for the images presented here as well as for high-frequency images of these sources which have been published earlier by us (MJZK; Konar et al. 2004).

From these multifrequency observations of the lobes we estimate the magnetic field strengths using three different approaches, namely estimating the minimum energy field by integrating from 10 MHz to 100 GHz which has been refereed to here as classical-1 (Miley 1980), integrating from a minimum frequency corresponding to $\gamma_{\rm min}$=10 at the estimated magnetic field to a maximum frequency of 100 GHz, called classical-2 (see Hardcastle et al. 2004; Croston et al. 2005), and lastly using the formalism of Beck & Krause (2005). We show that on the average the magnetic field strengths estimated using the Beck & Krause and classical-2 formalisms are larger than the classical-1 values by factors of $\sim$3 and $\sim$2 respectively.

The inverse-Compton losses dominate over synchrotron losses when estimates of the classical minimum energy magnetic field are used, consistent with earlier studies. However, this is often not true if the magnetic fields are close to the values estimated using the formalism of Beck & Krause (2005). In the latter case, synchrotron losses are more important in nearly half the cases. The increased synchrotron losses combined with the inverse-Compton losses would make it more difficult to detect the bridges of emission in high-redshift GRSs, thereby leading to the possible classification of the hotspots and the core as unrelated radio sources. Although for a sample of radio

galaxies with x-ray emission from at least one of the lobes which can be attributed to inverse-Compton scattering with the CMB photons, the estimated magnetic field ranges from $\sim$0.3 to 1.3 times the minimum energy field with a peak around 0.7 times this field (Croston et al. 2005), none of the radio lobes in clusters of galaxies studied by Dunn, Fabian & Taylor (2005) has equipartition between the relativistic particles and the magnetic field. Clearly more work is required in this area.

We also examine the spectral indices of the cores and any evidence of recurrent activity in these sources. In one of the sources, J1155+4029, the core has a GPS spectrum, while in two others, J0720+2837 and J1604+3731, the cores appear to have a steep spectrum. It would be interesting to determine the milliarcsec-scale structure of the core in J1155+4029 as well as J0720+2837 and J1604+3731 and thereby examine whether these show evidence of being a double double radio galaxy.

We probe the environment using the symmetry parameters of these sources. Approximately half the sources are more asymmetric in their separation ratio than would be expected for a galaxy inclined at $\gtrsim$45° to the line of sight with the hotspots moving outwards with a velocity of $\sim$0.1c. Also the nearer lobe is brighter in six of the sources, the asymmetry being most pronounced in the case of J1155+4029 which has the largest value of separation ratio and a GPS core. These trends suggest that the environments of these sources are often asymmetric on scales of $\sim$1 Mpc.

References

Baars J.W.M., Genzel R., Pauliny-Toth I.I.K., Witzel A. 1977, A&A, 61, 99

Beck R., Krause M., 2005, AN, 326, 414

Croston J.H., Hardcastle M.J., Harris D.E., Belsole E., Birkinshaw M., Worrall D.M., 2005, ApJ, 626, 733

Dunn R.J.H., Fabian A.C., Taylor G.B., 2005, MNRAS, 364, 1343

Garrington S.T., Conway R.G., Leahy J.P., 1991, MNRAS, 250, 171

Gopal-Krishna, Wiita P.J., Saripalli L., 1989, MNRAS, 239, 173

Hardcastle M.J., Harris D.E., Worrall D.M., Birkinshaw M., 2004, ApJ, 612, 729

Ishwara-Chandra C.H., Saikia D.J., 1999, MNRAS, 309, 100

Jamrozy M., Machalski J., Mack K.-H., Klein U., 2005, A&A, 433, 467

Jeyakumar S., Wiita P.J., Saikia D.J., Hooda J.S., 2005, A&A, 432, 823

Konar C., Saikia D.J., Ishwara-Chandra C.H., Kulkarni V.K., 2004, MNRAS, 355, 845

Konar C., Jamrozy M., Saikia D.J., Machalski J., 2007, MNRAS, submitted

Machalski J., Jamrozy M., Zola S., Koziel D., 2006, A&A, 454, 85 (MJZK)

Machalski J., Jamrozy M., Zola S., 2001, A&A, 371, 445

Marecki A., Barthel P.D., Polatidis A., Owsianik I., 2003, PASA, 20, 16

Miley G. K., 1980, ARA&A, 18, 165

O'Dea C.P., 1998, PASP, 110, 493

Saikia D.J., Konar C., Kulkarni V.K., 2006, MNRAS, 366, 1391

Scheuer P.A.G., 1995, MNRAS, 277, 331

Schoenmakers A.P., Mack K.-H., de Bruyn A.G., Röttgering H.J.A., Klein U., van der Laan H., 2000, A&AS, 146, 293

Subrahmanyan R., Saripalli L., Hunstead R.W., 1996, MNRAS, 279, 257

CHAPTER 5

A multifrequency study of giant radio sources II. Spectral ageing analysis of the lobes of selected sources

5.1 Abstract

Multifrequency observations with the GMRT and the VLA are used to determine the spectral breaks in consecutive strips along the lobes of a sample of selected GRSs in order to estimate their spectral ages. The maximum spectral ages estimated for the detected radio emission in the lobes of our sources range from ∼6 to 48 Myr with a median value of ∼23 Myr using the classical equipartition fields. Using the magnetic field estimates from the Beck & Krause formalism, the spectral ages range from ∼5 to 58 Myr with a median value of ∼24 Myr. These ages are significantly older than those of smaller sources. In all but one source (J1313+6937) the spectral age gradually increases with distance from the hotspot regions, confirming that acceleration of the particles mainly occurs in the hotspots. Most of the GRSs do not exhibit zero spectral ages in the hotspots, as is the case in earlier studies of smaller sources. This is likely to be largely due to contamination by more extended emission due to relatively modest resolutions. The injection

spectral indices range from ∼0.55 to 0.88 with a median value of ∼0.6. We discuss these values in the light of theoretical expectations, and show that the injection spectral index seems to be correlated with luminosity and/or redshift as well as with linear size.

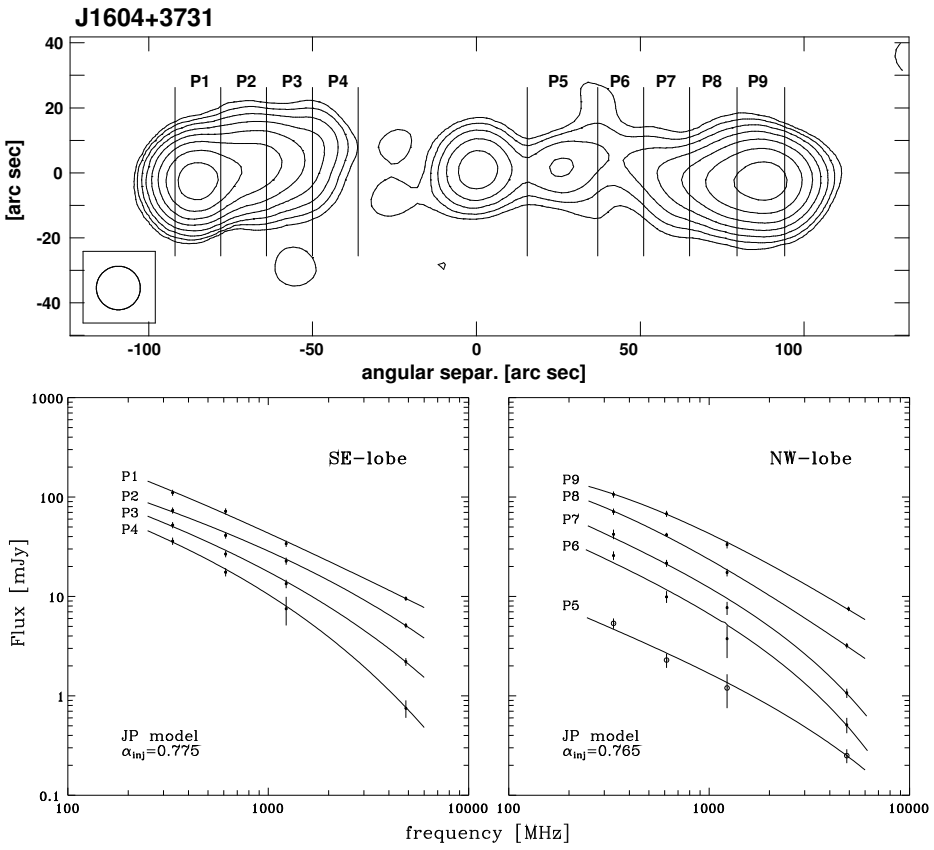

Figure 5.1: Upper panel: an example of how the lobes of analysed sources are cut into strips within which the spectral age of radiating particles is determined. Lower panels: the spectra fitted to the flux-density data in each of the strips.

5.2 Introduction

The radio continuum spectra in different parts of an extended radio source contain important information about the various energy losses and gains of

the radiating particles during the lifetime of the source. According to dynamical models for FRII-type (Fanaroff & Riley 1974) radio sources, the energy emitted by the nucleus squirts out in the form of narrow, collimated jets channeling their way through the external environment. These jets dissipate their energy at their leading edges giving rise to intense regions of emission called 'hotspots'. As the jets advance outwards, the relativistic particles flow out from the hotspots to form the extended lobes of radio emission. Assuming that there is no significant reacceleration within these lobes and no significant mixing of particles, there should be a spectral gradient across the radio source, in the sense that the spectrum should steepen with increasing distance from the hotspot. This prediction has been seen in many sources and used to estimate the radiative ages and expansion velocities in several samples of powerful 3CR sources (e.g. Myers & Spangler 1985; Alexander & Leahy 1987; Leahy, Muxlow & Stephens 1989; Carilli et al. 1991; Liu, Pooley & Riley 1992), in samples of low-luminosity and medium-luminosity radio galaxies (e.g. Klein et al. 1995; Parma et al. 1999), as well as a sample of compact steep-spectrum sources (Murgia et al. 1999). However, the observed spectral break and steepening of the spectrum beyond this break need not be entirely due to radiative energy losses. A possible role of the local magnetic fields, details of the backflow of the lobe material, or the difficulties in disentangling various energy losses of the radiating particles have been pointed out in a number of papers (e.g. Wiita & Gopal-Krishna 1990; Rudnick, Katz-Stone & Anderson 1994; Eilek & Arendt 1996; Jones, Ryu & Engel 1999; Blundell & Rawlings 2000).

Nevertheless, GRSs are suitable for the classical spectral-ageing analysis due to their large angular extent which can be covered by a significant number of resolution elements. In previous chapter (Chapter 4) extensive

Table 5.1: Break frequency, magnetic field strength, and spectral age of particles in consecutive strips through the lobes for J0912+3510

Strip	Dist. (kpc)	$\nu_{\rm br}$ (GHz)	$\chi^2_{\rm red}$	$B_{\rm eq}$(rev) (nT)	$\tau_{\rm spec}$ (Myr)
		N-lobe		$\alpha_{\rm inj} = 0.560$	
P1	543	$12.6^{+32.9}_{-7.7}$	0.07	0.39±.032	$20.1^{+9.8}_{-12.1}$
P2	466	$17.2^{>+85}_{-11.8}$	0.02	0.31±.028	$17.9^{+14.0}_{-17.0}$
P3	389	$18.6^{>+90}_{-12.5}$	0.35	0.31±.027	$17.2^{+12.9}_{-16.3}$
P4	313	$8.8^{+48.0}_{-4.9}$	0.08	0.29±.027	$25.1^{+12.5}_{-15.3}$
P5	236	$8.6^{>+70}_{-3.5}$	0.07	0.26±.025	$25.2^{+7.8}_{-23.8}$
P6	161	$4.9^{>+80}_{-2.5}$	0.38	0.22±.022	$32.6^{+14.5}_{-32.0}$
		S-lobe		$\alpha_{\rm inj} = 0.628$	
P7	498	$6.7^{>+90}_{-1.9}$	9.93	0.28±.031	$28.7^{+5.3}_{-28.6}$
P8	575	$8.1^{+38.6}_{-4.3}$	0.00	0.31±.034	$26.1^{+12.1}_{-15.3}$
P9	652	$14.9^{+13.2}_{-10.7}$	2.05	0.34±.037	$19.0^{+5.4}_{-16.9}$
P10	729	$21.6^{+35.2}_{-15.9}$	1.06	0.40±.042	$15.3^{+6.2}_{-14.4}$
P11	806	$39.6^{+96.7}_{-31.3}$	2.52	0.41±.042	$11.2^{+5.3}_{-10.3}$
P12	883	$22.6^{+23.0}_{-16.7}$	6.92	0.45±.046	$14.3^{+4.6}_{-13.8}$

low-frequency observations made with the GMRT of a sample of selected GRSs have been described and some of their properties analysed and discussed. In this chapter we analyse the spectral ages of these radio galaxies except for J0720+2837 for which we have data at only two frequencies and J1343+3758 whose spectral ageing analysis has been presented by Jamrozy et al. (2005). Our analysis is similar to the spectral ageing analysis for the GRS J1343+3758 (Jamrozy et al. 2005) and the double-double radio galaxy J1453+3308 (Konar et al. 2006). In Section 5.3 we discuss briefly the method of analysis, while in Section 5.4 we present our results. Discussion of the results and an examination of the correlations of the injection spectral index, $\alpha_{\rm inj}$, with luminosity, redshift and linear size are presented in Section 5.5. The conclusions are summarized in Section 5.6.

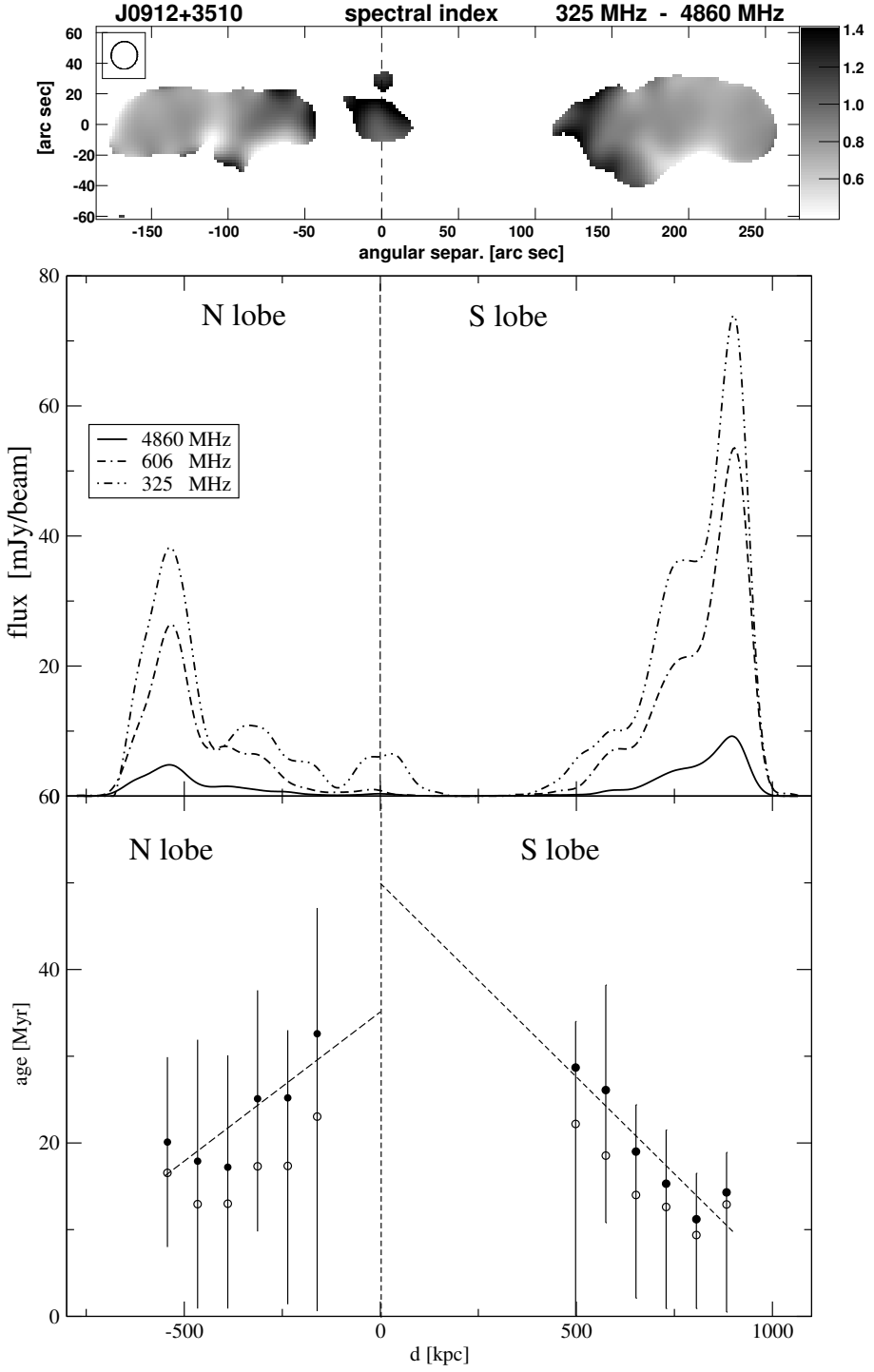

Figure 5.2: Spectral-index map, flux-density profiles, and the spectral age distribution for J0912+3510. The spectral ages have been estimated using magnetic field values determined using the Beck & Krause (2005) formalism (filled circles and with error bars) and the classical (e.g. Miley 1980; referred to as classical-1 in Chapter 4) formalism (open circles without error bars).

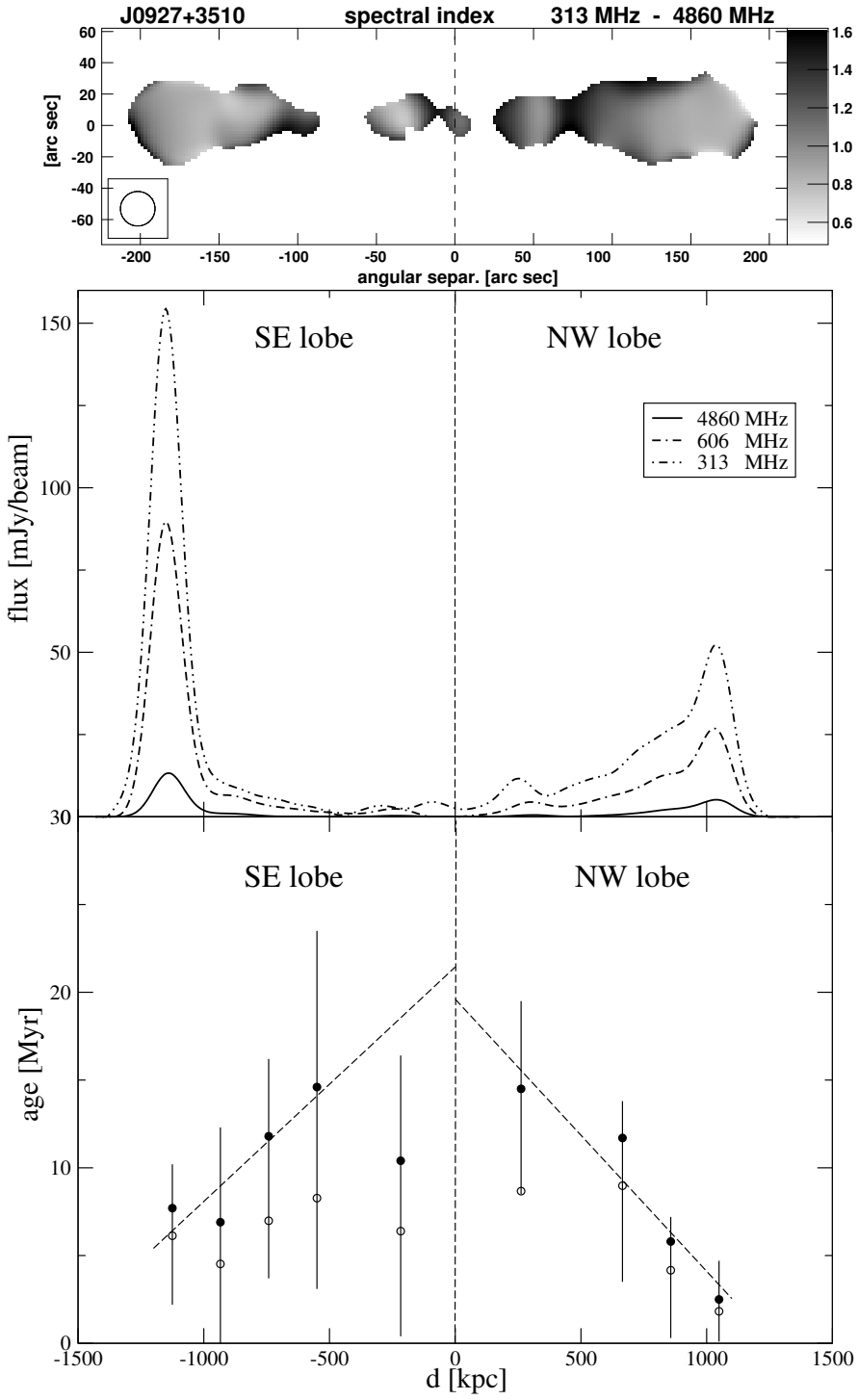

Figure 5.3: As in Fig. 5.2, but for J0927+3510

Table 5.2: As in Table 5.1 but for J0927+3510

Strip	Dist. (kpc)	$\nu_{\rm br}$ (GHz)	$\chi^2_{\rm red}$	Beq(rev) (nT)	$\tau_{\rm spec}$ (Myr)
		SE-lobe		$\alpha_{\rm inj} = 0.700$	
P1	1125	$20.6^{>+80}_{-9.4}$	0.36	0.47±.140	$7.7^{+2.5}_{-5.5}$
P2	934	$22.2^{+85.0}_{-15.9}$	0.02	0.28±.099	$6.9^{+5.4}_{-6.5}$
P3	742	$10.0^{+61.6}_{-5.7}$	0.05	0.24±.077	$11.8^{+4.4}_{-8.1}$
P4	550	$4.0^{+22.2}_{-2.5}$	0.01	0.20±.066	$14.6^{+8.9}_{-11.2}$
P5	217	$8.1^{>+90}_{-4.2}$	0.96	0.21±.069	$10.4^{+6.0}_{-10.0}$
		NW-lobe		$\alpha_{\rm inj} = 0.750$	
P6	262	$4.7^{+9.1}_{-1.9}$	0.14	0.25±.116	$14.5^{+5.9}_{-6.0}$
P7	665	$8.4^{+87.4}_{-2.0}$	2.89	0.34±.151	$11.7^{+2.1}_{-8.2}$
P8	857	$35.2^{>+90}_{-11.9}$	9.73	0.37±.166	$5.8^{+1.4}_{-5.5}$
P9	1049	$188.8^{>+85}_{-134.}$	4.19	0.40±.175	$2.5^{+2.2}_{-2.4}$

Table 5.3: As in Table 5.1 but for J1155+4029

Strip	Dist. (kpc)	ν_{br} (GHz)	χ^2_{red}	$\rm B_{eq}$(rev) (nT)	$\tau_{\rm spec}$ (Myr)
		SW-lobe		$\alpha_{\rm inj} = 0.838$	
P1	925	$193.1^{+85.0}_{-80.1}$	0.17	$0.84 \pm .275$	$2.2^{+2.1}_{4.1}$
P2	812	$40.7^{>+90}_{-32.9}$	0.25	$0.68 \pm .231$	$5.2^{+4.2}_{-5.0}$
		NE-lobe		$\alpha_{\rm inj} = 0.876$	
P3	226	$6.3^{+7.6}_{-2.7}$	0.06	$0.93 \pm .115$	$11.1^{+3.6}_{-4.3}$
P4	346	$51.7^{>+90}_{-20.6}$	1.17	$1.23 \pm .145$	$3.1^{+0.9}_{-3.0}$
P5	459	$81.8^{>+90}_{-34.6}$	1.26	$1.62 \pm .184$	$1.8^{+0.6}_{-1.5}$

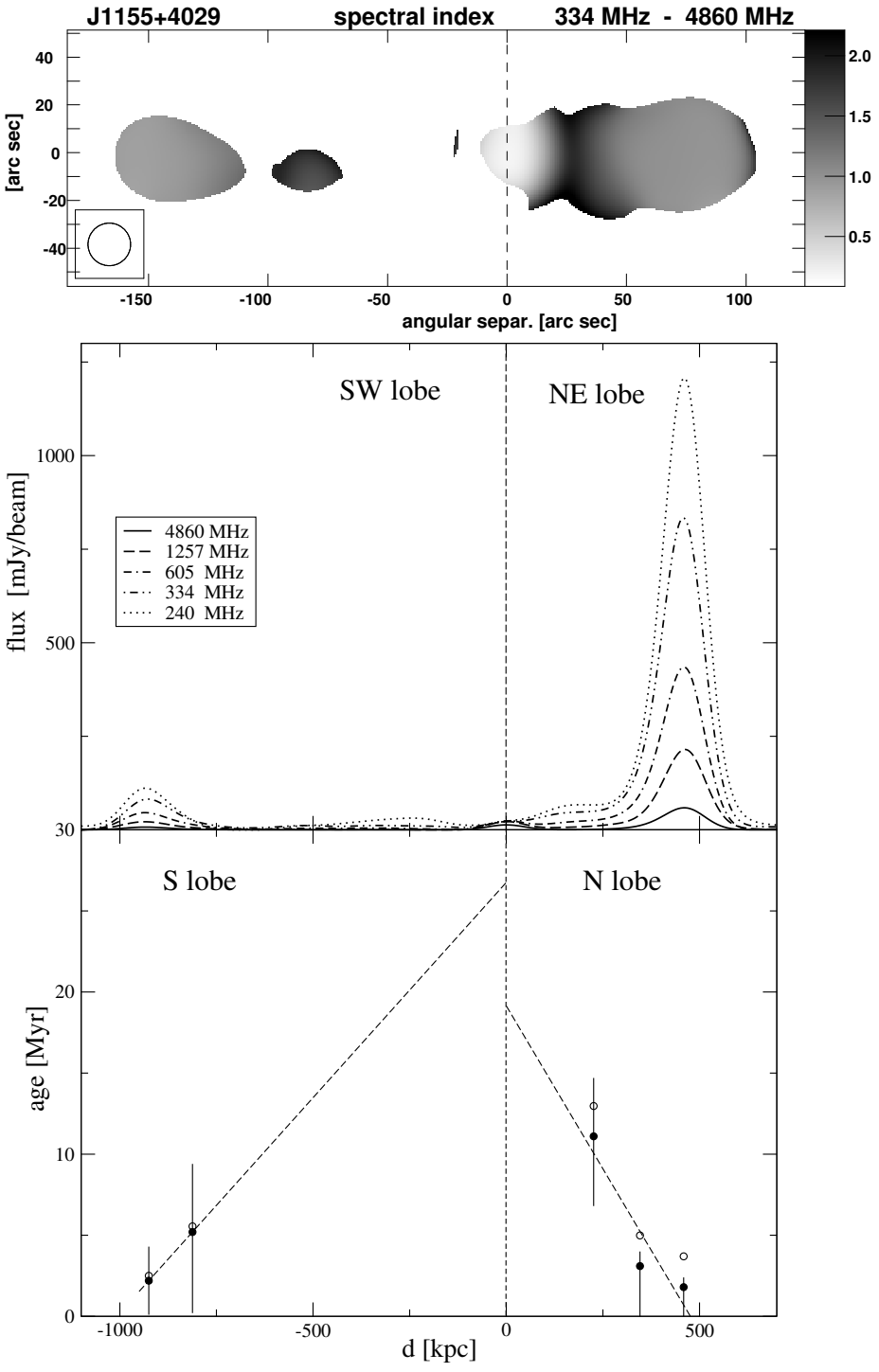

Figure 5.4: As in Fig. 5.2, but for J1155+4029

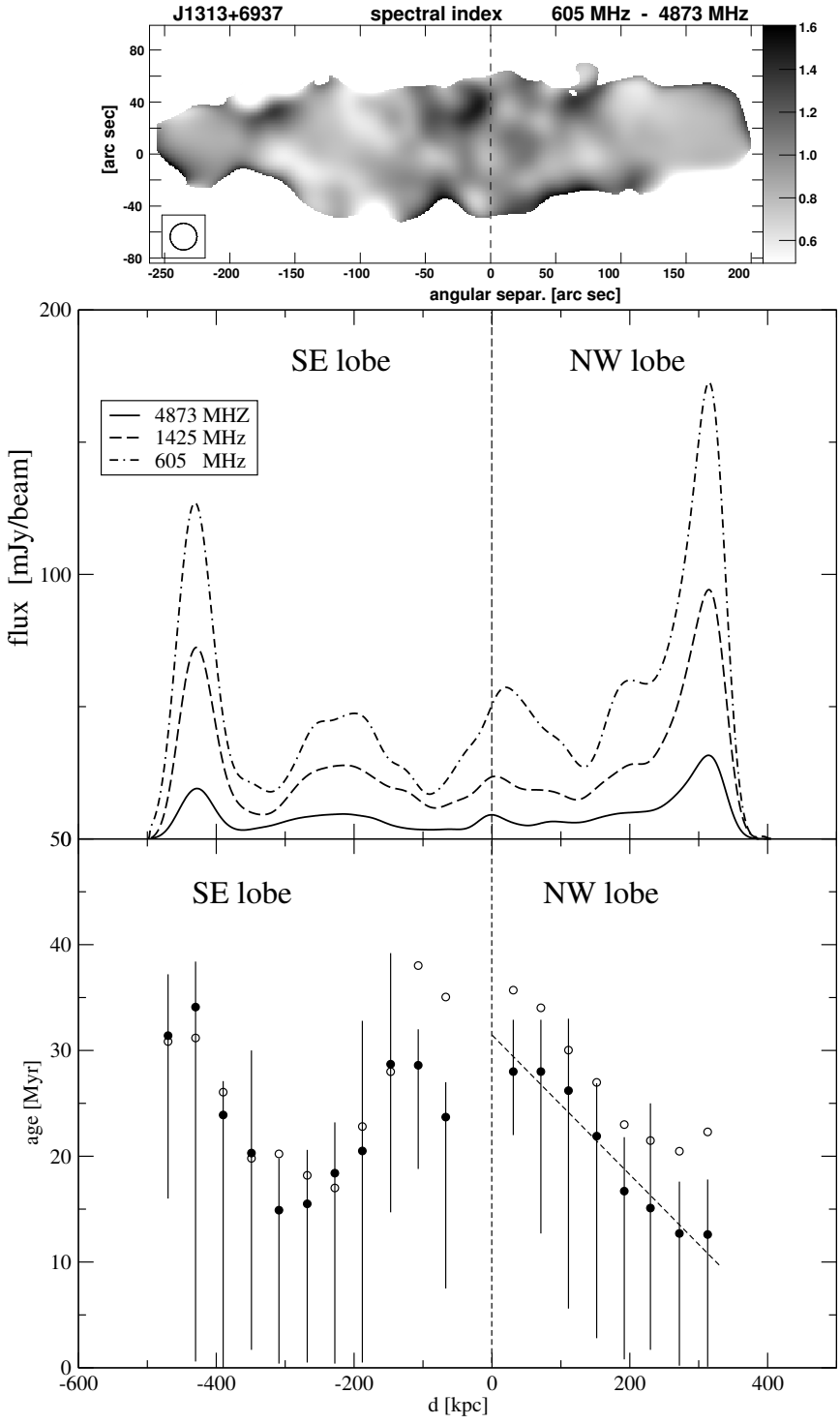

Figure 5.5: As in Fig. 5.2, but for J1313+6937

5.3 Spectral ageing analysis

(a) Spectral steepening and spectral age

The spectral age, i.e. the time which has elapsed since the particles were last accelerated in the hotspot region, can be derived from the steepening in the radio spectrum due to energy losses caused by synchrotron and inverse-Compton processes. The observed spectra have been fitted using the Jaffe & Perola (1973, JP) and the Kardashev-Pacholczyk (Kardashev 1962; Pacholczyk 1970; KP) models using the `SYNAGE` package (Murgia 1996). We found no significant difference between these two models over the frequency range of our observations and present only the results obtained from the JP model in this chapter. Also, while fitting the theoretical spectra to the observed ones, we find the spectra of the different strips in the lobes are better fitted with the JP model than with the continuous injection (Kardashev 1962; CI) model, though sometimes the CI model fits better in the area of a prominent hotspot.

Thus, under assumptions that (i) the magnetic field strength in a given lobe is constant throughout the energy-loss process, (ii) the particles injected into the lobe have a constant power-law energy spectrum with injection index γ ($N(E) \propto E^{-\gamma}$), and (iii) the time-scale of isotropization of the pitch angles of the particles is short compared with their radiative lifetime, the spectral age is given by

$$\tau_{\rm spec} = 50.3 \frac{B^{1/2}}{B^2 + B_{\rm iC}^2} \left\{\nu_{\rm br}(1+z)\right\}^{-1/2} [\rm Myr], \qquad (5.1)$$

where $B_{\rm iC}$=$0.318(1+z)^2$ is the magnetic field strength equivalent to the cosmic microwave background radiation. Here B and $B_{\rm iC}$ are expressed in units

of nT, $\nu_{\rm br}$ is the spectral break frequency in GHz above which the radio spectrum steepens from the initial power-law spectrum characterised by spectral index $\alpha_{\rm inj}$=$(\gamma - 1)/2$.

(b) Determination of $\alpha_{\rm inj}$ and $\nu_{\rm br}$ values

In order to determine a value of $\alpha_{\rm inj}$, we fit the JP model to the flux densities of the entire lobes (given in Chapter 4) treating $\alpha_{\rm inj}$ as a free parameter. We find that the uncertainties of the $\alpha_{\rm inj}$ values are sometimes large due to the low flux densities of the lobes. We have used the values of $\alpha_{\rm inj}$ which give the best fits to the spectra of the lobes, and note that there is usually no evidence for significantly different values of this parameter for the oppositely directed lobes. For sources with reliable flux densities at lower frequencies than our observations but with no information on the flux densities of the individual lobes at these frequencies, we have determined $\alpha_{\rm inj}$ from the integrated spectra of the sources. For these cases we have used the same value of $\alpha_{\rm inj}$ for both the lobes. Having estimated the $\alpha_{\rm inj}$ values, the total-intensity maps of the GRSs presented in Chapter 4 are convolved to a common angular resolution, which corresponds to the lowest resolution of our images. Each lobe is then split into a number of strips, separated approximately by the resolution element along the axis of the source in such a way that the extreme strips are centred at the peaks of brightness on the convolved maps. In each source a region around the radio core is excluded. As an example, the division of the source J1604+3731 into different strips is shown in Fig. 5.1. Using the `SYNAGE` software we determine the best fit to the spectrum in each strip over the entire observed frequency range using the JP model, and derive the relevant value of $\nu_{\rm br}$. The fitted spectra in the strips covering the

SE-lobe and the NW-lobe of J1604+3731 are plotted in the lower panels of Fig. 5.1.

(c) Magnetic-field strength determination

In order to estimate the spectral ages in different parts of the lobes, we have to estimate the magnetic-field strength in the consecutive strips. Following Konar et al. (2006, 2007), the values of the equipartition energy density and the corresponding magnetic field, $B_{\rm eq}$, are calculated using the revised formalism proposed by Beck & Krause (2005). This has been described in some detail in Chapter 4. The revised field strength within each of the consecutive strips is calculated assuming a filling factor of unity. Since the Beck & Krause formalism yields magnetic field strengths which are larger by a factor of $\sim$3 compared with the classical formalism (e.g. Miley 1980; hereinafter refererred to as classical-1, as in Chapter 4), we also estimate the spectral ages using the classical-1 magnetic field strengths. This shows the range of ages possible for different estimates of the magnetic field strength. It is relevant to note that in most of the previously published papers on spectral ageing analysis of smaller FRII-type radio sources the spectral ages were determined using the classical minimum-energy formalism.

5.4 The observational results

The results of our spectral ageing analysis for the eight GRSs selected from Chapter 4 are presented in Figs. 5.2 to 5.9 while some of the parameters are tabulated in Tables 5.1 to 5.8. In Figs. 5.2 to 5.9, (i) the spectral index map using the lowest frequency GMRT data and the VLA 4.86 GHz data, (ii) the intensity profiles of the lobes measured along the source axis at the

Table 5.4: The same as in Table 5.1 but for J1313+6937

Strip	Dist. (kpc)	$\nu_{\rm br}$ (GHz)	$\chi^2_{\rm red}$	$B_{\rm eq}$(rev) (nT)	$\tau_{\rm spec}$ (Myr)
		SE-lobe		$\alpha_{\rm inj} = 0.610$	
P1	470	$8.0^{+3.6}_{-4.4}$	0.73	0.47±.015	$31.4^{+5.8}_{-15.4}$
P2	430	$7.5^{>+80}_{-1.5}$	1.82	0.44±.014	$34.1^{+4.3}_{-33.5}$
P3	390	$14.5^{>+90}_{-3.2}$	11.1	0.46±.015	$23.9^{+3.2}_{-23.5}$
P4	349	$19.4^{>+80}_{-10.5}$	0.07	0.47±.015	$20.3^{+9.7}_{-18.6}$
P5	309	$34.7^{+40.0}_{-28.9}$	4.38	0.48±.015	$14.9^{+4.9}_{-14.5}$
P6	268	$30.9^{+34.5}_{-25.3}$	3.29	0.50±.016	$15.5^{+5.1}_{-15.0}$
P7	228	$23.8^{+17.7}_{-18.6}$	3.87	0.47±.015	$18.4^{+4.8}_{-18.0}$
P8	188	$22.9^{>+80}_{-17.1}$	0.42	0.40±.014	$20.5^{+12.3}_{-20.3}$
P9	147	$12.5^{+33.4}_{-5.8}$	0.16	0.38±.013	$28.7^{+10.5}_{-14.0}$
P10	107	$10.1^{+2.4}_{-4.5}$	6.34	0.46±.015	$28.6^{+3.4}_{-9.8}$
P11	67	$11.3^{+3.2}_{-7.3}$	4.25	0.55±.017	$23.7^{+3.3}_{-16.2}$
		NW-lobe		$\alpha_{\rm inj} = 0.610$	
P14	31	$8.1^{+4.4}_{-2.2}$	0.38	0.54±.017	$28.0^{+4.9}_{-6.0}$
P15	71	$9.0^{+3.6}_{-5.2}$	1.22	0.51±.016	$28.0^{+4.9}_{-15.3}$
P16	111	$11.3^{>+80}_{-4.2}$	0.27	0.48±.015	$26.2^{+6.8}_{-20.6}$
P17	152	$15.2^{>+85}_{-5.1}$	1.03	0.50±.016	$21.9^{+5.0}_{-19.1}$
P18	192	$22.5^{>+85}_{-9.3}$	0.99	0.55±.017	$16.7^{+5.1}_{-15.9}$
P19	230	$24.9^{>+85}_{-15.9}$	0.001	0.59±.018	$15.1^{+9.9}_{-13.4}$
P20	272	$28.4^{+42.8}_{-22.5}$	1.55	0.65±.019	$12.7^{+4.9}_{-12.5}$
P21	313	$24.6^{+42.2}_{-18.8}$	0.96	0.71±.020	$12.6^{+5.2}_{-12.4}$

different frequencies, and (iii) the resulting spectral age as a function of the distance from the radio core, are shown in the top, central and bottom panels respectively. Some of the numerical values are given in Tables 5.1 to 5.8, which are arranged as follows. Column 1: identification of the strip, column 2: projected distance of the centre of the strip from the radio core in units of kpc, column 3: break frequency of the spectrum of the strip according to the JP model in units of GHz, column 4: reduced χ^2 value of the fit, column 5: revised magnetic-field strength in units of nT, and column 6: spectral age of particles in the strip.

Table 5.5: The same as in Table 5.1 but for J1604+3438

Strip	Dist. (kpc)	$\nu_{\rm br}$ (GHz)	$\chi^2_{\rm red}$	$B_{\rm eq}$(rev) (nT)	$\tau_{\rm spec}$ (Myr)
		E-lobe		$\alpha_{\rm inj} = 0.554$	
P1	441	$26.9^{+69.9}_{-18.1}$	0.82	0.64±.021	$10.1^{+4.8}_{-7.9}$
P2	376	$33.6^{>+80}_{-17.5}$	0.67	0.52±.015	$10.2^{+4.7}_{-9.7}$
P3	312	$9.6^{+3.9}_{-5.4}$	0.98	0.50±.014	$19.4^{+10.1}_{-2.9}$
P4	248	$4.3^{+1.0}_{-0.8}$	0.16	0.53±.016	$28.2^{+2.5}_{-3.4}$
P5	183	$2.5^{+1.2}_{-0.3}$	0.26	0.51±.014	$37.5^{+3.9}_{-6.4}$
P6	119	$2.5^{+4.9}_{-0.5}$	1.87	0.57±.017	$35.8^{+5.0}_{-15.1}$
		W-lobe		$\alpha_{\rm inj} = 0.554$	
P7	87	$6.0^{>+90}_{-0.7}$	1.39	0.62±.020	$21.9^{+1.9}_{-21.0}$
P8	198	$3.6^{+4.1}_{-0.5}$	0.93	0.47±.013	$32.5^{+2.6}_{-10.3}$
P9	262	$6.0^{+2.3}_{-1.7}$	0.71	0.46±.012	$25.8^{+3.9}_{-4.9}$
P10	327	$11.4^{+3.3}_{-7.3}$	1.14	0.47±.013	$18.3^{+11.6}_{-2.2}$
P11	391	$20.2^{+25.8}_{-12.8}$	0.39	0.50±.014	$13.4^{+4.5}_{-9.0}$

Table 5.6: The same as in Table 5.1 but for J1604+3731

Strip	Dist. (kpc)	$\nu_{\rm br}$ (GHz)	$\chi^2_{\rm red}$	$B_{\rm eq}$(rev) (nT)	$\tau_{\rm spec}$ (Myr)
		S-lobe		$\alpha_{\rm inj} = 0.775$	
P1	647	$31.7^{>+80}_{-18.4}$	0.43	0.78±.252	$3.5^{+1.9}_{-2.9}$
P2	541	$20.0^{>+90}_{-10.6}$	3.67	0.70±.230	$4.5^{+2.0}_{-4.5}$
P3	435	$8.6^{+41.8}_{-2.0}$	3.98	0.64±.213	$6.9^{+0.9}_{-4.2}$
P4	329	$4.2^{+6.9}_{-0.6}$	2.14	0.52±.179	$9.7^{+0.8}_{-3.7}$
		N-lobe		$\alpha_{\rm inj} = 0.765$	
P5	208	$11.1^{>+80}_{-3.8}$	2.79	0.38±.141	$5.6^{+1.8}_{-5.1}$
P6	337	$4.4^{+9.7}_{-0.6}$	5.37	0.46±.167	$9.4^{+0.8}_{-4.2}$
P7	442	$5.0^{+10.4}_{-0.6}$	2.70	0.56±.197	$9.0^{+0.6}_{-4.0}$
P8	548	$8.5^{+48.6}_{-1.7}$	1.34	0.67±.230	$6.9^{+0.8}_{-4.4}$
P9	654	$16.4^{+40.8}_{-9.5}$	0.90	0.68±.234	$4.9^{+2.4}_{-2.7}$

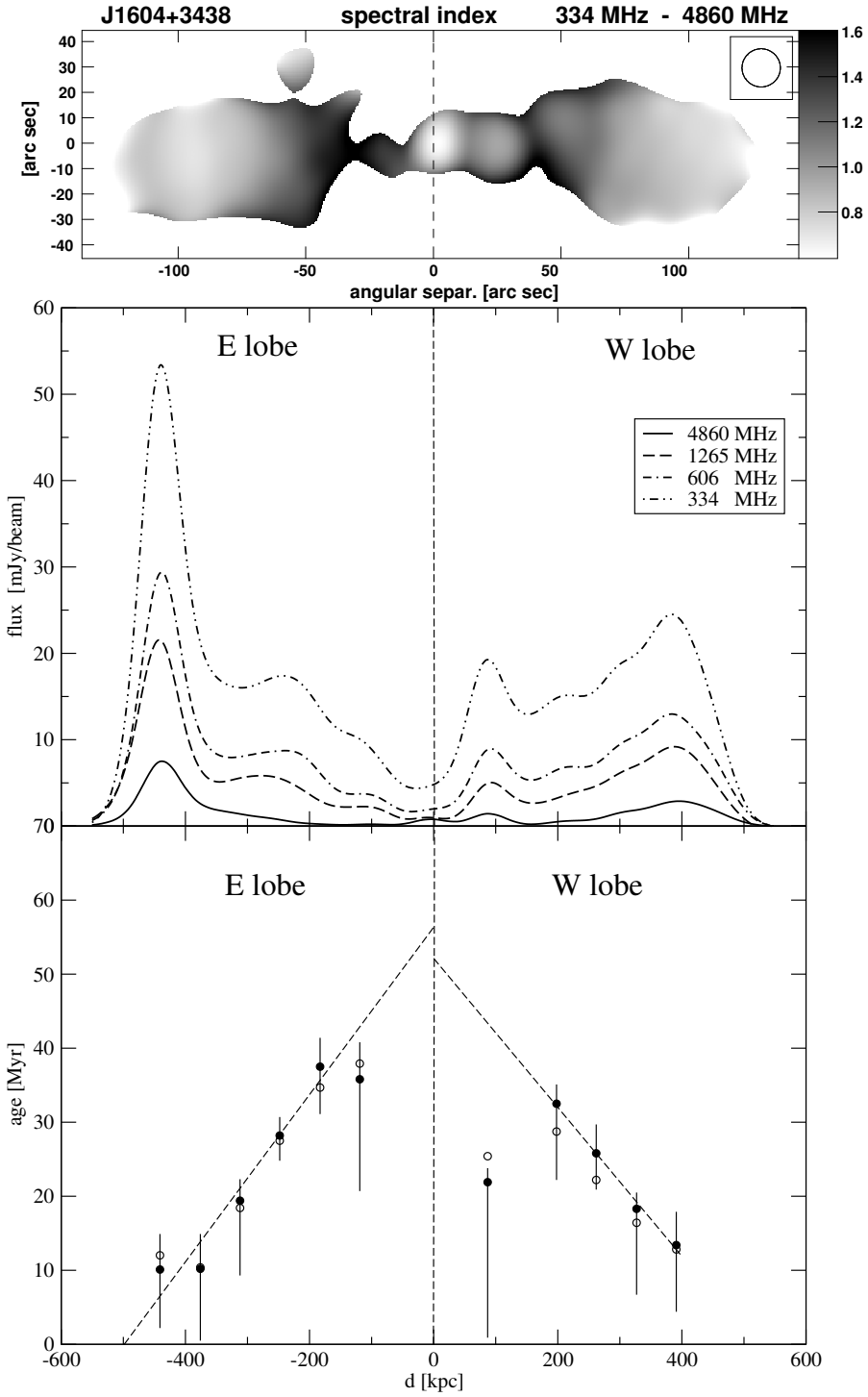

Figure 5.6: As in Fig. 5.2, but for J1604+3438

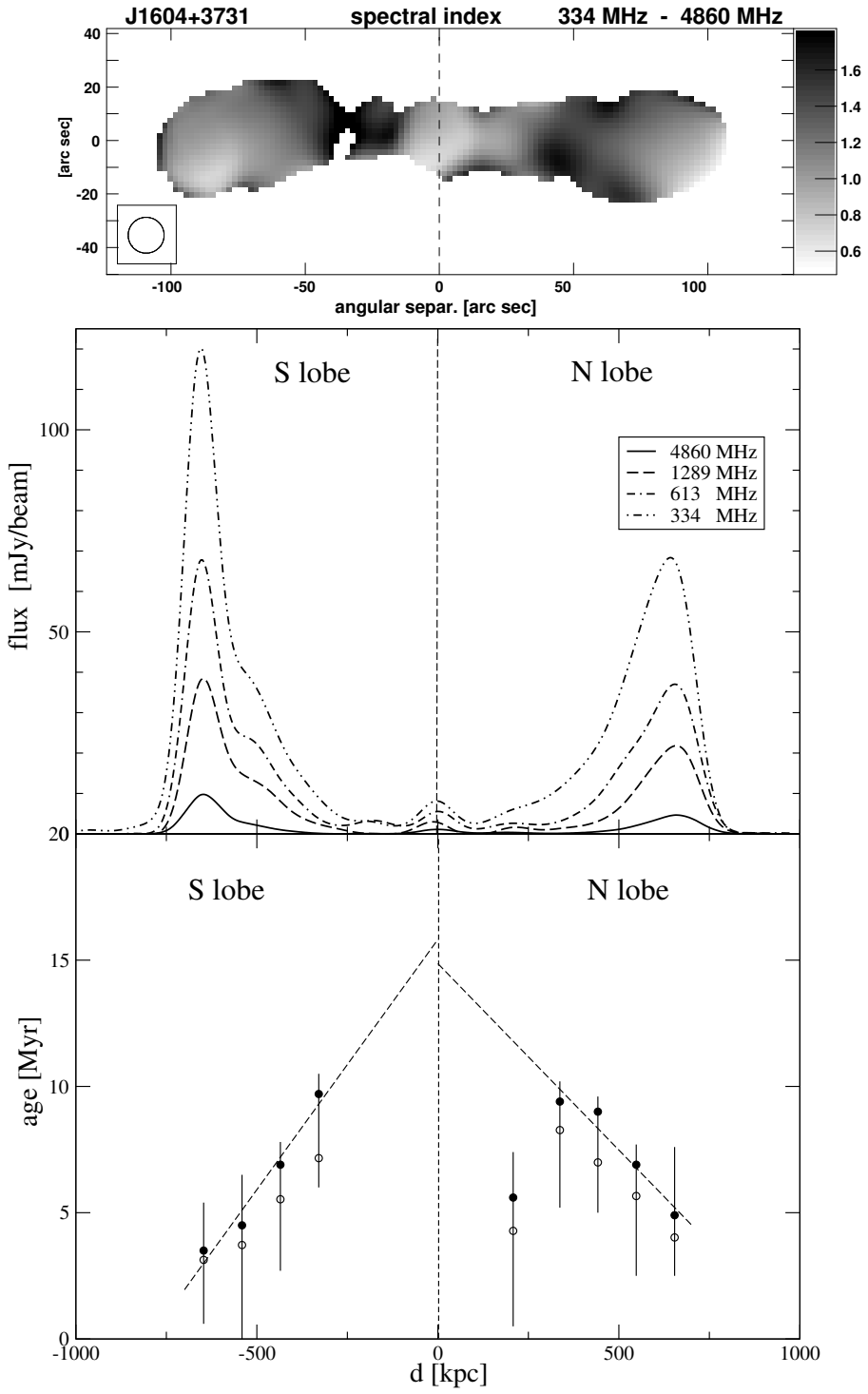

Figure 5.7: As in Fig. 5.2, but for J1604+3731

Table 5.7: The same as in Table 5.1 but for J1702+4217

Strip	Dist. (kpc)	$\nu_{\rm br}$ (GHz)	$\chi^2_{\rm red}$	$B_{\rm eq}$(rev) (nT)	$\tau_{\rm spec}$ (Myr)
		NE-lobe		$\alpha_{\rm inj} = 0.588$	
P1	500	$15.2^{+14.3}_{-10.3}$	1.77	0.49±.028	$10.5^{+3.2}_{-8.0}$
P2	411	$10.5^{+61.4}_{-3.4}$	0.02	0.41±.025	$12.8^{+2.7}_{-7.9}$
P3	317	$6.7^{+4.8}_{-3.2}$	0.29	0.45±.026	$15.9^{+3.8}_{-6.3}$
P4	222	$5.8^{+1.5}_{-2.8}$	1.97	0.49±.028	$17.0^{+6.5}_{-2.0}$
P5	128	$3.7^{+0.6}_{-0.7}$	2.09	0.40±.024	$21.6^{+2.5}_{-1.7}$
		SW-lobe		$\alpha_{\rm inj} = 0.588$	
P6	170	$2.8^{+0.3}_{-0.5}$	1.65	0.36±.022	$24.5^{+3.1}_{-0.9}$
P7	259	$4.1^{+1.1}_{-0.8}$	0.89	0.38±.024	$20.5^{+2.2}_{-2.4}$
P8	359	$6.0^{>+80}_{-1.4}$	0.61	0.39±.024	$16.9^{+2.5}_{-13.3}$
P9	454	$7.6^{>+90}_{-1.7}$	1.71	0.39±.024	$15.0^{+2.0}_{-14.6}$
P10	549	$12.9^{+6.2}_{-8.5}$	4.34	0.39±.024	$11.6^{+8.2}_{-2.1}$
P11	643	$11.3^{+6.4}_{-7.0}$	2.13	0.47±.027	$12.2^{+2.5}_{-7.7}$

Table 5.8: The same as in Table 5.1 but for J2312+1845

Strip	Dist. (kpc)	$\nu_{\rm br}$ (GHz)	$\chi^2_{\rm red}$	$B_{\rm eq}$(rev) (nT)	$\tau_{\rm spec}$ (Myr)
		NE-lobe		$\alpha_{\rm inj} = 0.820$	
P1	540	$73.4^{>+90}_{-35.6}$	1.56	1.44±.089	$2.4^{+0.9}_{-2.3}$
P2	450	$42.3^{>+80}_{-27.3}$	0.01	1.24±.078	$3.7^{+2.6}_{-2.7}$
P3	362	$14.7^{>+80}_{-3.1}$	1.26	1.17±.074	$6.7^{+0.9}_{-4.8}$
P4	273	$7.1^{+13.2}_{-0.9}$	1.45	1.03±.067	$10.9^{+0.8}_{-4.8}$
P5	184	$4.2^{>+90}_{-4.0}$	12.0	0.82±.055	$17.2^{+6.6}_{-17.0}$
		SW-lobe		$\alpha_{\rm inj} = 0.820$	
P6	150	$2.0^{+4.9}_{-0.4}$	16.6	0.82±.055	$25.2^{+2.7}_{-12.4}$
P7	239	$5.7^{+11.7}_{-0.5}$	11.0	0.99±.065	$12.6^{+0.6}_{-5.8}$
P8	323	$9.2^{+30.8}_{-1.1}$	3.03	1.26±.080	$7.8^{+0.5}_{-4.3}$
P9	418	$28.6^{>+90}_{-8.9}$	1.41	1.47±.091	$3.7^{+0.8}_{-3.7}$
P10	507	$152.6^{>+80}_{-80.0}$	0.10	1.50±.092	$1.6^{+1.7}_{-1.5}$

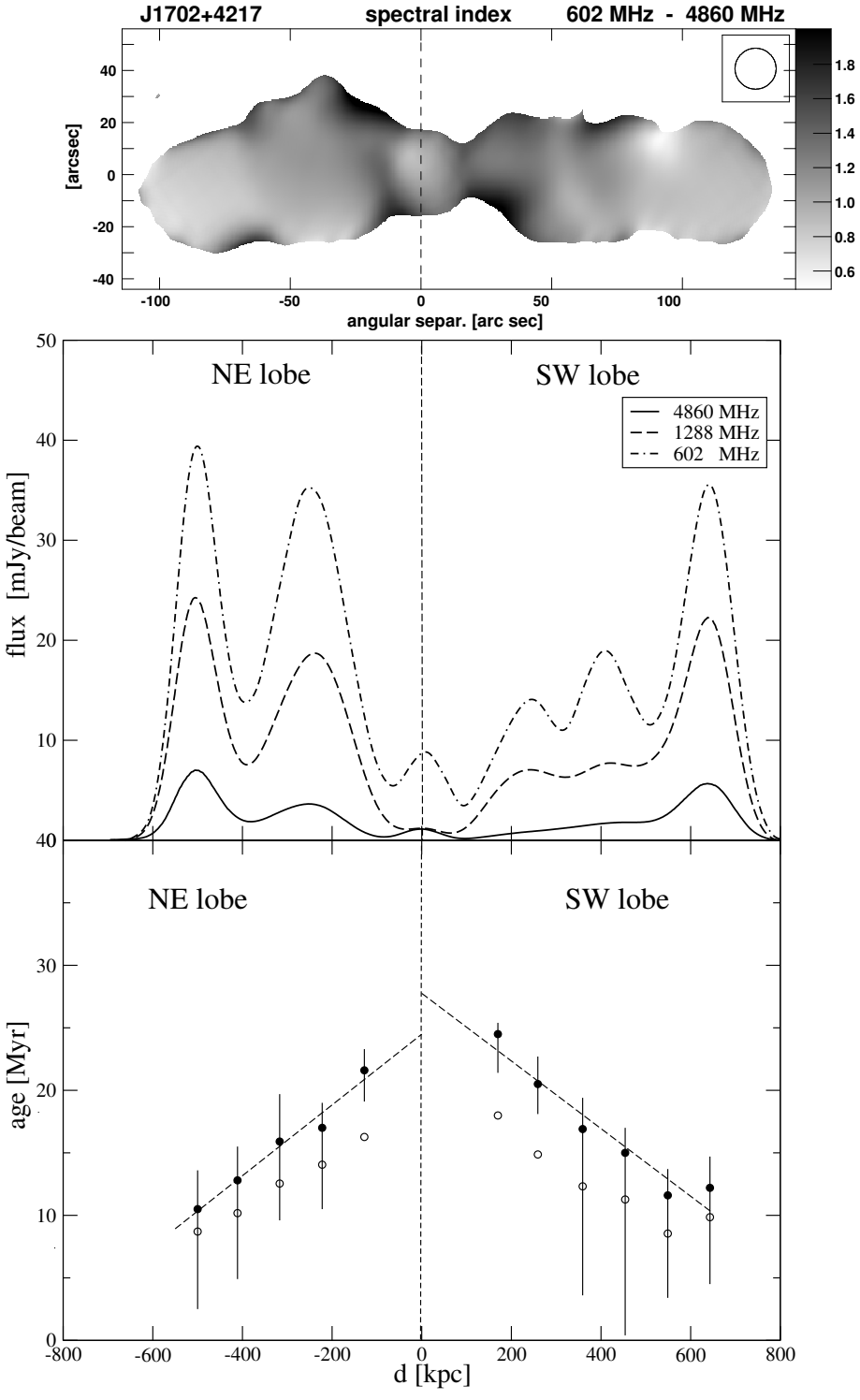

Figure 5.8: As in Fig. 5.2, but for J1702+4217

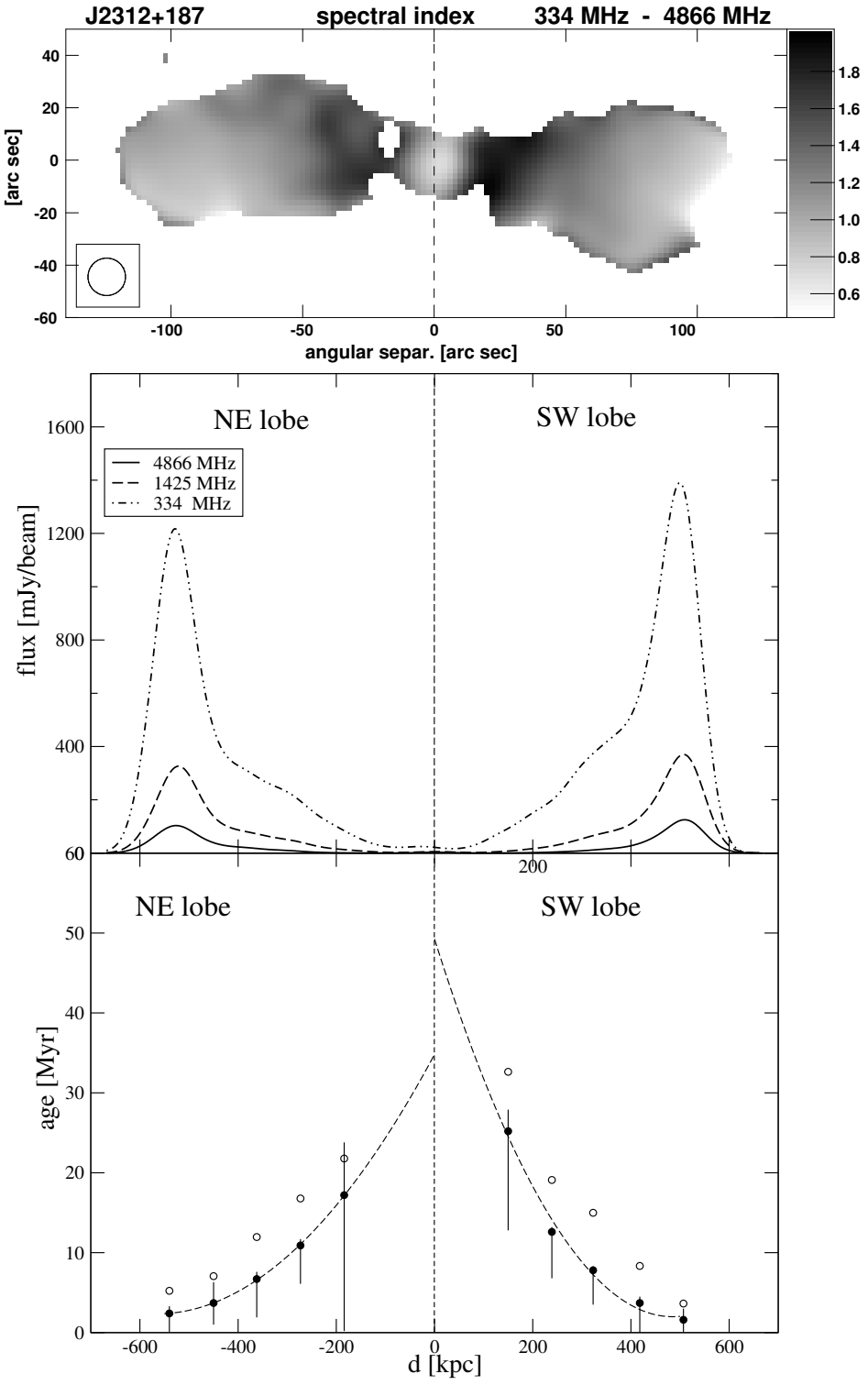

Figure 5.9: As in Fig. 5.2, but for J2312+1845/3C457

Table 5.9: Some of the phyiscal parameters of the sources

Source	Opt. Id.	red-shift	l (kpc)	$P_{1.4}$ (W Hz^{-1})	Lobe	age B&K (Myr)	ext-age B&K (Myr)	age class (Myr)	ext-age class (Myr)	v_{sep}/c B&K	v_{sep}/c class
(1)	(2)	(3)	(4)	(5)	(6)	(7)	(8)	(9)	(10)	(11)	(12)
J0912+3510	G	0.2489	1449	25.44	S	28.7	49.9	23.0	34.2	0.07	0.12
					N	32.6	35.1	22.2	23.2	0.09	0.18
J0927+3510	G	0.55*	2206	26.02	SE	14.6	21.4	8.3	10.4	0.24	0.70
					NW	14.5	19.6	8.7	12.2	0.21	0.37
J1155+4029	G	0.53*	1437	26.55	SW	5.2	26.8	5.6	27.5	0.12	0.12
					NE	11.1	19.1	13.0	21.0	0.08	0.08
J1313+6937	G	0.106	745	25.60	SE	23.7	–	35.1	–	–	–
					NW	28.0	31.5	35.7	36.4	0.05	0.06
J1343+3758[1]	G	0.2267	2463	25.32	NE	33.5	60.8	26.5	53.4	0.13	0.10
					SW	36.2	52.5	33.6	50.0	0.12	0.09
J1453+3308[2]	G	0.249	1297	25.93	S	58.4	65.0	47.9	61.8	0.04	0.05
					N	46.6	54.9	38.8	53.1	0.04	0.05
J1604+3438	G	0.2817	846	25.50	E	37.5	56.3	34.7	50.8	0.03	0.03
					W	21.9	52.1	28.7	44.5	0.03	0.04
J1604+3731	G	0.814	1346	26.60	S	9.7	15.8	7.2	11.3	0.16	0.25
					N	9.4	14.9	8.3	12.8	0.22	0.24
J1702+4217	G	0.476	1160	26.19	NE	21.6	24.5	16.3	18.8	0.12	0.16
					SW	24.5	27.8	18.0	19.9	0.12	0.18
J2312+1845	G	0.427	1056	27.11	NE	17.2	34.8	21.9	36.5	0.08	0.07[3]
					SW	25.2	49.2	32.6	54.1	0.05	0.04[3]

Notes: * denotes an estimated redshift; (1) recalculated from the data in Jamrozy et al. (2005); (2) calculated from the data in Konar et al. (2006); (3) speed estimated using the two extreme strips for each lobe.

(a) Notes on individual GRSs

J0912+3510: there is some uncertainty as to which galaxy is associated with the radio source (cf. Machalski et al. 2006, hereinafter referred to as MJZK).

J0927+3510: as mentioned in previous chapter (Chapter 4), the strips P5 and P6 in Table 5.2 overlap the region of emission which was suspected to be an inner double (cf. MJZK). However, the very steep spectra of about 1.17 and 1.35 in the strips P5 and P6 respectively suggest that this is likely to be old lobe emission. The resulting spectral ages are not significantly different from the expected trend of age with distance from the hotspot, with the age of P5 which is weaker and on the south-eastern side being only marginally lower. The somewhat higher separation speed of $\sim$0.7 and 0.4c for the eastern and western lobe material respectively (Fig. 5.3) suggests that the photometric-redshift estimate of 0.55 for this GRS (MJZK) may be overestimated.

J1155+4029: although we have tentatively identified it as a galaxy (MJZK; Konar et al. 2007), an optical spectrum of the faint host would help resolve the nature of the optical galaxy.

J1313+6937, DA 340: the spectral-index map and the intensity profiles along the source axis suggest that the synchrotron radiation observed in separate strips of this GRS may be related to a mixture of emitting particles which were injected or accelerated at different time epochs. The SE lobe of this GRS is the only one, among the other lobes studied in this Chapter, in which the synchrotron ages determined do not more or less gradually increase with distance from the hotspot area to the core. However, because these ages strongly depend on the frequency break $\nu_{\rm br}$ and we do not have

radio maps at frequencies below 605 MHz for this source, a distribution of the ages in Fig. 5.5 may be biased by observational circumstances. The spectral ageing analysis of the entire lobes of this galaxy was already published by Schoenmakers et al. (2000) where the radio spectrum of each of the lobes were determined within the frequency range of 325 MHz–10.5 GHz. Though their $\alpha_{\rm inj}$ values found fitting the JP model, i.e. 0.71±0.02 and 0.75±0.02 for the SE and NW lobes, respectively, differ from our values, their average synchrotron ages of these lobes of 28±1 Myr and 27±1 Myr are consistent with our results (cf. Table 5.4).

J1604+3438: the inner part of the structure comprising the flat-spectrum radio core and the two nearby peaks of emission seen most clearly in the image published by MJZK led them to classify as a possible DDRG. However as noted in Chapter 4 spectral indices of these features are steep and one needs to image them with higher resolution in both total intensity and linear polarisation to investigate the DDRG nature of the source. It is relevant to note that the spectral age of the western feature lies significantly below the age−distance relationship for the western lobe.

J1604+3731: this is the highest-redshift radio galaxy in the sample. The FIRST 1.4-GHz map shows bright hotspots at the leading heads of the outer 1376 kpc structure which may suggest a continuous reacceleration of the emitting particles.

J1702+4217: although there are peaks of emission visible in the lobe emission, especially at the lower frequency, the spectral age increases smoothly with distance from the hotspots.

J2312+1845, 3C457: the only source in the sample showing undoubtedly a curvature in the age−distance plot. This could be due to deceleration of the radial expansion velocity of the lobe material. The data in Table 5.8

give an expansion velocity of about $0.11c \pm 0.05c$ in the vicinity of the leading heads which slows to about $0.03c \pm 0.015c$ in the regions where the oldest particles are detected. Such curvatures may also be produced by re-acceleration of particles in different regions of the lobes.

(b) Separation speeds and spectral ages

The plots in the bottom panels of Figs. 5.2–5.9 show that, in general, the spectral age of the emitting particles increases systematically with distance from the leading heads of the lobes, i.e., the hotspot regions. These plots have been shown using the magnetic field strengths estimated using the Beck & Krause (2005) formalism (full circles) as well as the classical-1 (Miley 1980; see 4) minimum-energy one (open circles). These two field strengths differ by a factor of $\sim$3 (see 4). The numerical values we list here have been estimated using the Beck & Krause formalism. For most of these lobes we calculate the linear regression of the ages ($\tau_{\rm spec}$) on the corresponding distances (d), which is shown as a dashed line in Figs. 5.2–5.9. The slopes of these lines give a characteristic speed, $v_{\rm sep}$, which is an indication of the average speed of the lobe material relative to the hotspots. A clear exception is J2312+1845 (3C457) for which the speed, $v_{\rm sep}$, evidently decelerates with distance from hotspot regions. This source is much stronger than the remaining GRSs, therefore the errors of the spectral break frequency, $\nu_{\rm br}$, and the corresponding spectral age in each of the strips are much smaller than those in our remaining sources. In their cases the linear regression fits are the most conservative, though there is no physically justified reason for the material separation speeds to be constant.

Our estimates of the average speed and a 'characteristic' spectral age

for the lobes in the regions of the observed emission from the lobes as well as the values when extrapolated to the positions of the cores are presented in Table 5.9. These values have been presented for all the sources except for the SE-lobe of J1313+6937 which has a complex age−distance plot. In Table 5.9 the values have been presented for the estimates using the magnetic field values from both the Beck & Krause and the classical-1 formalisms. The table is arranged as follows. Column 1: source name; column 2: the optical identification; column 3: redshift; column 4: largest linear size l in kpc; column 5: log of the luminosity in units of W Hz^{-1}; column 6: lobe identification; column 7: spectral age using the Beck & Krause formalism till the most distant strip from the hotspot; column 8: spectral age when the age-distance relationship is extrapolated to the region of core; column 9 and 10: same as column 7 and 8 but using the classical-1 estimates of the magnetic field; column 11 and 12: estimates of the separation velocity for the Beck & Krause and classical-1 approaches.

5.5 Discussion

(a) Spectral ages

The maximum spectral ages estimated for the detected radio emission in the lobes of our sources range from ∼6 to 48 Myr with a median value of ∼23 Myr using the classical equipartition fields. Using the magnetic field estimates from the Beck & Krause formalism, the spectral ages range from ∼5 to 58 Myr with a median value of ∼24 Myr. These ages are significantly older than those of smaller sources. The median linear size of these large sources is 1300 kpc. For comparison, we first consider the sample of smaller

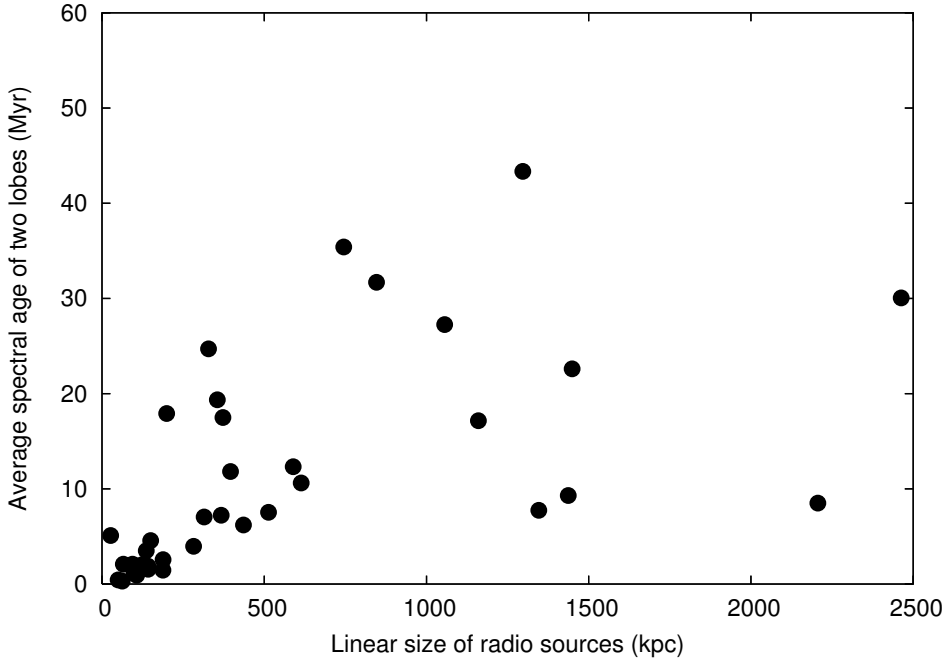

Figure 5.10: The spectral age in Myr as a function of the largest linear size in kpc

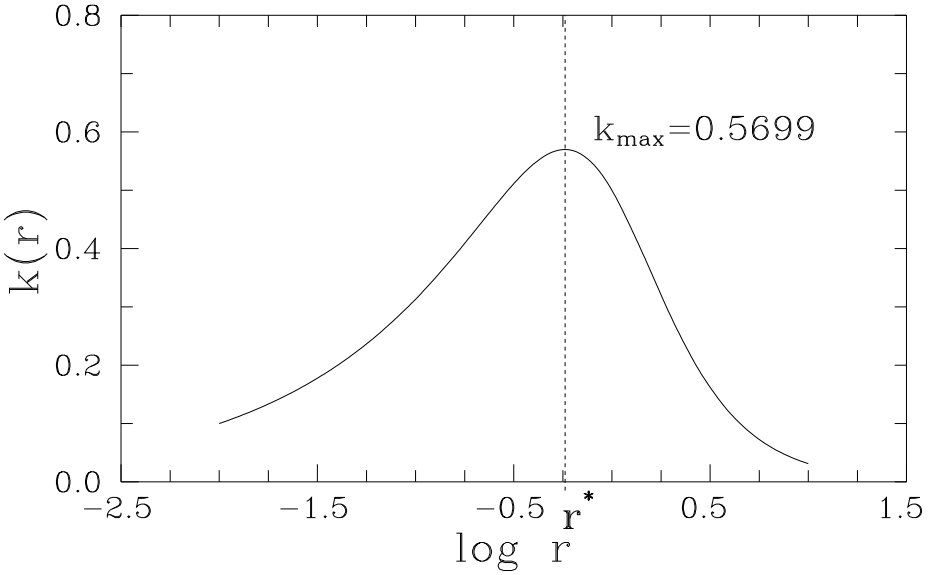

Figure 5.11: Function $k(r)$

sources studied by Leahy et al. (1989) which has been observed over a large frequency range. They estimated the spectral ages of a sample of 16 3CR radio sources from low-frequency observations with the Multi-Element Radio Linked Interferometer Network (MERLIN) at 151 MHz and high-frequency observations at 1500 MHz with the VLA. We have re-estimated their values using the cosmological parameters used in this thesis. The ages of the lobes of these sources range from ∼2.5 to 26 Myr with a median value of ∼8 Myr, significantly smaller than the value for the GRSs. The median value of the linear size for this sample of sources is 342 kpc.

Considering the sample of 14 high-luminosity double radio sources studied by Liu et al. (1992), we have again re-estimated the spectral ages using the cosmological parameters used in this thesis, and find that the values range from ∼0.3 to 5.3 Myr with a median value of ∼1.7 Myr. These sources have even smaller spectral ages and their median linear size is 103 kpc. Considering these different samples, there is a trend for the spectral ages to increase with linear size (Fig. 5.10) as has been noted earlier in the literature (e.g. Parma et al. 1999; Murgia et al. 1999; Murgia 2003). It is also interesting to note that the relative speeds of the lobe material has been estimated to be in the range of ∼0.03 to 0.2c with a median value of ∼0.1c for the Liu et al. sample. In comparison, the corresponding speeds for our sample of GRSs is about 0.03 to 0.25 (excluding J0927+3510 for which the photometric redshift value can be much overestimated, cf. Sect. 3.1), with a median value of ∼0.09c, similar to that of the the Liu et al. sample.

The above trend for spectral age to increase with size is broadly consistent with the expectations of dynamical models of the propagation of jets in an external medium (e.g. Falle 1991; Kaiser & Alexander 1997; Jeyakumar et al. 2005 and references therein) in which the linear size of the source

is a function of its (dynamical) age. Nevertheless, while interpreting these numbers caveats related to the evolution of the local magnetic field in the lobes need to be borne in mind (e.g. Rudnick, Katz-Stone & Anderson 1994; Jones, Ryu & Engel 1999; Blundell & Rawlings 2000). Also, while Kaiser (2000) have suggested that spectral and dynamical ages are comparable if bulk backflow and both radiative and adiabatic losses are taken into account in a self-consistent manner, Blundell & Rawlings (2000) suggest that this may be so only in the young sources with ages much less than 10 Myr. In the study of the FRII type giant radio galaxy, J1343+3758, Jamrozy et al. (2005) find the dynamical age to be approximately 4 times the maximum synchrotron age of the emitting particles.

In the plots of spectral age against distance from the hotspots, we note that none of the sources show zero age at the hotspots. In fact the ages in the hotspots usually range from a few to ∼20 Myr, except in the case of the south-eastern lobe of J1313+6937 where the age in the outer extremity is ∼30 Myr. This tendency for the hotspots to exhibit a non-zero age has been noted earlier by a number of authors (e.g. Liu et al. 1992). In the Liu et al. sample, ages in the hotspots are typically less than ∼1 Myr while in the case of Cygnus A, Carilli et al. (1991) find the ages of the hotspots to be 0.1 and 0.2 Myr for the north-western and south-eastern lobes respectively. The typical linear resolution of the sources observed by Liu et al. is ∼10 kpc for most sources while that of Cygnus A is ∼5 kpc. In comparison, the linear resolution of our GRSs ranges from ∼30 to 110 kpc with a median value of ∼80 kpc. For comparison, the sizes of hotspots range from about a few parsec to ∼10 kpc increasing with source size till the largest linear size is ∼100 kpc and then flattens for larger source sizes (e.g. Jeyakumar & Saikia 2000). Possible explanations for the non-zero ages include (i) the possibility that

the hotspots have been inactive for 10^5 to 10^6 yr, (ii) contamination by more extended emission and (iii) higher magnetic fields in the hotspots (cf. Liu et al.). The coarse resolution of our observations suggest that contamination by extended emission is the likely cause for the non-zero ages in the hotspots of our GRSs.

Another effect, visible in the bottom panels of Figs. 5.2–5.9 and related to the magnetic fields, is the age difference, $\Delta = \tau_{\rm spec}({\rm rev}) - \tau_{\rm spec}({\rm class})$, which is either positive or negative. This is a simple consequence of Eq. (1). Given $\nu_{\rm br}$ and z imply the maximum $\tau_{\rm spec}$ for $B{=}B_{\rm iC}/\sqrt{3}$. Substitution of the ratio $r \equiv B/B_{\rm iC}$ into Eq. 1 gives

$$\tau_{\rm spec} = 50.3 \frac{r^{1/2}}{1+r^2} B_{\rm iC}^{-3/2} \{\nu_{\rm br}(1+z)\}^{-1/2} =$$

$$= 50.3\, k(r) \{0.318(1+z)^2\}^{-3/2} \{\nu_{\rm br}(1+z)\}^{-1/2}.$$

The function $k(r)$ has a maximum at $r^*{=}3^{-1/2}$, thus the maximum of $\tau_{\rm spec}$ can be written as

$$\tau_{\rm spec}^{\rm (max)} = 159.8\, \nu_{\rm br}^{-1/2} (1+z)^{-7/2}$$

The function $k(r)$ as a function of r is plotted in Fig. 5.11.

In our calculations the values of the magnetic field calculated with the revised formula, $B_{\rm eq}({\rm rev})$, are always greater than the values of $B_{\rm eq}({\rm class})$ calculated with the classical formula of Miley (1980) where, for a comparison with several previously published papers on spectral ages of other radio sources, we have assumed the proton to electron energy ratio to be unity. Therefore, if both values of $B_{\rm eq}({\rm class})$ and $B_{\rm eq}({\rm rev})$ are less than $B_{\rm iC}/\sqrt{3}$ (or $r < r^*$ in Fig. 5.11), then the ages derived with the classical formula

(open circles in Figs. 5.2–5.9) are lower than these derived with the revised formula (full circles in Figs. 5.2–5.9). On the contrary, if both values of the magnetic field are either close to, or greater than $B_{\rm iC}/\sqrt{3}$, the 'classical' ages are greater than the 'revised' ages.

(b) Injection spectral indices

The injection spectral indices which have been estimated from fits to the spectra of the lobes or the entire source using our measurements as well as low-frequency flux density values at 151 MHz from the Cambridge surveys (Green 2002 and references therein) and the VLA Low-frequency Sky Survey (VLSS; Cohen et al. 2007) estimates for the stronger sources. $\alpha_{\rm inj}$ varies from $\sim$0.55 to 0.88 with a median value of $\sim$0.6 for our sources. For strong, non-relativistic shock in a Newtonian fluid $\alpha_{\rm inj} = 0.5$ (Bell 1978a,b; Blandford & Ostriker 1978). However, for relativistic shocks or shocks in which fields and relativistic particles alter the shock dynamics lead to values of $\alpha_{\rm inj}$ in the range of 0.35 to 0.65 (Heavens 1989; Kirk & Schneider 1989; Drury & Volk 1981; Axford, Leer & McKenzie 1982). Carilli et al. (1991) estimate the $\alpha_{\rm inj}$ to be 0.5 for Cygnus A while Meisenheimer et al. (1989) obtain similar values for a few powerful radio galaxies. For the sample of sources studied by Liu et al. (1992), the values of $\alpha_{\rm inj}$ have been estimated from the low-frequency spectral indices using data between 38 MHz and 1 GHz. Their values of $\alpha_{\rm inj}$ range from 0.65 to 1 with a median value of 0.77. The values of the spectral indices of the hotspots estimated from low-frequency measurements by Leahy, Muxlow & Stephens (1989), which is similar to $\alpha_{\rm inj}$, ranges from 0.64 to 1.16 with a median value of $\sim$0.8. Katz-Stone & Rudnick (1997) also estimate a steep injection spectral index of 0.8 for the compact steep spectrum source

3C190. It is important to determine the spectra of the lobes over a wide low-frequency range using the GMRT and upcoming instruments such as the Long Wavelength Array (LWA) and the Low Frequency Array (LOFAR) to get better estimates of the injection spectral indices, and also compare these with estimates from the inverse-Compton scattered **x**-ray spectrum (e.g. Harris 2005).

We have investigated any possible dependence of $\alpha_{\rm inj}$ on source size using our estimates and those of Liu et al. (1992) and Leahy et al. (1989). We find $\alpha_{\rm inj}$ to be strongly correlated with luminosity (Fig. 5.12, upper panel), consistent with the well-known spectral-index luminosity correlation for extragalactic radio sources (e.g. Laing & Peacock 1980, and references therein). However, lower frequency measurements than those we have used using instruments such as the GMRT, LOFAR and LWA would be extremely useful to better determine the values of $\alpha_{\rm inj}$. $\alpha_{\rm inj}$ also appears to be strongly correlated with redshift (Fig. 5.12, lower panel), but since most of our sources come from a reasonably narrow range of flux density it is difficult to distinguish whether the fundamental correlation is with luminosity or redshift. It is worth noting that while exploring correlations of $\alpha_{\rm inj}$ with either luminosity or redshift, K-correction factors due to cosmological redshifts should not play a significant role. A plausible scenario for such a correlation could be multiple shocks in the heads of the jets as suggested by Gopal-Krishna & Wiita (1990). We have also explored possible correlation of $\alpha_{\rm inj}$ with source size and find that our estimates for the GRSs are smaller than the corresponding values for the smaller sources from the Liu et al. and Leahy et al. samples (Fig. 5.13, upper panel). The inverse correlation of luminosity and size for these samples (Fig. 5.13, lower panel) which define the approximate upper envelop of the luminosity-size diagram (e.g. Kaiser, Dennett-Thorpe

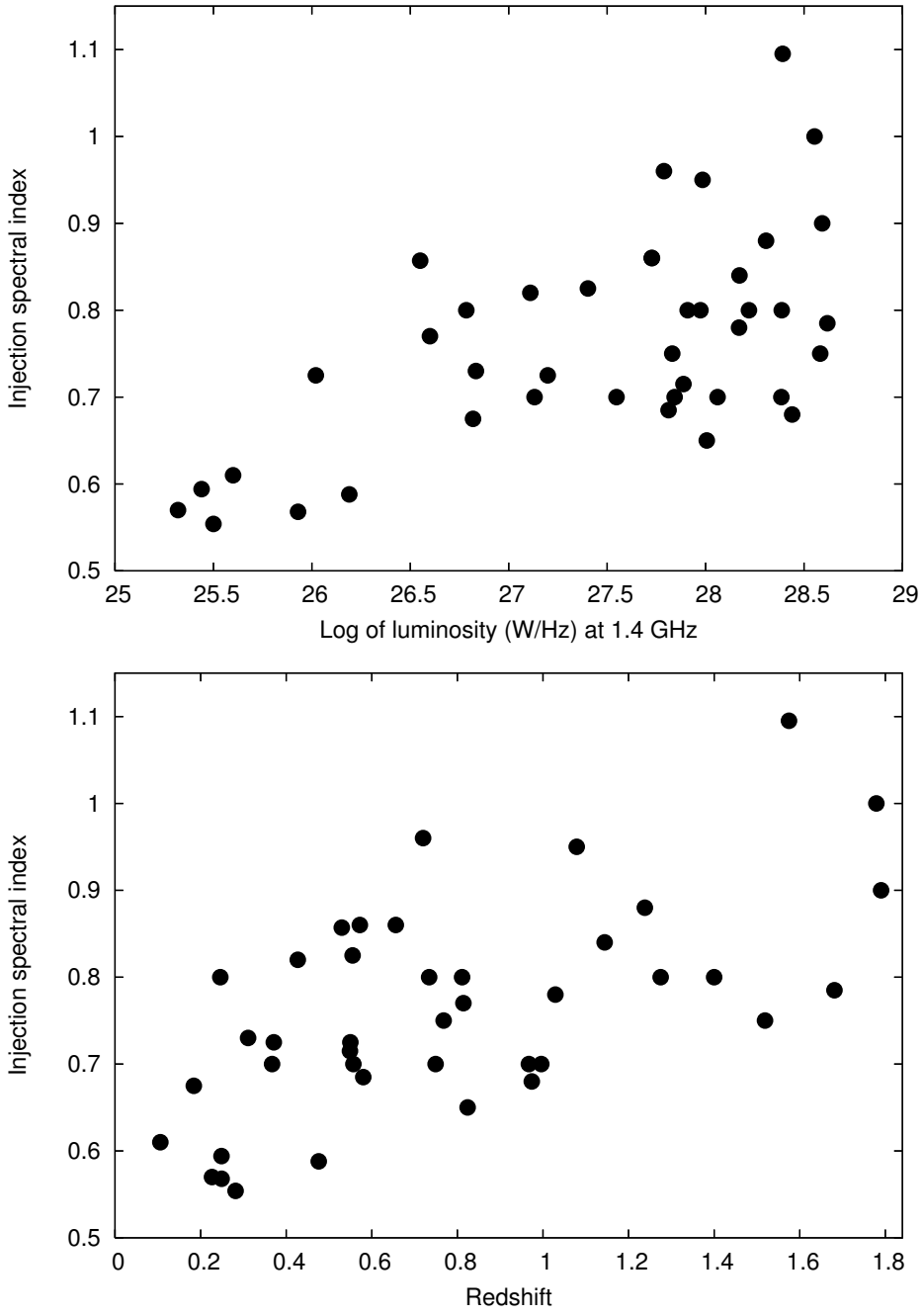

Figure 5.12: The injection spectral index, $\alpha_{\rm inj}$, as a function of radio luminosity at 1.4 GHz in units of W Hz^{-1} (upper panel) and redshift (lower panel).

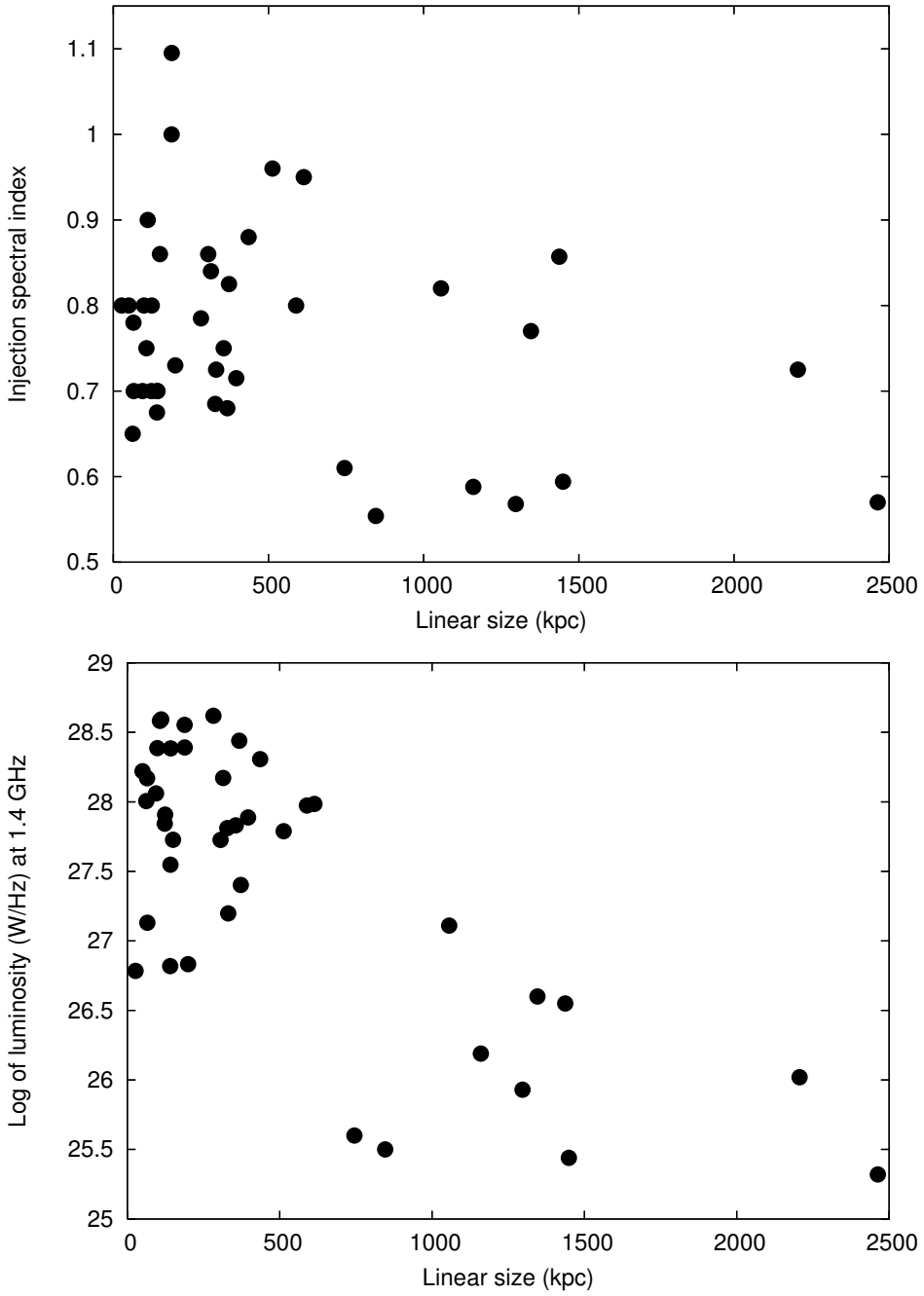

Figure 5.13: The injection spectral index, $\alpha_{\rm inj}$, as a function of the largest linear size in kpc (upper panel) and the luminosity−linear size diagram for the sample of sources (lower panel).

& Alexander 1997; Blundell, Rawlings & Willott 1999; Ishwara-Chandra & Saikia 1999) are consistent with the above trends.

5.6 Concluding remarks

We summarise briefly the main results of our analysis.

(i) The maximum spectral ages estimated for the detected radio emission in the lobes of our sources range from ∼6 to 48 Myr with a median value of ∼23 Myr using the classical equipartition fields. Using the magnetic field estimates from the Beck & Krause formalism the spectral ages range from ∼5 to 58 Myr with a median value of ∼24 Myr. These ages are significantly older than smaller sources (e.g. Leahy et al. 1989; Liu et al. 1992). The GRSs are older sources possibly evolving in under dense regions of the IGM (cf. Cotter 1998; Mack et al. 1998; Machalski et al. 2004), although the external medium is often asymmetric on scales of ∼1 Mpc (e.g. Ishwara-Chandra & Saikia 1999; Konar et al. 2004, 2007).

The spectral ages depend on the estimated magnetic fields. Strengths of the equipartition field calculated with the revised formalism proposed by Beck & Krause (2005) are greater than the corresponding values provided by the classical formula of Miley (1980) by a factor of ∼3 (Chapter 4). However, the inferred synchrotron age is a function of the ratio $B/B_{\rm iC}$. If B is greater than $B_{\rm iC}/\sqrt{3}$, the 'revised' age is lower than the 'classical' age.

(ii) The injection spectral indices range from 0.55 to 0.88 with a median value of ∼0.6. Our estimates for the GRSs are marginally smaller than those estimated for smaller sources by Leahy et al. (1989) and Liu et al. (1992). Reliable low-frequency measurements of the lobes using instruments such as GMRT, LWA and LOFAR are required to get more reliable estimates of the

injection spectral indices. We have explored possible correlations of $\alpha_{\rm inj}$ with other physical parameters and find that it appears to increase with luminosity and redshift, but shows an inverse correlation with linear size.

References

Alexander P., Leahy J.P., 1987, MNRAS, 225, 1

Axford, W.I., Leer E., McKenzie J.F., 1982, A&A, 111, 317

Beck R., Krause M., 2005, Astron. Nachr., 6, 414

Bell A.R., 1978a, MNRAS, 182, 147

Bell A.R., 1978b, MNRAS, 182, 443

Blandford R.D., Ostriker J.P., 1978, ApJ, 221, L29

Blundell K.M., Rawlings S., Willott C.J., 1999, AJ, 117, 677

Blundell K.M., Rawlings S., 2000, AJ, 119, 1111

Carilli C.L., Perley R.A., Dreher J.W., Leahy J.P., 1991, ApJ, 383, 554

Cohen, A.S., Lane, W.M., Cotton, W.D., Kassim, N.E., et al., 2007, AJ, (in press; astro-ph/0706.1191)

Cotter G., 1998, in Observational cosmology with the new radio surveys", eds. M.N. Bremer, N. Jackson, I. Pérez-Fournon, Kluwer, p. 233

Drury L. O'C., Volk J.H., 1981, ApJ, 248, 344

Eilek J.A., Arendt, P.N., 1996, ApJ, 457, 150

Falle S.A.E.G., 1991, MNRAS, 250, 581

Fanaroff B.L., Riley J.M., 1974, MNRAS, 167, 31

Gopal-Krishna, Wiita P.J., 1990, A&A, 236, 305

Green D.A., 2002, in The Universe at Low Radio Frequencies, IAU Symp 199, Eds A. Pramesh Rao, G. Swarup, Gopal-Krishna, Astronomical Society of the Pacific, California, p. 21

Harris D.E., 2005, in From Clark Lake to Long Wavelength Array: Bill Erickson's Radio Science, edss. N.E. Kassim, M.R. Pŕez, W. Junor, P.A. Henning, ASP Conf. Ser, 345, p. 254

Heavens A., 1989, in Radio Hotspots in Extragalactic Radio Sources, eds. K. Meisenheimer, H.-J. Röser (Heidelberg:Sringer-Verlag), 247

Ishwara-Chandra C.H., Saikia D.J., 1999, MNRAS, 309, 100

Jaffe W.J., Perola G.C., 1973, A&A, 26, 423

Jamrozy M., Machalski J., Mack K-.H., Klein U., 2005, A&A, 433, 467

Jeyakumar S., Saikia D.J., 2000, MNRAS, 311, 397

Jeyakumar S., Wiita P.J., Saikia D.J., Hooda J.S., 2005, A&A, 432, 823

Jones T.W., Ryu D., Engel A., 1999, ApJ, 512, 105

Kaiser C.R., 2000, A&A, 362, 447

Kaiser C.R., Alexander P., 1997, MNRAS, 286, 215

Kaiser C.R., Dennett-Thorpe J., Alexander P., 1997, MNRAS, 292, 723

Kardashev N.S., 1962, SvA, 6, 317

Katz-Stone D.M., Rudnick L., 1997, ApJ, 479, 258

Kirk J.G., Schneider P., 1987, ApJ, 315, 425

Klein U., Mack K.-H., Gregorini L., Parma P., 1995, A&A, 303, 427

Konar C., Saikia D.J., Ishwara-Chandra C.H., Kulkarni V.K., 2004, MNRAS, 355, 845

Konar C., Saikia D.J., Jamrozy M., Machalski J., 2006, MNRAS, 372, 693

Konar C., Jamrozy M., Saikia D.J., Machalski J., 2007, MNRAS, (submitted)

Laing R.A., Peacock J.A., 1980, MNRAS, 190, 903

Leahy J.P., Muxlow T.W.B., Stephens P.W., 1989, MNRAS, 239, 401

Liu R., Pooley G., Riley J.M., 1992, MNRAS, 257, 545

Machalski J., Chyży K.T., Jamrozy M., 2004, AcA, 54, 249

Machalski J., Jamrozy M., Zola S., Koziel D., 2006, A&A, 454, 85 (MJZK)

Mack K.-H., Klein U., O'Dea C.P., Willis A.G., Saripalli L., 1998, A&A, 329, 431

Meisenheimer K., Röser H.-J., Hiltner P., Yates M., Longair M., Chini R., Perley R., 1989, A&A, 219, 63

Miley G.K., 1980, ARA&A, 18, 185

Murgia M., 2003, PASA, 20, 19

Murgia M., 1996, Laurea Thesis, University of Bologna

Murgia M., Fanti C., Fanti R., et al., 1999, A&A, 345, 769

Myers S.T., Spangler S.R., 1985, ApJ, 291, 52

Pacholczyk A.G., 1970, *Radio Astrophysics* (ed.: Freeman, San Francisco)

Parma P., Murgia M., Morganti R., Capetti A., et al., 1999, A&A, 344, 7

Rudnick L., Katz-Stone D., Anderson M., 1994, ApJS, 90, 955

Schoenmakers A.P., Mack K.-H., de Bruyn A.G., et al., 2000, A&AS, 146, 293

Wiita P.J., Gopal-Krishna 1990, ApJ, 353, 476

CHAPTER 6

J0041+3224: a new double-double radio galaxy

6.1 Abstract

We report the discovery of a DDRG, J0041+3224, with the GMRT and subsequent high-frequency observations with the VLA. The inner and outer doubles are aligned within $\sim 4^{\circ}$ and are reasonably collinear with the parent optical galaxy. The outer double has a steeper radio spectrum compared with the inner one. Using an estimated redshift of 0.45, the projected linear sizes of the outer and inner doubles are 969 and 171 kpc respectively. The time scale of interruption of jet activity has been estimated to be $\sim$20 Myr, similar to other known DDRGs. We have compiled a sample of known DDRGs, and have re-examined the inverse correlation between the ratio of the luminosities of the outer to the inner double and the size of the inner double, l_{in}. Unlike the other DDRGs with $l_{in} \gtrsim 50$ kpc, the inner double of J0041+3224 is marginally more luminous than the outer one. The two DDRGs with $l_{in} \lesssim$few kpc have a more luminous inner double than the outer one, possibly due to a higher efficiency of conversion of beam energy as the jets propagate through the dense interstellar medium. We have examined the symmetry parameters and find that the inner doubles appear to be more asymmetric in both its armlength and flux density ratios compared with the outer doubles, although they appear marginally more collinear with the core than the outer double. We discuss briefly possible implications of these trends.

6.2 Introduction

Radio sources are sometimes seen to exhibit evidence of episodic jet activity, the most clear examples being the DDRGs which have an inner and an outer pair of radio lobes. There are only about a dozen or so of such objects known. To have a better understanding of the occurrence and time scales of episodic jet activity it is important to identify more examples of DDRGs as well as sources with multiple episodes of activity.

In this chapter we report the discovery of a new DDRG, J0041+3224, identified from observations made with the GMRT of candidate DDRGs from the B2 sample (Padrielli, Kapahi & Katgert-Merkelijn 1981; Saikia et al. 2002). Our candidates were identified by comparing the large- and smaller-scale images made either by us or those available in the literature. J0041+3224 was reported by Padrielli et al. (1981) to be double-lobed with an angular size of 32 arcsec. They identified the radio source to be associated with a galaxy with a visual magnitude of 20.0 and located at RA 00^h 41^m $46.^s11$, Dec: $+32^\circ$ $24'$ $53.''8$ in J2000 co-ordinates. There is no measured redshift of the galaxy. From the V magnitude−redshift diagram (Guiderdoni & Rocca-Volmerange 1987) we estimate the redshift to be ∼0.45 and use this value for this chapter.

6.3 Observations and analyses

The observations were made in the standard fashion, with each source observation interspersed with observations of the phase calibrator. The flux densities are on the Baars et al. (1977) scale.

The observations with the VLA were made in the snap-shot mode in the

Table 6.1: Observing log

Telescope	Array Conf.	Obs. Freq. MHz	Obs. Date
GMRT		617	2002 July 27
GMRT		1287	2002 June 21
VLA	C	1400	2002 November 28
VLA	C	4860	2002 November 28
VLA	C	8460	2002 November 28

L, C and X bands. The flux densities are again on the Baars et al. (1977) scale. All the data were calibrated and analysed in the standard way using the NRAO `AIPS` package.

The observing log for both the GMRT and the VLA observations are listed in Table 6.1 which is arranged as follows. Columns 1 and 2 show the name of the telescope, and the array configuration for the VLA observations; column 3 shows the frequency of the observations, while the dates of the observations are listed in column 4.

6.4 Observational results

All the images of the source are presented in Figs. 6.1, 6.2 and 6.4, while the observational parameters and some of the observed properties are presented in Table 6.2, which is arranged as follows. Column 1: frequency of observations in units of MHz, with the letter G or V representing either GMRT or VLA observations; columns 2−4: the major and minor axes of the restoring beam in arcsec and its position angle (PA) in degrees; column 5: the rms noise in units of mJy/beam; column 6: the integrated flux density of the source in mJy estimated by specifying an area around the sources; columns

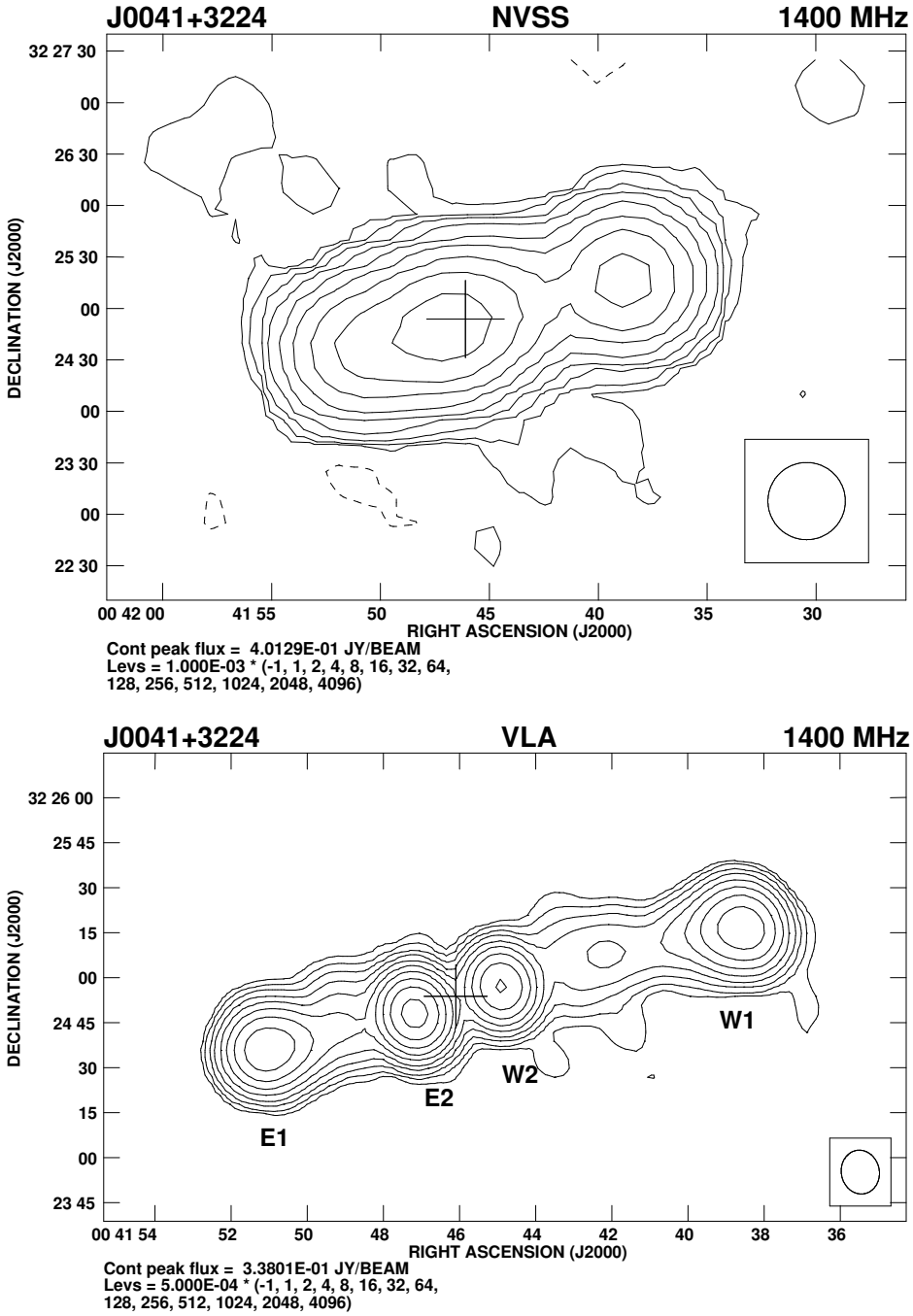

Figure 6.1: The NVSS image of J0041+3224 with an angular resolution of 45 arcsec (upper panel) and the VLA C-array image at 1400 MHz with an angular resolution of ∼13.6 arcsec. In all the images presented in this chapter the restoring beam is indicated by an ellipse, and the + sign indicates the position of the optical galaxy.

7, 10, 13 and 16: component designation where W1 and E1 indicate the western and eastern components of the outer double, W2 and E2 the western and eastern components of the inner double (Fig. 6.1, lower panel); columns 8 and 9, 11 and 12, 14 and 15, 17 and 18: the peak and total flux densities of the components in units of mJy/beam and mJy respectively. The flux densities have been estimated by specifying an area around each component.

The low-resolution NVSS image with an angular resolution of 45 arcsec (Fig. 6.1, upper panel) shows a more compact western component and a well-resolved eastern one. The VLA C-array image at 1400 MHz (Fig. 6.1, lower panel) with an angular resolution of ∼13.6 arcsec shows the source could be a DDRG with the eastern NVSS component being resolved into the inner double and the eastern component of the outer double. The optical galaxy lies between the components of the inner double-lobed source. The PAs of the outer and inner doubles are 104° and 108° respectively, showing the close alignment seen in a number of other DDRGs (cf. S2000).

In Fig. 6.2 we show the GMRT image at 617 MHz with an angular resolution of ∼5.6 arcsec and the VLA image at 4860 MHz with an angular resolution of ∼3.8 arcsec. These images show the lobes of the inner double to be well separated and lying on opposite sides of the parent optical galaxy. Weak tails of emission towards the optical galaxy are visible from both the components of the inner double in the VLA image. These tails merge to form a weak bridge of emission between the two components. The spectral index image between 617 and 4860 MHz obtained by smoothing the VLA image at 4860 MHz to that of the GMRT one is shown superimposed on the GMRT image, while the spectral index slices for the western and eastern lobes of the outer double are shown in Fig. 6.3. The spectral index image has been made for regions which are at least 5 times the rms value in both

Table 6.2: The observational parameters and observed properties of the sources

Freq.	Beam size			rms	S_I	Cp	S_p	S_t	Cp	S_p	S_t	Cp	S_p	S_t	Cp	S_p	S_t
MHz	$''$	$''$	$^\circ$	mJy /b	mJy		mJy /b	mJy		mJy /b	mJy		mJy /b	mJy		mJy /b	mJy
(1)	(2)	(3)	(4)	(5)	(6)	(7)	(8)	(9)	(10)	(11)	(12)	(13)	(14)	(15)	(16)	(17)	(18)
G617	6.5	4.8	165	0.49	2211	W1	98	542	W2	274	314	E2	567	691	E1	135	598
G1287	2.6	2.3	25	0.20	1104	W1	12	233	W2	92	145	E2	231	373	E1	13	227
V1400	45.0	45.0		0.51	967												
V1400	14.7	12.6	11	0.16	940	W1	108	207	W2	139	148	E2	338	377	E1	117	202
V4860	4.0	3.7	13	0.03	298	W1	7.4	50	W2	42	52	E2	126	154	E1	6.0	37
V8460	2.4	2.3	19	0.01	153	W1	1.4	12	W2	21	32	E2	75	100	E1	0.9	7.6

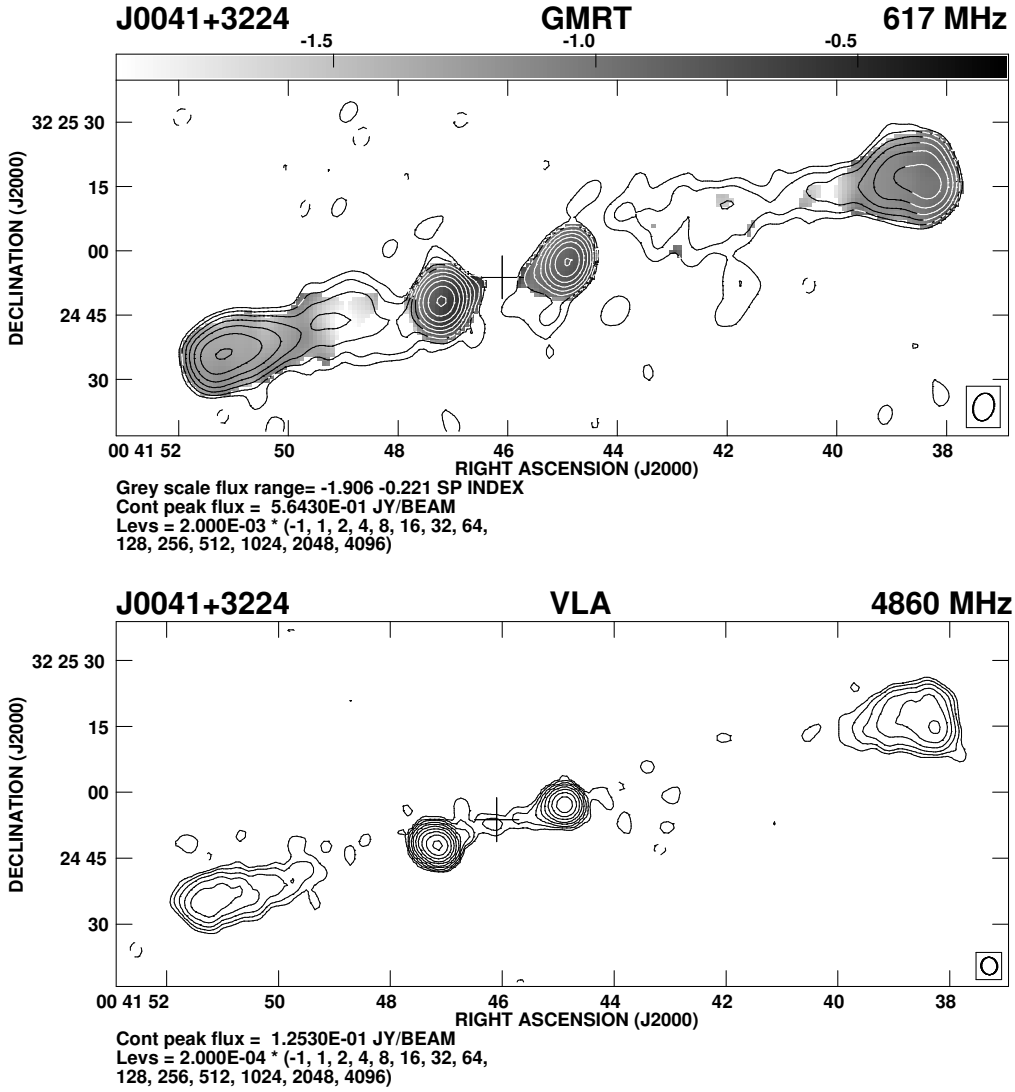

Figure 6.2: The GMRT image of J0041+3224 at 617 MHz with an angular resolution of ∼5.6 arcsec (upper panel) and the VLA C-array image at 4860 MHz with an angular resolution of ∼3.8 arcsec (lower panel). The spectral index image obtained by smoothing the 4860-MHz image to that of the 617-MHz one is shown superimposed on the 617-MHz image in grey scale.

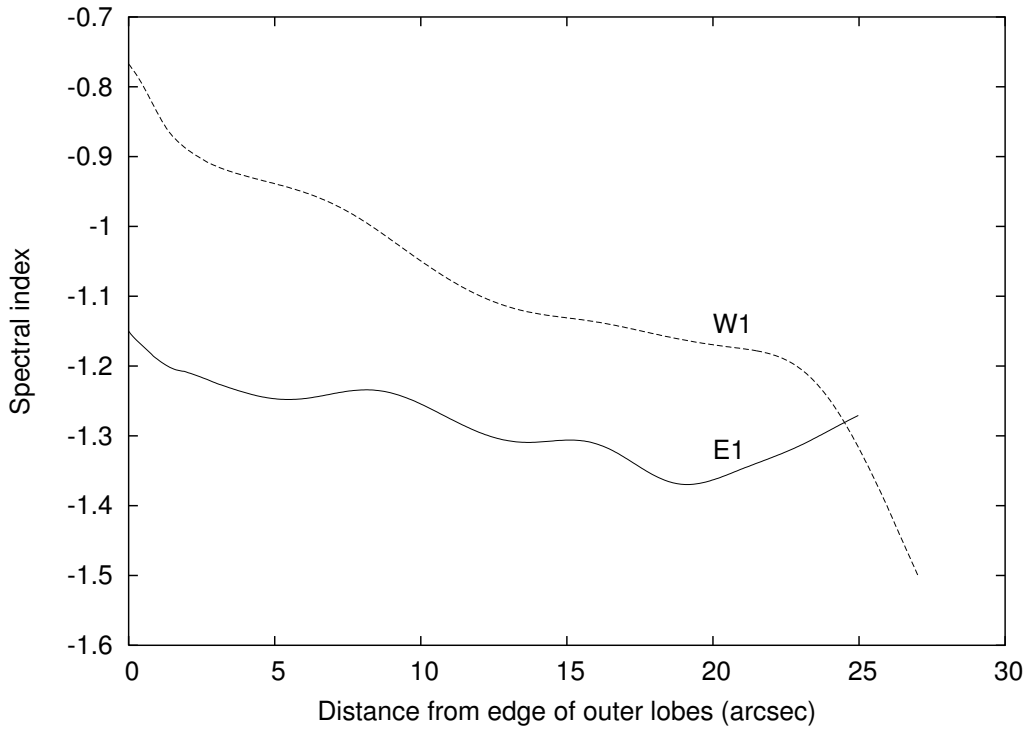

Figure 6.3: Slices of spectral index between 617 and 4860 MHz for the western and eastern components of the outer double.

images. The spectral index, α, defined as S$\propto \nu^{\alpha}$, varies from -0.8 to -1.5 in the western lobe, while for the eastern lobe it varies from -1.2 to -1.4. The typical error in the spectral index is $\sim$0.1 assuming an error of 5 per cent in the measured flux density. Using the formalism of Myers & Spangler (1985), the steepening in the western lobe (W1), which has an equipartition magnetic field (e.g. Miley 1980) of 0.75 nT, corresponds to a spectral age $\gtrsim 6\times10^6$ yr. The eastern component (E1) has a steeper spectrum but its spectral variation is small.

Our higher-resolution images with the GMRT at 1287 MHz and with the VLA at 8460 MHz with angular resolutions of $\sim$2.7 and 2.4 arcsec respectively are shown in Fig. 6.4. The inner components are resolved with angular sizes of 1.8×1.0 arcsec^2 along a PA of 105° for the western component and 2.8×0.8 arcsec^2 along a PA of 74° for the eastern one. These have been estimated

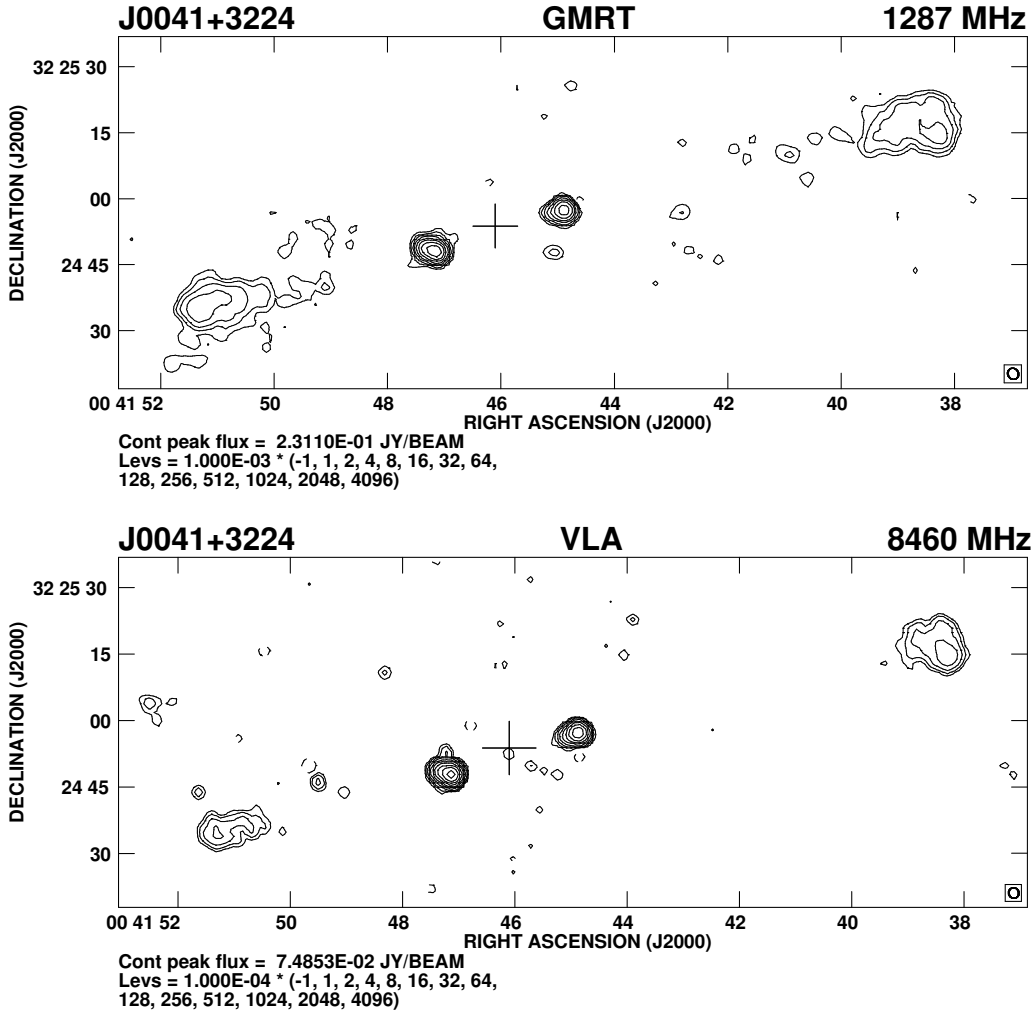

Figure 6.4: The GMRT image of J0041+3224 at 1287 MHz with an angular resolution of ∼2.7 arcsec (upper panel) and the VLA C-array image at 8460 MHz with an angular resolution of ∼2.4 arcsec (lower panel).

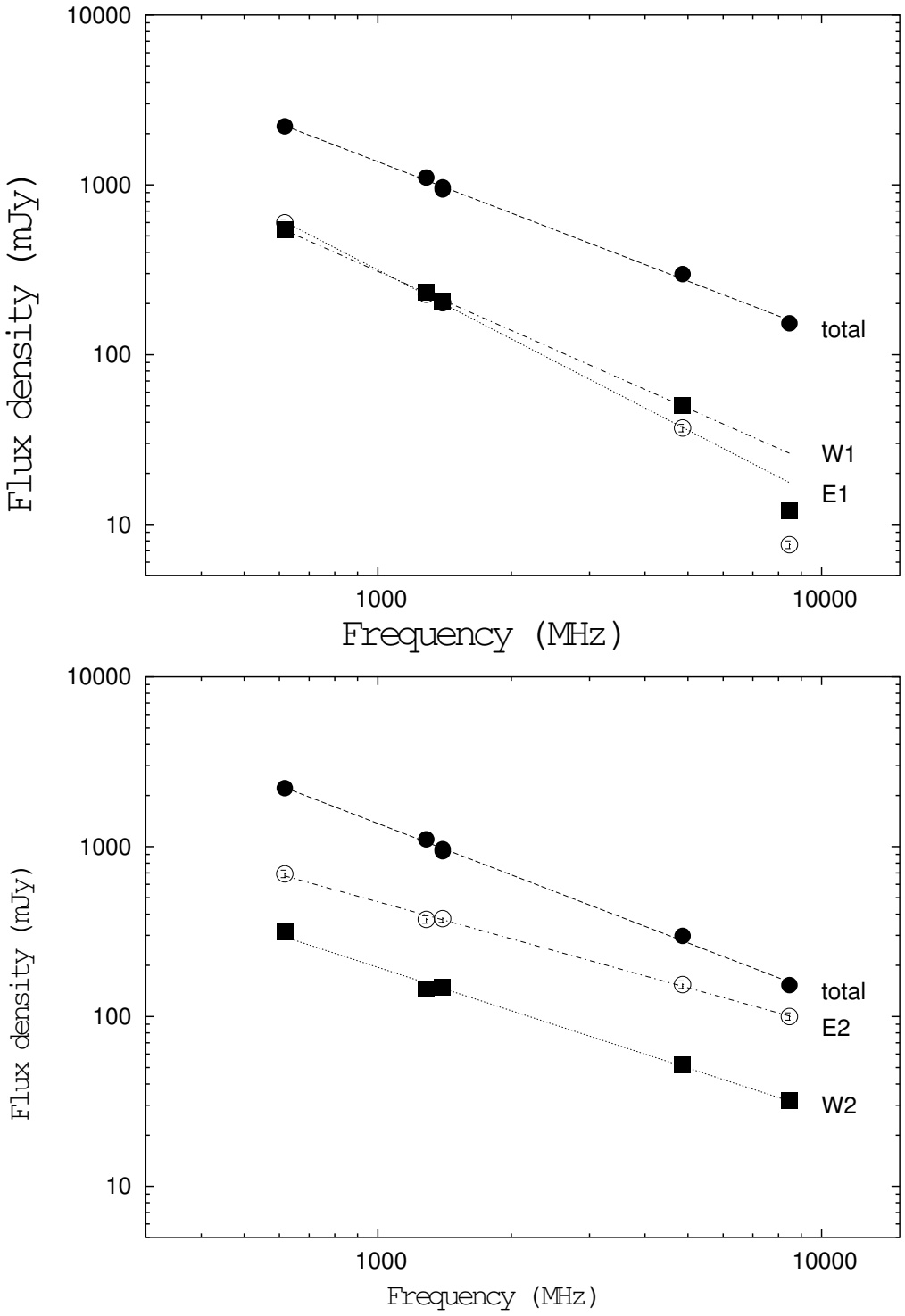

Figure 6.5: The spectra of the western and eastern components of the outer double (upper panel) and the inner double (lower panel). The integrated spectrum is shown in both the panels.

from the lower-frequency GMRT image. The values are similar using the VLA 8460-MHz image of similar resolution. The western component of the inner double is extended towards the direction of the optical object while the eastern component is extended at about 34° to the axis of the source. This is not surprising given the complexity of the structures of hotspots and emission in their vicinity (cf. Black et al. 1992; Leahy et al. 1997; Hardcastle et al. 1997).

There is a possible detection of a radio core in our data. The peak of emission in the weak bridge seen in VLA image at 4860 MHz, has a peak flux density of 0.57 mJy/beam and is within ∼1 arcsec of the optical position. If this is indeed the radio core, its flux density is likely to be lower since this value could be contaminated by emission from the bridge. The peak flux density near the optical position in the 8460-MHz image is 0.2 mJy/beam and is at the same location as the peak of emission in the 4860-MHz image. This feature could be the radio core, although it requires confirmation.

The integrated spectra of the entire source and of the individual components along with the linear least-square fits to the spectra using our measurements are shown in Fig. 6.5. The spectra of the components for the outer and inner doubles are shown in the upper and lower panels respectively, while the integrated spectrum is shown in both the panels. The spectral index of the entire source is -1.01 ± 0.02, while that of the western and eastern components of the outer double are -1.15 ± 0.01 and -1.35 ± 0.01 respectively. The corresponding values for the inner double are -0.85 ± 0.03 and -0.73 ± 0.02 respectively. For the outer double the fits have been made by excluding the flux densities at 8460 MHz. There is some evidence of spectral steepening above 4860 MHz, but we need to make lower resolution images at higher frequencies to estimate any missing flux density, and hence the degree of

spectral steepening.

6.5 Discussion and results

The images of J0041+3224 suggest that there have been two main episodes of activity, represented by the outer and inner double-lobed structures which are well aligned and roughly collinear with the parent optical galaxy. The lobes of the outer double are separated by 169 arcsec, corresponding to 969 kpc, while the inner double has a separation of 29.9 arcsec, corresponding to 171 kpc. The radio luminosities of the outer and inner doubles at an emitted frequency of 1.4 GHz are 3.3 and 3.6×10^{26} W Hz^{-1} respectively, both well above the FRI-FRII divide, and consistent with their observed structures.

The lobes of the outer double represent an earlier period of activity. These lobes have steeper spectral indices than the inner lobes (Fig. 6.5), possible evidence of spectral steepening and no prominent hotspots, while the inner lobes which represent ongoing activity are dominated by bright hotspots. The ratio of the average peak brightness of the inner double to the outer double in our VLA 8460-MHz images, which have angular resolutions of $\sim$2.4 arcsec, is $\gtrsim$40. The angular resolution in these images corresponds to a linear size of $\sim$14 kpc, which is within the range for sizes of hotspots for sources of similar linear size (cf. Leahy et al. 1997; Jeyakumar & Saikia 2000).

When the jet is interrupted and energy supply to the outer hotspots ceases, the channel will collapse due to the loss of pressure which is provided by the jet material (e.g. Kaiser & Alexander 1997). This implies that the restarted jet will have to drill out a new channel. However, unlike the earlier jet which propagates through the interstellar and intracluster or intergalactic medium, the restarted jet propagates into the relic synchrotron plasma

created by the earlier cycle of activity after ploughing its way through the interstellar medium of the host galaxy. The density of the synchrotron plasma is expected to be significantly smaller than the intergalactic medium (Clarke & Burns 1991; Cioffi & Blondin 1992; Loken et al. 1992), by up to a factor of 100, unless there is significant entrainment (Kaiser et al. 2000). Without entrainment, only weak shocks are expected as the jet propagates through the synchrotron plasma. In this case, the jets move ballistically without generating prominent hotspots and cocoons. This appears to be the case, for example, in J1548−3216 (Saripalli et al. 2003). In the case of J0041+3224, the detection of prominent hotspots in the inner lobes suggest the existence of significant thermal material, as has been suggested by Kaiser et al. (2000) to explain the formation of hotspots in their sample of DDRGs.

An estimate of the time scale of interruption and restarting of jet activity could provide insights in determining the cause of the interruption. A weak constraint on the upper limit to the time scale of interruption can be provided by the fact that the outer lobes are still visible. For a sample of 'relic' radio sources, Komissarov & Gubanov (1994) have estimated the time scales for the source to fade away to be a few times 10^7 yr, which is comparable to the kinematic age of the source itself. For example, for a velocity of advancement of $\sim$0.1c, the kinematic age of the outer double is $\sim 3.2\times10^7$ yr. One might expect the jets of the inner double to have higher velocities of advancement if it encounters only the low-density synchrotron plasma (e.g. Clarke & Burns 1991). However, the formation of strong hotspots suggests it is encountering a dense medium, possibly due to entrainment, and we assume the velocities to be similar. For a projected linear size of 171 kpc for the inner double, the age of the inner double is 5.6×10^6 yr. This leaves us with a time scale of $\sim$20 Myr between stopping and restarting of the jet.

(a) Luminosities of outer and inner doubles

The luminosities of the outer and inner doubles of J0041+3224 are comparable, the ratio, $P_{o:in}$, being ∼0.93 at an emitted frequency of 1400 MHz. This is unlike the sample of DDRGs compiled by S2000 where the outer lobes were always found to be more luminous than the inner ones. S2000 also noted that $P_{o:in}$ decreases with, l_{in}, the separation of the inner double. We have re-examined this relationship by enlarging the sample of DDRGs to include those which have been reported more recently, as well as those where the inner doubles are of subgalactic dimensions, as in J1006+3454 (3C236) and J1247+6723. Candidate DDRGs mentioned by S2000 such as 4C12.03, 3C16 (Leahy & Perley 1991) and 3C424 (Black et al. 1992) which require further observations to clarify their structures have not been presently included in the sample. The sample is listed in Table 6.3 and is arranged as follows. Column 1: source name; column 2: optical identification; column 3: redshift; columns 4 and 5: projected linear size of the inner and outer double-lobed source in kpc; columns 6: the locations of the components farther/closer from the core for the inner double. The symmetry parameters in columns 7 to 10 are all in the same sense as in column 6. Columns 7 and 8: the arm-length or separation ratio for the inner and outer doubles; columns 9 and 10: flux density ratios for the inner and outer doubles; columns 11 and 12: the misalignment angles, defined to be the supplement of the angle formed at the core by the hotspots or peaks of emission for the inner and outer lobes; columns 13 and 14: log of radio luminosity at an emitted frequency of 1.4 GHz for the inner and outer doubles; column 15: references for the radio structure.

In Fig. 6.6, we plot the ratio of the luminosities of the outer to the inner

Table 6.3: The sample of DDRGs

Source	Opt. Id.	Red-shift	l_{in} kpc	l_o kpc	Cmp.	$R_{\theta(in)}$	$R_{\theta(o)}$	$R_{s(in)}$	$R_{s(o)}$	Δ_{in} °	Δ_o °	P_{in} W/Hz	P_o W/Hz	Ref.
(1)	(2)	(3)	(4)	(5)	(6)	(7)	(8)	(9)	(10)	(11)	(12)	(13)	(14)	(15)
J0041+3224	G	0.45	171	969	W/E	1.17	1.49	0.39	1.02	0	3	26.55	26.52	1
J0116−4722	G	0.146	460	1447	N/S	1.06	1.42			4	20	25.14	26.16	2
J0921+4538	G	0.174	69	433	S/N	3.61	0.96	29.00	1.03	1	11	24.86	26.82	3,4,5
J0929+4146	G	0.365	652	1875	N/S	1.55	1.06	1.12	0.77	3	5	25.42	25.64	6
J1006+3454	G	0.101	1.7	4249	W/E	3.15	0.61	0.38	1.35	15	2	25.86	25.63	7,8,9
J1158+2621	G	0.112	138	483	N/S	1.23	0.99	1.74	1.13	0	1	25.31	25.48	10
J1242+3838	G	0.300	251	602	N/S	1.74	0.90	2.00	1.59	1	3	24.32	24.84	6
J1247+6723	G	0.107	0.014	1195								24.87	24.55	11,12
J1453+3308	G	0.249	159	1297	S/N	1.06	1.34	0.16	0.49	3	11	24.77	25.90	6
J1548−3216	G	0.108	313	961	S/N	1.24	1.07			4	4	24.34	25.69	13
J1835+6204	G	0.519	369	1379	N/S	1.03	1.02	0.89	1.89	1	0	26.27	26.81	6
J2223−0206	G	0.056	130	612	S/N	1.77	0.95	2.66	1.51	2	6	23.61	25.58	14,15

1: Saikia et al. 2006; 2: Saripalli, Subrahmanyan & Udaya Shankar 2002; 3: Perley et al. 1980; 4: Bridle, Perley & Henriksen 1986; 5: Clarke et al. 1992; 6: Schoenmakers et al. 2000; 7: Willis, Strom & Wilson 1974; 8: Strom & Willis 1980; 9: Schilizzi et al. 2001; 10: Owen & Ledlow 1997; 11: Marecki et al. 2003; 12: Bondi et al. 2004; 13: Saripalli, Subrahmanyan & Udaya Shankar 2003; 14: Kronberg, Wielebinski & Graham 1986; 15: Leahy et al. 1997.

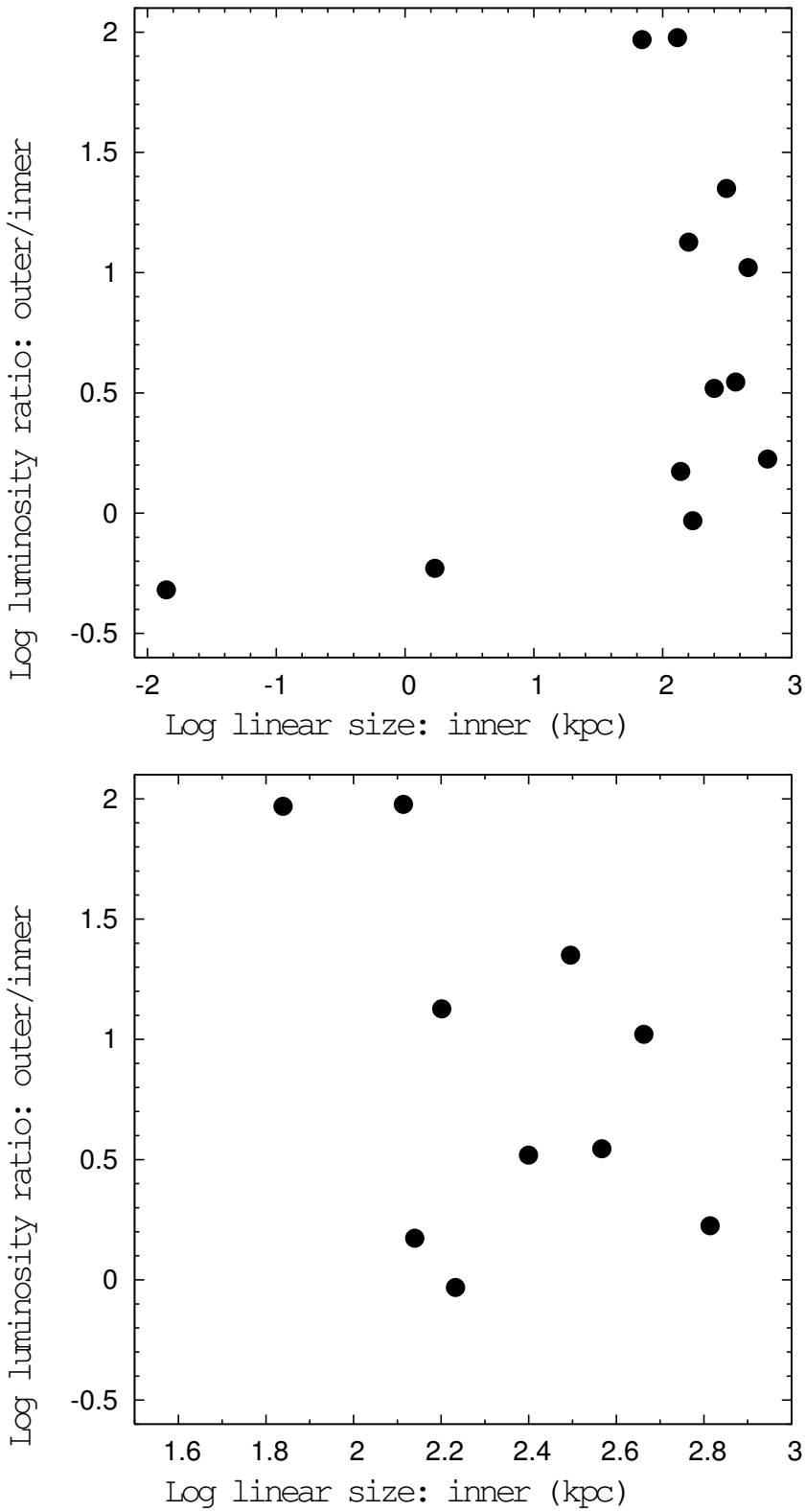

Figure 6.6: Luminosity ratio of the outer double to that of the inner double, $P_{o:in}$, at an emitted frequency of 1400 MHz is plotted against l_{in}, the projected linear size of the inner double (upper panel). The same plot for those with $l_{in} \gtrsim 50$ kpc is shown in the lower panel.

doubles against the separation of the inner double. Both the sources with $l_{in} \lesssim 1$ kpc have a more luminous inner double than the outer one, unlike all the sources in the sample of S2000 where $l_{in} \gtrsim 50$ kpc. For comparison with the plot by S2000 we have also plotted the sources with $l_{in} \gtrsim 50$ kpc separately. It is possible that in the early phase of the evolution of the inner double, where it is ploughing its way through the dense interstellar medium, conversion of beam energy into radio emission may be more efficient. This could lead to a ratio of the luminosities of the outer to the inner doubles being significantly less than unity. As the source expands and traverses through a more tenuous medium, the ratio could increase with size before approaching values of unity for large values of l_{in} (cf. S2000). We have re-examined the inverse correlation suggested by S2000 considering only those objects with $l_{in} \gtrsim 50$ kpc and find the correlation to have a Spearman rank correlation coefficient of -0.37, compared with a value of -0.57 for the objects in the sample of S2000.

(b) Symmetry parameters

A comparison of the symmetry parameters of the inner and outer doubles might provide insights into the environments in which the jets are propagating as well as any possible intrinsic asymmetries in the jets themselves. In the case of the restarted jets advancing into synchrotron relics from earlier epochs of activity, one might expect similar environments and hence more symmetric structures for the inner doubles.

In Fig. 6.7, we show the armlength and flux density ratios of the outer doubles plotted against the corresponding values for the inner doubles for the sample of DDRGs. The sense of direction of the components is described

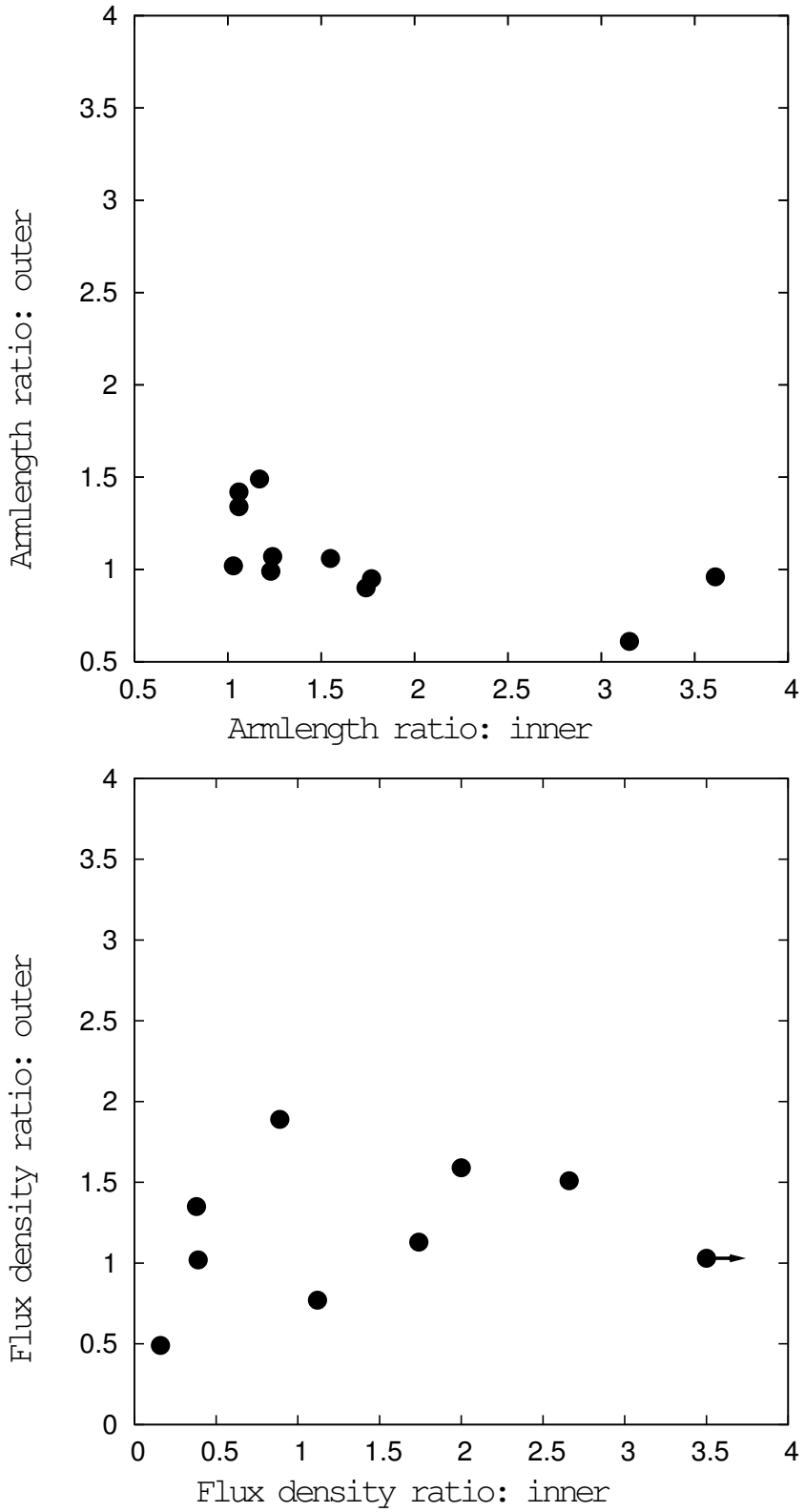

Figure 6.7: The armlength (upper panel) and flux density (lower panel) ratios of the inner doubles are plotted against the corresponding values for the outer doubles for the sample of DDRGs. The sense of direction of the components is described in Section 6.5 (a) and listed in Table 6.3.

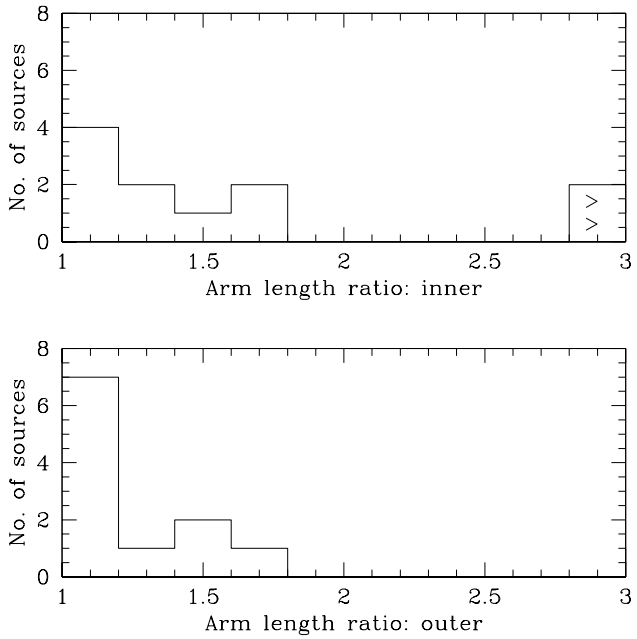

Figure 6.8: The distributions of the armlength ratios for the inner and outer doubles, defined to be ≥1. The > sign indicates a value larger than the range plotted in the histogram.

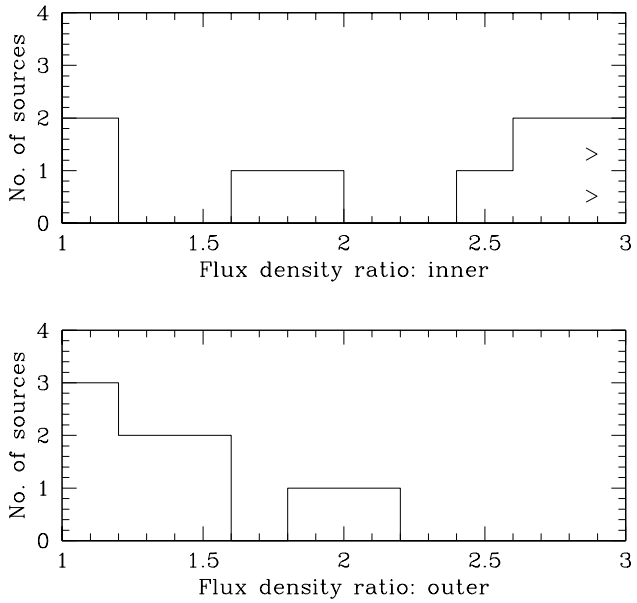

Figure 6.9: The distributions of the flux density ratios for the inner and outer doubles, defined to be ≥1. The > sign indicates a value larger than the range plotted in the histogram.

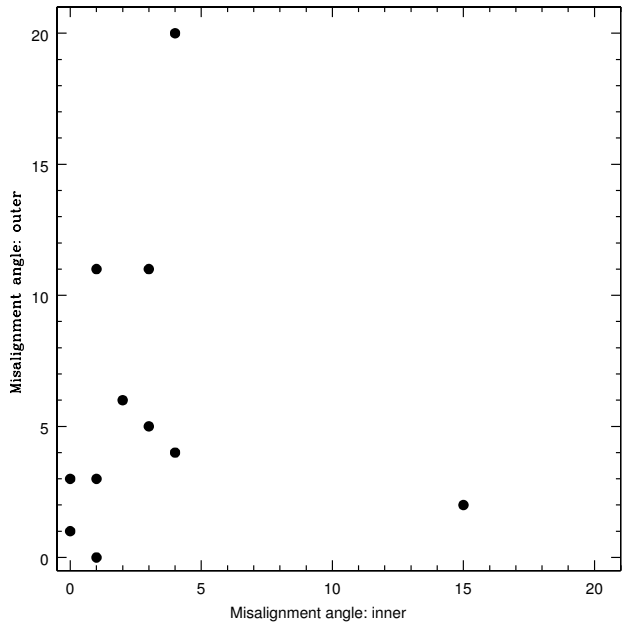

Figure 6.10: The misalignment angle of the outer double in degrees is plotted against the corresponding value for the inner double.

in Section 6.5 (a) and listed in Table 6.3. It appears that the inner doubles tend to be more asymmetric in both its armlength and flux density ratios compared with the outer doubles. The distributions for the armlength ratios, now defined to be always >1, show that the median values are ∼1.3 and 1.1 for the inner and outer doubles respectively (Fig. 6.8). A Kolmogorov–Smirnov test shows the distributions to be different at a significance level of 0.30. A similar trend is also seen in the distributions of the flux density ratios, again defined to be always >1, for the inner and outer lobes. The median values are ∼2.5 and 1.4 respectively (Fig. 6.9), and the two distributions are different at a significance level of 0.10. It is also worth noting (see Table 6.3) that the asymmetries in the inner and outer doubles are not in the same sense. Although these trends need to be confirmed with larger samples, they are possibly a reflection of different environments, possibly due to different degrees of entrainment in the cocoons on opposite sides coupled with effects

of relativistic beaming and any intrinsic jet asymmetries. For example, in the case of J0921+4538, the armlength ratio of 3.61 for the inner double can be understood in the relativistic beaming framework if the velocity is $\sim$0.8c for an inclination angle of 45°, the dividing line between radio galaxies and quasars in the unified scheme (Barthel 1989). This is also in reasonable agreement with the flux density ratio of 29. However, in the case of the inner double of J1006+3454, where the armlength ratio is 3.15, the flux density ratio is 0.38, suggesting intrinsic asymmetries.

The median values of the misalignment angle of the inner and outer doubles are $\sim$2 and 4° respectively (Fig. 6.10). A Kolmogorov–Smirnov test shows the distributions to be different at a significance level of 0.3. This could arise due to the lobes of the outer double responding to either large-scale density gradients or motion of the parent optical galaxy during the two cycles of jet activity.

6.6 Concluding remarks

We have reported the discovery of a new double-double radio galaxy, J0041+3224, with the GMRT and subsequent observations with the VLA. Using an estimated redshift of 0.45, the projected linear size of the outer double is 969 kpc. Large linear sizes are characteristic of most of the known DDRGs. The lobes of the outer double have steeper spectral indices compared with those of the inner double. The kinematic age of the outer double is $\sim 3\times10^7$ yr, while the time scale of interruption of jet activity is $\sim$20 Myr. Unlike most DDRGs with $l_{in}\gtrsim$50 kpc, the inner double of J0041+3224 is marginally more luminous than the outer one. S2000 reported an inverse correlation between the ratio of the luminosities of the outer and inner doubles, $P_{o:in}$, and l_{in}.

For their sample of DDRGs the luminosity ratio, $P_{o:in}$, is as high as $\sim$100 for $l_{in}\sim$50 kpc and approaches unity when l_{in} approaches values close to a Mpc, the ratio being always >1. Considering the more compact inner doubles with $l_{in} \lesssim$ few kpc, namely J1006+3454 (3C236) and J1247+6723, the inner doubles are significantly more luminous than the outer ones. This suggests that in the early phase of the evolution of the inner double, where it is ploughing its way through the dense interstellar medium, conversion of beam energy into radio emission may be more efficient. In this case, the ratio of the luminosity of the outer to the inner double could increase with size before decreasing and approaching a value of about unity when l_{in} approaches $\sim$1 Mpc. We have re-examined the inverse correlation for sources with $l_{in}\gtrsim$50 kpc with the addition of a few more sources and find the correlation to have a rank correlation co-efficient of -0.37, compared with a value of -0.57 for the objects in the sample of S2000.

We have compared the symmetry parameters of the inner and outer doubles and find that the inner doubles appear to be more asymmetric in both their armlength and flux density ratios compared with the outer doubles. Also, the asymmetries in the inner and outer doubles are not in the same sense. Although these trends need to be confirmed with larger samples, they are possibly a reflection of different environments due to different degrees of entrainment in the cocoons on opposite sides, coupled with any intrinsic jet asymmetries and effects of relativistic motion. However, the inner doubles appear marginally more collinear with the radio core than the outer doubles. This could arise due to the lobes of the outer double responding to large-scale density gradients, or motion of the parent optical galaxy during the two cycles of nuclear activity.

References

Baars J.W.M., Genzel R., Pauliny-Toth I.I.K., Witzel A. 1977, A&A, 61, 99

Barthel P.D., 1989, ApJ, 336, 606

Black A.R.S., Baum S.A., Leahy J.P., Perley R.A., Riley J.M., Scheuer P.A.G., 1992, MNRAS, 256, 186

Bondi M., Marchã, M.J.M., Polatidis A., Dallacasa D., Stanghellini C., Antón S., 2004, MNRAS, 352, 112

Bridle A.H., Perley R.A., Henriksen R.N., 1986, AJ, 92, 534

Cioffi D.F., Blondin J.M., 1992, ApJ, 392, 458

Clarke D.A., Burns J.O., 1991, ApJ, 369, 308

Clarke D.A., Bridle A.H., Burns J.O., Perley R.A., Norman M.L., 1992, ApJ, 385, 173

Clarke D.A., Burns J.O., Norman M.L., 1992, ApJ, 395, 444

Guiderdoni B., Rocca-Volmerange B., 1987, A&A, 186, 1

Hardcastle M.J., Alexander P., Pooley G.G., Riley J.M., 1997, MNRAS, 288, 859

Jeyakumar S., Saikia D.J., 2000, MNRAS, 311, 397

Kaiser C.R., Alexander P., 1997, MNRAS, 286, 215

Kaiser C.R., Schoenmakers A.P., Röttgering H.J.A., 2000, MNRAS, 315, 381

Komissarov S.S., Gubanov A.G., 1994, A&A, 285, 27

Kronberg P.P., Wielebinski R., Graham D.A. 1986, A&A, 169, 63

Leahy J.P., Perley R.A., 1991, AJ, 102, 537

Leahy J.P., Black A.R.S., Dennett-Thorpe J., Hardcastle M.J., Komissarov S., Perley R.A., Riley J.M., Scheuer P.A.G., 1997, MNRAS, 291, 20

Loken C., Burns J.O., Clarke D.A., Norman M.L., 1992, ApJ, 392, 54

Marecki A., Barthel P.D., Polatidis A., Owsianik I., 2003, PASA, 20, 16

Miley G. K., 1980, ARA&A, 18, 165

Myers S. T., Spangler S. R., 1985, ApJ, 291, 52

Owen F.N., Ledlow M.J., 1997, ApJS, 108, 41

Padrielli L., Kapahi V.K., Katgert-Merkelijn J.K., 1981, A&AS, 46, 473

Perley R.A., Bridle A.H., Willis A.G., Fomalont E.B., 1980, AJ, 85, 499

Saikia D.J., Konar C., Kulkarni V.K., 2006, MNRAS, 366, 1391

Saikia D.J., Thomasson P., Spencer R.E., Mantovani F., Salter C.J., Jeyakumar S., 2002, A&A, 391, 149

Saripalli L., Subrahmanyan R., Udaya Shankar N., 2002, ApJ, 565, 256

Saripalli L., Subrahmanyan R., Udaya Shankar N., 2003, ApJ, 590, 181

Schilizzi R.T. et al., 2001, A&A, 368, 398

Schoenmakers A.P., de Bruyn A.G., Röttgering H.J.A., van der Laan H., Kaiser C.R., 2000, MNRAS, 315, 371

Strom R.G., Willis A.G., 1980, A&A, 85, 36

Willis A.G., Strom R.G., Wilson A.S., 1974, Nature, 250, 625

CHAPTER 7

Spectral ageing analysis of the double-double radio galaxy J1453+3308

7.1 Abstract

We present new radio observations at frequencies ranging from 240 to 4860 MHz of the well-known DDRG, J1453+3308, using both the GMRT and the VLA. These observations enable us to determine the spectra of the inner and outer lobes over a large frequency range and demonstrate that while the spectrum of the outer lobes exhibits significant curvature, that of the inner lobes appears practically straight. The break frequency, and hence the inferred synchrotron age of the outer structure, determined from 16−arcsec strips transverse to the source axis, increases with distance from the heads of the lobes. The maximum spectral ages for the northern and southern lobes are ∼47 and 58 Myr respectively. Because of the difference in the lengths of the lobes these ages imply a mean separation velocity of the heads of the lobes from the emitting plasma of 0.036c for both the northern and southern lobes. The synchrotron age of the inner double is about 2 Myr which implies an advance velocity of ∼0.1c, but these values have large uncertainties because the spectrum is practically straight.

7.2 Introduction

It is evident from the morphology that the outer double of a DDRG is due to the previous cycle of jet activity, while the inner double is due to the current activity of the central engine of the host galaxy. To know the evolutionary history of the inner and the outer doubles, and estimate the time scales and duty cycles of such activity, we need to estimate their ages. Spectral ageing analysis provides an important input towards estimating these time scales.

In this chapter we investigate the radiative ages of particles emitting in different parts of the old cocoon (outer structure) of J1453+3308, as well as in the inner lobes of this DDRG, and compare these with the dynamical ages. The already available data indicate that the lobes of the outer double are separated by 336 arcsec corresponding to 1297 kpc, while the inner double has a separation of 41 arcsec corresponding to 159 kpc. The 1.4-GHz radio luminosities of the outer and inner doubles are 7.94×10^{25} W Hz^{-1} and 5.88×10^{24} W Hz^{-1} respectively. The luminosity of the outer double is above the FRI/FRII break, while that of the inner double is below it although it has an edge-brightened structure.

To achieve the above objectives we made new radio maps of J1453+3308 at a number of frequencies over a large range from 240 to 4860 MHz. These observations have been made with an angular resolution high enough to image the lobes with at least 6 resolution elements along their axes. The new observations and data reduction are described in Section 7.3. The observational results, such as the radio maps showing the source structure, spectra and polarisation parameters are presented in Section 7.4. The standard spectral-ageing analysis for the outer and inner structures is described and the results presented in Section 7.5, while the concluding remarks are given in Section

7.6.

7.3 Observations and data reduction

The analysis presented in this chapter is based on radio observations recently conducted with the GMRT and the VLA, as well as on VLA archival data. The observing log for both the GMRT and VLA observations is listed in Table 7.1, which is arranged as follows. Columns 1 and 2 show the name of the telescope, and the array configuration for the VLA observations; column 3 shows the frequency of observations in MHz; column 4: dates of the observations. The phase centre for all the observations was near the core of the radio galaxy.

(a) GMRT observations

The observations were made in the standard manner, with each observation of the target-source interspersed with observations of 3C286 which was used as a phase calibrator as well as flux density and bandpass calibrator. At each frequency the source was observed in a full-synthesis run of approximately 9 hours including calibration overheads. The rms noise in the resulting images range from about 1 mJy beam^{-1} at 240 MHz to about 0.06 mJy beam^{-1} at 1287 MHz. The data collected were calibrated and reduced in the standard way using the NRAO `AIPS` software package. The flux densities at the different frequencies are based on the scale of Baars et al. (1977).

(b) New and archival VLA observations

The source was observed with the CnD array at a frequency of 4860 MHz to image the outer lobes and determine their spectra by comparing with the

Table 7.1: Observing log.

Telescope	Array Conf.	Obs. Freq. MHz	Obs. Date
GMRT		240	2005 March 17
GMRT		334	2004 December 25
GMRT		605	2005 March 17
GMRT		1287	2005 December 22
VLA[a]	A	1365	2000 October 21
VLA[a]	A	4860	2000 October 22
VLA[a]	B	4860	2001 April 02
VLA[a]	AB	4860	1998 July 29
VLA	CnD	4860	2005 October 31
VLA[a]	A	8460	2000 October 22
VLA[a]	B	8460	2001 April 02

[a] VLA archival data.

low-frequency GMRT images. The integration time was about 6×20 min, which allowed us to reach an rms noise value of about 0.05 mJy beam^{-1}. The interferometric phases were calibrated every 20 min with the phase calibrator J1416+347. The source 3C286 was used as the primary flux density and polarisation calibrator. For the image produced from this data set correction for the primary beam pattern has been done.

As in the case of the GMRT data, the VLA data were edited and reduced using the `AIPS` package. The polarisation data reduction was done and the maps of the Stokes parameters I, Q and U were obtained using the procedures applied in the analysis of polarisation properties in a larger set of giant radio galaxies (Machalski et al. 2006).

To study the inner double-lobed structure of J1453+3308, derive its spectrum and estimate the radiative age, as well as to compare the resulting age with that of the outer lobes of the giant-sized structure, we supplemented our GMRT observations with VLA archival data. These observations which were made in the snap-shot mode in the L (1365 MHz), C (4860 MHz) and

X (8460 MHz) bands, also enabled us to study the spectrum and variability of the radio core. All flux densities are on the Baars et al. (1977) scale.

7.4 Observational results

(a) Structure

The images of the entire source using the GMRT and the VLA are presented in Figs. 7.1 and 7.2, while the observational parameters and some of the observed properties are presented in Table 7.2 which is arranged as follows. Column 1: frequency of observations in MHz, with the letter G or V representing either GMRT or VLA observations; columns 2−4: the major and minor axes of the restoring beam in arcsec and its position angle (PA) in degrees; column 5: the rms noise in mJy beam^{-1}; column 6: the integrated flux density of the source in mJy estimated by specifying an area around the source; columns 7, 10, 13 and 16: component designation where N1 and S1 indicate the northern and southern components of the outer double, N2 and S2 the northern and southern components of the inner double; columns 8 and 9, 11 and 12, 14 and 15, 17 and 18: the peak and total flux densities of the components in mJy beam^{-1} and mJy respectively. The flux densities have been estimated by specifying an area around each component. The error in the flux density is approximately 15 per cent at 240 MHz and 7 per cent at the higher frequencies. The integrated flux densities are plotted in Fig. 7.3.

All the images of the source show the well-known pair of doubles which are misaligned by $\sim$7.5°. The total luminosity of the outer double is in the FRII category although it has no prominent hotspot. On the other hand, the total luminosity of the inner double is in the FRI class although it has an

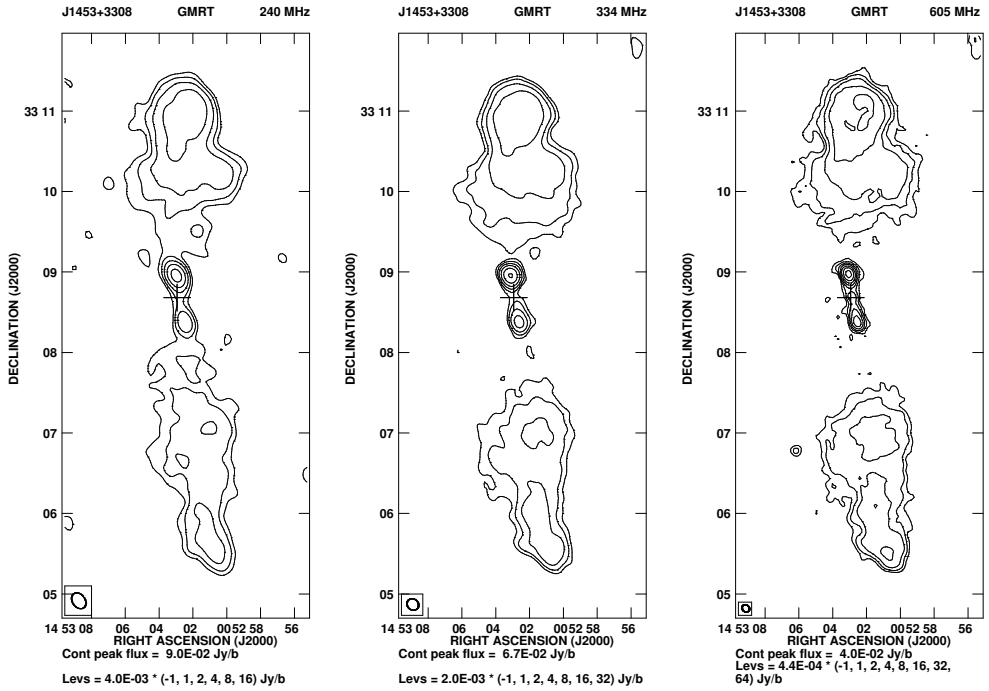

Figure 7.1: GMRT images of J1453+3308. Left panel: GMRT image at 240 MHz; middle panel: GMRT image at 334-MHz; right panel: GMRT image at 605 MHz. In all the images presented in this chapter the restoring beam is indicated by an ellipse, and the + sign indicates the position of the optical galaxy. The peak brightness and contour levels are given below each image.

edge-brightened structure characteristic of FRII sources. Such sources could provide useful insights towards understanding the FRI-FRII dichotomy and it would be useful to enquire whether the observed properties of the inner double might be due to evolutionary effects such as the emissivity increasing with time or due to differences in the environment or the central engine.

The high-resolution GMRT L-band image shows the radio core in addition to the lobes of radio emission. The structure of the inner double is better seen in the VLA A-array image at 1365 MHz and the B-array image at 4860 MHz, made from the archival data (Fig. 7.4).

The ratio of the separations of the southern lobe from the core to that of the northern one is 1.34 and 1.06 for the outer and inner doubles, respectively.

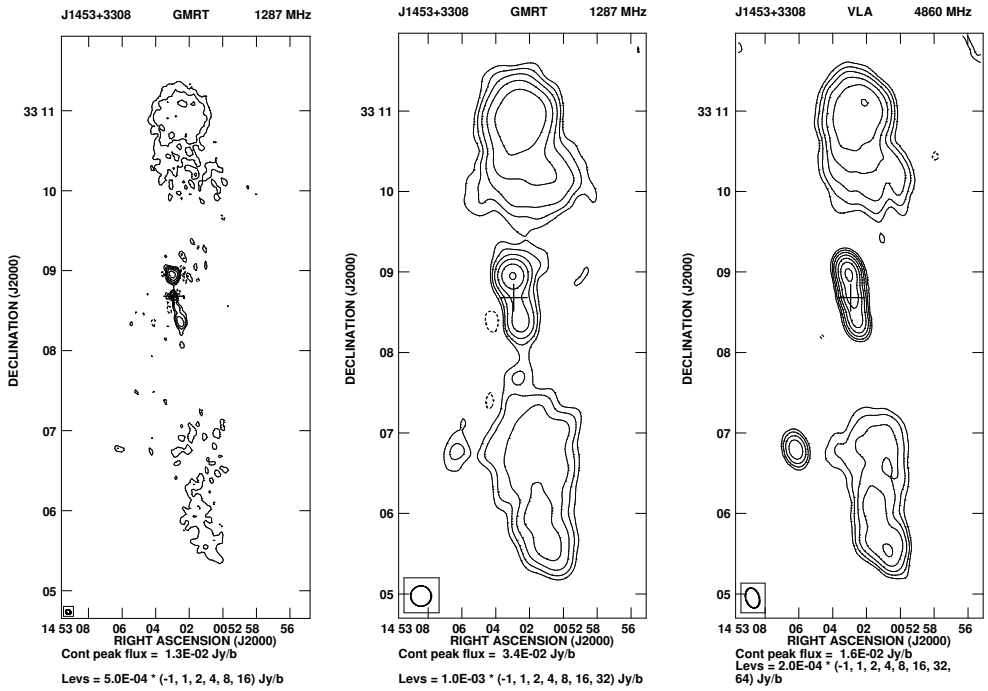

Figure 7.2: Left and middle panels: GMRT image of J1453+3308 at 1287 MHz with the full resolution (cf. Table 7.2) and smoothed to a resolution of 15.2×15.2 arcsec^2 respectively. Right panel: VLA image at 4860 MHz. A weak (∼2.5 mJy) unresolved source at R.A.: 14 53 06.20 and Dec: +33 06 47.8 is unrelated to J1453+3308

The outer double being more asymmetric is possibly due to asymmetries in the external environment on the scale of the outer double. The flux densities of the lobes are higher on the northern side, the ratio of the flux density of the southern component to that of the northern one for the outer and inner doubles are 0.57±0.06 and 0.44±0.05 respectively. This suggests an intrinsic asymmetry on scales ranging from the inner double to that of the outer one.

(b) Spectra

The integrated flux densities of the total source, as well as of the inner and outer doubles, are given in Table 7.3. All columns are self explanatory, with 'outer' and 'inner' denoting the outer lobes and the inner double. All the

Table 7.2: The observational parameters and flux densities of the outer (N1 and S1) and inner (N2 and S2) lobes of J1453+3308

Freq.	Beam size			rms	S_I	Cp	S_p	S_t	Cp	S_p	S_t	Cp	S_p	S_t	Cp	S_p	S_t
MHz	$''$	$''$	$^\circ$	mJy /b	mJy		mJy /b	mJy		mJy /b	mJy		mJy /b	mJy		mJy /b	mJy
(1)	(2)	(3)	(4)	(5)	(6)	(7)	(8)	(9)	(10)	(11)	(12)	(13)	(14)	(15)	(16)	(17)	(18)
G240	12.8	9.4	35	1.07	1843	N1	53	1055	N2	92	123	S2	31	48	S1	22	602
G334	9.2	8.1	48	0.52	1599	N1	29	902	N2	66	96	S2	23	47	S1	14	563
G605	6.0	5.0	43	0.11	1078	N1	8.3	606	N2	42	69	S2	13	29	S1	4.2	370
G1287	3.8	3.1	47	0.06	504	N1	2.4	272	N2	13	37	S2	3.8	17	S1	1.2	164
V1400	45.0	45.0		0.45	460	N1	121	258							S1	46	145
V4860	15.2	10.0	17	0.05	136	N1	6.5	71	N2+S2	16	32				S1	3.6	32
V1365	1.5	1.3	9	0.02					N2	6.1	38	S2	2.3	14			
V4860	1.3	1.2	44	0.02					N2	2.2	16	S2	0.8	4.9			
V8460	0.7	0.7	9	0.01					N2	0.5	9.5	S2	0.2	2.6			

Table 7.3: Flux densities of the total source, and its inner and outer lobes used for fitting a spectral shape.

Freqency	Component	S_t	Error	Component	S_t	Error	Component	S_t	Error	Reference
MHz		mJy	mJy		mJy	mJy		mJy	mJy	
(1)	(2)	(3)	(4)	(5)	(6)	(7)	(8)	(9)	(10)	(11)
74	total	2530	320							VLSS
151	total	2387	135				outer	2165	110	1
178	total	2220	220				outer	2020	200	2
240	total	1843	260	inner	176	25	outer	1667	250	3
325	total	1510	150				outer	1365	140	4
334	total	1599	113	inner	143	10	outer	1456	112	3
408	total	1330	125							5
605	total	1078	76	inner	108	8	outer	970	75	3
1287	total	504	36	inner	62	9	outer	442	34	3
1400	total	460	33				outer	426	26	4,6
4860	total	136	10	inner	32	3	outer	104	8	3
4800	total	121	18							4
10500	total	70	3	inner	20	4				4

References: VLSS: VLA Low-frequency Sky Survey; 1: Riley et al. (1999); 2: Pilkington & Scott (1965); 3: Konar et al. (2006); 4: Schoenmakers et al. (2000b) 5: Colla et al. (1970); 6: Schoenmakers et al. (2000a).

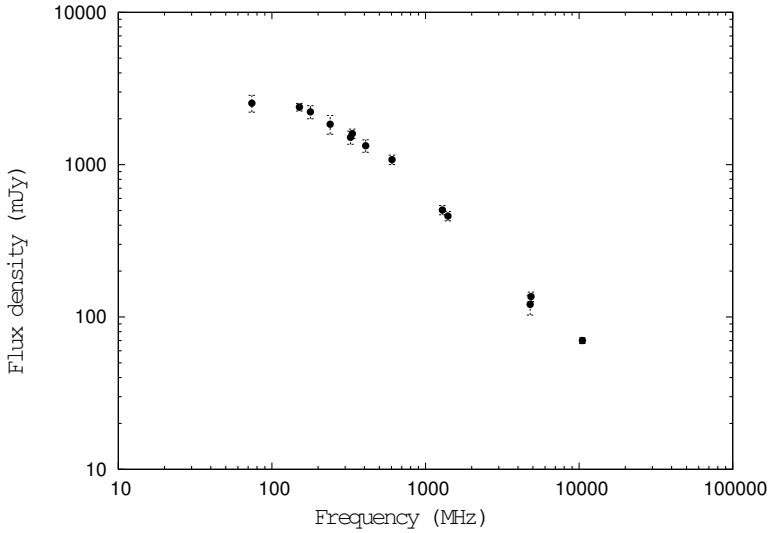

Figure 7.3: The integrated spectrum of J1453+3308.

flux densities quoted here are consistent with the scale of Baars et al. (1977). The flux densities of the outer lobes at 151, 178 and 325 MHz (column 9) are derived subtracting flux densities expected for the inner lobes at these frequencies from the total flux densities given in column 3. The former ones are simply determined fitting the form $\log S_\nu$=a + b$\log\nu$ + c$\exp(-\log\nu)$ to the measured flux density values in column 6.

The integrated spectrum is presented in Fig. 7.3. Clearly there is a distinct steepening in the integrated spectrum at ∼300 MHz. Our low-frequency measurements show a significant flattening of the spectrum below ∼300 MHz, consistent with the VLA Low-frequency Sky Survey (VLSS; `http://lwa.nrl.navy.mil/VLSS`) flux density. Since the low-frequency flattening is unlikely to be due to either synchrotron self-absorption or thermal absorption, the change in curvature must be due to spectral ageing with the low-frequency spectrum probably representing the injection spectrum of the relativistic particles. Further analysis of this aspect is described in Section 7.6.

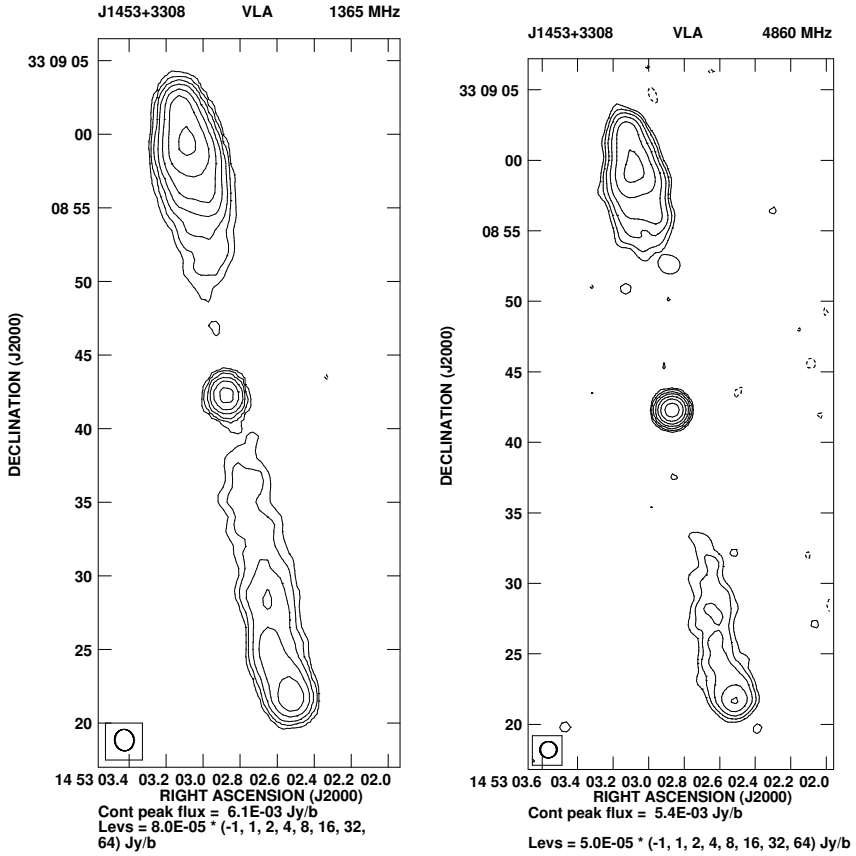

Figure 7.4: Images of the inner structure of J1453+3308 at 1365 MHz (left panel) and 4860 MHz (right panel) made from archival VLA data.

Table 7.4: Flux densities of the radio core

Telescope	Date of obs.	Freq. MHz	Flux density mJy
GMRT	2005 March 17	605	3.1
VLA-A	2000 October 21	1365	4.1
VLA-B	2001 April 02	4860	5.5
VLA-A	2000 October 22	4860	5.5
VLA-AB	1998 July 29	4860	4.6
VLA-B	2001 April 02	8460	6.2
VLA-A	2000 October 22	8460	3.6

The core flux density at 605 MHz is the peak value, due to contamination by the extended flux density, while for the others these are integrated values. The values have been estimated from two-dimensional Gaussian fits.

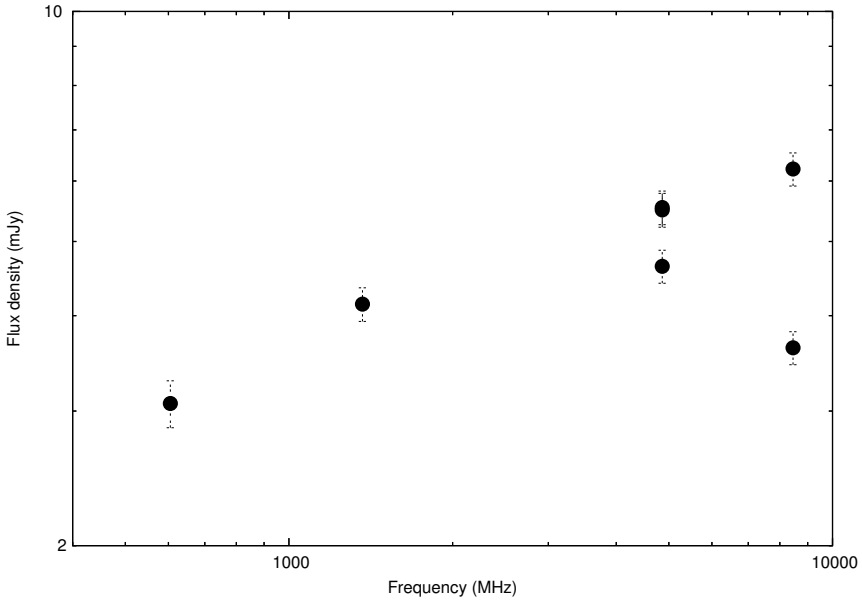

Figure 7.5: Spectrum of the core of J1453+3308.

(c) The radio core

The J2000.0 position of the radio core estimated from our high-resolution images is RA: $14^h\ 53^m\ 02.^s87$ and Dec: $33^\circ\ 08'\ 42.''3$, which is ∼2 arcsec away from the position of the optical galaxy (RA: $14^h\ 53^m\ 02.^s93$ and Dec: $33^\circ\ 08'\ 40.''8$) listed by Schoenmakers (1999). The radio core has a mildly inverted spectrum (Fig. 7.5) with only marginal evidence of variability at 4860 MHz but significant variability at 8460 MHz over a similar time scale.

(d) Polarisation properties

As in Machalski et al. (2006) the preliminary polarisation properties of J1453+3308 are derived using the NVSS data (Condon et al. 1998) and our VLA CnD-array 4860 MHz measurements. The E-vectors superimposed on the total-intensity as well as polarised-intensity images at 1400 and 4860 MHz are shown in Fig. 7.6. The lobes of the source show significant polarisation. The mean values of scalar polarisation at 4860 MHz for the northern and

southern lobes of the outer double are ∼8 and 20 per cent respectively. These values are determined after clipping the images at 4 times the rms noise and convolving the image with the NVSS beam of 45×45 arcsec^2. The average value for the inner double is ∼5 per cent. The average scalar polarisation at 1400 MHz for the northern and southern lobes of the outer double are ∼9 and 16 per cent respectively, while the corresponding value for the inner double is ∼5 per cent. The northern component of the outer double shows no evidence of depolarisation while the southern lobe is depolarised by ∼20 per cent. The inner double shows no significant evidence of depolarisation.

The rotation measure (RM) image of the source, obtained from the 1400-MHz and 4860-MHz maps by considering only those points which are 4 times above the rms noise, yields RM values within ∼25 rad m^{-2} (Fig. 7.7). Most regions of the source have an RM of only a few rad m^{-2}, the average value for the source being ∼6 rad m^{-2}. Although from two-frequency measurements it is not possible to resolve any nπ ambiguities in the PA of the E-vectors, the low value of RM is consistent with known values for large radio sources (e.g. Saikia & Salter 1988 for a review). The Galactic longitude and latitude of the source are 53.°3 and 63.°1 respectively. Considering the high Galactic latitude of the source, its RM is similar to other known sources in this direction suggesting that intrinsic contribution to the RM is likely to be less than 20 rad m^{-2}. However these results are preliminary; the RM distribution and the inferred magnetic field need to be determined from more detailed multi-frequency observations.

The inferred magnetic field vectors obtained at present by merely rotating the E-vectors at 4860 MHz by 90° shows that the field lines in the relaxed outer northern lobe are nearly circumferential in the outer periphery. The field lines are roughly along the axis of the lobes for both the outer and inner

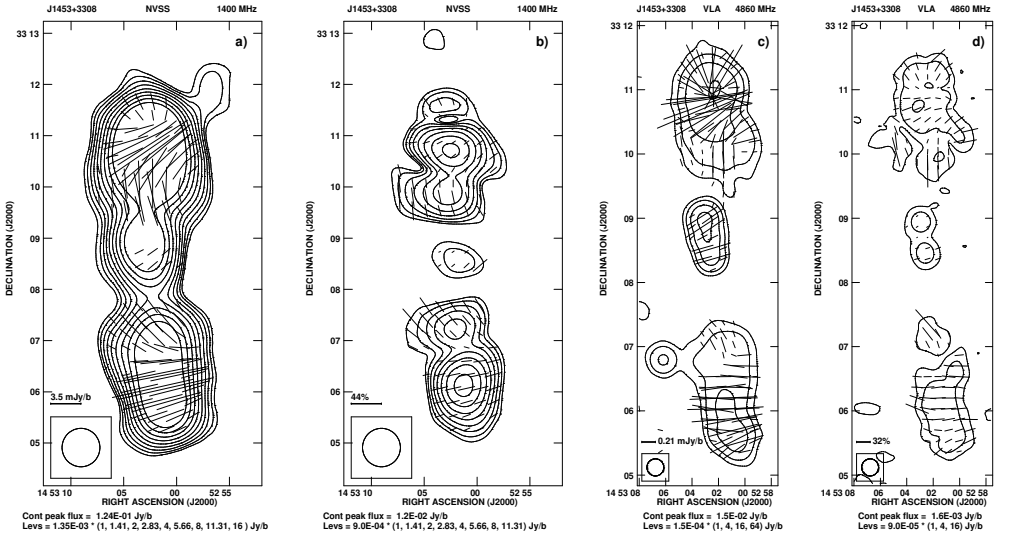

Figure 7.6: (a) The polarization E-vectors at 1400 MHz superimposed on the total-intensity and (b) the corresponding fractional polarization vectors superimposed on the polarized intensity contours. This is from the NVSS and has an angular resolution of 45 arcsec. (c) The polarization E-vectors at 4860 MHz superimposed on the total-intensity contours and (d) the corresponding fractional polarization vectors superimposed on the polarized intensity contours.

double, although the field lines tend to be orthogonal to the axis of the source in regions of the outer double which are closest to the core or inner double. The field directions for the northern and southern components of the inner double are ∼30 and 10° respectively. Some of the features appear somewhat unusual compared with the field distributions in other radio galaxies (cf. Saripalli et al. 1996; Mack et al. 1997; Lara et al. 2000; Schoenmakers et al. 2000b).

7.5 Spectral ageing analysis

In order to determine the spectral age in different parts of the lobes, i.e. the time which elapsed since the radiating particles were last accelerated, we apply the standard theory describing the time-evolution of the emission

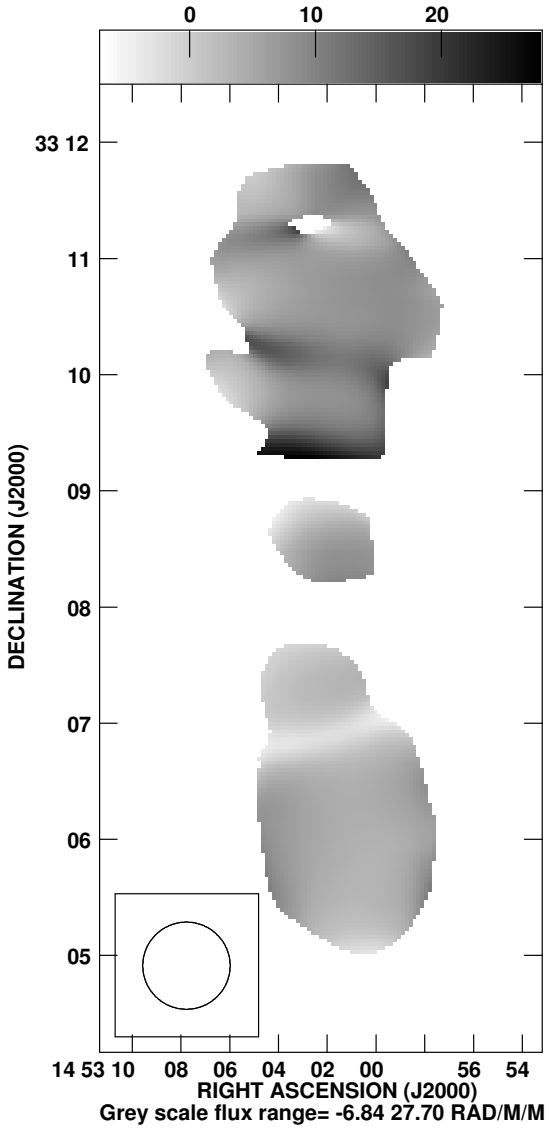

Figure 7.7: Rotation measure distribution between 1400 and 4860 MHz with an angular resolution of 45 arcsec. This is only indicative and requires confirmation from multi-frequency observations.

spectrum from particles with an initial power-law energy distribution and distributed isotropically in pitch angle relative to the magnetic field direction. The initial energy distribution corresponds to the initial (injection) spectral index $\alpha_{\rm inj}$ (defined as $S_\nu \propto \nu^{-\alpha_{inj}}$). The spectral break frequency above which the radio spectrum steepens from the injected power law, $\nu_{\rm br}$, is related to the spectral age and the magnetic field strength through

$$\tau_{\rm rad} = 50.3 \frac{B^{1/2}}{B^2 + B_{\rm iC}^2} \{\nu_{\rm br}(1+z)\}^{-1/2} {\rm Myr},$$

where $B_{\rm iC}$=0.318$(1+z)^2$ is the magnetic field strength equivalent to the CMB; B and $B_{\rm iC}$ are expressed in units of nT, while $\nu_{\rm br}$ is in GHz.

(a) Determination of $\alpha_{\rm inj}$ and $\nu_{\rm br}$ values

In order to determine a value of $\alpha_{\rm inj}$, we first fitted the CI (continuous injection; Pacholczyk 1970) and JP (Jaffe & Perola 1973) models of radiative losses to the flux densities of the outer lobes, and found that the uncertainties of the fitted $\alpha_{\rm inj}$ values are large. Also there is no evidence for significantly different values of this parameter in the opposite lobes. The typical sizes of hotspots are $\lesssim$10 kpc (e.g. Jeyakumar & Saikia 2000 and references therein) which at the redshift of 0.249 for this source corresponds to an angular size of $\sim$3 arcsec. This is similar to our GMRT full-resolution image at 1287 MHz which shows no significant hotspots in either of the outer lobes. We have therefore preferred to use the JP rather than the CI model for the outer lobes. Also the JP model gives an overall better fit to the spectra of the different strips discussed below. The fit of the model to the flux densities of both the outer lobes together (column 9 in Table 7.3) is shown in Fig. 7.8 a. This fit is used to estimate the value of $\alpha_{\rm inj}$ for the ageing analysis of the

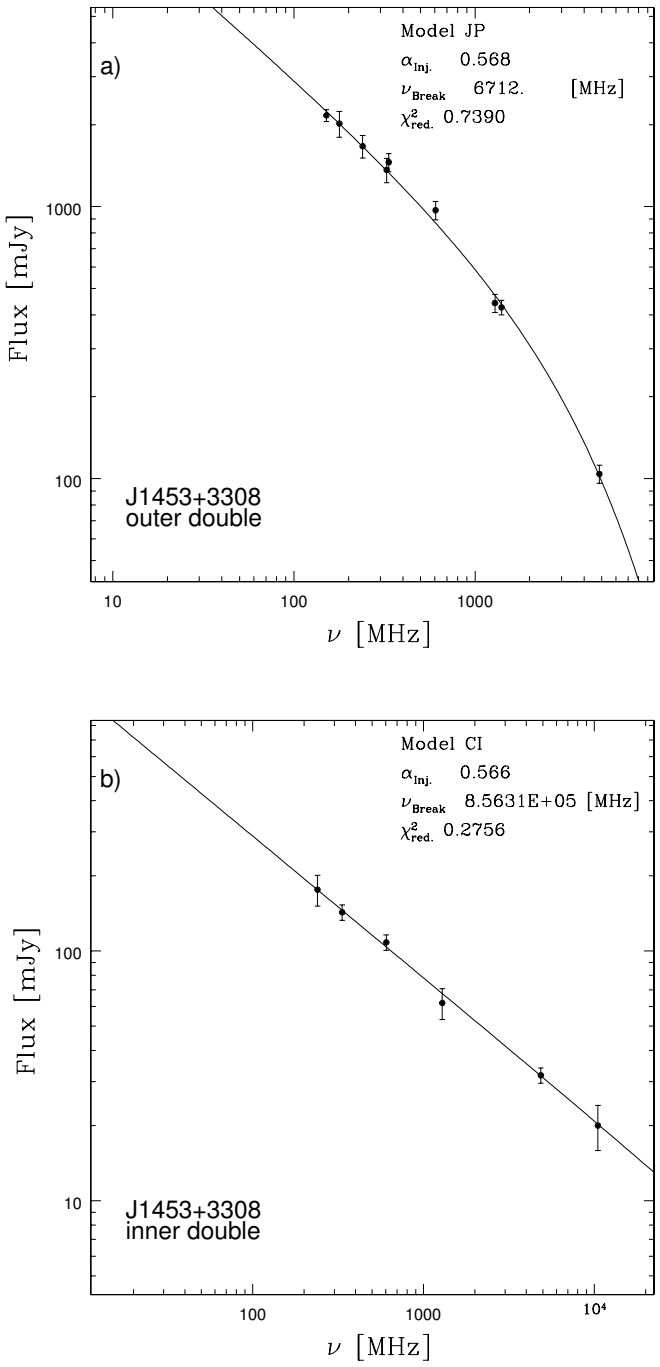

Figure 7.8: Spectra of the outer and inner doubles fitted with the models of radiative losses, as described in the text. (a) the outer double fitted with the JP model; (b) the inner double fitted with the CI model.

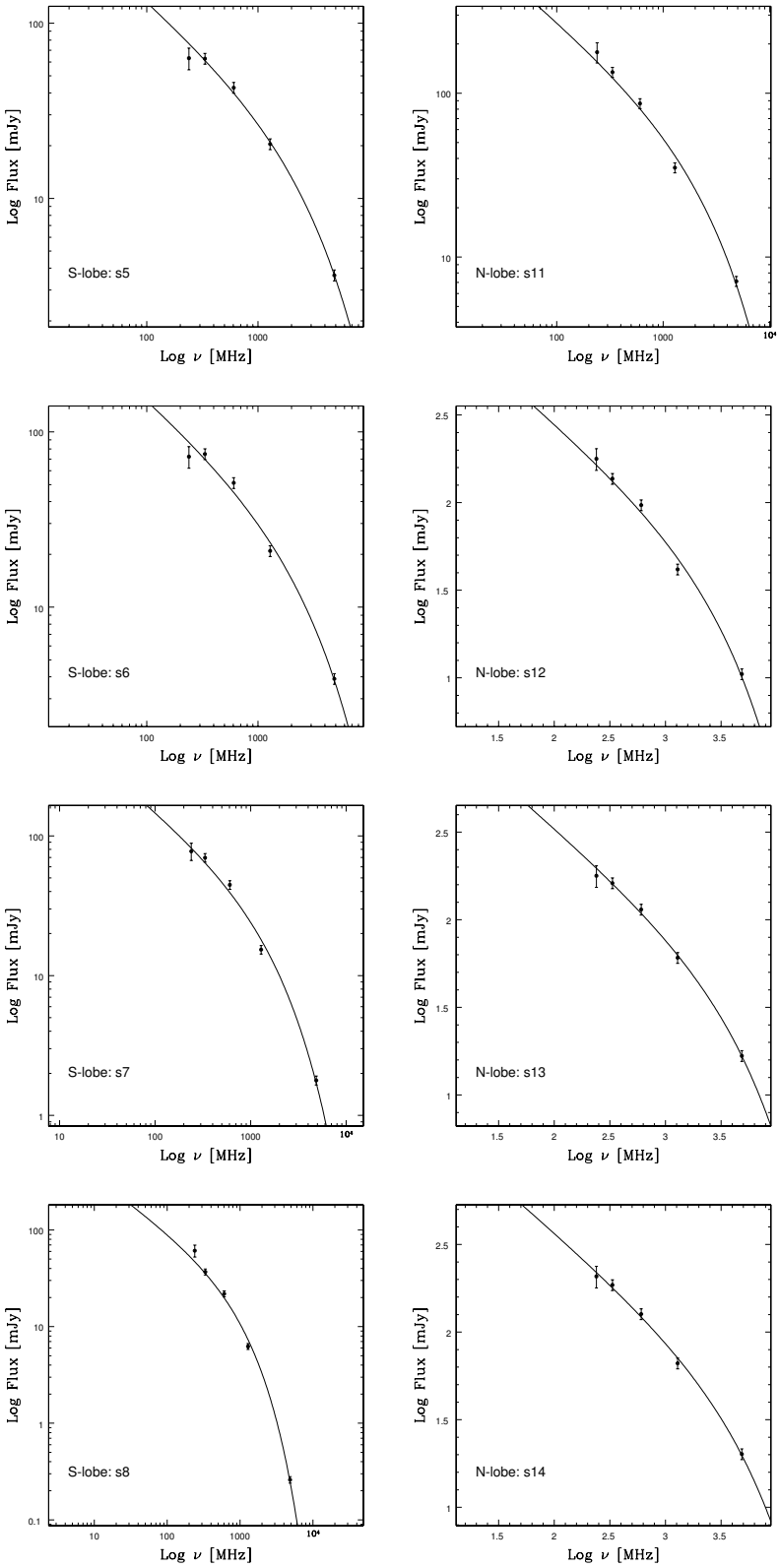

Figure 7.9: Typical spectra of the slices for the northern (upper panel) and southern (lower panel) lobes of the outer double.

outer structure of the source. The corresponding fit, but with the CI model applied to the flux densities of the inner double, is shown in Fig. 7.8 b. It is worth noting that both the fitted values of $\alpha_{\rm inj}$ are similar ~ 0.6.

Next, the total-intensity maps at the frequencies of 240, 334, 605, 1287 and 4860 MHz were convolved to a common angular resolution of 15.2 arcsec. Each lobe was then split into a number of strips, separated approximately by the resolution element along the axis of the source, and the spectrum of each strip determined from 235 to 4860 MHz. Using the SYNAGE software (Murgia 1996) we searched for the best fit applying the JP model to the spectra in the six strips covering the outer, northern lobe and the other eight covering the outer, southern lobe. Although the resulting values of $\alpha_{\rm inj}$ for different strips show significant variations, the best fits with the same injection spectrum are achieved for $\alpha_{\rm inj}$=0.568. The results for a few typical strips are shown in Fig. 7.9. In cases where the flux density of a particular strip at 235 MHz appeared discrepant from the overall fit, we attempted to determine the values of $\nu_{\rm br}$ with and without the discrepant point and found no significant difference. The values of $\nu_{\rm br}$ including the 1σ errors for the northern and southern lobes are listed in Table 7.5.

(b) Magnetic field determination and radiative ages

To determine the age of the particles in particular strips we have to estimate the magnetic field strength in the corresponding strips. The values of the equipartition energy density and the corresponding magnetic field, $B_{\rm eq}$, are calculated using the revised formula given by Beck & Krause (2005). This formula (their equation (A18)) accounts for a ratio $\mathbf{K}_0$ between the number densities of protons and electrons in the energy range where radiation losses

Table 7.5: Results of JP model calculations with $\alpha_{\rm inj}$=0.568

Strip	Dist. kpc	$\nu_{\rm br}$ GHz	χ^2_{red}	$B_{\rm eq}$(rev) nT	$\tau_{\rm rad}$ Myr
		S-lobe			
s1	735	15^{+6570}_{-3}	4.45	0.35±0.07	$18.7^{+2.3}_{-18}$
s2	673	$9.1^{+253}_{-1.3}$	2.06	0.36±0.07	$24.1^{+2.0}_{-9.9}$
s3	611	$6.9^{+16}_{-1.4}$	1.27	0.35±0.07	$27.7^{+3.2}_{-13}$
s4	549	$5.8^{+2.9}_{-1.7}$	0.59	0.35±0.07	$30.3^{+5.7}_{-5.5}$
s5	487	$4.9^{+2.6}_{-1.1}$	0.33	0.36±0.07	$32.8^{+4.4}_{-6.3}$
s6	425	$4.6^{+21}_{-0.4}$	2.53	0.38±0.07	$33.7^{+1.4}_{-19}$
s7	363	$2.9^{+4.1}_{-0.2}$	3.18	0.37±0.07	$42.7^{+1.2}_{-15}$
s8	301	$1.6^{+1.6}_{-0.1}$	3.15	0.31±0.06	$58.2^{+0.9}_{-17}$
		N-lobe			
s9	244	$2.5^{+9.7}_{-0.1}$	17.9	0.32±0.06	$46.6^{+1.4}_{-25}$
s10	286	$3.8^{+4.0}_{-0.3}$	3.69	0.37±0.07	$37.3^{+1.4}_{-11}$
s11	348	$4.7^{+349}_{-0.4}$	2.79	0.40±0.08	$32.6^{+1.4}_{-29}$
s12	410	$6.6^{+43}_{-0.7}$	2.04	0.41±0.08	$27.4^{+1.6}_{-17}$
s13	472	$10^{+6.3}_{-4.6}$	0.46	0.42±0.08	$21.8^{+7.5}_{-4.7}$
s14	534	$11^{+36}_{-3.3}$	0.47	0.44±0.08	$20.3^{+3.8}_{-10}$

are small. Assuming $\mathbf{K}_0$=70 implied by their equation (7) for $\alpha \approx \alpha_{\rm inj}$=0.568, we obtain the revised magnetic field strength, $B_{\rm eq}$, which depends on the low-frequency spectral index α in the observed synchrotron spectrum. The revised field, calculated assuming a filling factor of unity, $\alpha_{\rm inj}$=0.568, the flux densities at 334 MHz and a rectangular box for each strip are listed in Table 7.5 which is arranged as follows. Column 1: identification of the strip; column 2: the projected distance of the strip-centre from the radio core; column 3: the break frequency in GHz; column 4: the reduced χ^2 value of the fit; column 5: the revised magnetic field in nT; column 6: the resulting synchrotron age of the particles in the given strip. These latter values as a function of distance are plotted in Fig. 7.10. We have repeated the calculations using the classical equipartition magnetic field (e.g. Miley

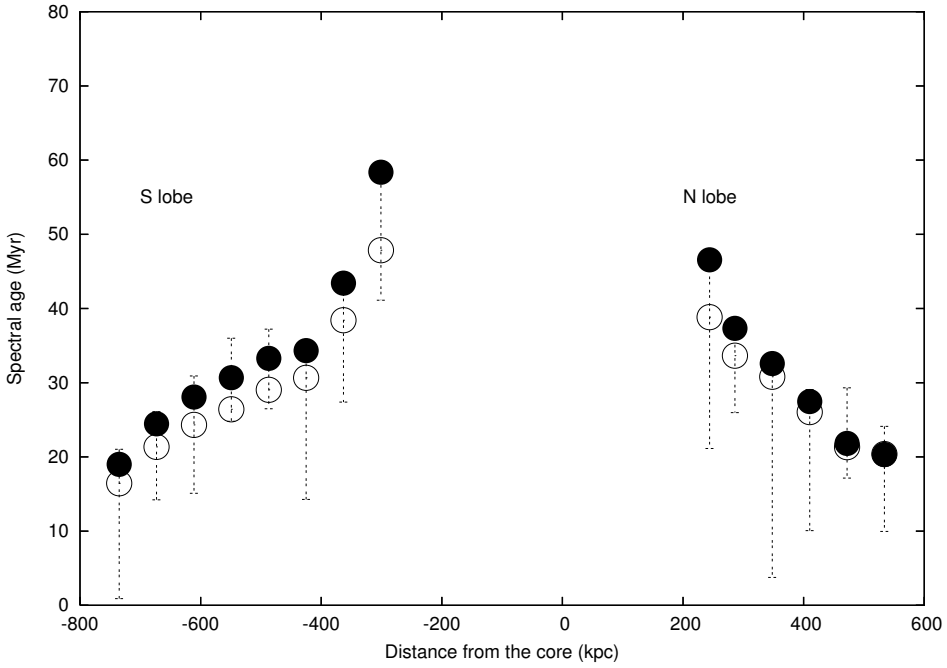

Figure 7.10: Radiative age of the relativistic particles in the outer lobes of J1453+3308 plotted against the distance from the radio core using the revised (filled circles) and classical (open circles) equipartition magnetic fields.

1980) and have also plotted the variation of age with distance using these fields. Within the uncertainties there is no significant difference between the age estimates using the revised and classical equipartition magnetic fields.

As expected, the synchrotron age for both the outer lobes increases with distance from the edges of the lobes. The maximum ages for the northern and southern lobes are ∼47 and 58 Myr respectively. The northern lobe has a higher surface brightness along most of its length, is closer to the nucleus and hence its younger spectral age may be due to a combination of reacceleration of particles and better confinement. A weighted least-squares fit to the ages yields a mean separation velocity of the head from the radio-emitting plasma of 0.036c for both the northern and southern lobes. However, these separation velocities are referred to a region of the last acceleration of emitting particles (shock at the end of the lobe) which advances from the origin of the jets, i.e.

the radio core, with an advance speed, $v_{\rm adv}$. If the backflow has a speed of $v_{\rm bf}$, and $v_{\rm bf} \approx v_{\rm adv}$, then an average expansion speed is $\sim$0.018c. This would imply an age of the outer structure of $\sim$96 and 134 Myr for the northern and southern lobes respectively, significantly smaller than the $t_{\rm out}$ estimate of 215 Myr given by K2000.

It is worth noting that our derived age estimate for the inner double structure is similar to that of K2000. Indeed, the fit with the CI model (cf. Fig. 7.8 b) gives $\alpha_{\rm inj} = 0.566^{+0.052}_{-0.064}$ and $\nu_{\rm br} = 856^{+1E11}_{-848}$ GHz (the $\pm 1\sigma$ error is enormous due to the practically straight spectrum). Our calculation of the magnetic field in the inner lobes gives $B_{\rm eq} = 0.56 \pm 0.11$ nT which implies its spectral age to be $\sim$2 Myr and an apparent advance velocity of $\sim$0.1c for the lobe heads. However these values have large uncertainties because the spectrum is practically straight.

Nevertheless, while interpreting these numbers caveats related to the evolution of the local magnetic field in the lobes need to be borne in mind (e.g. Rudnick, Katz-Stone & Anderson 1994; Jones, Ryu & Engel 1999; Blundell & Rawlings 2000). While K2000 have suggested that spectral and dynamical ages are comparable if bulk backflow and both radiative and adiabatic losses are taken into account in a self-consistent manner, Blundell & Rawlings (2000) suggest that this may be so only in the young sources with ages much less than 10 Myr. In the study of the FRII type giant radio galaxy, J1343+3758, Jamrozy et al. (2005) find the dynamical age to be approximately 4 times the maximum synchrotron age of the emitting particles.

7.6 Concluding remarks

We present the results of multifrequency radio observations of the double-double radio galaxy (DDRG), J1453+3308, using both the GMRT and the VLA.

1. The images show more details of the well-known pair of doubles which are misaligned by $\sim$7.°5. The symmetry parameters of the outer- and inner-double lobes suggest intrinsic asymmetries over these length scales. The luminosity of the outer double is in the FRII category although it has no prominent hotspot, while the luminosity of the inner double is below the dividing line although it has an edge-brightened structure characteristic of FRII sources.

2. The radio core has a mildly inverted spectrum, with some evidence of variability. The weak, compact source close to the southern lobe of the outer double is unrelated.

3. The magnetic field lines exhibit significant structure, with the lines being orthogonal to the source axis in the outer lobes closest to the radio core. The rotation measure is only a few rad m^{-2} over most of the source, with the maximum value being $\sim$25 rad m^{-2}. These results are tentative since they are based on observations at only two frequencies and require confirmation from multi-frequency observations.

4. The integrated spectrum is curved with evidence of significant flattening below $\sim$300 MHz. Using our images from 235 to 4860 MHz smoothed to a similar resolution of $\sim$15 arcsec, we fit the observed spectra of the outer and inner double structures with the models of radiative losses, and we determine the characteristic frequency breaks

in fourteen strips cut through the outer lobes and transverse to the source axis. The best fits for the outer lobes are obtained with the JP model and the injection spectrum $\alpha_{\rm inj}$=0.568, while the best fit to the spectrum of the inner double is obtained with the CI model and $\alpha_{\rm inj}$=0.566. The injection spectra for both the outer and inner doubles are similar within the uncertainties.

5. The synchrotron age of emitting particles in both the lobes of the outer double increases with distance from the edges of the lobes. The maximum ages for the northern and southern lobes are ∼47 Myr and ∼58 Myr respectively. The dependences of the radiative age vs. distance from the core imply a mean separation velocity of the lobe's head from the radio-emitting plasma of 0.036c for both the northern and southern lobes. However, assuming presence of a backflow with its backward speed comparable to the advance speed of the (jet) head, an average advance speed would be about 0.018c which yields a maximum age of ∼134 Myr which is significantly smaller than the value suggested by K2000.

6. The spectral age of ∼2 Myr obtained for the inner double is similar to that estimated by K2000. The value of 2 Myr implies an apparent advance velocity of ∼0.1c for the lobe heads of the inner structure. However these values have large uncertainties because the spectrum is practically straight.

References

Baars J.W.M., Genzel R., Pauliny-Toth I.I.K., Witzel A. 1977, A&A, 61, 99

Beck R., Krause M., 2005, Astron. Nach., 326, 414

Blundell K.M., Rawlings S., 2000, AJ, 119, 1111

Colla G., et al., 1970, A&AS, 1, 281

Condon J.J., Cotton W.D., Greisen E.W., Yin Q.F., Perley R.A., Taylor G.B., Broderick J.J., 1998, AJ, 115, 1693

Jaffe W.J., Perola G.C., 1973, A&A, 26, 423

Jamrozy M., Machalski J., Mack K.-H., Klein U., 2005, A&A, 433, 467

Jeyakumar S., Saikia D.J., 2000, MNRAS, 311, 397

Jones T.W., Ryu D., Engel A., 1999, ApJ, 512, 105

Kaiser C.R., Schoenmakers A.P., Röttgering H.J.A., 2000, MNRAS, 315, 381 (K2000)

Konar C., Saikia D.J., Jamrozy M., Machalski J., 2006, MNRAS, 372, 693

Lara L., Mack K.-H., Lacy M., Klein U., Cotton W.D., Feretti L., Giovannini G., Murgia M., 2000, A&A, 356, 63

Machalski J., Jamrozy M., Zola S., Koziel D., 2006, A&A, 454, 85

Mack K.-H., Klein U., O'Dea C.P., Willis A.G., 1997, A&AS, 123, 423

Miley G.K., 1980, ARA&A, 18, 165

Murgia M., 1996, Laurea Thesis, University of Bologna

Pacholczyk A.G., 1970, Radio Astrophysics, W.H. Freeman, San Francisco

Pilkington J.D.H., Scott P.F., 1965, MemRAS, 69, 183

Riley J.M.W., Waldram E.M., Riley J.M., 1999, MNRAS, 306, 31

Rudnick L., Katz-Stone D.M., Anderson M.C., 1994, ApJS, 90, 955

Saikia D.J., Salter C.J., 1988, ARA&A, 26, 93

Saikia D.J., Konar C., Kulkarni V.K., 2006, MNRAS, 366, 1391

Saripalli L., Mack K.-H., Klein U., Strom R., Singal A.K., 1996, A&A, 306, 708

Schoenmakers A.P., 1999, PhD thesis, Universiteit Utrecht

Schoenmakers A.P., de Bruyn A.G., Röttgering H.J.A., van der Laan H., Kaiser C.R., 2000a, MNRAS, 315, 371 (S2000a)

Schoenmakers A.P., Mack K.-H., de Bruyn A.G., Röttgering H.J.A., Klein U., van der Laan H., 2000b, A&AS, 146, 293

CHAPTER 8

Intermittent jet activity in the radio galaxy 4C29.30?

8.1 Abstract

We present radio observations at frequencies ranging from 240 to 8460 MHz of the radio galaxy 4C29.30 (J0840+2949) using the GMRT, the VLA and the Effelsberg telescope. We report the existence of weak extended emission with an angular size of ∼520 arcsec (639 kpc) within which a compact edge-brightened double-lobed source with a size of 29 arcsec (36 kpc) is embedded. We determine the spectrum of the inner double from 240 to 8460 MHz and show that it has a single power-law spectrum with a spectral index of ∼0.8. Its spectral age is estimated to be $\lesssim$33 Myr. The extended diffuse emission has a steep spectrum with a spectral index of ∼1.3 and a break frequency $\lesssim$240 MHz. The spectral age is $\gtrsim$200 Myr, suggesting that the extended diffuse emission is due to an earlier cycle of activity. We reanalyse archival x-ray data from Chandra and suggest that the x-ray emission from the hotspots consists of a mixture of nonthermal and thermal components, the latter being possibly due to gas which is shock heated by the jets from the host galaxy.

8.2 Introduction

Outer doubles of DDRGs are due to relic radio emission of the previous cycle of radio activity of the AGNs. In addition, diffuse relic radio emission due to an earlier cycle of activity may also be visible around radio sources that are not characterised by a 'classical double' structure with hotspots at the outer edges. The relic radio emission is expected to remain visible for $\sim 10^8$ yr or so (e.g. Owen, Eilek & Kassim 2000; Kaiser & Cotter 2002; Jamrozy et al. 2004), and have a steep radio spectrum due to radiative losses. Such radio emission, possibly due to an earlier cycle of activity, has been suggested for a number of sources from both structural and spectral information. These include 3C338 and 3C388 (Burns, Schwendeman & White 1983; Roettiger et al. 1994), Her A (Gizani & Leahy 2003), 3C310 (van Breugel & Fomalont 1984; Leahy et al. 1986), and Cen A (Burns, Feigelson & Schreier 1983; Clarke, Burns & Norman 1992; Junkes et al. 1993; Morganti et al. 1999). There have also been a few candidates amongst compact radio sources. For example, a lobe of emission seen on one side of the nuclear region in the GPS source B0108+388 has been suggested to be a relic of a previous cycle of jet activity (Baum et al. 1990), although the one-sidedness of the emission is puzzling (cf. Stanghellini et al. 2005). A search for small-scale halos, on scales larger than the known milliarcsec-scale structures of compact steep spectrum and GPS sources, using interplanetary scintillation observations with the Ooty Radio Telescope at 327 MHz led to the identification of a few possible candidates (Jeyakumar et al. 2000). However, such features are not very common in either small or large radio sources. For example, a number of searches for such features have not yielded clear and striking examples of relic emission around bright radio sources (e.g. Reich et al. 1980; Stute, Reich &

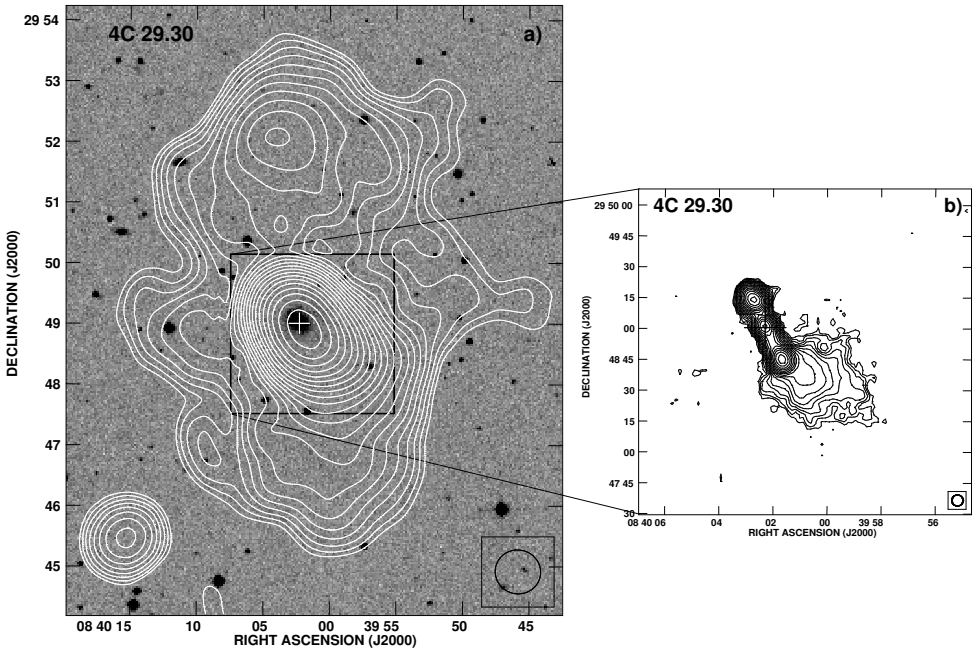

Figure 8.1: 1400-MHz VLA images of 4C 29.30. **a)** D-array contour map of the entire source overlayed on the optical field from the Digital Sky Survey (DSS). The contour levels are spaced by factors of $\sqrt{2}$ and the first contour is 0.3 mJy beam^{-1}. **b)** B-array contour map of the central part of the source from FIRST. The contour levels are spaced by factors of $\sqrt{2}$, and the first contour is 0.45 mJy beam^{-1}. The size of the beam is indicated by an ellipse in the bottom right corner of each image. The cross marks the position of the radio core.

Kalberla 1980; Perley, Fomalont & Johnston 1982; Kronberg & Reich 1983; van der Laan, Zieba & Noordam 1984; Jones & Preston 2001).

In this chapter we concentrate on the radio galaxy 4C29.30 (J0840+2949) which is associated with a bright (R $\sim 15^{\rm m}$) host elliptical galaxy (RA: 08^h 40^m $02.^s370$, Dec: $+29^\circ$ $49'$ $02.''60$; all positions being in J2000 co-ordinates) at a redshift of 0.06471±0.00013. The corresponding luminosity distance is 287 Mpc and 1 arcsec corresponds to 1.228 kpc. The published images show a double-lobed radio source which has two prominent hotspots at the outer edges with an overall angular separation of 29 arcsec (36 kpc) and a prominent jet towards the south-west (e.g. van Breugel et al. 1986; Parma

et al. 1986 and references therein). In addition there is a diffuse blob of emission towards the south-west (SW blob) with a size of ∼40 arcsec (50 kpc) extending beyond the south-western hotspot. The radio luminosity of the inner double at 1400 MHz is 5.5×10^{24} W Hz^{-1}, which is significantly below the dividing line of the Fanaroff-Riley classes, while that of the entire source is 7.4×10^{24} W Hz^{-1}. It is interesting to note that in some of the DDRGs, the luminosity of the inner double is in the FRI category although its structure resembles that of FRII radio sources (cf. Saikia et al. 2006). A detailed radio and optical study of this galaxy (van Breugel et al. 1986) shows optical line-emitting gas adjacent to the radio jet along a position angle (PA) of ∼20° and evidence of the radio jets interacting with dense extranuclear gas.

The host galaxy of 4C29.30 appears to have merged with a gas-rich galaxy, as it shows presence of shells and dust (Gonzalez-Serrano, Carballo & Perez-Fournon 1993), and is associated with an IRAS source F08369+2959 (Keel et al. 2005). At x-ray wavelengths Chandra detects emission from the hot spots in the southwestern radio lobe and also in the counterlobe (Gambill et al. 2003; Sambruna et al. 2004). Both hotspots have also been detected in observations with the Hubble Space Telescope (Sambruna et al. 2004).

In this chapter we show the presence of diffuse extended emission on an angular scale of ∼520 arcsec (639 kpc) which could be due to an earlier cycle of activity, from observations with the VLA, the GMRT and the Effelsberg telescope. This feature is also visible clearly in the WENSS (Rengelink et al. 1997) at 325 MHz and the NVSS (Condon et al. 1998) at 1400 MHz. We also present multifrequency observations of the inner double and the diffuse SW blob of emission with the GMRT and the VLA. This should enable us to determine the spectrum more reliably and estimate the spectral ages and

perhaps constrain the time scales of episodic activity in this source. For example, in the DDRG J1453+3308 we have been able to show using both GMRT and VLA observations that the spectrum of the outer lobes exhibits significant curvature while that of the inner lobes appears practically straight (Konar et al. 2006).

Our multifrequency observations and data reduction are described in Section 8.3. The observational results, such as the radio maps showing the source structure and spectra are presented in Section 8.4. The results are presented in Section 8.5, while the concluding remarks are given in Section 8.6.

8.3 Observations and data reduction

The analysis presented in this chapter is based on radio observations made with the Effelsberg telescope, GMRT and VLA, as well as on VLA archival data. The observing log for both the GMRT and VLA as well as Effelsberg observations is listed in Table 8.1 which is arranged as follows. Columns 1 and 2 show the name of the telescope, and the array configuration for the VLA observations; columns 3 and 4 show the frequency and bandwidth used in making the images; column 5: the primary beamwidth in arcmin; column 6: dates of the observations. The phase centre for all the observations was near the core of the radio galaxy except for the VLA CnD array observations at 5 GHz where the antennas were pointed about 2 arcmin north and south of the core in an effort to detect the diffuse extended emission.

(a) GMRT observations

The observations were made in the standard manner, with each observation of the target source interspersed with observations of either J0735+331 or

Table 8.1: Observing log.

Telescope	Array Conf.	Obs. Freq. (MHz)	Bandwidth (MHz)	Primary beam (arcmin)	Obs. Date
(1)	(2)	(3)	(4)	(5)	(6)
GMRT		240	4.5	114	2005 Dec 28
GMRT		333	12.5	81	2005 Dec 24
GMRT		605	12.5	43	2005 Dec 28
GMRT		1287	12.5	26	2005 Dec 22
VLA[a]	D	1400	25	30	2001 Nov 30
VLA[a]	D	1400	25	30	2001 Dec 24
VLA[a]	C	4860	50	9	1988 Apr 14
VLA	CnD	4860	50	9	2005 Oct 9, 10
VLA	CnD	8460	50	5.4	2005 Oct 12
Effelsberg		4850	500	2.1	2004 Jun 25

[a] VLA archival data.

J0741+312 which were used as phase calibrators. 3C48 was observed as a flux density and bandpass calibrator. At each frequency the source was observed in a full- synthesis run of approximately 9 h including calibration over- heads. The rms noise in the resulting full-resolution images ranges from about 1 mJy beam^{-1} at 240 MHz to about 0.06 mJy beam^{-1} at 1287 MHz. The data collected were calibrated and reduced in the standard way using the NRAO `AIPS` software package. Several rounds of self-calibration were done to improve the quality of the images. The absolute position uncertainty could be up to several arcsec in the low-frequency images due to phase errors introduced by the ionosphere (cf. Rengelink et al. 1997). The flux densities at the different frequencies are consistent with the scale of Baars et al. (1977).

(b) New and archival VLA observations

The source was observed with the CnD array at a frequency of 4860 and 8460 MHz to determine the spectra over a large frequency range by combining these results with those from the low-frequency GMRT images. The source

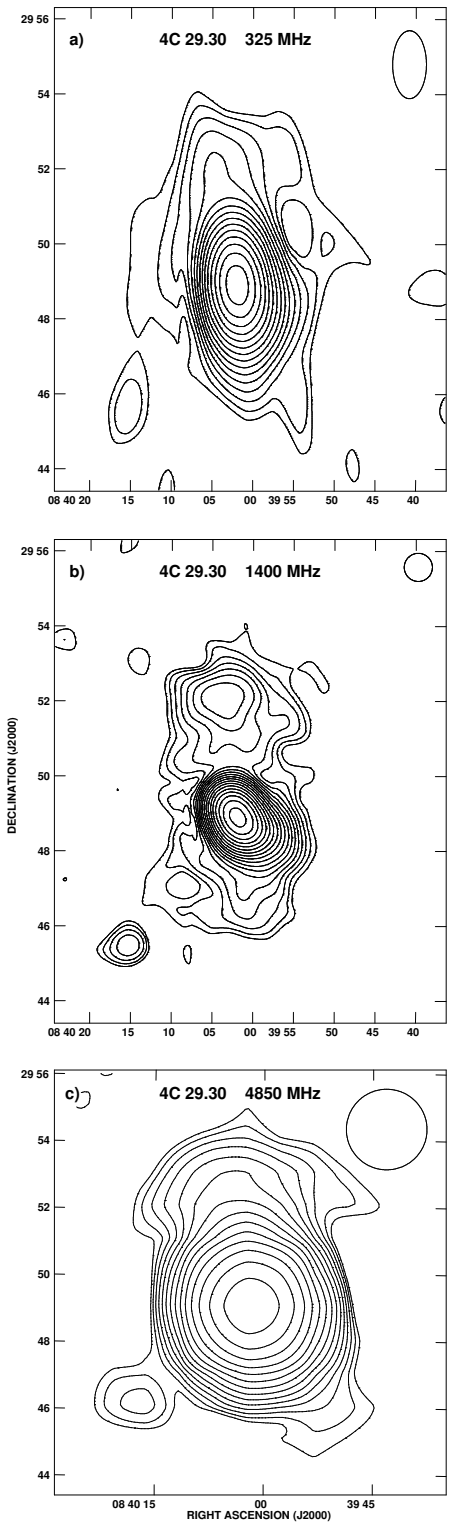

Figure 8.2: Atlas of the radio source 4C 29.30 at three different radio frequencies. **a)** 325-MHz map from the WENSS, **b)** 1400-MHz map from the NVSS, **c)** 4850-MHz map from the Effelsberg observations. The contours spaced by factors of $\sqrt{2}$ in brightness are plotted starting with 9, 0.9 and 1.8 mJy beam^{-1} respectively. The size of the beam is indicated by an ellipse in the top right corner of each image.

was observed in the snapshot mode, the integration time for each scan being ∼20 min. At 4860 MHz the source was also observed with the phase centres shifted by ∼2 arcmin towards the north and south of the core to image the diffuse extended emission. The interferometric phases were calibrated with the phase calibrator J0830+241. The source 3C286 was used as the primary flux density calibrator. For the images produced from the data sets where the phase centres have been shifted by ∼2 arcmin, correction for the primary beam pattern has been done. We also supplemented our observations with VLA archival data to examine evidence of variability of the core and determine the spectrum of the inner double-lobed source. These observations were made with the C-array at 4860 MHz.

We retrieved the L-band data of 4C29.30 from the VLA archive. The unpublished observations (proposal number AL515) were carried out in the D-array configuration using the 'Correlator Mode 4' with a bandwidth of 25 MHz and central frequencies of 1365 and 1435 MHz. The observations were performed in two runs on 2001 November 30 and December 24 with the pointing centre at RA: $08^h\ 40^m\ 02.^s3$, Dec: $+29^\circ\ 49'\ 03.''0$ and a total integration time of 2×50 min. The telescope gains were calibrated using the calibration source 3C147. The source J0741+312 was used as a phase calibrator. After the initial data reduction the two data sets were merged using the task DBCON. After preliminary CLEANing of the map with the routine IMAGR, several self-calibrations were performed to improve its quality. Finally, the map was corrected for primary beam attenuation. As in the case of the GMRT data, all the VLA data were edited and reduced using the `AIPS` package. All flux densities are on the Baars et al. (1977) scale.

(c) Effelsberg observations

The 4850-MHz observations of 4C 29.30 were carried out on 2004 June 25 with the 2-horn receiver system (Thierbach, Klein & Wielebinski 2003) at the secondary focus of the Effelsberg 100−m telescope. A total of 6 coverages, with a size of 20×20 arcmin^2 in azimuth and elevation, were obtained. The scanning speed was 40 arcmin/min and the scan separation 1 arcmin. Calibration and pointing performance of the system were checked by mapping and cross-scanning the point-like sources, 3C286 and B0851+20. We adopt the flux density scale of Baars et al. (1977). The standard MPIfR-NOD2 (Haslam 1974) software package was used for the data reduction. Firstly, all single-pixel noise spikes were removed by hand from each of the scans. Then the individual maps were combined using the PLAIT algorithm by Emerson & Gräve (1988). The rms noise of 0.9 mJy beam^{-1} in total power was estimated from off-source regions of the image well away from its edges and the half-power beam width was determined to be 144.5 arcsec. Finally, the NRAO `AIPS` software package was used for imaging the source.

8.4 Observational results

(a) Overall structure

Our VLA image at 1400 MHz with an angular resolution of ∼45 arcsec (Fig. 8.1) shows the entire structure of 4C29.30 which has a largest angular extent of 520 arcsec (639 kpc), in addition to the inner structure with an angular size of 29 arcsec (36 kpc). The rms noise in the image is 0.13 mJy beam^{-1} while the total flux density is 756 mJy. There is a peak of emission with a peak brightness of 10 mJy beam^{-1} located at RA: $08^h\ 40^m\ 04.^s03$, Dec: $+29^\circ$

$52'\ 04.''4$ in the northern region of the extended emission which is brighter than the south which has a peak brightness of $\sim$3.5 mJy beam^{-1} at RA: $08^h\ 39^m\ 59.^{ss}29$, Dec: $+29^\circ\ 46'\ 32.''3$. We have reproduced in Fig. 8.1 the FIRST (Becker, White & Helfand 1995) image of the source with an angular resolution of 5.4 arcsec which shows the inner double-lobed structure and the SW blob of emission. Due to lack of short baselines this VLA B-array survey is insensitive to the extended structures.

The diffuse extended structure can also be seen in our Effelsberg image at 4850 MHz as well as the WENSS image at 325 MHz and the NVSS image at 1400 MHz (Fig. 8.2). The 325-MHz WENSS map of the total intensity emission of 4C29.30 with the angular resolution of about 54×109 arcsec^2 (Fig. 8.2 a) has an rms noise of 3.9 mJy beam^{-1} while the total flux density of the entire source is 2170 mJy. The total intensity 1400-MHz VLA D-array NVSS map of the source with an angular resolution of 45×45 arcsec^2 and an rms noise of 0.45 mJy beam^{-1} (Fig. 8.2 b) has a total flux density of 731 mJy, which is only marginally smaller than the estimate of 756 mJy from our image (Fig. 8.1).

Although only the inner double and the SW blob of emission are visible in the full-resolution GMRT images as discussed below, tapered images with an angular resolution of 45 arcsec were made from the GMRT data at 240, 333, 605 and 1287 MHz to detect the diffuse extended emission. These images are presented in Fig. 8.3 and have an rms noise of 4.6, 1.6, 0.9 and 0.5 mJy beam^{-1} respectively, while the total flux densities are 3541, 2647, 1465 and 727 mJy respectively. A comparison of the GMRT low-resolution images with our VLA D-array image (Fig. 8.1) shows that although the northern peak and some diffuse emission have been detected, weaker diffuse emission have been missed in these images. While at the lower frequencies this is due

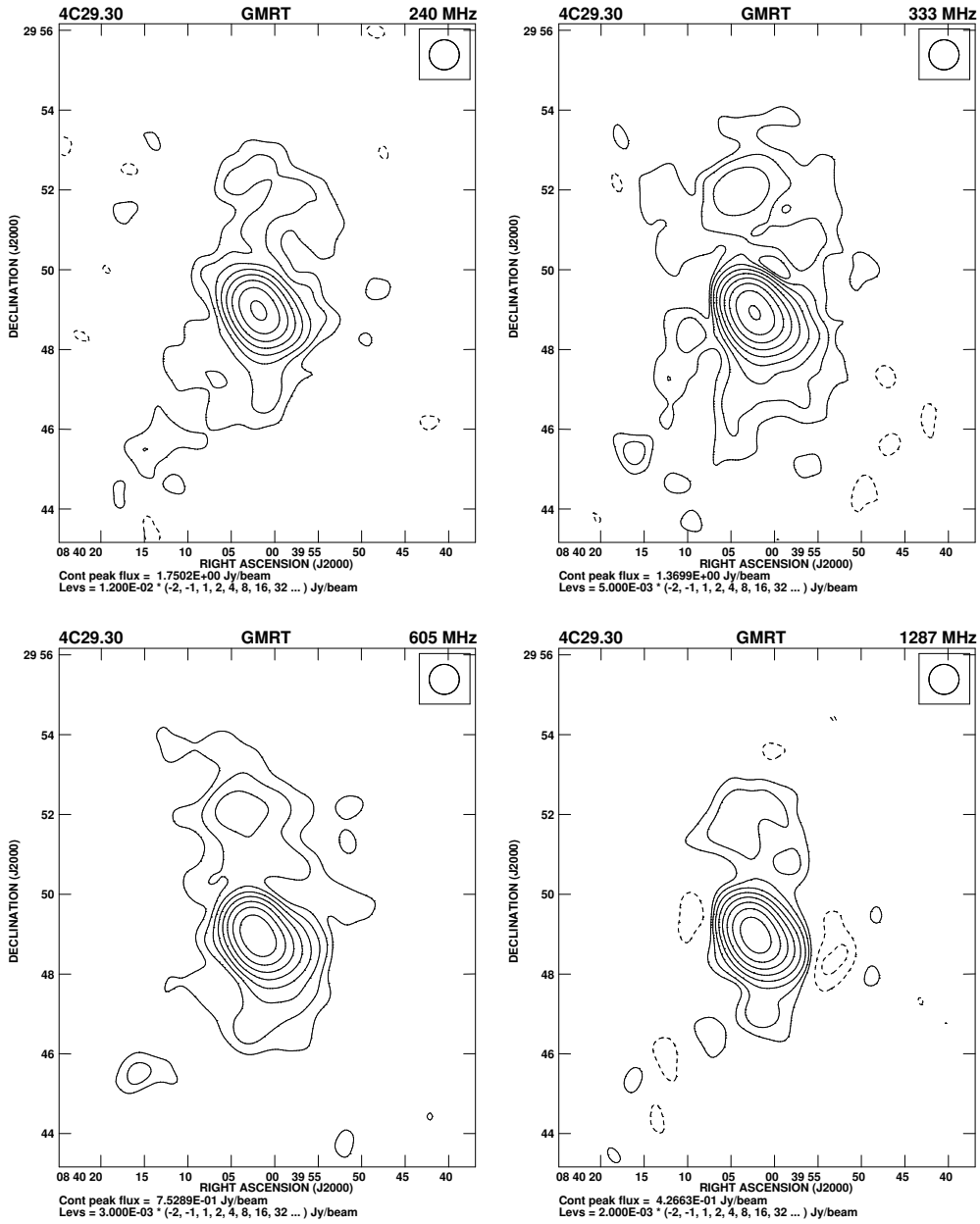

Figure 8.3: The GMRT images of 4C29.30 at 240 MHz (upper left), 333 MHz (upper right), 605 MHz (lower left) and 1287 MHz (lower right). All these images have been made with an angular resolution of 45 arcsec which is shown as a circle in the top right-hand corner.

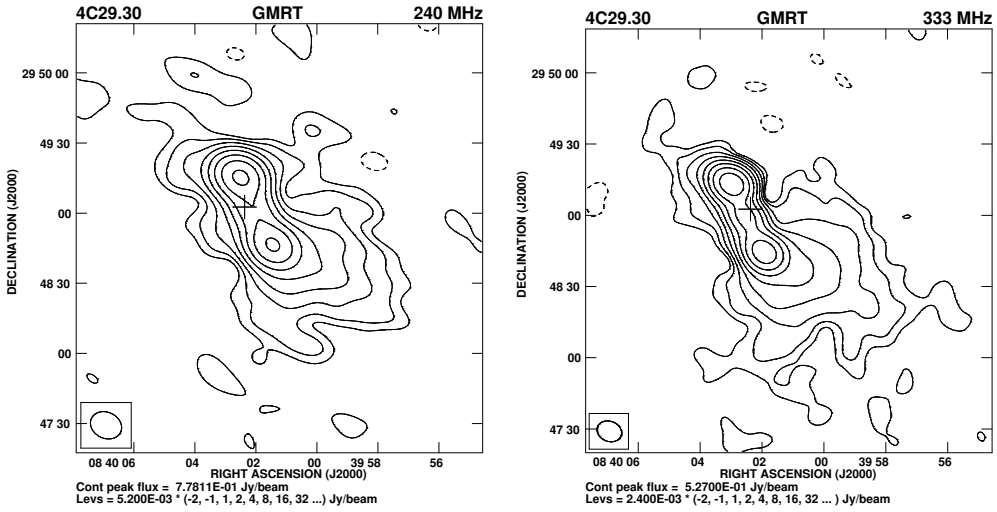

Figure 8.4: The GMRT images of 4C29.30. Left panel: image at 240 MHz with an angular resolution of 13.8×11.1 arcsec^2 along PA 64°. Right panel: the 333-MHz image with an angular resolution of 10.6×8.5 arcsec^2 along PA 68°. The resolution is shown as an ellipse in the bottom left-hand corner while the + sign marks the position of the optical galaxy.

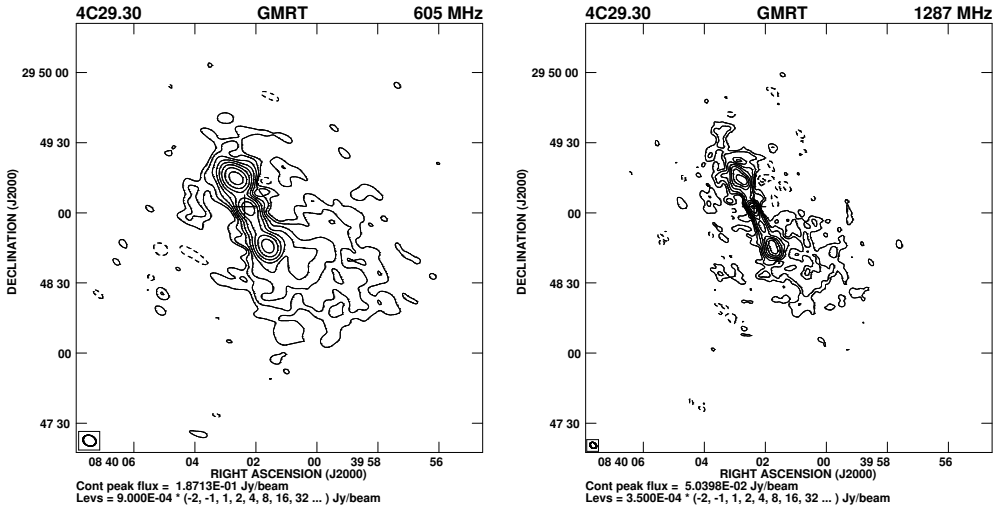

Figure 8.5: The GMRT images of 4C29.30. Left panel: image at 605 MHz with an angular resolution of 5.66×4.50 arcsec^2 along PA 66°. Right panel: image at 1287 MHz with an angular resolution of 2.97×2.30 arcsec^2 along PA 46°. The resolution is shown as an ellipse in the bottom left-hand corner while the + sign marks the position of the optical galaxy.

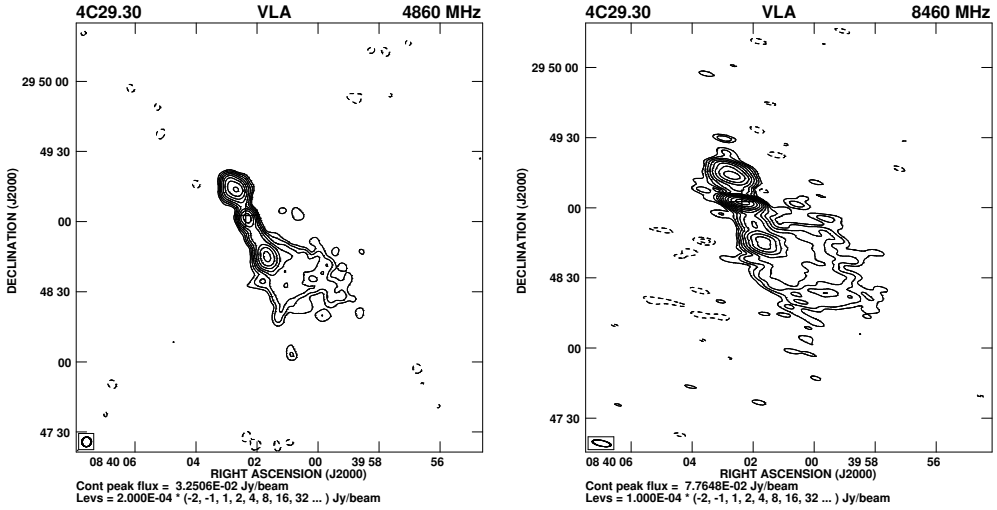

Figure 8.6: Left panel: the VLA image of 4C29.30 at 4860 MHz with an angular resolution of 4.13×3.90 arcsec^2 along PA 162°. Right panel: the VLA image at 8460 MHz with an angular resolution of 7.90×2.46 arcsec^2 along PA 78°. The resolution is shown as an ellipse in the bottom left-hand corner while the + sign marks the position of the optical galaxy.

to the higher rms noise values, the flux density at 1287 MHz could also be affected by the lack of short spacings.

(b) The inner structure

The inner structure of 4C29.30 has been observed several times at different frequencies, viz. at ∼1400 MHz (Fanti et al. 1977, van Breugel et al. 1986, Parma et al. 1986, Capetti et al. 1993), ∼5000 MHz (Fanti et al. 1977, van Breugel et al. 1986, Giovannini et al. 1988), and ∼15000 MHz (van Breugel et al. 1986). The maps show two arrow-shaped lobes. The more compact, northern lobe is located close to the radio core while the southern one, which is connected with the nucleus by a distinct radio jet, is more extended. The inner double−lobed structure is oriented along a PA of ∼26° which is misaligned from the outer extended emission by ∼18°. The outer emission is oriented close to that of the optical filament towards the south

noted by van Breugel et al. (1986).

The GMRT low-frequency images at 240, 333, 605 and 1287 MHz which show the inner double and the SW blob of emission are shown in Figs. 8.4 and 5, while the VLA images at 4860 and 8460 MHz are presented in Fig. 8.6. The flux densities estimated from these images are listed in Tables 8.2 and 8.3. The observational parameters and some of the observed properties are presented in Table 8.2, where we list the values estimated from the full-resolution images as well as those estimated from the images made by tapering and weighting the data to match the resolution of the GMRT image at 240 MHz. Table 8.2 is arranged as follows. Column 1: frequency of observations in MHz, with the letter G or V representing either GMRT or VLA observations; columns 2−4: the major and minor axes of the restoring beam in arcsec and its PA in degrees; column 5: the rms noise in units of mJy beam^{-1}; column 6: the peak flux density in the image in units of mJy beam^{-1}; column 7: the total flux density of only the inner double in units of mJy; column 8: the total flux density of the inner double along with its small extension to the south-west in units of mJy. The flux densities have been estimated by specifying a polygon around the source. The error in the flux density is approximately 15 per cent at 240 MHz and 7 per cent at the higher frequencies.

(c) The radio core

Our higher-resolution images (Figs. 8.5 and 8.6) clearly show the radio core in addition to the lobes of radio emission. The J2000.0 position of the radio core estimated from our high-resolution image at 8460 MHz is RA: $08^h\ 40^m\ 02.^s35$, Dec: $+29^\circ\ 49'\ 02.''5$, which is consistent with the position of the

Table 8.2: The observational parameters and flux densities of the inner structure.

Freq.	Beam size			rms	S_p	S_t^{id}	S_t^{id+SW}
(MHz)	(″)	(″)	(°)	(mJy /b)	(mJy /b)	(mJy)	(mJy)
(1)	(2)	(3)	(4)	(5)	(6)	(7)	(8)
G240	13.8	11.1	64	1.58	778	2149	2623
G333	10.6	8.5	68	1.37	527	1680	2109
	13.8	11.1	64	0.90	589	1805	2141
G605	5.66	4.50	66	0.37	187	891	1127
	13.8	11.1	64	0.24	310	1046	1196
G1287	2.97	2.30	46	0.11	50	390	490
	13.8	11.1	64	0.42	169	601	670
V4860	4.13	3.90	162	0.05	33	172	208
	13.8	11.1	64	0.13	70	208	238
V4860	16.3	4.51	65	0.10	67	242	282
V4860	14.3	4.37	72	0.22	67	242	291
V4860	14.0	4.24	71	0.09	65	242	290
V8460	7.90	2.46	78	0.03	78	188	217
	13.8	11.1	64	0.06	90	199	227

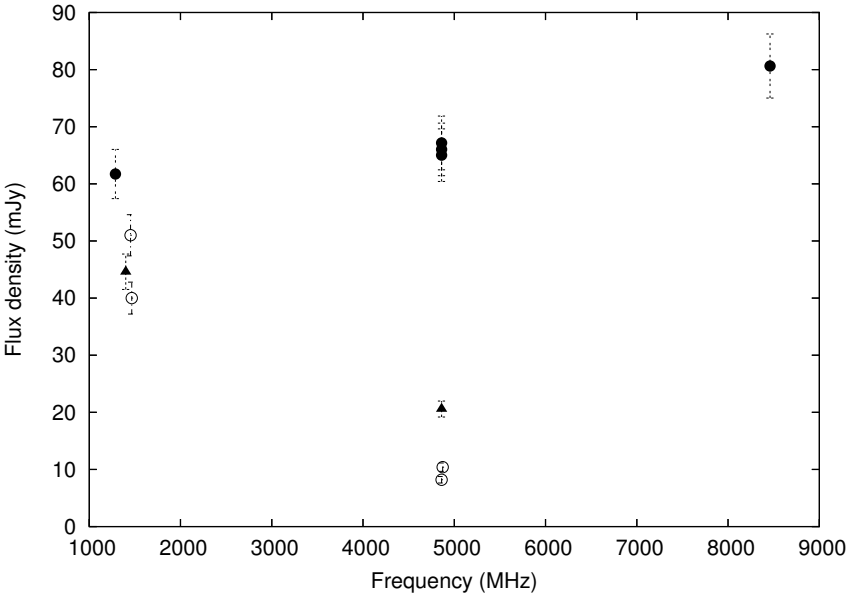

Figure 8.7: Spectrum of the core of 4C29.30. The measurements in 2005 with an angular resolution of 5.4 arcsec along the jet axis are shown by filled circles, while earlier observations from FIRST and our analysis of archival VLA data with a similar resolution are shown as filled triangles. The values from the literature listed in Table 8.3 are shown as open circles.

Table 8.3: Flux densities of the radio core.

Telescope	Date of obs.	Freq.	Resn.	Flux density[a]	Refs.
		(MHz)	($''$)		
(1)	(2)	(3)	(4)	(5)	(6)
GMRT	2005 Dec 22	1286	$\sim$2.6	50^p (62^p)	1
VLA-B	1993 Apr 02	1400	5.4	46^p (46^p)	2
VLA-A	1982 Feb	1452	1.3	51	3
VLA-B	1982 Aug, Sep	1465	$\sim$4.0	40	4
VLA-A	1982 Feb	4873	0.3	10.4	3
VLA-A	1985 Jan	4860	$\sim$0.4	8.2	5
VLA-C	1988 Apr 14	4860	$\sim$4.0	19^p (21^p)	1
VLA-CnD	2005 Oct 9, 10	4860	$\sim$7.5	63^p (66^p)	1
VLA-CnD	2005 Oct 12	8460	$\sim$4.5	78^p (81^p)	1

[a]: The core flux densities from our data and FIRST are peak values in units of mJy beam^{-1} estimated from two-dimensional Gaussian fits to minimise contamination from extended emission. These have been marked with the superscript ^{p}. The remaining values are from the literature and are in units of mJy. The values within brackets are from images made with an angular resolution of 5.4 arcsec approximately along the jet axis so that the contamination from jet emission is similar.
References. 1: Jamrozy et al. 2007. 2: FIRST image. 3: van Breugel et al. (1986). The flux density of C=C1+C2 in their nomenclature which would not be resolved by a $\sim$5 arcsec beam is 16.5 mJy at 4873 MHz and 51 mJy at 1452 MHz, which is listed in the Table here. 4: Parma et al. (1986). 5: Giovannini et al. 1988. The flux density of c+A+B in their nomenclature which would be unresolved by a $\sim$5 arcsec beam is 16 mJy.

optical galaxy (RA: $08^h\ 40^m\ 02.^s370$, Dec: $+29^\circ\ 49'\ 02.''60$) from NED. van Breugel et al. (1986) and Giovannini et al. (1988) have reported observations of this source with the VLA A-array. These subarcsec-resolution images show a compact core and a radio jet towards the south-west with a prominent knot in the jet separated from the core by ∼3 arcsec (3.7 kpc). With our relatively coarse resolution of a few arcsec the core flux density is contaminated by emission from the jet. From the high-resolution observations the core flux density is 10.4 mJy at 4873 MHz and 8.2 mJy at 4860 MHz (van Breugel et al. 1986; Giovannini et al. 1988), although the flux density including the knot is ∼16.5 mJy.

Although our observations are of different resolutions, we have attempted to examine evidence of variability by making images with an angular resolution of 5.4 arcsec along the jet axis, which is similar to the resolution of the FIRST image, so that contamination by emission from the jet is similar at the different frequencies. A comparison of the flux densities in 2005 suggests that there was a strong outburst between about 1990 and 2005 which is apparent in the core flux densities at 4860 and also possibly at ∼1300 MHz (Fig. 8.7). It is relevant to note that in the DDRG J1453+3308 Konar et al. (2006) reported evidence of significant variability of the core flux density at cm wavelengths. Other examples of cores which have been monitored and show evidence of variability are 3C338 and B2 1144+352 (Giovannini et al. 1998, 1999; Schoenmakers et al. 1999). It is interesting to note that both these objects are possible examples of episodic jet activity (cf. Burns, Schwendeman & White 1983; Schoenmakers et al. 1999). It is important to determine from more extensive monitoring whether strong core variability may be a common characteristic of sources with renewed jet or nuclear activity even if the cores are relatively weak. However, it is also relevant to note that strong

core variability and superluminal motion may be seen in sources inclined at small angles to the line of sight. Such sources are also expected to have dominant cores due to Doppler boosting of the core flux density. Amongst the sources discussed here, the arcsec scale core in B2 1144+352 contributes almost 80 per cent of the total observed flux density at 1400 MHz, while for the other three objects it contributes $\lesssim$5 per cent, similar to other galaxies of comparable luminosity (cf. Saikia & Kulkarni 1994; Ishwara-Chandra & Saikia 1999). This is consistent with the detection of superluminal motion in B2 1144+352 (Giovannini et al. 1999), while 3C338 exhibits two reasonably symmetric parsec-scale jets and evidence of subluminal motion (Giovannini et al. 1998). The cores of 4C29.30 and J1453+3308 are weak and have not been studied with mas resolution.

(d) Spectra

The flux densities of the source, 4C29.30, from the literature as well as from our images which show the extended structure (Figs. 8.1, 8.2 and 8.3) are summarised in Table 8.4 which is self explanatory. All the flux densities are consistent with the scale of Baars et al. (1977) and where necessary have been converted to this scale using the conversion factors listed by Kühr et al. (1981). The spectrum obtained from these measurements is presented in Fig. 8.8 (upper panel). There are some caveats which need to be borne in mind while examining this spectrum. For the low-frequency measurements where the diffuse extended emission is more likely to make a significant contribution the noise levels are often very high and the diffuse emission may not be 'visible' in these observations. This can be seen clearly in the VLSS image (`http://lwa.nrl.navy.mil/VLSS`) where the rms noise is approximately 80

Table 8.4: The radio flux densities of 4C 29.30.

Freq. (MHz) (1)	Flux density (mJy) (2)	Err (mJy) (3)	Ref. (4)	Note (5)
74	5393	755	1	
151	2753	147	2	
178	2220	445	3	
240	3541	496	8	(a)
325	2170	217	4	(a)
333	2647	370	8	(a)
408	1763	88	5	
605	1465	103	8	(a)
1287	727	51	8	(a)
1400	738	30	6	
1400	731	37	7	(a)
1400	756	23	8	(a)
2700	430	10	9	
4850	266	40	10	
4850	239	24	11	
4850	269	35	12	
4850	271	14	8	(a)

References along with the names of some of the well-known surveys. (1) VLSS: VLA Low-frequency Sky Survey; (2) 7C: Riley et al. 1999; (3) 4C: Pilkington & Scott 1965; (4) WENSS: Rengelink et al. 1997; (5) B2: Colla et al. 1970; (6) White & Becker 1992; (7) NVSS: Condon et al. 1998; (8) Jamrozy et al. 2007; (9) Bridle et al. 1977; (10) Becker, White & Edwards 1991; (11) Langston et al. 1990; (12) Gregory & Condon 1991.
Notes: (a) The diffuse extended emission is visible in these images (Figs. 8.1, 8.2 and 8.3), although the entire flux density is possibly seen only in the VLA D-array image at 1400 MHz (Fig. 8.1) and the Effelsberg image at 4850 MHz (Fig. 8.2).

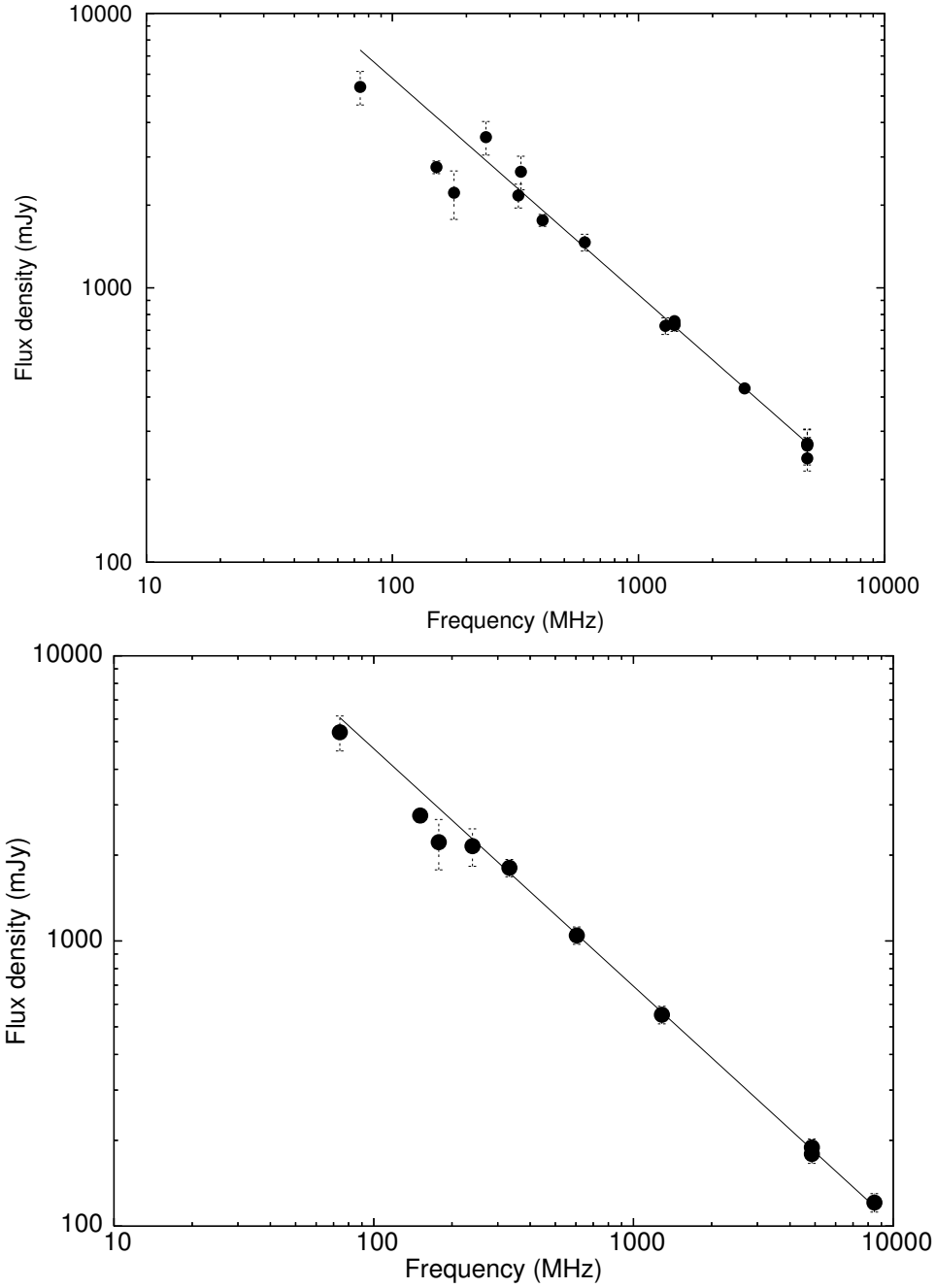

Figure 8.8: Upper panel: Spectrum of 4C29.30 using the flux densities listed in Table 8.4. The linear least-squares fit has been made using measurements only between 240 and 4850 MHz. Lower panel: Spectrum of the inner double using our GMRT and VLA images between 240 and 8460 MHz. The contributions of the core component within a region of ∼4 arcsec (4.9 kpc) have been subtracted at frequencies $\gtrsim$1300 MHz. The spectrum shows the low-frequency measurements at 74, 151 and 178 MHz listed in Table 8.4, although the linear least squares fit has been made using measurements only between 240 and 8460 MHz. This fit has been extrapolated to lower frequencies.

mJy beam^{-1} (Fig. 8.9) and there is no evidence of the diffuse extended emission. The deconvolved size of this component is 64×18 arcsec^2 along a PA of 51°. The Cambridge 7C image of 4C29.30 at 151 MHz is towards the edge of the field and may also represent only the flux density of the inner double. The spectral index α ($S_\nu \propto \nu^{-\alpha}$), determined from the total flux density of the source between 240 and 4850 MHz is 0.79±0.02.

In the lower panel of Fig. 8.8 we present the spectrum of the inner-double lobed source obtained from our GMRT and VLA images after subtracting the contribution of the core component at frequencies of ∼1300 MHz and above. The total flux densities have been estimated from images which have been tapered and weighted to have the same resolution as that of the 240−MHz image. The core contribution is particularly important at 8460 MHz although it does appear to make a significant contribution at 4860 MHz. Its effect at 1400 MHz is small, its contribution being within the errors in the flux density. Our observations between 240 and 8460 MHz are consistent with a straight spectrum yielding a spectral index of 0.83±0.01 for the inner double. The extrapolation of the spectrum to lower frequencies shows that the 74−MHz flux density from the VLSS is consistent with this spectral index while the Cambridge measurements at 151 and 178 MHz are marginally below the expected values. We have also attempted to fit the spectrum of the inner double including the south-western blob of emission. It yields similar results with a spectral index of 0.82±0.02.

(e) Polarization properties

The distributions of the 1400 and 4850 MHz linear polarization of 4C29.30 are shown in Fig. 8.10. Panels a) and c) show contours of total intensity,

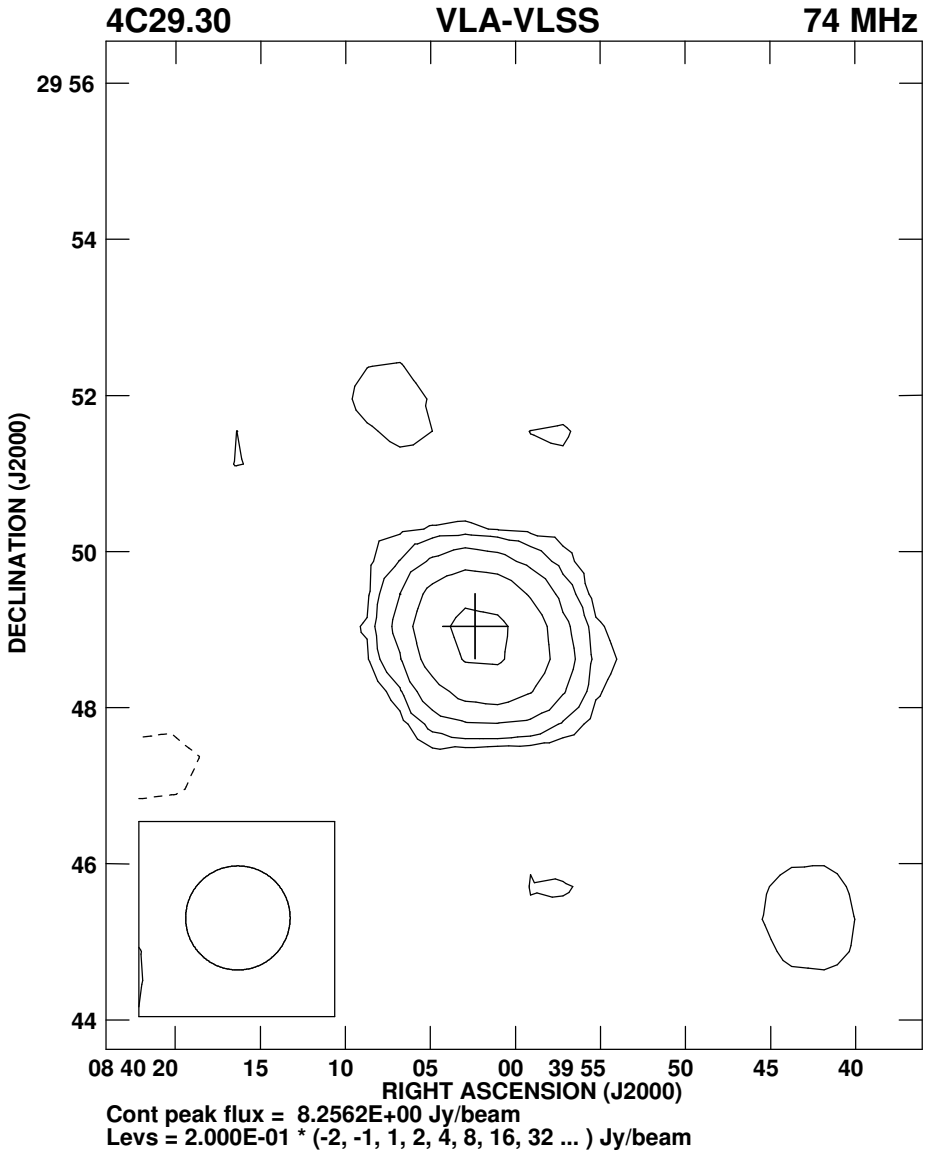

Figure 8.9: VLSS image of 4C29.30 with an angular resolution of 80 arcsec showing only the inner double as a single source. The resolution is shown as an ellipse in the bottom left-hand corner while the + sign marks the position of the optical galaxy.

with E-field polarization vectors superimposed. The lengths of the vectors are proportional to the polarized intensity. Panels b) and d) show contours of polarized intensity, with E-field polarization vectors superimposed. Here, the lengths of the vectors are proportional to the fractional polarization. The integrated polarized flux densities of the central component are 41.7 ± 2.2 mJy and 7.9 ± 0.5 mJy at 1400 and 4850 MHz, respectively. The corresponding degrees of linear polarization are 6.7 ± 0.4 and 3.3 ± 0.3 per cent. We find different orientations of the electric E-vectors in different regions of the lobes, as well as differences in the levels of polarization, suggesting Faraday rotation and depolarization effects. In order to determine the distribution of the magnetic B-field directions, it is necessary to correct the radio data for the Faraday rotation measure, and for that purpose subsequent radio polarisation measurements at other wavelengths with high angular resolution are needed. At 4850 MHz, the orientation of the E-field in the central parts of the source agrees with that reported by van Breugel et al. (1986) for the inner radio lobes (the southern one in particular). Also the large Faraday rotation measure between 5000 and 1400 MHz observed by van Breugel et al. are consistent with those indicated by our analysis. This suggests that the polarized flux is largely from the inner radio structure. However, weak linear polarization is also detected from the outer regions far beyond the inner jets and their lobes.

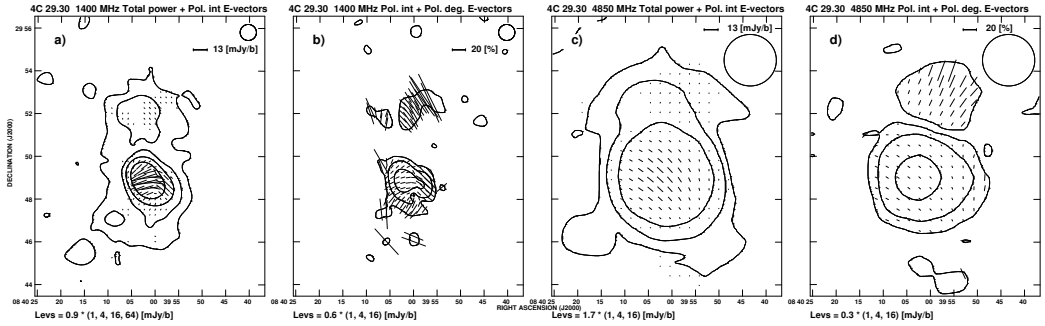

Figure 8.10: Polarization maps of 4C 29.30. **a)** The polarization E-vectors at 1400 MHz superimposed on the total-intensity contours and **b)** the corresponding fractional polarization vectors superimposed on the polarized intensity contours. **c)** The polarization E-vectors at 4850 MHz superimposed on the total-intensity contours and **d)** the corresponding fractional polarization vectors superimposed on the polarized intensity contours. The size of the beam is indicated by the circles in the top right corners of the images and bars indicate the scale beams of the polarization vectors.

8.5 Discussion

(a) Spectral ageing analysis

The spectra using the total flux densities between 240 and 4860 MHz and that of the inner double using our measurements between 240 and 8460 MHz are consistent with a single power-law. We have fitted the spectrum of the inner double after subtracting the core flux density for the Jaffe & Perola (1973; JP), Kardashev-Pacholczyk (KP, Kardashev 1962; Pacholczyk 1970) and the continuous injection (CI, Pacholczyk 1970) models using the `SYNAGE` package (Murgia 1996). The break frequency obtained from these fits are rather large ($\gtrsim 7\times10^5$ GHz) and have huge uncertainties because the spectrum is practically straight. These conclusions remain unaffected even if the flux density at 74 MHz is included in the analysis.

In order to calculate the global mean magnetic field strength and estimate the spectral age we have adopted the formula given by Miley (1980), a

spheroidal and cylindrical geometry for the diffuse extended emission and the inner double respectively, a filling factor of ∼1, a proton to electron energy ratio of unity and lower- and higher-frequency cutoffs of 10 MHz and 100 GHz respectively. The equipartition magnetic field estimate for the inner double is 0.43±0.06 nT, indicating that for the above-mentioned break frequency the inferred age is $\lesssim$0.12 Myr. (For conversion of the magnetic field to μG which is also commonly used, 1nT = 10 μG). However, adopting a more conservative break frequency of $\gtrsim$10 GHz from the observed spectrum, the spectral age is $\lesssim$33 Myr.

We have attempted to determine the spectrum of the diffuse extended emission by subtracting the flux density of the inner double from that of the total emission in the images where this is reliably seen. For this purpose we have used our low-resolution GMRT images at 240, 333 and 605 MHz, our VLA D-array and NVSS images at 1400 MHz and our Effelsberg measurements at 4850 MHz to represent the total flux density of the source. Our GMRT image at 333 MHz has a better rms noise than the WENSS image and gives a larger value of the total flux density. After subtracting the contribution of the inner double-lobed source, estimated from our GMRT and VLA images of similar angular resolution of ∼12 arcsec, we plot the spectrum of the diffuse emission in Fig. 8.11. Although there are significant uncertainties, a least-squares fit yields a spectral index of 1.26±0.07. However, given the possibility that we are still missing significant amounts of flux density at the lower frequencies, as discussed earlier, the spectral index could be steeper. Making a very rough estimate of the possible increase in the flux density by assuming that the diffuse emission not detected at the low frequencies compared with the VLA D-array image (Fig. 8.1) is just below the first contour level yields a spectral index of 1.34±0.05 for the diffuse emission. These

points are indicated by open circles in Fig. 8.11. The above two values are consistent within the errors. These estimates suggest that the halo is likely to be much older than the inner double.

We have also estimated the spectral index from 240 to 1400 MHz in the vicinity of the peak in the northern diffuse emission by considering a box with a size of ∼150 arcsec centred on the peak in the 45-arcsec resolution images. The flux densities at 240, 333, 605 and 1400 MHz are 188±26, 139±19, 87±6 and 44±3 mJy respectively. A least-squares fit yields a spectral index of 0.81±0.01 for this region, which is similar to the spectral index of the inner double, suggesting that this value might be close to the injection spectrum, which is rather steep. The magnetic field strength in the vicinity of the peak in the northern diffuse emission is 0.12±0.02 nT. The straight spectrum of this region till ∼1400 MHz yields a spectral age of $\lesssim$100 Myr, consistent with an interruption of activity for $\lesssim$100 Myr. For the diffuse extended emission, the spectral break is likely to be lower than ∼240 MHz, which yields a spectral age $\gtrsim$200 Myr. To get a reliable value of the spectral break and estimate the age using `SYNAGE` we need more sensitive images at low frequencies, especially below ∼240 MHz.

Nevertheless, while interpreting these numbers caveats related to the evolution of the local magnetic field in the lobes need to be borne in mind (e.g. Rudnick, Katz-Stone & Anderson 1994; Jones, Ryu & Engel 1999; Blundell & Rawlings 2000). While Kaiser, Schoenmakers & Röttgering (2000) have suggested that spectral and dynamical ages are comparable if bulk backflow and both radiative and adiabatic losses are taken into account in a self-consistent manner, Blundell & Rawlings (2000) suggest that this may be so only in the young sources with ages much less than 10 Myr. More recently Machalski et al. (2007) have examined the dynamical ages of FRII radio sources and find

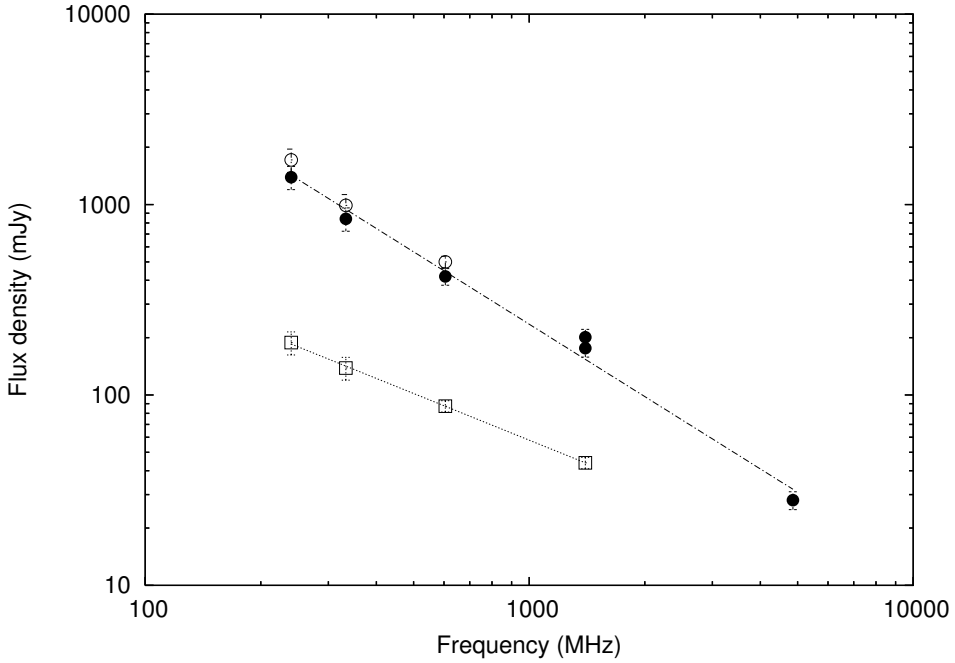

Figure 8.11: The radio spectrum of the diffuse emission. Filled circles denote the flux density of the diffuse extended emission after subtracting the contribution of the inner double-lobed source, the latter being estimated from our GMRT and VLA images of similar angular resolution of ∼12 arcsec. The open circles denote the flux density after incorporating a rough estimate of the flux density not seen in the GMRT low-frequency images compared with the VLA D-array image. The open squares denote the flux densities in a box with a size of ∼150 arcsec centred in the peak of the northern diffuse emission. The dashed lines represent the least-square fits to the points. For the diffuse emission this has been done considering only the points represented by the filled circles.

that while these agree with the spectral ages for objects less than 10 Myr, their method may be applicable for older sources as well. For all objects they find realistic jet advance velocities.

(b) X-ray observations of the inner double

The existing Chandra data for 4C29.30 obtained on 2001 April 8 (OBSID=2135, previously analyzed by Gambill et al. 2003 and Sambruna et al. 2004) reveal x-ray emission associated with the inner radio structure. Although the photon statistics from the archival 7.5 ksec exposure is very low, several x-ray components are visible, namely a highly obscured nucleus, a diffuse galactic-scale halo, hotspot ('HS'), counter-hotpsot ('C-HS'), and possibly both jets connecting hotspot and counter-hotspot with the nucleus. There is also a possible x-ray excess to the south-west from the nucleus, co-spatial with a region of enhanced optical-line emission.

We reprocessed the archival Chandra data using CALDBv.3. The 7.7-ksec ACIS-S observation detected a total of 123±11 counts from the core (a circle of 1.5 arcsec radius). Most of these counts (105) exceed 2-keV energies, which indicate a very hard spectrum. The absorbed power-law model fit shows strong evidence for large intrinsic absorption of $N_{\rm H} \sim (3.5 \pm 0.9) \times 10^{23}$ cm^{-2} for the fixed photon index of $\Gamma = 1.7$, implying the intrinsic unabsorbed luminosity of $L_{2-10\,{\rm keV}} \approx 3 \times 10^{43}$ erg s^{-1}. This is in agreement with the results by Gambill et al. (2003), although our number of total detected counts is larger because we used the updated Chandra calibration to process the data. Such high values of column density have been reported for some compact radio sources (e.g. Guainazzi et al. 2006; Vink et al. 2006). We note that the nucleus of 4C29.30 reveals optical features typical of Seyfert 2

and narrow-line radio galaxies (van Breugel et al. 1986).

Both hotspot and the counter-hotspot regions are pronounced in x-rays (Sambruna et al. 2004). Note that low-power radio galaxies like 4C 29.30 usually do not exhibit strong shocks at the terminal regions of the jets. The Chandra data indicate significant differences in the spectra of both features. In particular, in the case of the hotspot the number of soft ($0.5 - 2$ keV) and hard ($2 - 10$ keV) total counts is $S = 16$(B=1), where B indicates background counts, and $H = 6$(B=1), respectively, giving the hardness ratio $S/H = 2.9^{+3.9}_{-1.3}$; in the case of the counter-hotspots the analogous numbers are $S = 9$(B=1), $H = 1$(B=1), and $S/H = 10.5^{+11.3}_{-6.5}$ (see Park et al. 2006 for the description of the Bayesian methods we used to calculate the hardness ratio and errors). This suggests that the observed hotspot-related x-ray emission, especially in the counter hotspot, may be a mixture of the thermal and non-thermal radiation. The thermal scenario may be particularly relevant for the counter-hotspot region, which is in fact co-spatial with a zone of strong optical lines emission. It is interesting to note that in the radio galaxy Cen A, sharing many morphological similarities with the object discussed here, Kraft et al. (2003) reported detection of thermal x-ray emission at the counter-jet termination region due to galactic gas compressed by the expanding radio outflow. We suggest that the Chandra data may indicate similar jet/ambient medium interactions in the counter hotspot of 4C29.30, although deeper observations are needed to confirm such a scenario. In this context it is relevant to note that the line-emitting gaseous filaments extending along the inner radio structure seem to be heated and accelerated by the expanding jet rather than photoionised by the ambient medium (van Breugel et al. 1986). Evidence of similar jet-cloud interactions have been reported for many radio sources such as the compact steep-spectrum sources 3C48 (Gupta, Srianand

& Saikia 2005) and 3C67, 277.1, and 303.1 (O'Dea et al. 2002).

Another interesting constraint is offered by the polarization studies. As discussed previously, the polarized flux-density from the central parts of 4C 29.30 is most likely dominated by the inner lobes. As argued by van Breugel et al. (1986), large differences between the orientations of the E-vectors in this region when observed at 1400 MHz and 4850 MHz suggest Faraday rotation effects, most likely not due to the observed optical emission-line gaseous clouds, but rather due to the 'intercloud medium'. However, similar rotation of the electric field vector is observed by us also in the outer regions, far (> 100 kpc) beyond the inner radio structure studied by van Breugel et al. This may suggest that the Faraday screen should not be identified with the gaseous medium co-spatial with the inner ($\sim$ few kpc-scale) optical line-emitting clouds, but rather with the ambient thermal gas on larger scales, pushed-out and compressed by the expanding fossil halo, eventually partly mixed with the plasma of the lobes.

8.6 Concluding remarks

We present the results of multifrequency radio observations of the radio galaxy 4C29.30 using the GMRT, the VLA and the Effelsberg telescope.

1. The low-resolution images with the VLA, GMRT and the Effelsberg telescope show evidence of a large scale diffuse emission with an angular scale of $\sim$520 arcsec (639 kpc) in addition to the small-scale inner double which has an angular size of $\sim$29 arcsec (36 kpc). The structure of the inner double is similar to that of FRII radio sources although its radio luminosity is in the FRI category. This is similar to some of the inner doubles in the DDRGs.

2. The GMRT and VLA observations of the inner double show that it has a spectral index of ∼0.8 with no evidence of curvature in its spectrum from 240 to 8460 MHz, suggesting that the inner double which has an edge-brightened structure is young. We have fitted the spectrum using `SYNAGE` for the JP, KP and CI models. The break frequency is large ($\gtrsim 10^6$ GHz) but this value has huge uncertainties because the spectrum is practically straight. Its equipartition magnetic field is 0.43±0.06 nT using the classical formula. The inferred spectral age for the inner double for a conservative lower limit of ∼10 GHz for the break frequency is $\lesssim$33 Myr.

3. The diffuse outer emission represents emission from an earlier cycle of activity. Its total spectrum is steep with a spectral index of ∼1.3, with the break frequency being $\lesssim$240 MHz. Using the classical formula the equipartition magnetic field is 0.07±0.01 nT which yields a radiative age of $\gtrsim$200 Myr.

4. The spectral index for the inner double as well as in the vicinity of the northern peak of the diffuse extended emission is ∼0.8, suggesting that the injection spectral index is close to this value. Although the injection spectrum is somewhat steep, the similarity for the inner double and the outer diffuse emission is reminiscent of J1453+3308 where the outer and inner doubles have similar injection spectral indices (Konar et al. 2006).

5. The magnetic field in the vicinity of the northern peak of the diffuse extended emission is 0.12±0.02 nT. Given its straight spectrum between 240 and 1400 MHz, this yields a spectral age of $\lesssim$100 Myr. Although higher frequency observations are required to extend the spectrum for

both the inner double and the diffuse extended emission, the present data suggests a time scale of interruption of activity of $\lesssim$100 Myr. However, the known caveats regarding estimation of spectral ages should be borne in mind.

6. The radio core exhibits evidence of variability. This is similar to that of the DDRG J1453+3308, suggesting that significant core variability may often occur in galaxies with evidence of recurrent activity.

7. The hotspots of the inner double have been detected at x-ray and optical wavelengths using the Chandra x-ray Observatory and the Hubble Space Telescope. Our reanalysis of the x-ray data suggests that the counter hotspot consists of both thermal and nonthermal material. The thermal x-ray emission may be due to hot gas compressed by the expanding radio-emitting outflow on kpc scales.

References

Baars J.W.M., Genzel R., Pauliny-Toth I.I.K., Witzel A., 1977, A&A, 61, 99

Baum S.A., O'Dea C.P., de Bruyn A.G., Murphy D.W., 1990, A&A, 232, 19

Becker R.H., White R.L., Helfand D.J., 1995, ApJ, 450, 559

Becker R.H., White R.L., Edwards A.L., 1991, ApJS, 75, 1

Blundell K.M., Rawlings S., 2000, AJ, 119, 1111

Bridle A.H., Kesteven M.J.L., Brandie G.W., 1977, AJ, 82, 21

Burns J.O., Feigelson E.D., Schreier E.J., 1983, ApJ, 273, 128

Burns J.O., Schwendeman E., White R.A., 1983, ApJ, 271, 575

Capetti A., Morganti R., Parma P., Fanti R., 1993, A&AS, 99, 407

Clarke D.A., Burns J.O., Norman M.L., 1992, ApJ, 395, 444

Colla G., et al., 1970, A&AS, 1, 281

Condon J.J., Cotton W.D., Greisen E.W., Yin Q.F., Perley R.A., Taylor G.B., Broderick J.J., 1998, AJ, 115, 1693

Emerson D.T., Gräve R., 1988, A&A, 190, 353

Fanti C., Fanti R., Gioia I.M., Lari C., Parma P., Ulrich M.H., 1977, A&A, 61, 487

Gambill J.K., Sambruna R.M., Chartas G., Cheung C.C., Maraschi L., Tavecchio F., Urry C.M., Pesce J.E., 2003, A&A, 401, 505

Giovannini G., Feretti L., Gregorini L., Parma P., 1988, A&A, 199, 73

Giovannini G., Cotton W.D., Feretti L., Lara L., Venturi T., 1998, ApJ, 493, 632

Giovannini G., Taylor G.B., Arbizzani E., Bondi M., Cotton W.D., Feretti L., Lara L., Venturi T., 1999, ApJ, 522, 101

Gizani N.A.B., Leahy J.P., 2003, MNRAS, 342, 399

Gonzalez-Serrano J.I., Carballo R., Perez-Fournon I., 1993, AJ, 105, 1710

Gregory P.C., Condon J.J., 1991, ApJS, 75, 1011

Guainazzi M., Siemiginowska A., Stanghellini C., Grandi P., Piconcelli E., Azubike Ugwoke C., 2006, A&A, 446, 87

Gupta N., Srianand R., Saikia D.J., 2005, MNRAS, 361, 451

Haslam C.G.T., 1974, A&AS, 15, 333

Ishwara-Chandra C.H., Saikia D.J., 1999, MNRAS, 309, 100

Jaffe W.J., Perola G.C., 1973, A&A, 26, 423

Jamrozy M., Klein U., Mack K.-H., Gregorini L., Parma P., 2004, A&A, 427, 79

Jamrozy M., Konar C., Saikia D.J., Stawarz Ł., Mack K.-H., Siemiginowska A., 2007, MNRAS, 378, 581

Jeyakumar S., Saikia D.J., Pramesh Rao A., Balasubramanian V., 2000,

A&A, 362, 27

Jones D.L., Preston R.A., 2001, AJ, 122, 2940

Jones T.W., Ryu D., Engel A., 1999, ApJ, 512, 105

Junkes N., Haynes R.F., Harnett J.I., Jauncey D.L., 1993, A&A, 269, 29

Kaiser, C.R., Cotter, G., 2002, MNRAS, 336, 649

Kaiser C.R., Schoenmakers A.P., Röttgering H.J.A., 2000, MNRAS, 315, 381

Kardashev N.S., 1962, SvA, 6, 317

Keel W.C., Irby B.K., May A., Miley G.K., Golombek D., de Grijp M.H.K., Gallimore J.F., 2005, ApJS, 158, 139

Konar C., Saikia D.J., Jamrozy, M., Machalski, J., 2006, MNRAS, 372, 693

Kraft R.P., Vázquez S.E., Forman W.R., Jones C., Murray S.S., Hardcastle M.J., Worrall D.M., Churazov E., 2003, ApJ, 592, 129

Kronberg P.P., Reich W., 1983, A&A, 125, 146

Kühr H., Witzel A., Pauliny-Toth I.I.K., Nauber U., 1981, A&AS, 45, 367

Langston G.I., Heflin M.B., Conner S.R., Lehar J., Carrilli C.L., Burke B.F., 1990, ApJS, 72, 621

Leahy J.P., Pooley G.G., Riley J.M., 1986, MNRAS, 222, 753

Machalski J., Chyzy K.T., Stawarz Ł., Koziel D., 2007, A&A, 462, 43

Miley G.K., 1980, ARA&A, 18, 165

Morganti R., Killeen N.E.B., Ekers R.D., Oosterloo T.A., 1999, MNRAS, 307, 750

Murgia M., 1996, Laurea Thesis, University of Bologna

O'Dea C.P. et al., 2002, AJ, 123, 2333

Owen F.N., Eilek J.A., Kassim N.E., 2000, ApJ, 543, 611

Pacholczyk A.G., 1970, Radio Astrophysics, W.H. Freeman, San Francisco

Park T., Kashyap V.L., Siemiginowska A., van Dyk D.A., Zezas A., Heinke C., Wargelin B.J., 2006, ApJ, 652, 610

Parma P., de Ruiter H.R., Fanti C., Fanti R., 1986, A&AS, 64, 135

Perley R.A., Fomalont E.B., Johnston K.J., 1982, ApJ, 255, 93

Pilkington J.D.H., Scott P.F., 1965, MemRAS, 69, 183

Reich W., Stute U., Reif K., Kalberla P.M.W., Kronberg P.P., 1980, ApJ, 236, 61

Rengelink R.B., Tang Y., de Bruyn A.G., Miley G.K., Bremer M.N., Röttgering H.J.A., Bremer M.A.R., 1997, A&AS, 124, 259

Riley J.M.W., Waldram E.M., Riley J.M., 1999, MNRAS, 306, 31

Roettiger K., Burns J.O., Clarke D.A., Christiansen W.A., 1994, ApJ, 421, 23L

Rudnick L., Katz-Stone D.M., Anderson M.C., 1994, ApJS, 90, 955

Saikia D.J., Kulkarni V.K., 1994, MNRAS, 270, 897

Saikia D.J., Konar C., Kulkarni V.K., 2006, MNRAS, 366, 1391

Sambruna R.M., Gambill J.K., Maraschi L., Tavecchio F., Cerutti R., Cheung C.C., Urry C.M., Chartas G., 2004, ApJ, 608, 698

Schoenmakers A.P., de Bruyn A.G., Röttgering H.J.A., van der Laan H., 1999, A&A, 341, 44

Schoenmakers A.P., de Bruyn A.G., Röttgering H.J.A., van der Laan H., Kaiser C.R., 2000, MNRAS, 315, 371

Stanghellini C., O'Dea C.P., Dallacasa D., Cassaro P., Baum S.A., Fanti R., Fanti C., 2005, A&A, 443, 891

Stute U., Reich W., Kalberla P.M.W., 1980, A&AS, 42, 299

Thierbach M., Klein U., Wielebinski R., 2003, A&A, 397, 53

van Breugel W., Fomalont E.B., 1984, ApJ, 282, 55L

van Breugel W.J.M., Heckman T.M., Miley G.K., Filippenko A.V., 1986, ApJ, 311, 58

van der Laan H., Zieba S., Noordam J.E., 1984, in IAU Symp. 110: VLBI

and Compact Radio Sources, p. 9.

Vink J., Snellen I., Mack K.-H., Schilizzi R., 2006, MNRAS, 367, 928

White R.L., Becker R.H., 1992, ApJS, 79, 331

CHAPTER 9

Conclusions and future work

9.1 Concluding remarks

Our multifrequency observations of GRSs and DDGRs with the GMRT and the VLA have helped clarify various issues regarding their structure, evolution, effect of inverse-Compton scattering against the CMB photons on the bridge emission, their environments, ages, radio spectra and the injection spectral indices ($\alpha_{\rm inj}$, defined as $S_\nu \propto \nu^{-\alpha}$) of the radio lobes.

GRSs: We have observed a sample of 17 GRSs at frequencies starting from $\sim$240 to $\sim$8000 MHz using GMRT at low frequencies and the VLA at high frequencies. These observations have either helped clarify the radio structures or provided new information at a different frequency. The broad line radio galaxy, J0313+413, has an asymmetric, curved radio jet and a variable radio core, consistent with a moderate angle of inclination to the line of sight. We suggest that the lobes of emission in J0139+399 and J0200+408 may be due to an earlier cycle of nuclear activity. We attempt to identify either GPS or steep spectrum radio cores, which may be a sign of renewed activity. We identify a few possible candidates. If confirmed, this would indicate a trend for steep spectrum cores to occur preferentially in GRSs.

To understand the evolution of GRSs one needs to consider the effects of synchrotron and inverse-Compton losses as well as the external environment.

The equipartition magnetic field strength in the radio lobes, B_{eq}, estimated using the classical formula (see, e.g., Miley 1980), is smaller than the equivalent magnetic field of the microwave background radiation, B_{iC}, for giant sources; while the reverse is true for the smaller powerful sources such as those chosen from the 3CR sample. If the values of B_{eq} are representative of the true magnetic field, the inverse-Compton losses dominate for the GRSs, while synchrotron radiation losses are more important for the smaller powerful sources. Although the difference is less marked if one uses the magnetic field estimates using the Beck & Krause (2005) formalism, this is still likely to limit the number of GRSs at large redshifts.

We have imaged the highest redshift giant quasar, J1432+1548, at a redshift of 1.005 with the GMRT at 333 and 617 MHz. Although we detect a radio jet and have been able to demonstrate the outer components are related we do not detect prominent bridge emission, possibly due to inverse-Compton losses.

Spectral ageing analysis has been done for a sample of 10 GRSs. Although some caveats regarding the variation of magnetic field in the lobes need to be borne in mind (e.g. Blundell & Rawlings 2000; Carilli et al. 1991; Katz-Stone 1995), spectral ageing analysis provides an importnat and interesting input towards understanding the physical properties of the lobes of these sources. The maximum spectral ages estimated for the detected radio emission in the lobes of our sources range from $\sim$6 to 36 Myr with a median value of $\sim$20 Myr using the classical equipartition fields. Using the magnetic field estimates from the Beck & Krause formalism the spectral ages range from $\sim$5 to 38 Myr with a median value of $\sim$22 Myr. These ages are significantly older than smaller sources (e.g. Leahy et al. 1989; Liu et al. 1992). The spectral ages depend on the estimated magnetic fields. Strengths of the

equipartition field calculated with the revised formalism proposed by Beck & Krause (2005) are greater than the corresponding values provided by the classical formula of Miley (1980) by a factor of $\sim$3. However, the inferred synchrotron age is a function of the ratio $B/B_{\rm iC}$. If B is greater than $B_{\rm iC}/\sqrt{3}$, the 'revised' age is lower than the 'classical' age. Even though the estimates of magnetic field using classical-equipartition (e.g. Miley 1980) and Beck & Krause (2005) methods differ by a factor of 3, the spectral ages ('revised' age and 'classical' age) have similar values. A study of the symmetry parameters of these sources show that their environments are asymmetric on these large scales.

The injection spectral indices range from 0.55 to 0.88 with a median value of $\sim$0.6. Our estimates for the GRSs are smaller than those estimated for smaller sources by Leahy et al. (1989) and Liu et al. (1992). We have explored possible correlations of $\alpha_{\rm inj}$ with other physical parameters and find that it appears to increase with luminosity and redshift, but shows an inverse correlation with linear size.

DDRGs: We have reported the discovery of a new DDRG, namely J0041+3224, with the help of the GMRT. A study of the symmetry parameters of the inner doubles and outer doubles of a dozen DDRGs reveals that the inner doubles tend to be statistically more asymmetric in both its armlength and its flux density ratios compared to the outer doubles. If we define all the symmetry parameters to be greater than 1 then for armlength ratio the median values are 1.3 and 1.1 for the inner and outer doubles respectively. For the flux density ratio the median values are 2.5 and 1.4 for inner and outer doubles respectively. These trends need to be understood since the jets of the inner double are advancing outwards through the cocoon created by the earlier

cycle of activity, and one might expect them to be more symmetric. We also find that the outer doubles are more misaligned than the inner ones. This could be due to large scale density gradients and possible motion of the host galaxy between the two cycles of activity.

We have made a detailed multifrequency study of the well-known DDRG J1453+3308 using both the GMRT and the VLA. The VLA high-resolution images show the edge brightened structure of the inner double, while the lower resolution GMRT and VLA images show both the inner and outer pair of doubles. The spectrum of the outer double has a curvature towards the low-frequency part of the spectrum, whereas the spectrum of the inner double is practically a single power law over the wide frequency range. The spectral age of the outer double is about 50 Myr while that of the inner double is about $\leq$ 2 Myr. The core exhibits some evidence of variability.

In addition to the DDRGs, diffuse relic radio emission due to an earlier cycle of activity may also be visible around a young radio source with a classical double-lobed structure. We report the discovery of one such object, namely 4C29.30, where the diffuse emission has an extent of $\sim$640 kpc while the young inner double-lobed structure has an overall size of about 36 kpc. The spectral indices of the outer diffuse emission and the inner double are about 1.3 and 0.8 respectively. The estimated age for the outer emission is $\gtrsim$200 Myr while that of the inner double is $\lesssim$33 Myr. The core in 4C29.30 also exhibits evidence of variability. A remarkable result obtained through the spectral ageing analyses of J1453+3308 and 4C29.30 is the similarity of the values of $\alpha_{\rm inj}$ in the previous and the current cycles of jet activity.

9.2 Future work

(a) On x-ray and radio observations of GRSs

The very existence of GRSs raises important questions about the properties of the IGM they inhabit. For radio lobes to exist, there must be a medium to confine them, either through thermal pressure or ram pressure. On Mpc scales, the external pressure even in a rich cluster must be several orders of magnitude lower than in the typical environments of smaller radio galaxies, and in fact we know already that GRSs do not inhabit particularly rich environments. What phase of the IGM governs the dynamics of GRSs? If we could answer this question, it would be possible to use GRSs at cosmological redshifts to probe the evolution of this phase over cosmic time.

To answer this question we need to measure the pressures in the lobes of GRSs. X-ray observations allow us to do this via the inverse-Compton process, in which the relativistic electrons in the lobe scatter photons of the CMB, the dominant photon field on the relevant size scales. Detections of inverse-Compton emission have the potential to clarify the particle content and magnetic field strength because they allow direct measurements of the electron energy density, unlike observations of radio synchrotron emission where the electron density and the magnetic field strength cannot be decoupled (cf. Croston et al. 2005). This technique has been used successfully to estimate magnetic field strengths in the lobes and hotspots of many smaller FRII (Fanaroff & Riley 1974) sources, and constrain source dynamics and particle content by comparing the internal pressure with that of the external pressure from x-ray emitting hot gas (Hardcastle et al. 2002; Croston et al. 2004). A study of x-ray emission from the lobes of a sample of FRII radio galaxies and quasars has shown that although a few may be magnetically

dominated by factors of 2 or more, about 70 per cent of the sample have magnetic field strengths within ∼35 per cent of the equipartition value, or electron dominance (U_e/U_p) by a factor of ∼5 (Croston et al. 2005). The key point, however, is that observations of inverse-Compton radiation allow us to measure the internal pressure in the lobes of individual objects. This then allows us to understand the dynamics of the radio source.

To date there has been little attempt to study the lobes of powerful giant radio galaxies using this technique. Partly this is a consequence of much of the early work having been done with the *Chandra* x-ray telescope, with its relatively small field of view and limited surface brightness sensitivity. Inverse-Compton detections of true giant sources are essential if we are to measure the lobe pressures, and thus the pressure of the confining medium, in this poorly understood population.

XMM (X-ray Multi-mirror Mission) observations of GRSs will go some way towards providing this information, probing the class of luminous, relatively distant GRSs that present the greatest problems for confinement models. In addition, such observations will allow us to compare the measured magnetic field strengths and energy densities with those already derived from smaller sources, to look for evidence of the evolution of the magnetic field and electron population as a function of source size and therefore age. The magnetic field values will also help us constrain which of the formalisms described in this thesis for estimating equipartition fields would be most appropriate.

With sensitive x-ray observations which are sufficient to measure fluxes and spectra for these objects, one can

- try to establish that we are indeed seeing inverse-Compton emission from the lobes of our targets, and so measure lobe pressures.

- measure, and separate from the lobes, any x-ray emission from a hot-gas environment, and thus

- determine the pressure of the medium required to confine the radio lobes, compare it with the available pressure from any hot-gaseous environment present, and so establish whether GRSs are simply probing the extreme edge of the intra-group or intra-cluster media, or whether they require some other medium for lobe formation on these scales to be possible.

This will mean that we can

- gain an understanding of what the properties of GRSs are telling us, and how they can be used as cosmological probes.

and, in addition, we will be able to

- compare the magnetic fields and energy densities measured for our targets with those already determined for smaller FRII sources, and compare any relationship with size and radio source age to the predictions of models.

(b) On identification of episodic activity in FRI and FRII radio sources

The duration of the AGN phase of galaxies, what physical conditions determine radio loudness and time scales of episodic activity are important issues in our understanding of galaxies. An interesting way of probing the history of radio-loud objects is via the structural and spectral information of the lobes of extended radio emission. It is important to study FRI and FRII

radio sources not only for understanding episodic jet activity and examining their time scales, but also for studying the propagation of jets in different media. In DDRGs we see two episodes of activity, but the number of such episodes of activity may not be confined to only two. It would be astrophysically interesting to search for a 'triple-double' or identify multiple episodes of activity in an AGN.

(c) On spectral ageing analysis

For a sample of GRSs and a couple of DDRGs we have done a detailed spectral ageing analyses. We found that the spectral ageing models fit the data reasonably well. According to Blundell & Rawlings (2000) spectral ages are representative of true ages when they are $\lesssim$ 10 Myr. Machalski et al. (2007) found for a few GRSs that the spectral ages are lower than dynamical ages at most by a factor of 4. Extensions of the spectral ageing analyses would be dynamical ageing analyses of these sources. Comparing the spectral and dynamical ages for a sample of GRSs could provide further insights into the properties and evolution of these sources.

The spectral ageing analyses of our two DDRGs have found that they are consistent with the hypothesis that their double-double morphology is due to two episodes of nuclear activity. These analyses have also found that the injection spectral indices of previous and current episodes of activity is the same in each DDRG. To establish whether this is something universal or just a coincidence, a study of a large sample of DDRGs is important.

References

Beck R., Krause M., 2005, Astron. Nach., 326, 414

Blundell K.M., Rawlings S., 2000, AJ, 119, 1111

Carilli C.L., Perley R.A., Dreher J.W., Leahy J.P., 1991, ApJ, 383, 554

Croston J.H., Birkinshaw M., Hardcastle M.J., Worrall D.M., 2004, MNRAS, 353, 879

Croston J.H., Hardcastle M.J., Harris D.E., Belsole E., Birkinshaw M., Worrall D.M., 2005, ApJ, 626, 733

Fanaroff B.L., Riley J.M., 1974, MNRAS, 167, 31

Hardcastle M.J., Birkinshaw M., Cameron R.A., Harris D.E., Looney L.W., Worrall D.M., 2002, ApJ 581, 948

Katz-Stone, D.M., 1995, Ph.D. thesis, University of Minnesota

Leahy J.P., Muxlow T.W.B., Stephens P.W., 1989, MNRAS, 239, 401

Liu R., Pooley G., Riley J.M., 1992, MNRAS, 257, 545

Machalski J., Chyży K.T., Stawarz L., Koziel D., 2007, A&A, 462, 43

Miley G., 1980, ARA&A, 18, 165

APPENDIX : A

Estimating classical equipartition magnetic field

In this paper we estimate the magnetic field using the revised equipartition method (Beck & Krause 2005) as well as the widely used classical minimum energy approach summarised by Miley (1980) and also a variant of this method which is described below. The latter two approaches are referred to as classical-1 and classical-2 in this paper. Since the expressions in the literature for the classical-1 approach are for a power law spectrum, and many of the GRSs show evidence of curvature in the integrated spectrum, we estimate the magnetic field by numerically integrating over the non power-law spectrum.

To derive a general formula for the minimum energy magnetic field for non power-law spectra we proceed as follows. The equations used are summarised here. The critical frequency at which an electron of energy E radiates most of its energy is given by

$$\nu = C_1 B(sin\phi)E^2 \tag{A.1}$$

where $C_1 = 6.266 \times 10^{18}$ in cgs units, and is a constant (Pacholczyk 1970). The energy loss of a single electron is given by

$$-\frac{dE}{dt} = C_2 B^2(sin^2\phi)E^2 \tag{A.2}$$

where $C_2 = 2.368 \times 10^{-3}$ in cgs units, is also a constant (Pacholczyk 1970).

Let us assume that the number of electrons between E and $E + dE$ is given by $N(E)dE$. They will radiate via synchrotron emission between ν and $\nu+d\nu$, where ν and E are related by the equation (A.1). The monochromatic luminosity, $L(\nu)$, is given by

$$L(\nu)d\nu = N(E)dE \times (-\frac{dE}{dt}). \tag{A.3}$$

Substituting the value of $-\frac{dE}{dt}$ from equation (A.2) we get

$$N(E)dE = \frac{C_1}{C_2}\frac{1}{Bsin\phi}\frac{L(\nu)}{\nu}d\nu. \tag{A.4}$$

The total kinetic energy of the electrons is given by

$$U_e = \int EN(E)dE = \frac{1}{B^{3/2}sin^{3/2}\phi}C_4\int\frac{L(\nu)}{\sqrt{\nu}}d\nu, \tag{A.5}$$

where E has been substituted from equation (A.1) and C_4=$\frac{\sqrt{C_1}}{C_2}$ is 1.05709×10^{12} in cgs units.

The above expression can be re-written as

$$U_e = \frac{A}{B^{3/2}sin^{3/2}\phi}, \tag{A.6}$$

where

$$A = C_4\int\frac{L(\nu)}{\sqrt{\nu}}d\nu. \tag{A.7}$$

Assuming the proton to electron energy density ratio to be κ we get the total energy expression as

$$U_{tot} = (1+\kappa)U_e + U_B = \frac{(1+\kappa)A}{B^{3/2}sin^{3/2}\phi} + V\frac{B^2}{8\pi}. \tag{A.8}$$

Differentiating U_{tot} with respect to B and equating $\frac{dU_{tot}}{dB}$ to zero we get the minimum energy expression

$$B_{min} = (\frac{6\pi A(1+\kappa)}{V sin^{3/2}\phi})^{2/7}, \tag{A.9}$$

where A is given by equation (A.7), while V and $L(\nu)$ can be written as follows:
$V = \eta f_s \frac{d_A^2 \theta_x'' \theta_y'' s}{(206265)^2}$, and $L(\nu) = 4\pi d_L^2 S(\nu)$. Here, η is the filling factor, f_s is a shape factor for the volume of the emission region, which assumes a value of $\frac{\pi}{4}$ for a cylinder and $\frac{\pi}{6}$ for an ellipsoid, d_A and d_L are angular-diameter and luminosity distances respectively, θ_x'' and θ_y'' are the two projected dimensions of the emission region, s is the depth of the emission region.

So far, all ν and $S(\nu)$ values are in emitter's frame. Converting them into the quantities of observer's frame and expressing the quantities in practical units we get

$$B_{min}(\mu G) = 10^6(1+z)[\frac{3.26604 \times 10^{-32}}{sin^{3/2}\phi} \frac{(1+\kappa)A'}{\eta f_s \theta_x'' \theta_y'' s(kpc)}]^{2/7}. \tag{A.10}$$

Here $A' = C_4 \int_{\nu_1^o}^{\nu_2^o} \frac{S^o_{mJy}(\nu^o)}{\sqrt{\nu^o_{MHz}}} d\nu^o_{MHz}$. The superscript 'o' indicates that the quantities are in the observer's frame. The integration should be carried out within a frequency interval which is compatible with the emitter's frame frequency interval set by us; $(2/3)^{3/4}$ has been substituted for $sin^{3/2}\phi$ in the above equation to estimate B_{min}, as the average value of $sin^2\phi = \frac{2}{3}$.

As a first step, we fit the observed flux density measurements with the spectral ageing models of Jaffe & Perola (1973, hereinafter referred to as JP) as well as Kardashev (1962) and Pacholczyk (1970), hereinafter referred

as KP, with the help of the *SYNAGE* package (Murgia 1996), and then extrapolate to very low and high frequencies. For the integration limits, we first use the range 10 MHz − 100 GHz in the emitter's frame for the classical-1 approach. For classical-2 we set the integration limit such that the lower limit corresponds to a Lorentz factor, γ_{min} of ∼10 while the upper limit corresponds to 100 GHz, as in classical-1 (see Myers & Spangler 1985; Hardcastle et al. 2004; Croston et al. 2005). Since, we don't have an independent estimate of the magnetic field to start with, we assume a lower limit, say, 10 MHz to start with, keeping the upper limit fixed at 100 GHz. Then we calculate the magnetic field and check what value of γ_{min} does the lower limit of frequency correspond to using the relation $\nu = C_1 B sin\phi(\gamma - 1)^2 m_e c^2$, where m_e is the rest mass of the electron and c represents the velocity of light. Then we vary the lower limit iteratively till we get γ_{min} close to 10.